Multiphase flows with phase change and boiling in quenching processes

Mehdi Khalloufi

THÈSE DE DOCTORAT

de l'Université de recherche Paris Sciences et Lettres
PSL Research University

Préparée à MINES ParisTech

MULTIPHASE FLOWS WITH PHASE CHANGE AND BOILING IN QUENCHING PROCESSES

Ecoulements multiphasiques avec changement de phase et ébullition dans les procédés de trempe

École doctorale n°364 Sciences Fondamentales et Appliquées
Spécialité Mécanique Numérique et Matériaux

COMPOSITION DU JURY :

Pr. Antonio HUERTA
Universitat Politècnica de Catalunya, Président

Pr. Marek BEHR
RWTH Aachen University, Rapporteur

Pr. Johan HOFFMAN
KTH Royal Institute of Technology, Rapporteur

Pr. Boniface NKONGA
Université Nice Sophia Antipolis, Examinateur

Pr. Peter SPELT
Ecole Centrale Lyon, Examinateur

Pr. Rudy VALETTE
Mines ParisTech, Examinateur

Pr. Elisabeth MASSONI
Mines ParisTech, Examinateur

Pr. Elie HACHEM
Mines ParisTech, Examinateur

Soutenue par **Mehdi KHALLOUFI**
le 11 décembre 2017

Dirigée par
Rudy VALETTE
Elisabeth MASSONI
Elie HACHEM

MINES ParisTech | PSL RESEARCH UNIVERSITY PARIS

Contents

List of Figures

List of Tables

Chapter 1

Introduction

Contents

1.1 Introduction to quenching

Quenching processes of metals are widely adopted procedures in the industry, in particular automotive, nuclear and aerospace industries, since they have direct impacts on changing mechanical properties, controlling microstructure and releasing residual stresses of critical parts. Safety being the highest priority in these industries, the elaboration of a part must be compliant with the highest standards.

Quenching is a process that belongs to the family of heat treatments. Heat treatments aim at giving a certain microstructure to the metal to obtain desired mechanical properties. A part is heated in a furnace to allow the diffusion of specific atoms (e.g. carbon atoms). To prevent segregation of theses atoms during the cooling phase and therefore inhomogeneity of the microstructure, the cooling must be sudden. As a consequence, the control of the cooling rate is of the utmost importance in the quenching.

Quenching is generally carried out by immersing the part in a medium that will extract the heat contained therein (see Fig. 1.1). The medium may be a liquid (water, oil, polymer,...) or a gas (air, nitrogen, helium, argon,...). An inhomogeneous cooling of the part leads to uncontrolled distortion and cracks. In the case of complex geometries, the control of the cooling rate is even more difficult to achieve. During quenching, heat transfers are performed through a solid/fluid interface.

In the case of a liquid quenching medium (known as the quenchant), a vapor film surrounds the part because of the high thermal gradient at the interface, insulating the part from cooling (see 1st picture in Fig. 1.2). This phenomenon, known as calefaction, can last several hours in the case of massive parts. The main heat transfer mechanisms during calefaction are radiation and conduction through the vapor. The cooling rate is therefore very low and this phase needs to be shortened in order to improve the efficiency of the process. When the surface temperature of the metal is lower than a critical temperature, the liquid comes into contact with the surface and the liquid boils from the surface; this is nucleate boiling. The heat transfer during this

phase is the most efficient of the whole process and the maximum cooling rate is reached. At the end of the process, when the surface temperature of the metal is lower than the temperature of vaporization of the quenchant, the boiling ceases and the cooling is achieved by convection (see last picture in Fig. 1.2).

Figure 1.1: Quenching of industrial parts in a liquid medium.
Pictures taken from: a) thermalhire.com, b) westernindiaforgings.com, c)d) conmecheng.com, e) heattreatmentsservices.com, f) heattreatmart.com, g) Tata, h) Tenaxol.

The cooling rate of the part depends on several parameters: thermal properties of the metal and their evolution w.r.t. temperature, geometry of the part, thermal and physical properties of the quenching medium and their evolution w.r.t. temperature, operating conditions (volume and agitation of the quenching medium, orientation of the part, surface state of the part,...)[1].

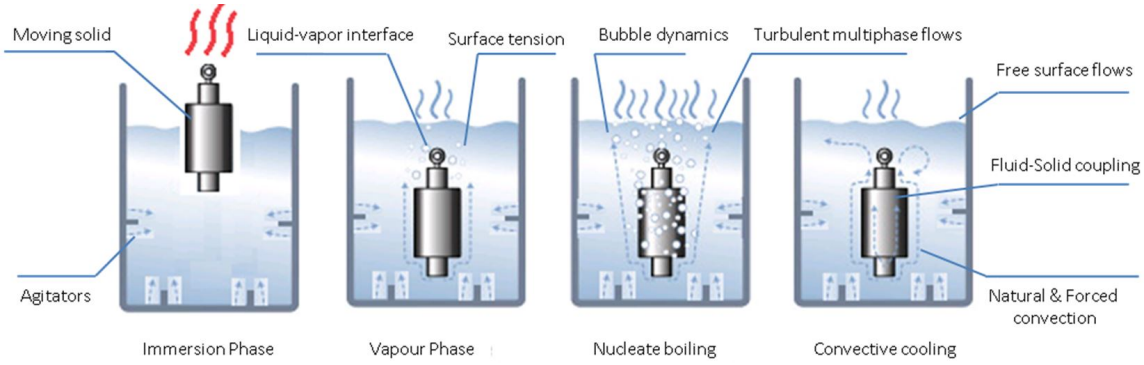

Figure 1.2: Interactions and complexity of the involved physics at different time and space scale during the successive stages of immersed quenching. (credit : www.wizcol.com & Infinity ANR Chair)

However, manufacturers only have few means to control the cooling rate while all the aforementioned parameters have to be taken into account. The efficiency of the process relies on the ability of the quenching medium to achieve maximum cooling of the part without heating up. For instance, using a large quenching tank with constant renewal of the quenchant avoids excessive heating of the quenchant. To take another example, an efficient quenching requires that no vapor is trapped in a cavity due to an unfavorable orientation of the part. This can be avoided if the part is oriented in the right way, with possibility for a stirred quenching medium to be in contact with the whole surface.

1.2 Motivation

Today there is a strong demand from many industrial companies to control this cooling process taking into account optimal combinations of quench parameters with their complexity in order to obtain the desired metallurgical properties such as hardness and yield strength. This demand is accented by the severe requirements in shorter deadlines to design new materials and high quality product. Indeed, the mastering of the cooling rates respecting the metallurgical route with a good homogeneity and reliability is essential to achieve the required microstructure and the mechanical performance.

A full experimental optimization of this process is not a viable strategy due to the cost of the processes involved (see the size of the ingot in Fig. 1.3). A physical modeling of the system and a numerical simulation is then the alternative since Computational Fluid Dynamics (CFD) offers a powerful tool due to the increasing performance of computational resources. However, a clear knowledge of the physical phenomena occurring during this process is required. The heat transfer of a metallic part under extreme conditions such as quenching still represents a challenging issue in industrial processes and will be tackled in this thesis.

Numerical simulation is a quite standard tool in the framework of metallurgical industry for forming processes but at this time no software is predictable enough due to the complexity of the boiling multiphase flows during immersed or jet quenching. A precise numerical modeling that offers detailed understanding of the complex behavior of fluid flow and its impact on part cooling is then a subject of major importance. Indeed, it allows first to reduce the time and cost of developing new materials (by reducing time experimentation), and therefore to continually develop safe and reliable products that meet the customer specifications and second, to improve the designing of quenching systems, limiting production costs and decreasing energy

Figure 1.3: Ingot - Areva NP

consumption.

Despite the evident industrial interest for modeling precisely quenching process during alloy heat treatment, there is no global study neither global answer addressing this problem in an industrial context. In order to predict precisely the liquid-to-vapor phase transition during boiling as well as to study the optimal combinations of quench parameters to reduce residual stresses in solid ingots, an innovative coupled numerical framework needs to be designed and implemented.

Modeling the liquid-to-vapor phase change, predicting different boiling modes with the transition between them and modeling the fluid-solid-heat coupling with solid phase transformation are mainly aimed. The main representative quenching environments that will be considered is immersed quenching. Moreover a large part of the proposed work will be also dedicated to analytic and experimental investigations.

A variety of numerical codes for quenching processes have been developed with variable levels of success since the late 1980s [2]. The work by Garwood et al. [3] is one of the first attempts to characterize a quench tank using computational fluid dynamics. Almost 20 years later, an agitated quench tank was analyzed during the heat treatment of an aluminum cylinder [4].

Although computational fluid dynamics are being used increasingly in quenching tank design, there is still considerable imprecision due to assumptions that must be made in particular the use of simple geometries and approximated quenching environment. Under the pressure of industrial needs and taking advantage of the rapid increase of affordable computer performance, many developments were tested in laboratories and introduced in actual heat treatment commercial codes. Today there is a strong demand from many industrial companies to introduce more realistic physical behavior and also to predict precisely the liquid-to-vapor phase transition during boiling as well as the fluid-solid-heat coupling with solid phase transformations which are both interrelated and of major importance concerning the final metallurgical properties.

A precise numerical modeling that offers detailed understanding of the complex behavior of fluid flow and its impact on part cooling is then a subject of major importance. Indeed, it allows first to reduce the time and cost of developing new materials, and therefore to continually develop safe and reliable products that meet the customer specifications and second, to improve the design of quench systems. Detailed cooling rates can then be used to predict part metallurgical properties.

The classical well known methods for thermal treatment of a solid generally refer to the

use of experimentally deduced heat transfer coefficients. These latter replace the quenching environment. This approach is obviously simple but limited by any necessity to develop either new materials or new quench devices. On the other hand, the quenching fluid environment is classically modeled using a multiphase framework that consists on the resolution of a fluid motion with an interface tracking, which separates liquid from vapor, combined with additional film and boiling heat transfer coefficients. This framework is quite convenient for coupling thermal, mechanical with empirical physical computations, but it suffers severe limitations and needs generally a large amount of experiments to identify precisely, according to a new geometry, agitation rate, fluid viscosity, tank size, and other variables, the transfer coefficients describing different boiling modes and the transition between them.

Finally a coupled approach that models both the fluid-solid interactions is then potentially much more accurate. But due to the differences between existing numerical methods and to the computational cost related to the strategy of coupling them, such approach seems today limited.

Indeed, providing advanced metallurgical solutions is progressively required in the most demanding industries especially aerospace, automotive or energy generation. This covers all the range of production for high performance steels, titanium alloys, aluminum or next generation nickel-based superalloys, from elaboration to machining. For all these materials, many mechanical and microstructural properties are required. These characteristics are strongly dependent on the thermal history during all the manufacturing process. Consequently, cooling rates or temperature history have to be predicted at any location of the parts, during heat treatments.

Moreover, increasingly stringent demands by customers, concerning product quality and consistency and the need to continually process new grades of steel, require that steel producers develop improved control of process routes and quenching systems.

Direct economic and societal benefits are expected for the different industries, in particular automotive, nuclear and aerospace. The improvement of the quenching process must enable them to continuously develop high quality products that meet the increasingly stringent demands by customers while minimizing residual stresses, controlling microstructure, improving the thermo-mechanical and metallurgical behavior and finally optimizing the energy efficiency. It allows the industrials to make considerable savings (>30%) not only in energy but also in consumption of waste metal, quenching liquids and services and CO_2 emission.

This work was done within the consortium THOST (THermal Optimization SysTem), which is supported by 6 industrial partners: Areva NP, Aubert & Duval, Faurecia, Industeel CRMC (Arcelor Mittal), Lisi Aerospace and Safran. All the numerical developments will serve to extend the software THOST towards industrial quenching. Indeed, the scientific editor Science Computer and Consultants (SCC), working in close relation with the CFL research group, will use these developments and insert them in the upcoming version of THOST and will distribute it to the partners. This allows an outstanding dissemination for the results of the thesis. This software is supported today by 8 industrial partners, regroups almost 20 industrial users and will be completed by a newly obtained ANR (French National Research Agency) industrial chair regrouping a consortium of 12 industrials.

The success of this project will be instrumental in developing innovative framework that has the ability to design advanced engineering systems using multiphase CFD with boiling. Note also that these developments will serve also in the in-house C++ library Cimlib-CFD, developed by the CFL research group, bringing two-phase flow applications in other areas of engineering: microfluidic, renewable energy, medicine, biology and more.

1.3 State of the art

Several studies in the literature, most of them are experimental investigations under simplified conditions, shows that quenching severity is dependent on different parameters: agitation rate, size of the tank, fluid viscosity, type and placement of agitators, and other variables [5, 6, 7]. It is know that agitation clearly affects the hardness and depth of hardening during the quenching because of the mechanical rupture of the relatively unstable film boiling cooling process that typically occurs in vaporizable quenchants such as oil, water, and aqueous polymers [5]. However, other variables such as fluid viscosity and vapor pressure of the fluid are clearly important as well. For instance, it has been reported in [6] that the ability to through-harden given steel in a conventional quench oil increased with increasing agitation. Authors in [7, 8, 9, 10] also showed that increasing agitation increased cooling rates and the through-hardening ability of both oil and water quenchants [5, 11, 12]. They showed that agitation of a quenching oil was necessary to destabilize film boiling and nucleate boiling processes if uniform heat transfer throughout the quenching operation was to be achieved. Moreover, the relative efficiency of using immersion or spray quenching with an aqueous polymer and a mineral oil quenchant was studied in [9]. Their results showed that depth of hardness increased with increasing agitation. In [1], the author proposed that cracking and deformation are predominantly affected by the uniformity of the quenching and not the quenchant itself. Simulations of wall nucleate boiling (WNB) were done by Dhir et al. in [13, 14, 15]. Since WNB is dominated by solid-wall, thin-film nanophysics, Dhir et al. coupled their two-dimensional DNS code with a nanofilm, lubrication-theory model. This model is applied at the base of the nucleating bubble [14] and provides the vapor mass source near heated wall.

In view of this review, it is clear that the physical phenomena taking place are rich and that the experimental investigations remains time consuming, difficult to realize and not reliable in a real industrial context. Thus, direct numerical simulation would open up for detailed study and new insights. Indeed, it becomes of prime importance to simulate and visualize the complexity of the flows (liquid-vapor phase transition, agitation,...) and to deal with fluid-solid-heat coupling. Of course both challenges are intrinsically linked.

In the literature, various efforts were proposed to deal with this process. They can be gathered into two groups : one-fluid flow model with boiling heat transfer coefficients or two-fluid model with heat transfer coefficients for the solid part. In the latter case, the classical approach is to combine the fluid motion with interface tracking technique such as level set [16], phase field [17], Volume Of Fluid [18], etc. For example, Garwood et al. [3] have characterized a quenching tank for the heat treatment of superalloy via finite difference methods and heat transfer coefficients. Srinivasan et al. [4] developed a specific CFD modeling procedure to simulate particular immersion quench cooling process using boiling transfer coefficients. Engine cylinder heads have also been modeled using heat transfer coefficients.

As expected, computational fluid dynamics is now being used increasingly for multiphase flows and quenching design. However there are still considerable uncertainties due to assumptions that must be made in particular: (i) the use of simple geometries, (ii) the use of decoupled fluid-solid resolution and finally, (iii) the use of transfer coefficients that approximate the complex quenching environments. Moreover, the consequences of the numerical method limitations are the set of physical model assumptions, e.g. : incompressibility, low density ratio between phases, omission of heat conduction in one of the phases, low-fidelity for boiling phenomena, laminar flows, ... Most of these assumptions are justifiable for their intended applications; however their use remains generally limited and suffers from systematic re-validation when facing new materials, new geometries or new thermomechanical conditions ... Indeed one needs to

predict precisely the liquid to vapor phase change during boiling as well as to study the optimal combinations of quenching parameters to reduce residual stresses in solid ingots. Therefore an innovative couple numerical framework remains to be designed and implemented.

1.4 Contribution of the thesis

We believe that achieving a breakthrough requires first the development of a unified ground-breaking numerical multiscale framework for quenching and, second, the development of an immersed multiphase strategy with implicit representation of each phase (liquid-vapor-solid) in order to leverage the simplicity and flexibility of fluid-solid-heat coupling.

An innovative multiscale numerical framework to design industrial quenching process safely will be proposed. It should provide the industrial partners access to the cooling efficiency of their quenching devices, but also to deeply understand the process issues and to classify which phenomenon plays a major role on the thermal homogeneity of the product. It should allow the industrials to continuously improve the product quality, and even to create new microstructures, in order to fulfill the current and future demands of customers. Finally, it should support the industrials to adjust and to regulate their quenching devices limiting though several tests and trials and empirical calibrations.

Therefore we propose a new Finite Element numerical immersed framework based on an implicit representation of different phases (liquid, gas, solid) using a level set description combined with remeshing capabilities. Several validations will be conducted and comparison will be proposed with benchmark solutions and experimental results.

Indeed, the immersed volume methods is intensively used for two fluid modeling in the context of multiphase flows and for the fluid-structure interactions in the context of heat and mass transfer [19, 20, 21, 22, 23].

To achieve high-fidelity spatial resolution, we will use the work done in CEMEF by the CFL research group on anisotropic parallel adaptive meshing techniques [23, 24, 25, 26, 27, 28]. Indeed, it is shown in recent works that edge-based error estimator allows to dynamically track moving interfaces, thus enabling high-accuracy not only in the bulk fluid, but also near the interface, where high gradients are concentrated. The computational cost remains reasonable for simple applications and improving our parallel 3D remeshing method is another promising route for this objective.

Finally, it is important to mention that classical Finite Element methods to solve the unsteady Navier-Stokes and heat transfer equations suffer from lack of stability, in particular at high Reynolds and Peclet numbers. Another numerical issue related to the transport level set equation is the mass conservation. These sources of numerical difficulties have been treated using different approaches (for an overview, see [29, 30, 31, 32, 33, 34, 35, 36]).

We completed this framework by developing a unified Variational Multiscale LES (Large Eddy simulation) formulation to handle turbulent multiphase flows with high density ratio, phase change model, interface forces, surface tension and bubbles dynamics [37, 38]. We propose here to test this parallel 3D framework with the level set method and remeshing capabilities for quenching simple industrial parts inside a water tank with and without agitation. We also examined the orientation of a cylinder part.

To conclude, the real breakthroughs and innovation of the proposed work, allowing to deal with realistic industrial conditions and quenching devices (compared to other codes), and robustness by limiting the assumptions made and restraining non-physical use of quenching parameters are translated by the following summarized objectives:

1. To achieve high fidelity simulations of the multiphysics and multiscale nature of practical boiling flows in quenching applications, gaining insight into the physics of multiphase flow regimes, and generating a basis for effective-field modeling in terms of its formulation/closure laws;

2. To build up a unified 3D numerical framework allowing, relevant boiling multiphase flows and their impact on part cooling. This objective implies also to develop high-fidelity treatment of interfacial dynamics during quenching processes;

3. To develop a ground breaking unified immersed method for quenching environments and to enhance the adaptive Finite Element numerical strategy following a two-fold logic of simplicity and flexibility for the fluid-solid-heat coupling;

4. To propose experimental investigations and validations allowing (1) to validate the previous numerical objectives and (2) to give insights on physically based boiling heat transfer.

Author's contribution during the PhD

The work presented in this thesis was developed in the Computing & Fluids research group of the Centre for Material Forming (CEMEF), Mines ParisTech - PSL Research University, from November 2014 to October 2017. The contributions of the author in terms of publications, oral communications and prizes are presented below.

Refereed Journal Articles

[Art1] M. Khalloufi, Y. Mesri, R. Valette, E. Massoni, E. Hachem, *High fidelity anisotropic adaptive Variational Multiscale method for multiphase flows with surface tension*, Computer Methods in Applied Mechanics and Engineering, Vol. 307, pp 44-67, 2016

[Art2] E. Hachem, M. Khalloufi, J. Bruchon, R. Valette, Y. Mesri, *Unified adaptive Variational MultiScale method for two phase compressible–incompressible flows*, Computer Methods in Applied Mechanics and Engineering, Vol. 308, pp 238-255, 2016

[Art3] Y. Mesri, M. Khalloufi, E. Hachem, *On optimal simplicial 3D meshes for minimizing the Hessian-based errors*, Applied Numerical Mathematics, Vol. 109, pp 235-249, 2016

[Art4] L. Marioni, M. Khalloufi, F. Bay, E. Hachem, *Two-fluid flow under the constraint of external magnetic field: revisiting the dam-break benchmark*, International Journal of Numerical Methods for Heat and Fluid Flow, Vol. 27, 10.1108/HFF-09-2016-0371, 2017

[Art5] J. Sari, F. Cremonesi, M. Khalloufi, F. Cauneau, P. Meliga, Y. Mesri, E. Hachem, *Anisotropic adaptive stabilized Finite Element solver for RANS models*, International Journal for Numerical Methods in Fluids, doi: 10.1002/fld.4475, 2017

[Art6] M. Khalloufi, R. Valette, E. Hachem, *Adaptive level set method for simulating phase change and boiling flows*, submitted to Journal of Computational Physics, 2017

[Art7] M. Khalloufi, R. Valette, E. Massoni, Y. Mesri, E. Hachem, *Simulation of turbulent boiling with phase change in industrial steel quenching processes*, submitted to Applied Thermal Engineering, 2017

[Art8] M. Khalloufi, R. Valette, E. Hachem, *An adaptive conservative level set method for multiphase flows with surface tension*, preprint for Computers & Fluids, 2017

[Art9] M. Khalloufi, R. Valette, S. A. Butler, M. Mackley, *The effect of yield stress rheology characteristics and surface tension on fast filament deformation profile stretching and breakup*, in preparation

Communications

1. M. Khalloufi*, R. Valette, Y. Mesri, E. Massoni, E. Hachem, *Turbulent boiling & multiphase flows using Variational Multiscale FEM*, 14th US National Congress on Computational Mechanics (USNCCM 14), Montreal, Canada, July 2017

2. G. Guiza, M. Khalloufi*, P. Meliga, Y. Mesri, E. Hachem, *Adaptive Variational Multiscale Method for turbulent flows past complex geometries*, 14th US National Congress on Computational Mechanics (USNCCM 14), Montreal, Canada, July 2017

3. M. Khalloufi*, R. Valette, E. Massoni, E. Hachem, I. Poitrault, Z. Chebbo, C. David, *Simulation of turbulent boiling with phase change and industrial steel quenching processes*, 24th IFHTSE Congress - European Conference on Heat Treatment and Surface Engineering, Nice, France, June 2017

4. M. Khalloufi*, E. Hachem, P. Meliga, R. Valette, Y. Mesri, *Parallel adaptive Finite Element simulation of turbulent flow and fluid-structure interaction with complex geometries*, ERCOFTAC Workshop on Fluid-Structure Interaction with impact on industrial applications, Toulouse, France, June 2017

5. M. Khalloufi*, Y. Mesri, R. Valette, E. Massoni, E. Hachem, *Stabilized Finite Element method for the simulation of industrial quenching processes*, Computational Structural Mechanics Association Congress (CSMA 2017), Gien, France, May 2017

6. M. Khalloufi*, R. Valette, Y. Mesri, E. Hachem, *Adaptive Variational Multiscale method for Newtonian multiphase flows*, 12th International Workshop on Variational Multiscale and Stabilized Finite Element (VMS 2017), Seville, Spain, Apr. 2017

7. M. Khalloufi*, R. Valette, Y. Mesri, E. Hachem, *High fidelity adaptive FEM towards physical couplings occurring in turbulent boiling*, Finite Element in Flow Problems (FEF 2017), Rome, Italy, Apr. 2017

8. E. Hachem*, M. Khalloufi, R. Valette, Y. Mesri, *Parallel Finite Element framework for the numerical simulation of multiphase flows involving moving solids*, Workshop on reduced order methods for wind and marine current power, Sophia-Antipolis, France, Feb. 2017

9. E. Hachem*, M. Khalloufi, R. Valette, *High fidelity adaptive FEM towards physical couplings occurring in turbulent boiling*, Workshop on Numerical Modeling of liquid-vapor interfaces in fluid flows, Paris, France, Dec. 2016

10. M. Khalloufi*, R.Valette, Y. Mesri, E. Hachem, *High fidelity anisotropic adaptive variational method for turbulent multiphase flows*, Colloque Couplages Numériques, Nice, France, Sept. 2016

11. M. Khalloufi*, R. Valette, E. Hachem, *Unified compressible/incompressible Variational MultiScale method for liquid-vapor dynamics*, World Congress on Computational Mechanics XII (WCCM 2016), Seoul, Korea, July 2016

12. E. Hachem*, S. Riber, M. Khalloufi, Y. Mesri, R. Valette, *Modeling of Non-Newtonian multiphase flow using adaptive stabilized finite element method*, European Congress on Computational Methods in Applied Sciences and Engineering (ECCOMAS 2016), Crete Island, Greece, June 2016

Fellowship and Awards

- *USACM Travel award* to attend the 14th US National Congress on Computational Mechanics (USNCCM 14), Montreal, Canada, July 2017

- *Tom Bell Young Author Award* for a paper of exceptional merit presented at the 24th Congress of the International Federation for Heat Treatment and Surface Engineering (IFHTSE 24), Nice, France, June 2017

Résumé en français

Présent dans l'élaboration de pièces critiques aussi bien dans le domaine aérospatiale, nucléaire, la trempe est un procédé largement utilisé par les métallurgistes dans l'élaboration des aciers. Ce procédé, qui vise à donner des propriétés mécaniques bien précises à une pièce appartient à la famille des traitements thermiques. Ces pièces sont chauffées dans des fours afin de permettre la diffusion des atomes de carbone. Afin d'empêcher la diffusion de ces atomes de carbone lors du refroidissement souvent inhomogène de la pièce, la pièce est refroidie brutalement. Ce refroidissement peut s'effectuer en plongeant la pièce dans un bain liquide à température proche de la température ambiante mais peut aussi s'effectuer par application d'un jet d'eau (ou spray).

L'amélioration et le contrôle de ce procédé suscitent un intérêt grandissant et deviennent un axe majeur de progrès pour les industriels. Les forts gradients thermiques présents aux interfaces, le changement de phase du liquide de trempe, l'agitation et la transformation de phase dans le solide sont autant d'éléments rendant la trempe extrêmement difficile à modéliser. La multiplicité des échelles spatiales, du mm à la dizaine de mètres et des échelles temporelles, de la ms à plusieurs heures, rend encore plus compliquée l'utilisation de modèles uniques et simplifiés.

Les coûts engendrés par les expérimentations effectuées dans le but d'améliorer ce procédé sont rédhibitoires et rendent les expériences difficiles a mener. Le fait que les installations soient préexistantes limitent aussi les axes de progression du procédé.

La simulation numérique représente un outil puissant permettant aussi de déterminer l'efficacité du procédé en se basant sur des indicateurs pertinents développés par l'industriel mais aussi de modifier les configurations possibles de la pièce métallique à tremper. Ainsi l'orientation de la pièce et sa position dans le bain de trempe sera étudiée. Une trempe efficace nécessite que le liquide de trempe puisse extraire le maximum de chaleur tout en ne s'échauffant pas immodérément. Pour cela, il est nécessaire d'avoir un large volume de liquide et une forte agitation de celui-ci. Les vitesses d'agitation ainsi que les dispositifs d'agitation peuvent être incorporés dans la simulation numérique.

Dans cette thèse de doctorat sera montrée la construction d'un environnement numérique permettant de simuler de manière précise et robuste un procédé industriel aussi exigeant que la trempe. Une étude des mécanismes physiques du procédé de trempe nous a permis de déterminer les axes prioritaires de développement du nouvel environnement numérique.

En se basant sur les outils existants au sein de la librairie de calcul élément finis de l'équipe Calcul Intensif et Mécanique des Fluides (CFL) du Centre de Mise en Forme des Matériaux (CEMEF) de l'école des Mines de Paris (Mines ParisTech), nous avons identifié les nouveaux besoins numériques. La méthode d'immersion de volume largement développée au sein de l'équipe CFL est utilisée dans ce travail, pour son aptitude à prendre en compte toutes les composantes du procédé de manière unifiée. Alliée à des méthodes puissantes d'adaptation de maillage, la méthode des volumes immergés permet une résolution fine des physiques aux interfaces, déterminante dans l'obtention de résultats précis et fiables.

Le cadre de travail ainsi proposé répondra aux besoins des industriels en leur permettant de simuler le procédé de trempe dans des conditions réalistes, supprimant ainsi toute hypothèse simplificatrice et limitant l'utilisation de paramètres non physiques.

Chapter 2

Physical mechanisms involved in quenching tanks

Contents

2.1 Introduction

The present chapter is dedicated to the study of the physical mechanisms in the quenchant during the process. In this work, only the physics of the fluid (the quenchant) in quenching tank is addressed. The purpose here is to give an insight of the main physical mechanisms involved in quenching. Once these phenomena are identified, we will investigate their impact by quantifying characteristic time and scale of the different mechanisms involved in boiling. From vaporization of the quenchant and therefore the formation of a vapor film, to the dynamics of the vapor film due to gravity and surface tension, the main mechanisms are investigated.

Unsteady 3D simulations of turbulent boiling still require large computational resources. A way to circumvent the need of tremendous computational resources is to identify the phenomena to simulate, with satisfactory precision and fidelity with respect to the real process. To enable the numerical tool to be predictive, only phenomena with no significant impact on the results must be neglected.

Choice has been made to prioritized the physics involved in boiling according to the dynamics of the interface. The interface position and the interface velocity will be quantified for each phenomenon and compared. Phase change, hydrodynamic instability and vapor film expansion are considered here. Other phenomena such as radiation are not considered in this work.

First we will investigate the creation of vapor from water through the resolution of the well known Stefan problem. Then we will investigate the destabilization of the vapor film due to the gravity and surface tension through the Rayleigh-Taylor instability. In the case of a compressible vapor, vaporization creates an over-pressurization and the containment by the surrounding water therefore requires a relaxation and an expansion of the vapor phase.

According to the results, emphasis will be put on the modeling and the implementation of the predominant mechanisms/phenomena.

2.2 Phase change

Phase change is present in various industrial but also in natural phenomena: boiling of water, condensation that creates clouds, the dew and the mist, cavitation in ship propellers, icing of aircraft wings. Each kind of phase change is characterized by triggering mechanisms induced by temperature or pressure. In the quenching process, the phase change is boiling and it is due to the metallic part that provides the required heat.

Boiling modes play an essential role in the cooling of a metallic part. Nukiyama [39] highlighted in 1934 the different boiling regimes of water in contact with a heated metal. As one progresses from the saturation temperature to higher temperatures, more and more bubbles appear and then merge into a vapor film, which act as a thermal insulation. The boiling curve, when the temperature at the surface of the part is controlled (see Fig. 2.1), describing the boiling modes, reads as follows:

(1) Free convection: Starting before saturation, it is due to the change of density of the fluid, the higher the temperature, the lower the density. Bubbles do not appear yet.

(2) Nucleate boiling at low heat flux: Isolated bubbles start to appear in preferential sites called nucleation sites.

(3) Nucleate boiling at high heat flux: Bubbles tend to collapse and to form columns. This is the most efficient heat transfer mode as the heat is convected by the bubble and its wake.

(4) Transition boiling: A vapor film, restraining the contact between the liquid and the solid starts to appear on a periodic and spatial way. The vapor film is not stable.

(5) Beyond the Leidenfrost point, the surface is entirely covered by permanent vapor film, preventing any contact between the water and the metal.

When the excess temperature is larger than 300K, the surface heat flux due to radiation -the latter being a function of T^4 (T temperature)- is of the same order as the heat flux due to boiling. That is all the more true when the excess temperature exceeded the Leidenfrost point, as the vapor film is stable and radiation becomes the dominant heat transfer mode. Thus, this heat transfer mode should be investigated.

In the case of industrial applications, nucleate boiling represents the most efficient boiling heat transfer regime. Therefore, steel manufacturer aim at improving their processes by reaching this regime. In quenching processes, the temperature is considerably larger than the Leidenfrost temperature. Steel in water, for example, is quenched at $T_{\text{surface}} - T_{\text{staturation}} > 400K$. Therefore, a vapor film surrounds instantaneously the part and prevents it from cooling.

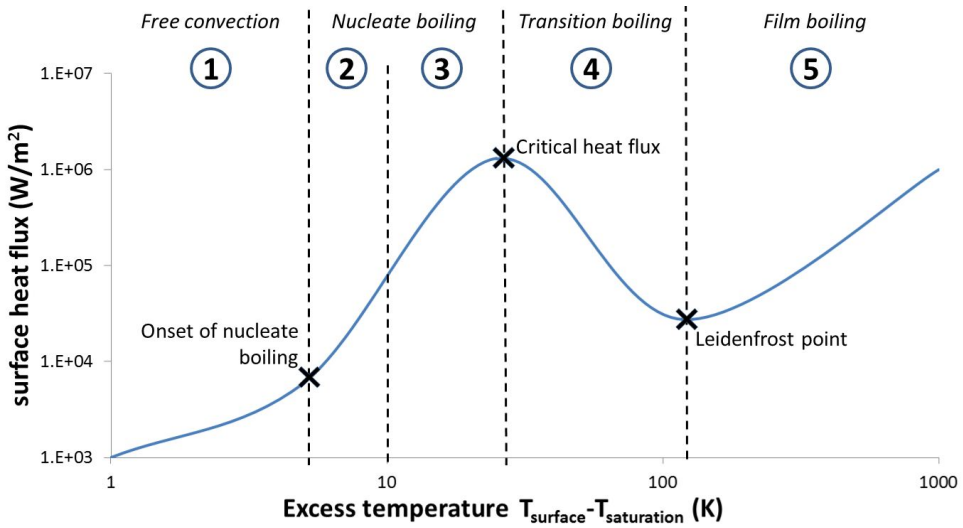

Figure 2.1: Nukiyama curve. Evolution of the surface heat flux as a function of the excess temperature

2.2.1 The Stefan problem

The Stefan problem is a widely used and studied problem. It was originally proposed by Jozef Stefan to study the formation of ice in the polar seas. Nowadays, a large class of free boundary problems are referred to as Stefan problem. From a set of physical parameters defining two phases and for a given heat source, one seeks to find the evolution of the interface between the phases. Since heat is the driving force of this phenomenon, the transfer of energy has to be finely described between the phases.

The popularity of this class of problems lies in the fact that analytical solutions can be found. This makes the Stefan problem a good candidate to assess the validity of a numerical method for phase change. Several assumptions are usually required to find an analytical solution. For example, most of the Stefan problem in the literature deal with phases of equal density. This assumption, if applicable in case of the melting of a solid or the solidification of a liquid, shows its limits when dealing with two phases of a density ratio of about 1000 such as water and vapor. We will solve the Stefan problem for the general case of two phases of different densities even if a special care will be given to water and vapor in this thesis since it is the most used quenchant.

The purpose here is not to propose a literature review on the Stefan problem. Therefore we will refer to the standard formulation of the problem. The solution of the Stefan problem is found by solving the heat equation, with additional assumptions regarding convection in the phases as well as boundary conditions.

2.2.2 Resolution of the classical Stefan problem

We consider the one-dimensional Stefan problem. The problem is defined schematically in Fig. 2.2. We consider a semi-infinite domain in the x-direction and infinite in the other direction. Initially the domain is filled with a liquid. The temperature at the wall T_{wall} is set constant and larger than the saturation temperature T_{sat}. The water is at saturation temperature. At $t > 0$, a phase change occurs and induces a motion of the interface between vapor and water. The convective term in the energy conservation equation is neglected in both phases even if in quenching, convection will play an important role.

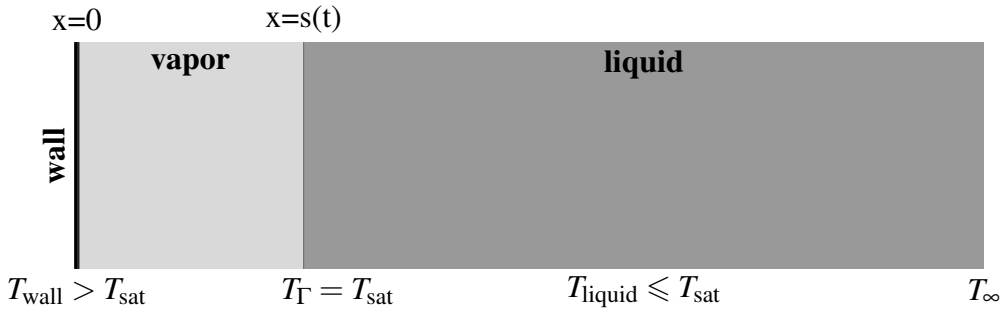

Figure 2.2: Initial setup for the classic Stefan problem.

We consider the following heat equations:

$$\rho_l c_p^l \frac{\partial T_l}{\partial t} - k_l \frac{\partial^2 T_l}{\partial x^2} = 0 \qquad \text{in the liquid} \tag{2.1}$$

$$\rho_v c_p^v \frac{\partial T_v}{\partial t} - k_v \frac{\partial^2 T_v}{\partial x^2} = 0 \qquad \text{in the vapor} \tag{2.2}$$

where ρ is the density, c_p is the specific heat, T is the temperature, and k the thermal conductivity. We assume continuity of temperature at the interface. Furthermore, we assume that the temperature at the interface T_Γ equals the temperature of saturation. Therefore the initial boundary conditions for this problem read:

$$T(x=s,t) = T_\Gamma = T_{\text{sat}} \tag{2.3}$$

$$T(x=0,t) = T_{\text{wall}} = \text{constant} \tag{2.4}$$

We can recast the heat equation, using $\alpha = k/\rho c_p$ the thermal diffusivity:

$$\frac{\partial T}{\partial t} - \frac{k}{\rho c_p}\frac{\partial^2 T}{\partial x^2} = \frac{\partial T}{\partial t} - \alpha \frac{\partial^2 T}{\partial x^2} = 0 \tag{2.5}$$

We use the similarity variable referred to as the Neumann solution $\xi = x/\sqrt{t}$. Then the temperature is expressed as a function F such as $T(x,t) = F(\xi)$. The heat equation as a function of ξ reads:

$$\frac{\xi}{2\alpha}\frac{dF}{d\xi} + \frac{d^2F}{d\xi^2} = 0 \tag{2.6}$$

Using separation of variables gives:

$$\frac{d\ln G}{d\xi} = -\frac{\xi}{2\alpha} \tag{2.7}$$

$$G = \frac{dF}{d\xi} \tag{2.8}$$

By integration, we obtain the following expression for $F(\xi)$:

$$F(\xi) = A\int_0^\xi \exp\left(-\frac{s^2}{4\alpha}\right) ds + B \tag{2.9}$$

where A and B are integration constants, whose values are given by the boundary conditions. By a change of variable:

$$F(\xi) = 2A\sqrt{\alpha} \int_0^{\frac{\xi}{2\sqrt{\alpha}}} \exp\left(-y^2\right) dy + B \tag{2.10}$$

Recall the definition of the error function erf:

$$\mathrm{erf}(x) = \frac{2}{\sqrt{\pi}} \int_0^x \exp(-t^2) dt \tag{2.11}$$

and the complementary error function erfc:

$$\mathrm{erfc}(x) = 1 - \mathrm{erf}(x) \tag{2.12}$$

The temperature is given by:

$$F(\xi) = A\sqrt{\alpha\pi}\,\mathrm{erf}\left(\frac{\xi}{2\sqrt{\alpha}}\right) + B \tag{2.13}$$

Using the boundary conditions (2.3)-(2.4), the temperature in vapor and water at time t are given then by:

$$T_v(x,t) = T_{\mathrm{wall}} + \frac{T_{\mathrm{sat}} - T_{\mathrm{wall}}}{\mathrm{erf}\left(\frac{s}{2\sqrt{\alpha_v t}}\right)} \mathrm{erf}\left(\frac{x}{2\sqrt{\alpha_v t}}\right) \tag{2.14}$$

$$T_l(x,t) = T_\infty + \frac{T_{\mathrm{sat}} - T_\infty}{\mathrm{erfc}\left(\frac{s}{2\sqrt{\alpha_l t}}\right)} \mathrm{erfc}\left(\frac{x}{2\sqrt{\alpha_l t}}\right) \tag{2.15}$$

Let $\chi_v = \dfrac{s}{2\sqrt{\alpha_v t}}$ and $\chi_l = \dfrac{s}{2\sqrt{\alpha_l t}}$. The position of the interface is given by:

$$s(t) = 2\chi_v\sqrt{\alpha_v t} \tag{2.16}$$

In the vapor, the gradient of the temperature is:

$$\frac{\partial T_v}{\partial x} = \frac{T_{\mathrm{sat}} - T_w}{\mathrm{erf}(\chi)} \frac{1}{\sqrt{\pi}} \frac{1}{\sqrt{\alpha_v t}} \exp\left(-\frac{x^2}{4\alpha_v t}\right) \tag{2.17}$$

In the liquid, the gradient of the temperature is:

$$\frac{\partial T_l}{\partial x} = -\frac{T_{\mathrm{sat}} - T_\infty}{\mathrm{erfc}(\chi_l)} \frac{1}{\sqrt{\pi}} \frac{1}{\sqrt{\alpha_l t}} \exp\left(-\frac{x^2}{4\alpha_l t}\right) \tag{2.18}$$

At the interface, for $x = s$, we therefore obtain:

$$\frac{\partial T_v}{\partial x} = \frac{T_{\mathrm{sat}} - T_w}{\mathrm{erf}(\chi_v)} \frac{1}{\sqrt{\pi}} \frac{1}{\sqrt{\alpha_v t}} \exp\left(-\chi_v^2\right) \tag{2.19}$$

$$\frac{\partial T_l}{\partial x} = -\frac{T_{\mathrm{sat}} - T_\infty}{\mathrm{erfc}(\chi_l)} \frac{1}{\sqrt{\pi}} \frac{1}{\sqrt{\alpha_l t}} \exp\left(-\chi_l^2\right) \tag{2.20}$$

The velocity of the interface, referred to as the Stefan condition is:

$$\rho_v L \frac{ds}{dt} = \left(-k_v \frac{\partial T_v}{\partial t} + k_l \frac{\partial T_l}{\partial t} \right) \tag{2.21}$$

where L is the latent heat of vaporization.

In the classical Stefan problem, the liquid being at saturation temperature, the Stefan condition reduces to:

$$-k_v \frac{\partial T}{\partial x} = \rho_v L \frac{ds}{dt} = \rho_v L \chi_v \sqrt{\frac{\alpha}{t}} \tag{2.22}$$

By combining (2.19) and (2.22), we obtain the following relation describing the evolution of the interface:

$$\frac{T_w - T_{\text{sat}}}{\sqrt{\pi} L} c_p^v = \chi_v \, \text{erf}(\chi_v) \exp\left(\chi_v^2\right) \tag{2.23}$$

The resolution of (2.23) gives the temperature and the position of the interface using equations (2.14)-(2.16).

Considering the following physical properties for water and vapor defined in Table 2.1 and setting $T_{\text{wall}} - T_{\text{sat}} = 900\text{K}$, we solve the transcendental equation (2.23) using a Newton algorithm to find χ_v.

Table 2.1: Density, dynamic viscosity, specific heat and thermal conductivity for vapor and water at atmospheric pressure

	ρ [kg/m^3]	μ [Pa·s]	c_p [J/(kg·K)]	k [W/(m·K)]	L_{vap} [J/kg]
Vapor	0.597	1.26×10^{-5}	2030	0.025	
Water	958.4	2.8×10^{-4}	4216	0.679	2.26×10^6

The temperature profile at t=1s is depicted in Fig.2.3. The analytical evolution in time of the interface is given in Fig. 2.4. The Fig. 2.5 shows the evolution of the velocity. The velocity of the interface is of the order of m/s at the very beginning of the problem. This indicates that almost instantaneously, a thickness of vapor of about few millimeters was already formed. It is an additional information to the curve in Fig 2.1 regarding the boiling regime for which this work should focus on.

2.2.2.1 Stefan condition for $\rho_v/\rho_l \neq 1$

In the literature, the Stefan problem is usually solved using a constant density. To consider a two-phase Stefan problem, the density ratio has to be taken into account. In order to conserve heat, an additional term appears in the balance of fluxes (2.21). The derivation of the Stefan condition, neglecting inertial effects, for two phases of variable densities was derived in [40] and reads:

$$-\rho_v L_{\text{vap}} \frac{ds}{dt} - \frac{1}{2}\rho_v \left(1 - \frac{\rho_v}{\rho_l}\right)^2 \left(\frac{ds}{dt}\right)^3 = (-k_l \nabla T_l + k_v \nabla T_v) \cdot \vec{e}_x \tag{2.24}$$

If $\rho_v = \rho_l$, we retrieve the case with no density change. This condition does not allow a similarity solution. However, because of the high value of the latent heat, the influence of the cubic term is negligible except when the velocity of the interface is very large [41, 42, 43]. The velocity reaches its highest values at the very early times of the problem, at a time scale of

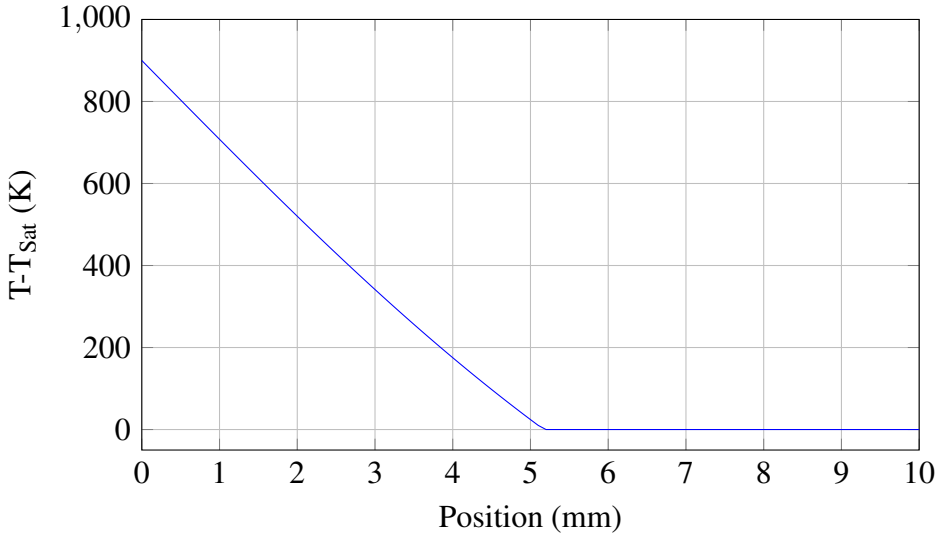

Figure 2.3: Temperature profile at t=1s

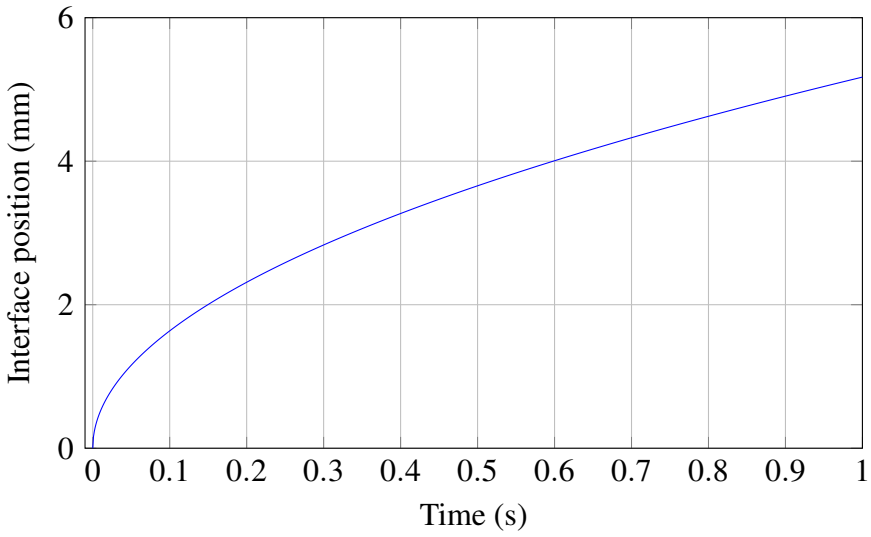

Figure 2.4: Stefan problem: Evolution of the interface position

micro- or nano-seconds, which is out of the scope of this work. The modified Stefan condition was shown to be essential in the case of the melting of nanoparticles [44]. We will refer to the standard Stefan condition (2.21) in this work.

Some partial conclusions can be made according to the results of this problem. When we consider the range of excess temperature in quenching, since a thickness of vapor forms very quickly at the beginning of the process, we can assume that there is no need to simulate nucleation of bubbles. Therefore we will start all the simulations with a pre-existing vapor film surrounding the metallic part.

2.3 Rayleigh Taylor instability

When a light fluid lies below a heavy fluid, if the interface is unstable, fluids will interpenetrate, creating fingers or spikes and afterwards, bubbles. Depending on the fluids at play, the rising

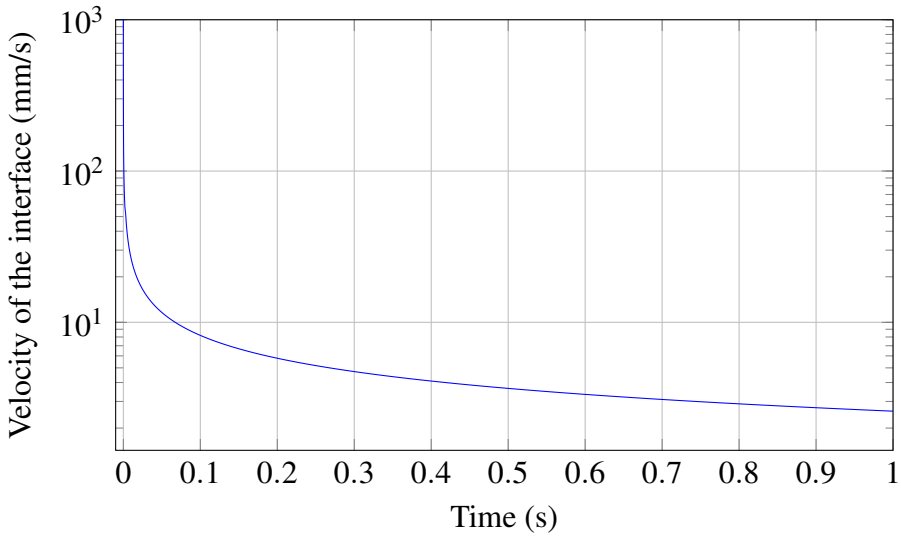

Figure 2.5: Stefan problem: Velocity of the interface.

velocity of the light fluid and the shape of the interface will differ. Several factors influence the growth of this instability, called Rayleigh-Taylor instability, such as the density, the viscosity, the surface tension or the compressibility of the fluids. Fig.2.6 shows the configuration of a 2D Rayleigh-Taylor instability.

This instability occurs during quenching after the creation of the vapor film. A comparison of the evolution of the interface position due to the Rayleigh-Taylor instability and vaporization of water is therefore relevant. Indeed, if at some point, the dynamics of the interface is mainly due to this instability, this phenomenon cannot be neglected.

Figure 2.6: Setup for the 2D Rayleigh-Taylor instability. A light fluid lies below a heavy fluid.

At the early stage of this instability, using a linearization of the physical equations, a small perturbation will grow exponentially in time. Rayleigh Taylor instabilities of small amplitude are widely studied in the literature [45]. We recall briefly the linearized growth of the instability to describe the rise of the vapor film after its creation. The interface perturbation is given by:

$$s(t) = s_0 \exp(\omega t) \exp(ikx) \tag{2.25}$$

where s_0 is the initial perturbation of the interface. The growth rate ω is defined by:

$$\omega = \sqrt{gAk} \tag{2.26}$$

where $A = (\rho_l - \rho_v)/(\rho_l + \rho_v)$ is the Atwood number, g is the acceleration of the gravity and $k = 2\pi/\lambda$ is the wave number.

When using the physical properties of Table 2.1, we can obtain the following simplification for the growth rate

$$\omega = \sqrt{g\frac{\rho_l - \rho_v}{\rho_l + \rho_v}\frac{2\pi}{\lambda}} \approx \sqrt{g\frac{2\pi}{\lambda}} \tag{2.27}$$

For a Rayleigh Taylor instability, the critical Taylor wavelength is:

$$\lambda = \sqrt{\frac{\gamma}{(\rho_l - \rho_g)g}} \tag{2.28}$$

where γ is the surface tension and g is the acceleration due to the gravity. For the set of parameters given in Table 2.1, the critical wavelength is about $\lambda = 0.0027$m.

Fig. 2.7 shows the evolution of the interface according to (2.25). It is worth mentioning that the theory of the linearized regime is valid for a growth between 10% to 40% of the critical wavelength. However, since we use this theory to obtain an order of magnitude of the rising velocity and the interface position at the early time of the phenomenon, we will assume that a comparison with other phenomena using this theory is valid.

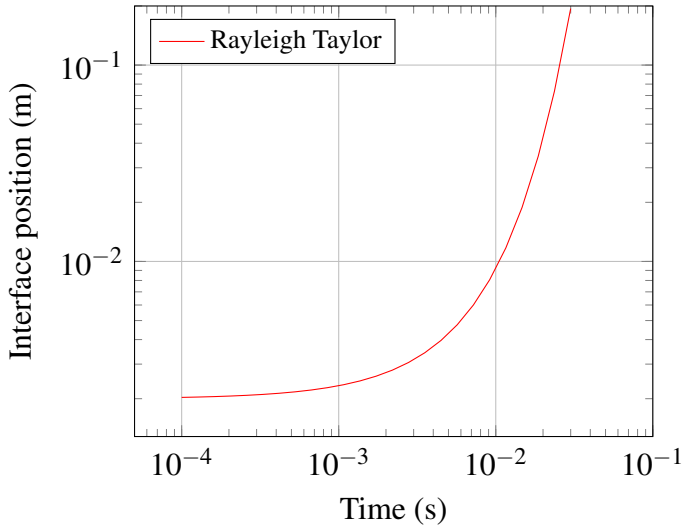

Figure 2.7: Rayleigh Taylor instability: Evolution of the interface position

2.4 Expansion of a compressible medium

Vaporization of a thickness s_0 implies expansion of the gas. The principle of expansion is depicted in Fig. 2.8, . This expansion requires to accelerate the whole mass of surrounding water. A 1D expansion model would be then:

$$\rho_l \ddot{s}(t) = \frac{\Delta p}{L_c} = \frac{p_\infty}{L_c}\left(\frac{\rho_l}{\rho_v}\frac{s_0}{s(t)} - 1\right) \tag{2.29}$$

where L_c is a characteristic length taken as the length of the water column in the current study, p_∞ is the pressure at the top of the water column.

An approximation of the solution of (2.29), using a finite difference method is:

$$s^{n+1} = 2s^n - s^{n-1} + \Delta t^2 \frac{p_\infty}{\rho_l L_c}\left(\frac{\rho_l}{\rho_v}\frac{s_0}{s^n} - 1\right) \tag{2.30}$$

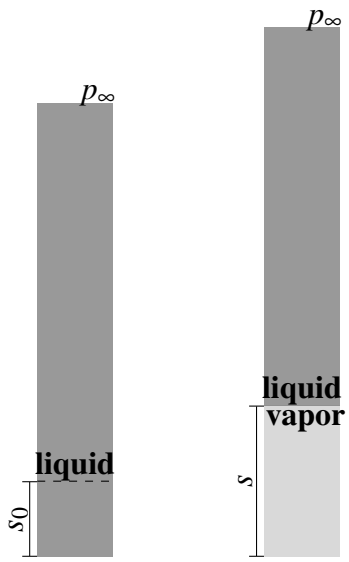

Figure 2.8: Expansion of the vapor phase after vaporization of a thickness s_0 of water.

where n is the time iteration. The pressure is set up to $p_\infty = 10^5$Pa and L_c will be taken as the length of the column of water. Results on the evolution of s according to (2.30) are given in the the following paragraphs.

2.5 Comparison

In this section, we will compare the interface evolution due to vaporization, due to the Rayleigh-Taylor instability and due to the expansion of the vapor film. The growth of the vapor film is done in the opposite direction of gravity in order to assess the effect of the column of water lying above the vapor film. The principle of the comparison is the following. First, we have to consider a minimal thickness to compare the phenomena. This thickness will be given by the solution of the Stefan problem. When a thickness s_0 is reached, we additionally compute the solution of the Rayleigh-Taylor instability and the solution of the expansion of the vapor phase using equations (2.25)-(2.30). This enables us to show the interface evolution according to each phenomenon after the creation of a certain thickness of vapor. We consider in the following examples, s_0=10^{-4}, 10^{-3} and 10^{-2} m.

We approximate the interface position given by the resolution of the Stefan problem, using the Stefan condition (2.22). Approximating the gradient of the temperature gives:

$$\dot{s} \approx -\frac{k_v}{\rho_v L}\frac{T_{\text{vap}} - T_w}{s} \tag{2.31}$$

The previous equation can be rewritten in the following way:

$$\frac{\partial}{\partial t}\left(\frac{1}{2}s^2\right) = \alpha_v (T_w - T_{\text{vap}})\frac{c_p^v}{L} \tag{2.32}$$

By integration, we obtain:

$$s(t) = \sqrt{2\alpha_v (T_w - T_{\text{vap}})\frac{c_p^v}{L}\,t} = \sqrt{2\alpha_v \frac{T_w - T_{\text{vap}}}{T_{\text{ref}}}\,t} \tag{2.33}$$

where $\alpha_v = 2.10^{-5} m^2/s$, $T_{\text{ref}} = 10^3 K$ and the excess temperature $T_w - T_{\text{vap}} = 900K$.

Thus, a good approximation of the position of the interface is given by:

$$s(t) \approx 2.10^{-4} \sqrt{(T_w - T_{\text{vap}})\, t} \tag{2.34}$$

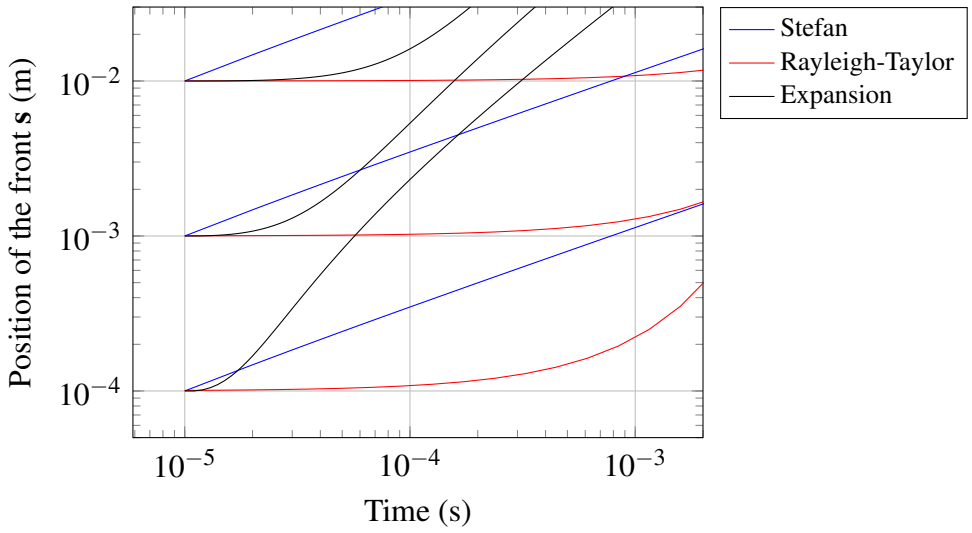

Figure 2.9: Evolution of the interface position with a water column of 0.1 m height. Comparison of the evolution of the position of the interface starting from an initial position s_0 of the interface s_0=1e-4 (bottom), 1e-3 (middle) and 1e-2 (top).

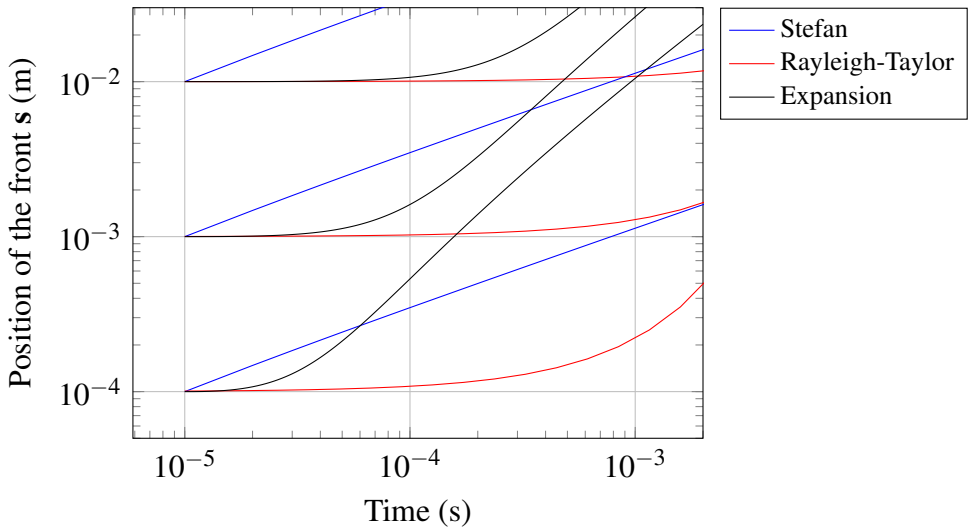

Figure 2.10: Evolution of the interface position with a water column of 1 m height. Comparison of the evolution of the position of the interface starting from an initial position s_0 of the interface. s_0=1e-4 (bottom), 1e-3 (middle) and 1e-2 (top).

In Figs. 2.9-2.10, the evolution of the interface according to each phenomenon is shown. In Fig. 2.9, a column of water of 0.1m is considered and in Fig. 2.10, a column of 1m. As it is clearly visible in Figs 2.9-2.10, the dominant phenomenon is vaporization. Indeed, the excess temperature being very large, the wall is still close enough to supply a large amount

of heat. However its effect decreases with the distance from the wall beacause the vapor acts as a thermal insulator and therefore conduction of heat is not as efficient as in water. Then, vaporization leads to a pressure increase in the vapor phase that requires an expansion. The evolution of the interface is faster when the column of fluid is 0.1m compared to a column of 1m. The comparison between Fig.2.9 and Fig. 2.10 emphasizes the influence of the column of water on the displacement of the interface. With a higher column of water, the expansion is more difficult to achieve. The results of the Rayleigh-Taylor instability clearly show that for this excess temperature $T_w - T_{\text{vap}} = 900K$, gravity effects and surface tension do not balance the formation of the vapor film and its expansion. As a consequence, a permanent vapor film surrounds the part.

To sum up, at the early stage of boiling, due to the heat transfer between the solid and the water, a vapor thickness is created and tends to expand. At high temperature, such as the ones considered in quenching, these phenomena prevent water to reach the part. After a certain period of time, the temperature of the part will enable gravity and surface tension to play a role in the dynamics of the vapor film. This is the nucleate boiling regime, carrying vapor and heat away from the solid.

2.6 Modeling strategy

Boiling still represents a challenging subjects of physics. Several complex and coupled physics are involved. This work intends to tackle some of the most relevant phenomena involved in boiling; the purpose being to build a numerical framework allowing the simulation of such a complex phenomenon. Therefore a coherent and realistic strategy must be set, enabling to consider additional physics. The numerical tools will be used as predictive tools for the improvement of large industrial process. A major effort will thus be made to reduce the computational requirement to perform such simulations. Furthermore, this numerical framework should be open to evolution and to the addition of new physics, such as radiation.

We choose not to consider compressible flows using an equation of state. From a numerical point of view, considering a fluid as compressible would result in additional complexity such as shock, time step restriction due to the celerity of sound, low Mach approximation, etc. Instead, as a first step, we will consider distinct phases that will exchange heat and mass. Therefore one needs to quantify the right amount of heat and mass transferred from one phase to the other. A mass transfer rate is required for the phase change model. The mass transfer rate will quantify the amount of water transformed into vapor. The Stefan condition gives us access to such a mass transfer rate. The set of conservation equations (mass, momentum, energy) and the level set equation have to be derived to take into account a transfer of heat and mass to model vaporization. Details are presented in Chapters 3,4 and 5.

Once the vapor film is created, the dynamics of the vapor film is given by the surface tension. The boiling regime at a given time depends on the competition between the creation of the vapor film and the rise of bubbles formed from the vapor film. In the case of a low surface tension, slugs of vapor will detach quickly from the film and then rise to the free surface. On the contrary, a high surface tension will favor the formation of a continuous and stable vapor film. However, for a given value of surface tension, a large excess temperature will lead to the formation of a stable vapor film. Several challenges arises from a numerical point of view. Indeed the implementation of the surface tension imposes a severe restriction on the time step, one or two order of magnitude smaller than other time step restriction such as the Courant-Friedrichs-Lewy (CFL) condition.

It was demonstrated in the last section that in some cases the expansion of a compressed medium leads to a fast evolution of the vapor film thickness. Furthermore, in the presence of stirring mechanism in the quenching tank that inject water at a velocity in the order of tens of m/s, the vapor film is compressed against the metallic part and therefore the dynamics of the vapor film changes.

The objective of this work being the development of a numerical framework to simulate quenching, we will address the aforementioned points and include them in unified multiphase framework. Several features are required in this framework:

- Resolution of the unsteady multiphase Navier-Stokes equations
- Computation of the mass transfer rate and derivation of the set of equations taking into account heat and mass transfer
- Alleviation of the time step restriction due to the implementation of surface tension
- Inclusion of a compressible medium

In the introduction of this thesis, a literature review of the numerical simulation of quenching showed that the most common way to treat the interaction between the fluid and the solid is through boundary conditions and heat transfer coefficients. If the use of heat transfer coefficients seems appealing by its simplicity of implementation, from a practical point of view, it relies on the knowledge of such empirical coefficients. For any new configuration, a new coefficient has to be identified.

In this work, we use a monolithic approach, meaning that a single domain is used and discretized and only one set of equations in solved in this domain. All the phases of the problem (solid, liquid, gas) are immersed in this domain. Therefore an interface capturing method is required to distribute the physical properties of each phases and to capture the evolution of those interfaces. In the present work, a level set method is chosen to its ability to deal with complex topology change of the interface. Furthermore, the ease to compute from the level set function quantities such as the curvature of the interface or the normal field to the interface makes the level set a very useful and very used tool in multiphase applications and in particular for surface tension. Since at very high excess temperature the vapor film is instantaneously created, the nucleation of bubbles will be neglected and a fully developed film with a certain thickness will be considered pre-existing. This is easily done using a standard level set method without any assumptions on a distribution of nucleation site. The heat transfer are treated naturally using a monolithic approach and solving the Navier-Stokes equations in the whole domain. No arbitrary boundary condition for the heat equation are applied to the immersed solid. A thorough presentation of the monolithic approach will be given in the next chapter.

2.7 Conclusion

In this chapter, we discussed the complexity of boiling in quenching tanks. Several physical mechanisms are involved and make the understanding of this phenomenon difficult to achieve. We choose to prioritized the phenomena according to their influence on the vapor film dynamics. Therefore, focus is put on 3 phenomena: phase change, hydrodynamic instability of the interface and vapor film expansion. We decomposed the phenomenon into simpler problems that we solved. We draw some conclusions about the requirements of the future numerical framework that will be developed in the following chapters.

Résumé en français

Dans ce chapitre, les principaux mécanismes physiques présents dans la trempe sont identifiés et étudiés. Des échelles caractéristiques de temps et d'espace sont associées à ces différents mécanismes. Le changement de phase de l'eau en vapeur est tout d'abord considéré à travers la résolution d'un problème de Stefan. Le second mécanisme est la détente d'une phase vapeur compressible confinée par un certain volume d'eau. Le dernier mécanisme est la remontée de la phase vapeur au sein de l'eau, dont l'évolution est obtenue par l'étude d'une instabilité de Rayleigh-Taylor. La résolution de ces différents problèmes nous permet pour une épaisseur de vapeur créée de déterminer quelle sera l'évolution du film de vapeur. Ainsi, pour une certaine épaisseur de vapeur créée, la détente est le phénomène le plus rapide. Une fois la détente de la phase vapeur achevée, c'est la compétition entre l'hydrodynamique et la vaporisation qui va reguler le procédé. Pour des gradients thermiques très élevés comme ceux présents dans le procédé de trempe, il apparaît clairement que l'hydrodynamique de la phase vapeur est le facteur limitant dans le refroidissement d'une pièce solide puisqu'il se crée beaucoup plus de vapeur au contact du solide chaud qu'il ne s'en évacue.

Cette étude nous permet de lister les différents composants nécessaires à l'élaboration d'un cadre numérique pour la simulation de la trempe. Tout d'abord, il faudra être capable de résoudre les équations de Navier-Stokes multiphasiques pour des écoulements turbulents. Ensuite, la tension de surface devra être prise en compte pour modéliser de manière la plus fidèle possible la dynamique de la phase vapeur. Un modèle de changement de phase devra être développé, permettant de calculer les échanges de masse et d'énergie à travers l'interface vapeur/eau. Finalement, la compressibilité de la phase vapeur devra être considérée pour avoir une description de la compression du film de vapeur soumis à une forte agitation.

Chapter 3

Eulerian framework

Contents

3.1 Introduction

Immersed methods are gaining popularity in many scientific and engineering applications such as Fluid-Structure Interaction or multiphase flows. All the different approaches, such as the Cartesian method [46], the Immersed Boundary method [47], the fictitious domain method [48], the embedded boundary method [49], the immersed volume method [19], among many others, are attractive because they simplify several inherent issues related to Fluid-Structure interaction or multiphase applications: meshing the fluid domain, the use of fully Eulerian algorithm, problems involving large structural motion and deformation [50] or topological changes [51].

When the grid is not body-fitted, the interface requires a special treatment. Indeed, recent developments are focusing on the immersion of a surface mesh for 3D complex geometries, the detection of interfaces, the computation of intersections and the transmission of boundary conditions between the solid and the fluid region [52, 53].

In this work, we present the immersed volume method and its extension. It uses the level set function to describe the immersed phase. For simple geometries, we resort to the use of analytical functions (i.e. sphere, square, ...) to compute the distance function whereas for a complex geometry we used its surface, described and discretized by a hyperplan simplex

mesh (a set of triangles for 3D simulations or a set of segments for 2D simulations). Then, we compute the distance from any given point (a node of the computational domain) to the surface mesh. It is clear that in this case, the description of the immersed structure is limited by the quality and the accuracy of the given surface mesh. Therefore, we rely on the use of anisotropic mesh adaptation technique [54, 27] to obtain a high-fidelity description of the immersed objects.

The Immersed Volume Method is an interesting tool for computational engineers, in particular for conjugate heat transfer analysis. It can be easily implemented in Finite Element codes. It allows solving a single set of equations for the whole computational domain and treating different subdomains as a single fluid with variable material properties. This offers a great flexibility to deal with different shapes or to change easily the physical properties for each immersed structure. Therefore, we start by computing the signed distance function of a given geometry to each node in the mesh. Using the zero isovalue of this function, we can easily identify the fluid-solid interface. Consequently, we can apply an anisotropic mesh adaptation at this interface and then mix the thermo-physical properties appropriately for both domains.

3.2 Level set

3.2.1 Standard level set method

The level set method enables the localization of the interface between two phases. It is a signed function distance and is a widely used tool in many applications such as multiphase flow, crystal growth, image restoration or surface reconstruction [55]. Let Ω the whole domain, Ω_f the fluid domain and Ω_s the solid domain. The level-set function is a signed distance function from the interface $\Gamma = \Omega_f \cap \Omega_s$ defined at each node X of Ω as follows:

$$\alpha(X) = \begin{cases} -\text{dist}(X,\Gamma) & \text{if } X \in \Omega_f \\ 0 & \text{if } X \in \Gamma \\ \text{dist}(X,\Gamma) & \text{if } X \in \Omega_s \end{cases} \tag{3.1}$$

The evolution of the level set is given using a transport equation as follows:

$$\frac{d}{dt}\alpha(x,t) = \frac{\partial \alpha}{\partial t} + u \cdot \nabla \alpha = 0 \tag{3.2}$$

The level set, as a distance function, verifies $\|\nabla\alpha\| = 1$. However, when the interface is convected by a velocity, the level set can lose this property and need to be reinitialized to recover it. A way to reinitialize the level set is to solve the Hamilton-Jacobi equation [16]:

$$\frac{\partial \alpha}{\partial \tau} + \text{s}(\alpha)(\|\nabla\alpha\| - 1) = 0 \tag{3.3}$$

where τ is a fictitious "time step" and $s(\alpha)$ the sign function of α. The steady state is reached when the gradient of the level set recovers its analytical value. Therefore, the solution of this nonlinear hyperbolic equation will be a distance function from the interface while keeping the zero isovalue unchanged. By using this approach, we avoid to find explicitly the zero isovalue.

This property is of utmost importance since all physical properties at the interface will be distributed in space according to the level set. As a demonstration, we perform the simulation of 2D rising bubble in a channel full of water (see Fig. 3.2). We plot some isovalues of the level set at the initial time in Fig. 3.2(a). As time elapses, if the level set is not reinitialized,

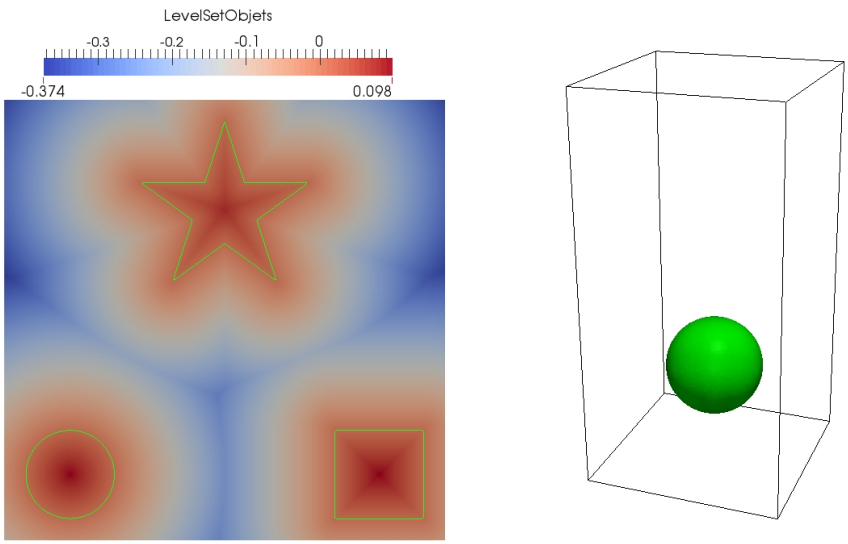

Figure 3.1: Immersion of several objects (left) and a sphere (right). The zero isovalue of the level set is represented in green. On the left picture, color represents the signed distance function to the interface.

the isovalues start to spread far from the interface as it is depicted in Fig. 3.2(b). It means that the level set is not a function distance anymore. If we distribute the material properties according to this non-distance function, we will change the physics of the problem since a non-physical thickness is created due to the diffusion of the isovalues. On the contrary, the level set is reinitialized properly in Fig. 3.2(c) and therefore we still solve the physical problem. The effect of the reinitialization of the physics of the problem is also confirmed by the difference in the height reached in both cases.

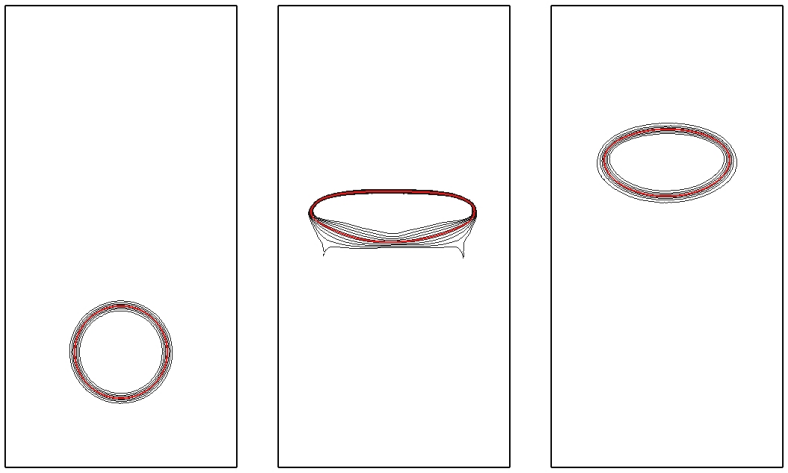

(a) (b) (c)

Figure 3.2: 2D rising bubble. Isovalues of the level set in black and zero isovalue (the interface) in red. Initial setup (left). Results at t=3s when the level set is not reinitialized (middle). Results at t=3s when the level set is reinitialized (right).

The Hamilton-Jacobi procedure being iterative, the computational cost induced can be pro-

hibitive for large computations. A method to alleviate this burden is proposed in [56]: the so-called *convected level set method*.

3.2.2 Convected level set method

This method consists first on truncating the level set function using for the following function:

$$\tilde{\alpha} = E \tanh\left(\frac{\alpha}{E}\right) \tag{3.4}$$

where E is the thickness of the truncation.

An interesting feature of this method is the possibility of imposing Dirichlet boundary conditions since the level set defined in (3.4) is bounded, Furthermore, the gradient of this level set far from the interface is close to 0. This enables to save computational time and to prevent singularity because of corners (2D) or sharp edges (3D) which is really adapted to mesh adaptation procedure.

The truncated level set now verifies the following property:

$$\|\nabla\tilde{\alpha}\| = 1 - \left(\frac{\tilde{\alpha}}{E}\right)^2 \tag{3.5}$$

For sake of simplicity in the notations, we drop in the following the tilde and α will design the truncated level set. We linearize the gradient to express it as a function of the level set at previous time step:

$$\|\nabla\alpha\| \approx \frac{\nabla\alpha^-}{\|\nabla\alpha^-\|}\nabla\alpha \tag{3.6}$$

As a consequence, the Hamilton-Jacobi can be recasted into the convective form:

$$\frac{\partial\alpha}{\partial\tau} + \mathrm{s}(\alpha)\frac{\nabla\alpha^-}{\|\nabla\alpha^-\|}\nabla\alpha = \mathrm{s}(\alpha)\left(1 - \left(\frac{\alpha}{E}\right)^2\right) \tag{3.7}$$

We define $U = s(\alpha)\frac{\nabla\alpha^-}{\|\nabla\alpha^-\|}$ as the reinitialization velocity. Following the lines in [56], we combine the transport and the reinitialization equations into the following equation:

$$\frac{\partial\alpha}{\partial t} + u\cdot\nabla\alpha + \lambda\mathrm{s}(\alpha)\left(\|\nabla\alpha\| - \left(1 - \left(\frac{\alpha}{E}\right)^2\right)\right) = 0 \tag{3.8}$$

where λ is homogeneous to a velocity and E is the thickness of the truncation. Solving the following equation insures that the level set remains a signed function distance.

The equation to solve now reads:

$$\frac{\partial\alpha}{\partial t} + (u + \lambda U)\cdot\nabla\alpha = \lambda\mathrm{s}(\alpha)\left(1 - \left(\frac{\alpha}{E}\right)^2\right) \tag{3.9}$$

It is shown in [56, 57, 58] that the proposed method reduces the computational cost and ensure a better mass conservation than the classical level set method.

3.3 Mesh adaptation

One key for success in innovation in industry is the ability to test new ideas as quick as possible and progress to the optimal solution. However, the accurate prediction of the dynamics of multiphase flows and heat transfer at the industrial scale requires large computational resources that are not affordable for most manufacturers. Reliability in the description of the physical phenomena involved is essential and cannot be compromised in critical application such as aerospace or nuclear industry.

To alleviate this burden, locally refined meshes represents an appealing solution. The computational cost can thus be drastically reduced compared to globally refined mesh. However, if this approach is efficient to mesh complex motionless geometry, an expertise in the problem at hand is required in transient problem to locally refined the region that needed it. Such meshes are valid only for a specific configuration and if the problem exhibits unpredictable evolution in space of the solution, the mesh is to be rebuilt. Underresolved meshes must be recreated to meet the requirements of accuracy necessary to solve properly the problem. Furthermore, even the generation of the first locally refined mesh from a CAD geometry is a time consuming task that requires for a company additional manpower and additional software to be achieved. In the automotive, aerospace, and ship building industries, mesh generation may represent up to 80% of the overall analysis time [59]. The mesh generation can be an endless task and one seeks to circumvent this process.

A large variety of methods were proposed to optimize the computational cost in Computational Fluid Dynamics (CFD) but keeping a certain level of accuracy with limited resources still represents a challenge. For a given computational facility, a compromise between accuracy and computational cost has to be found. We propose in this work the use of an anisotropic dynamic mesh adaptation method with physics-based criteria. More specifically, an automatic mesh adaptation procedure of unstructured mesh, working under the constraint of a fixed number of elements will be used. This method involves the construction of a metric field that contains the information regarding the principal direction in space and the size with respect to each direction. An error estimate is used to build the metric field. In the case of anisotropic mesh adaptation, highly stretched element are allowed, with a ratio of anisotropy up to 1000:1. This feature is very useful in CFD where anisotropy is common such as in turbulent boundary layers or interfaces between phases whose artificial thickness should tend to zero. The numerical methods used to solve PDE's (partial differential equations) on this mesh are therefore modified adequately to take into account the anisotropy of the elements.

In multiphase flows, the concern is to be able to accurately compute the velocity and temperature fields in the whole domain, follow interfaces moving at high velocity and quantify mass transfer rate in a small thickness around the interface to model the phase change. We describe in this section a multi-criteria functional that estimates the error on a combination of several variables including the velocity norm, all the velocity components, the temperature and the level set function. Consequently, computation will benefit from the relevance of the criteria chosen.

3.3.1 Anisotropic mesh adaptation for interface capturing

In the following paragraphs, we will show how to accurately capture an interface using a simple and efficient *a priori* anisotropic mesh adaptation procedure. this will allows us to introduce some notations and the purpose of using mesh adaptation. We combine the level set definition of the interface and build a metric map according to it. Since the level set is an implicit definition

of the interface, the interface intersects the elements of the mesh arbitrarily. As a consequence, when considering two phases, discontinuities due to the high ratio in the physical properties may lead to numerical oscillations during the resolution of PDEs. Instead, we will consider a regularized interface, meaning that the properties are distributed smoothly over a certain thickness around the interface. However, since this interface thickness does not have a physical meaning, it has to be reduced to the minimum. Using anisotropic mesh adaptation with highly stretched elements along the interface will help reducing the interface thickness, will increase the accuracy of the computation due to a higher mesh resolution.

The anisotropic mesh adaptation procedure is performed using a metric map that prescribes a mesh size according to the principal directions in the domain. These principal directions are given by the eigenvectors of this metric and the mesh size is related to the eigenvalues of this metric. The metric $\mathbf{M}$ is a symmetric positive definite tensor [60, 61, 62, 63] representing a local base that modifies the distance computation from the Euclidean space to the metric space, such that:

$$||\mathbf{x}||_{\mathrm{M}} = \sqrt{{}^t\mathbf{x}\cdot\mathbf{M}\cdot\mathbf{x}} \tag{3.10}$$

where $\mathbf{x}$ are the Cartesian coordinates. The definition of the scalar product in the metric space is given by:

$$<\mathbf{x},\mathbf{y}>_{\mathrm{M}} = {}^t\mathbf{x}\cdot\mathbf{M}\cdot\mathbf{y}\ . \tag{3.11}$$

To obtain an accurate description of the interface using the level set function, we consider the normal direction as the principal direction of mesh refinement. Therefore, a given mesh size h_d can be prescribed in the whole domain while a smaller one can be prescribed in a thickness around the interface. A choice to achieve this purpose is to consider the following evolution for the mesh size h:

$$h = \begin{cases} h_d & \text{if } |\alpha(\mathbf{x})| > \varepsilon/2 \\ \dfrac{2h_d(m-1)}{m\,\varepsilon}|\alpha(\mathbf{x})| + \dfrac{h_d}{m} & \text{if } |\alpha(\mathbf{x})| \leq \varepsilon/2 \end{cases} \tag{3.12}$$

where ε represents the desired thickness and m represents a gradation parameter.

According to the prescribed mesh size h and the prescribed direction $\mathbf{n} = \nabla\alpha/||\nabla\alpha||$, we can define the following metric:

$$\mathbf{M} = C\,(\mathbf{n}\otimes\mathbf{n}) + \frac{1}{h_d}\,\mathbf{I} \qquad \text{with} \qquad C = \begin{cases} 0 & \text{if } |\alpha(\mathbf{x})| \geq \varepsilon/2 \\ \dfrac{1}{h^2} - \dfrac{1}{h_d^2} & \text{if } |\alpha(\mathbf{x})| < \varepsilon/2 \end{cases} \tag{3.13}$$

where $\mathbf{I}$ is the identity tensor. This metric corresponds to an isotropic metric far from the interface (with a mesh size set equal to h_d for all directions) and to an anisotropic metric near the interface (with a mesh size set equal to h in the normal direction to the interface and set equal to h_d in the other directions).

As an illustration, Figure 3.3 presents the zero isovalues of the level set function for an immersed F1 car (left) and a helicopter (right). It clearly emphasizes the extremely stretched elements along the interfaces whereas the rest of the domain keeps the same background mesh size.

This step is commonly used to initialize an industrial setup. This approach was extended recently to account for boundary layers capturing in complex flows. Mesh size gradation and curvature analysis were introduced to handle very complex geometries (see [28] for details).

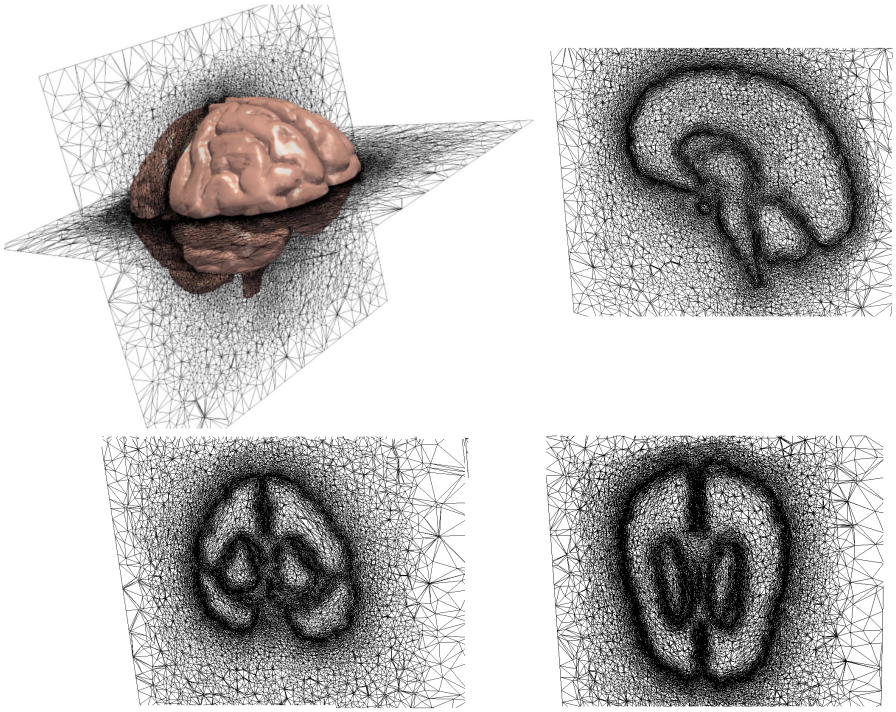

Figure 3.3: Anisotropic mesh adaptation for the detailed representation of a brain.

3.3.2 Edge based metric

The mesh adaptation procedure presented here is an automatic procedure that does not require to deal with case dependent parameter linked to the error analysis. The mesh adaptation strategy relies on the *a posteriori* definition of a metric field able, in some specified sense, to drive the re-meshing procedure so that the interpolation error on the Finite Element solution is minimized. It relies on a statistical representation of the distribution of edges sharing a vertex, a quantity we call length distribution tensor. In order to relate the length distribution tensor to the interpolation error, following [54] we define an edge based error estimator based on a gradient recovery procedure. Once the optimal metric has been obtained, the mesh generation and adaptation procedure described in [27], based on a topological representation, is applied to obtain the new mesh. This metric construction is commonly used for dynamic mesh adaptation based on the variation of several fields such as the velocity, the temperature and the level set.

3.3.2.1 Definition of the length distribution tensor: a statistical representation

Let the triangulation Ω, a subset of $\mathbb{R}^d$, such as Ω is the union of simplex K. Ω reads:

$$\Omega = \bigcup_{K \in \mathscr{K}} K$$

Let $\mathbf{x}^i$ be a mesh vertex and $\mathbf{x}^{ij}$ the edge connecting $\mathbf{x}^i$ to $\mathbf{x}^j$ as in Figure 3.4.

Let $\Gamma(i)$ be the "patch" associated to the mesh vertex $\mathbf{x}^i$, defined as the set of nodes $\mathbf{x}^j$ sharing an edge with $\mathbf{x}^i$.

The problem of finding a unitary metric $\mathbf{M}^i$ associated to the i^{th} node can be formulated as

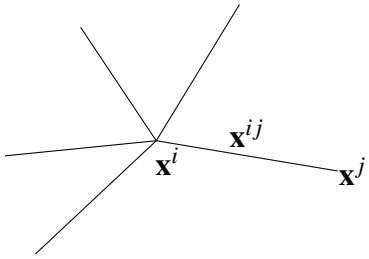

Figure 3.4: Patch associated with node $\mathbf{x}^i$.

the least squares problem [54]:

$$\mathbf{M}^i = \underset{\mathbf{M}\in\mathbb{R}^{d\times d}_{sym}}{\operatorname{argmin}} \left(\sum_{j\in\Gamma(i)} \mathbf{M}\mathbf{x}^{ij}\cdot\mathbf{x}^{ij} - |\Gamma(i)| \right)^2 . \tag{3.14}$$

In the case of a valid mesh, vertices of $|\Gamma(i)|$ form at least d non co-linear edges with vertex $\mathbf{x}^i$. Then, an approximate solution of (3.14) is given by:

$$\mathbf{M}^i = \frac{1}{d}\left(\mathbf{X}^i\right)^{-1}, \tag{3.15}$$

where we introduce the *length distribution tensor* $\mathbf{X}^i$ defined as:

$$\mathbf{X}^i = \frac{1}{|\Gamma(i)|}\left(\sum_{j\in\Gamma(i)} \mathbf{x}^{ij}\otimes\mathbf{x}^{ij} \right) \tag{3.16}$$

whose purpose is to give an average representation of the distribution of edges in the patch.

3.3.2.2 Edge based interpolation error estimate

We consider $u \in C^2(\Omega) = \mathscr{V}$ and $\mathscr{V}_h$ a simple P^1 Finite Element approximation space:

$$\mathscr{V}_h = \left\{ w_h \in C^0(\Omega), w_h|_K \in P^1(K), K \in \mathscr{K} \right\}$$

We denote by U^i the nodal value of u at $\mathbf{x}^i$ and we let Π_h be the Lagrange interpolation operator from $\mathscr{V}$ to $\mathscr{V}_h$ such that:

$$\Pi_h u(\mathbf{x}^i) = u(\mathbf{x}^i) = u_h(\mathbf{x}^i) = U^i, \forall i = 1,\cdots,N$$

Using the analysis carried in [54], we can set the following results:

$$\nabla u_h \cdot \mathbf{x}^{ij} = U^{ij}, \tag{3.17}$$

and:

$$||\nabla u_h\cdot\mathbf{x}^{ij} - \nabla u(\mathbf{x}^i)\cdot\mathbf{x}^{ij}|| = ||U^{ij} - \nabla u(\mathbf{x}^i)\cdot\mathbf{x}^{ij}|| \leq \max_{Y\in[x^i,x^j]} |\mathbb{H}(u)(Y)\mathbf{x}^{ij}\cdot\mathbf{x}^{ij}|, \tag{3.18}$$

where $\mathbb{H}(u) = \nabla^{(2)}u$ is the associated Hessian of u. Recall that taking $u \in C^2(\Omega)$ we obtain $\nabla u \in C^1(\Omega)$.

Applying the interpolation operator on ∇u and using (3.17) we obtain a definition of the projected second derivative of u in terms of only the values of the gradient at the extremities of the edge:

$$\nabla g_h \mathbf{x}^{\mathbf{ij}} \cdot \mathbf{x}^{\mathbf{ij}} = g^{ij} \cdot \mathbf{x}^{\mathbf{ij}} \tag{3.19}$$

where $\nabla g_h = \Pi_h \nabla u$, $\mathbf{g}^i = \nabla u(\mathbf{x}^{\mathbf{i}})$ and $\mathbf{g}^{ij} = \mathbf{g}^j - \mathbf{g}^i$.

Using a mean value argument, we set that:

$$\exists Y \in [x^i, x^j], \quad \mathbf{g}^{ij} \cdot \mathbf{x}^{\mathbf{ij}} = \mathbb{H}(u)(Y)\mathbf{x}^{ij} \cdot \mathbf{x}^{ij}.$$

However this equation cannot be evaluated exactly as it requires that the gradient of u to be known and continuous at the nodes of the mesh. For that reason, we resort to a gradient recovery procedure.

3.3.2.3 Gradient recovery procedure

Using u_h, a P1 Finite Element approximation obtained by applying the Lagrange interpolation operator to a regular function $u \in C^2(\Omega)$, we seek the recovered gradient $\mathbf{g}^i$ of u_h, defined at node $\mathbf{x}^i$ by:

$$\mathbf{g}^i = \underset{\mathbf{g}\in\mathbb{R}^d}{\operatorname{argmin}} \sum_{j\in\Gamma(i)} \left|(\mathbf{g} - \nabla u_h) \cdot \mathbf{x}^{ij}\right|^2 = \underset{\mathbf{g}\in\mathbb{R}^d}{\operatorname{argmin}} \sum_{j\in\Gamma(i)} \left|\mathbf{g} \cdot \mathbf{x}^{ij} - \left(u_h(\mathbf{x}^j) - u_h(\mathbf{x}^i)\right)\right|^2. \tag{3.20}$$

The solution to (3.20) is expressed as:

$$\mathbf{g}^i = \frac{1}{|\Gamma(i)|} \left(\mathbf{X}^i\right)^{-1} \sum_{j\in\Gamma(i)} \left(u_h(\mathbf{x}^j) - u_h(\mathbf{x}^i)\right) \mathbf{x}^{ij}. \tag{3.21}$$

The quantity $|\mathbf{g}^i \cdot \mathbf{x}^{ij}|$ gives a second order accurate approximation of the second derivative of u along the edge $\mathbf{x}^{ij}$ [54]:

$$\left|\left(\mathbf{g}^i - G^i\right) \cdot \mathbf{x}^{\mathbf{ij}}\right| \sim \left(\mathbb{H}(u)\mathbf{x}^{ij} \cdot \mathbf{x}^{ij}\right)$$

where $\mathbf{g}^i$ is the recovery gradient at node i (given by (3.21)), G^i being the exact value of the gradient at node i.

It is proved in [64] that for $P1$ Finite Elements on anisotropic meshes, edge residuals dominate a posteriori errors. Therefore, it is suitable to define an error indicator function associated to the edge $\mathbf{x}^{ij}$ as:

$$e^{ij} = \left|\mathbf{g}^{ij} \cdot \mathbf{x}^{ij}\right|. \tag{3.22}$$

Moreover, this quantity can be easily extended to account for several sources of error, instead of just the scalar field v_h, by applying formula (3.22) to each component separately.

3.3.2.4 Metric construction

We seek to relate the error indicator e^{ij} defined in (3.22) to a metric suitable for a mesh adaptation procedure. For that purpose, we introduce the concept of stretching the factor s^{ij} defined as the ratio between the length of the edge $\mathbf{x}^{ij}$ after the adaptation procedure and before the adaptation procedure. The new metric, denoted by $\widetilde{\mathbf{M}}^i$, will then be given by:

$$\widetilde{\mathbf{M}}^i = \frac{1}{d} \left(\widetilde{\mathbf{X}}^i\right)^{-1} \tag{3.23}$$

where

$$\widetilde{\mathbf{X}}^i = \frac{1}{|\Gamma(i)|}\left(\sum_{j\in\Gamma(i)} (s^{ij})^2 \mathbf{x}^{ij}\otimes\mathbf{x}^{ij}\right) \tag{3.24}$$

is the new length distribution tensor. To relate the metric to the interpolation error, following [26] we set a target total number of nodes N. Because of the quadratic behavior of the error as a function of the scaling factor, denoting by $\tilde{e}^{ij}$ the quantity defined in (3.22) computed after the mesh adaptation process we have:

$$s^{ij} = \left(\frac{\tilde{e}^{ij}}{e^{ij}}\right)^{1/2}. \tag{3.25}$$

Moreover, the number of nodes in the new mesh resulting from the application of the scaling factor s^{ij} to the edge will be roughly equal to:

$$N^{ij} = \frac{1}{s^{ij}}, \tag{3.26}$$

so that the total contribution of node i (in the old mesh) to the number of nodes in the new mesh will be given by

$$N^i = \det\left(\left(\mathbf{X}^i\right)^{-1}\sum_{j\in\Gamma(i)} N^{ij}\mathbf{x}^{ij}\otimes\mathbf{x}^{ij}\right) \tag{3.27}$$

By combining (3.25) and (3.26), it is possible to consider N^i in (3.27) is a function of $\tilde{e}^{ij}$. Assuming that the total error is equidistributed among all edges such that each edge contributes a constant error e to the total, one can see that $N^{ij} = \left(\frac{e^{ij}}{e}\right)^{1/2}$, which results in the relation

$$N^i(e) = N^i(1)e^{-d/2}. \tag{3.28}$$

By summing over all the nodes of the old mesh, an expression for the global error as a function of the number of nodes in the new mesh is obtained:

$$e = \left(\frac{1}{N}\sum_i N^i(1)\right)^{2/d} \tag{3.29}$$

The corresponding stretching factors are given by:

$$s^{ij} = \frac{\left(\sum_i N^i(1)\right)^{1/d}}{N^{1/d}\left(e^{ij}\right)^{1/2}}. \tag{3.30}$$

3.3.2.5 Mesh adaption criteria

In the last paragraphs, we showed the construction of a metric from a field u under the constraint of a fixed number of nodes. In coupled problems, the mesh may require to be adapted according to several fields. If we apply the mesh adaptation to both the Navier-Stokes and heat transfer equations, different fields can be used as a criterion: the velocity norm, the velocity components, the temperature field, the temperature gradient components, and/or their combinations. In this case, the adaptivity will account for the both the change of direction of the velocity, its magnitude and the temperature field T.

A way to adapt a mesh according to several variables is to construct a metric field for each variable and then produce a unique metric by intersection of metrics [65]. The resulting metric should yield the largest mesh size in any direction that still fulfills the size constraint given by all the metrics. The intersection operation between several metric fields is not uniquely defined. The most common technique, consisting of a sequence of simultaneous reductions of two metrics, does not provide the optimal metric, is not commutative and incurs a relatively high computational cost. Robust techniques, based on the optimization problems, are even more costly.

In what follows, we simplify this operation by using one field that accounts for different variables. It consists on constructing a unique metric directly using a multi-component error vector containing, for instance, all the components of the velocity field, the temperature field, the level set function α, etc. Consequently, we do not need to intersect several metrics.

Let us introduce $u = \{u_1, u_2, \cdots, u_n\}$. By applying the above theory for each component of u, we end up obtaining a single metric and it comes out immediately that the error is now a vector given by the following expression:

$$\vec{e_{ij}} = \left\{e_{ij}^1, e_{ij}^2, \cdots, e_{ij}^n\right\} \tag{3.31}$$

and then the stretching factor reads:

$$s_{ij} = \left(\frac{||e(N)||}{||\overrightarrow{e_{ij}}||}\right)^{\frac{1}{2}} \tag{3.32}$$

For example, a vector of error sources can be locally defined in two dimensions as:

$$\mathbf{Y}(\mathbf{x}^i) = \left\{\frac{v_x^i}{\|\mathbf{v}^i\|}, \frac{v_y^i}{\|\mathbf{v}^i\|}, \frac{\|\mathbf{v}^i\|}{\max\limits_j \|\mathbf{v}^j\|}, \frac{T^i}{T_{\max}}, \frac{\tilde{\alpha}}{\tilde{\alpha}_{\max}}\right\}. \tag{3.33}$$

The field used as input for the error estimator (3.22) is the norm $\left(\sum_k Y_k^2\right)^{1/2}$ of $\mathbf{Y}$, with Y_k the components of $\mathbf{Y}$. This definition measures the error in the norm as well as in the direction of the velocity vector $\mathbf{v}$, in addition to the error on the temperature T. Because all fields are normalized (the velocity components v_x, v_y and v_z by the local velocity norm, the velocity norm $\|\mathbf{v}\|$, the temperature and he filtered level set function $\widetilde{\alpha}$ by their respective global maximum), a field that is much larger in absolute value does not dominate the error estimator, and the variations of all variables are fairly taken into account.

Note also that there are different possibilities to compute the norm (L_2, L_1 or L_∞) and to produce a simple error value for each edge and thus from a unique e_{ij} value, the scalar theory exposed in the previous section can be used and provides a unique metric. Since we did not observe a significant difference between the norms, we used in the numerical example only the L_2 norm to compute the error.

3.4 Mixing laws

In the monolithic approach, all the different phases considered (solid, liquid, gas) are immersed in a single domain. As explained previously we use an implicit definition of the interfaces by mean of level set functions. Therefore, the level set function will be used to distribute in space the respective material properties. In order to avoid discontinuity at the interface, we compute

a smooth Heaviside function to distribute in space the corresponding physical properties. This Heaviside function is given by:

$$H(\alpha) = \begin{cases} 1 & \text{if } \alpha > \varepsilon \\ \frac{1}{2}\left(1 + \frac{\alpha}{\varepsilon} + \frac{1}{\pi}\sin\left(\frac{\pi\alpha}{\varepsilon}\right)\right) & \text{if } |\alpha| \leq \varepsilon \\ 0 & \text{if } \alpha < -\varepsilon \end{cases} \tag{3.34}$$

where α is the level set function, ε is a small parameter such that $\varepsilon = O(h_{\text{im}})$, known as the interface thickness, and h_{im} is the mesh size in the normal direction to the interface. In the vicinity of the interface, it can be computed using the following expression:

$$h_{\text{im}} = \max_{j,l \in K} \nabla\alpha \cdot \mathbf{x}^{jl}, \tag{3.35}$$

where $\mathbf{x}^{jl} = \mathbf{x}^l - \mathbf{x}^j$ and K is the mesh element under consideration. Consequently, the PDE's are solved in the whole domain, using the same set of equations. All phases are considered as "one phase" with continuous heterogeneity in their physical properties. It should be underlined that the accuracy in the distribution of the material properties will benefit from the anisotropic mesh adaption procedure that reduces the thickness of the transition.

The material properties such as density ρ, heat capacity c_p, dynamic viscosity μ and initial temperature are therefore computed as follows:

$$\begin{aligned} \rho &= \rho_f H(\alpha) + \rho_s(1 - H(\alpha)) \\ \mu &= \mu_f H(\alpha) + \mu_s(1 - H(\alpha)) \\ \rho C_p &= \left(\rho_f C_{pf} H(\alpha) + \rho_s C_{ps}(1 - H(\alpha))\right) \\ \rho C_p T &= \rho_f C_{pf} T_f H(\alpha) + \rho_s C_{ps} T_s (1 - H(\alpha)) \end{aligned} \tag{3.36}$$

However, using a linear mixing law for the thermal conductivity λ would lead to inaccurate results. According to [66], a harmonic mixing laws is recommended to ensure the conservation of the heat flux:

$$\lambda = \left(\frac{H(\alpha)}{\lambda_f} + \frac{1 - H(\alpha)}{\lambda_s}\right)^{-1} \tag{3.37}$$

The Immersed Volume Method enables to consider a direct thermal coupling without the need of heat transfer coefficient. This method only requires the knowledge of the material properties an deals naturally with conjugate heat transfer.

3.5 Numerical applications

We present in this section two numerical tests with validations to illustrate the propose adaptive Eulerian framework. The first one focuses on fixed geometries and their corresponding obtained anisotropic meshes, while the second one focuses on dynamic mesh adaptation using different criteria and its utility.

3.5.1 High-fidelity anisotropic meshing

In the first test case, we aim to show the flexibility of the proposed mesh adaptation technique to deal with multiphase flows. Therefore we consider three fixed objects defined by level set functions inside a squared domain (see Figure 3.5). The circle of radius 0.1m is centered at (0.15;0.15). The square of 0.20m size is centered at (0.85;0.15). The regular pentagram is centered at (0.5;0.75) and the radius of the circumcircle is 0.2m. We choose to position them close to the wall to assess the capacity of the method to capture the features of the geometry close to a boundary.

In multiphase simulations, we use the level set function to define the properties in each phase. The physical properties are usually discontinuous across the interface. To avoid discontinuities which lead to numerical errors, we use a smooth Heaviside function computed from the level set function. This creates an interface transition with a thickness of few elements. The use of mesh adaptation techniques enables to reduce this thickness. As it is depicted in Figure 3.5, for a given number of elements (10000), the transition is finer with an anisotropic adaptive mesh.

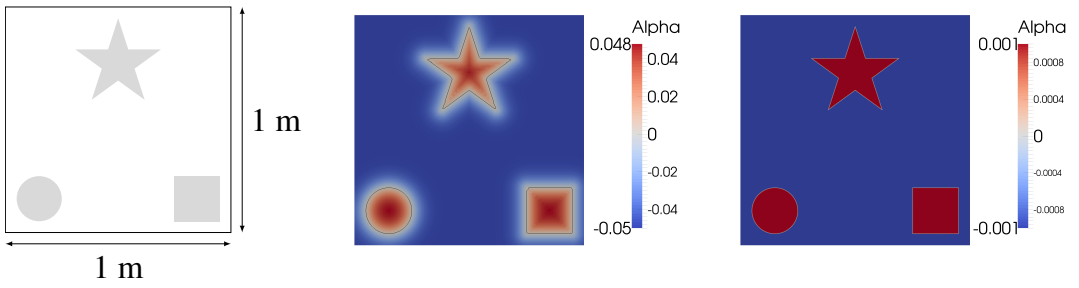

Figure 3.5: Three immersed objects inside a squared cavity (left). Filtered level set function for 10000 elements in a structured mesh (middle) and in an adaptive mesh (right).

Figure 3.6 shows the obtained zero isovalue of the level set functions using different number of nodes. The comparison with structured meshes using the same number of nodes shows that anisotropic mesh adaptation allows easily to keep very good accuracy of the geometry, even for a low number of nodes. Figure 3.7 shows the correct orientation and deformation of the mesh elements (longest edges parallel to the boundary). This yields a great reduction of the number of triangles. These results give confidence that the proposed framework allows to deal with different shapes, with angles, singular point and curvatures.

Finally, we measure the accuracy of the mesh adaptation technique. We compute the total perimeter and the total area of the three immersed objects and we plot the error between the analytic and the numerical solutions. We also plot the error for a structured mesh. Figure 3.8 confirms the advantage of using anisotropic adaptive meshes for multiphase flows. For a given accuracy, at least ten times more elements are required in a structured mesh.

3.5.2 Dam break

In this test case, we consider the collapse of a column of water of size $\omega^2 a \times a$. This is a widely used benchmark in the field of multiphase flows. The initial setup for this test case is given in Fig. 3.9. A fictitious wall, the dam, is removed at initial time. The water is thus free to fall and evolve from left to right. Experimental results are available from [67] and make this benchmark suitable for validation. The position of the front over time on the bottom side of the

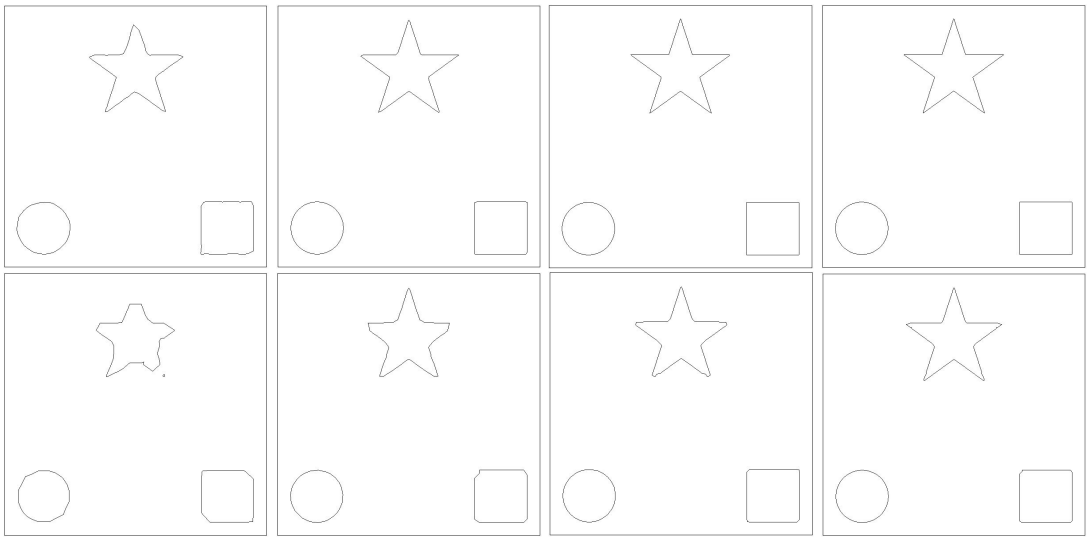

Figure 3.6: Zero isovalue of the level set function for 1000, 2000, 5000 and 10000 elements. First line: result with adaptive meshing. Second line: result with structured meshes

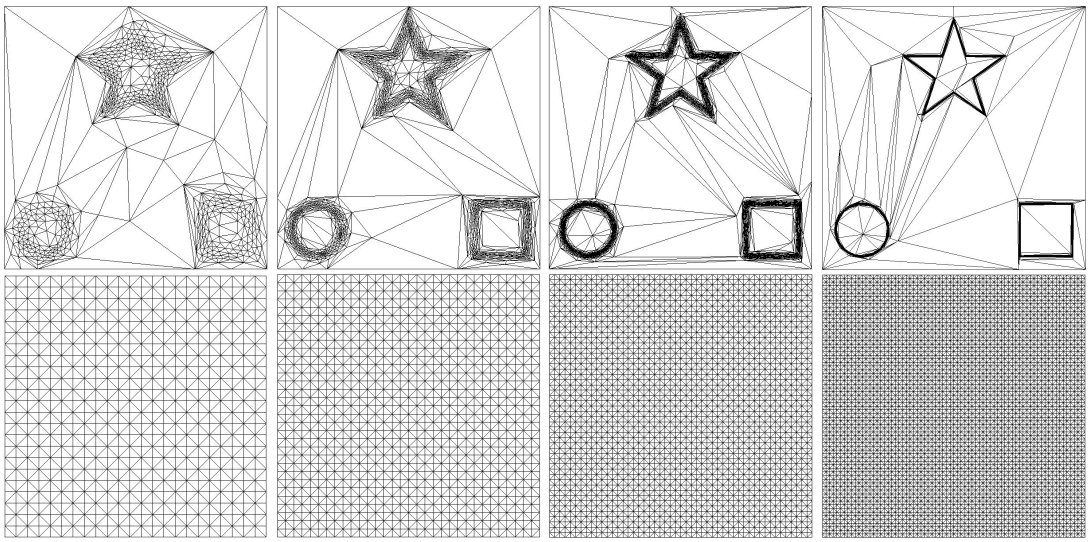

Figure 3.7: The obtained mesh for 1000, 2000, 5000 and 10000 elements

domain or the evolution of the water height on the left side of the domain were validated against experiment in [68]. We reproduce in Fig.3.10 the evolution of the front position. In this figure are also plotted results from literature using various numerical methods [69, 70]. The evolution of the water is depicted in Fig. 3.11. It shows that the proposed framework deals naturally with complex topological changes of the interface. Water hits the wall on the right side of the domain and splashes into several slugs. This test case represents a real challenge using a fully Lagrangian framework because of the possible interpenetration of mesh elements during the motion of the interface. Using an Eulerian framework enables to avoid such difficulties. However, to obtain a better accuracy in the description of the interface and the evolution of the flow motion, it would be helpful to use the anisotropic mesh adaptation procedure presented earlier.

As mentioned earlier in this chapter, mesh adaptation can be performed using several variables all at once. This benchmark is an opportunity to see the effect of the mesh adaptation on

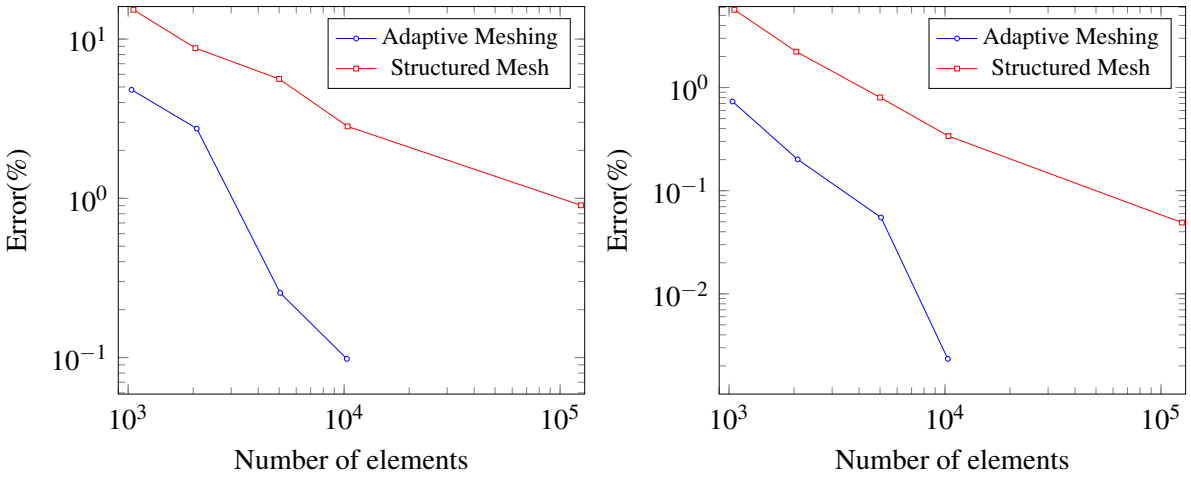

Figure 3.8: Percentage of error for the computation of the perimeter (left) and the area (right)

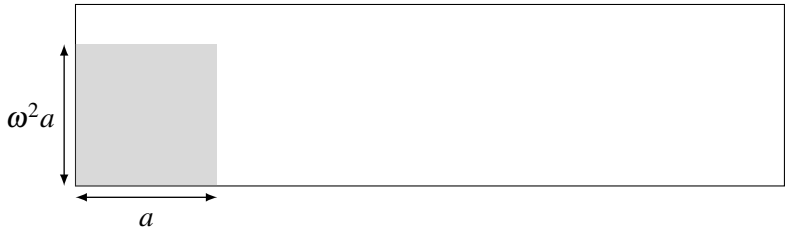

Figure 3.9: Initial setup for the 2D dam break test case. The column of water is represented in gray.

the resolution of the problem. Therefore we propose to adapt the mesh according to the level set function but also according to an additional criterion. We performed first a simulation using viscous dissipation and a second one using shear stress. The evolution of the mesh according to each criterion is given in Fig.3.12. On the left of Fig.3.12, we notice that only the free surface is well captured. Other features related to the flow evolution such as eddies, recirculation at the corner are missing. The simulation reaches a quasi-steady state after only few physical seconds. In the second case, using shear stress as a mesh adaptation criterion enables the mesh to capture key features of the flow. We clearly see the evolution of the wave from one side to the other, recirculation at the corner, boundary layers. The importance of the criteria is therefore highlighted. Further investigation are still required to validate this observation.

3.6 Conclusion

In this chapter, we presented the different components of the Immersed Volume method that will be extended in the following chapters to deal with boiling and the simulation of quenching processes. A single domain is discretized and all the phases and geometries are immersed in this domain. Therefore, only a single set of equation is solved. The different phases are represented using a level set method that is shown to be favorable in the simulation of multiphase flows. Physical properties are distributed to their respective phases using mixing laws that enable a smooth transition over a small thickness at the interface. Then we introduced the mesh adaptation procedure using metric field built from *a priori* or *a posteriori* error estimator taking into account the interfaces but also physical features such as velocity, temperature,... The

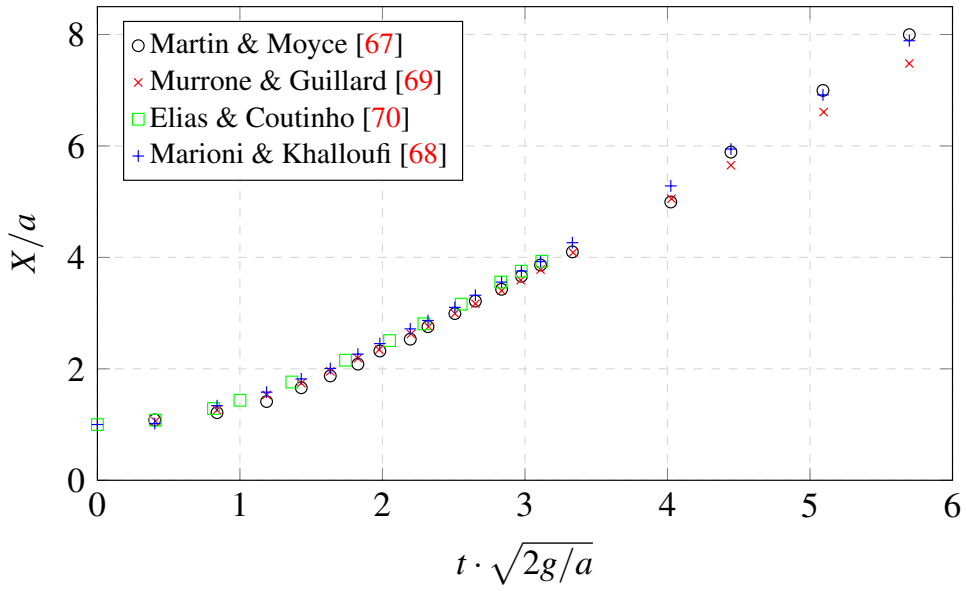

Figure 3.10: Non-dimensional front position evolution

dynamics mesh adaptation procedure is performed under the constraint of a fixed number of elements thus drastically reducing the computational while preserving high accuracy where it is required. Finally we tested the proposed framework with a coupling of all these components. The proposed framework is shown to be very accurate for the description of interface and in the resolution of numerical problem, with a very limited computational cost.

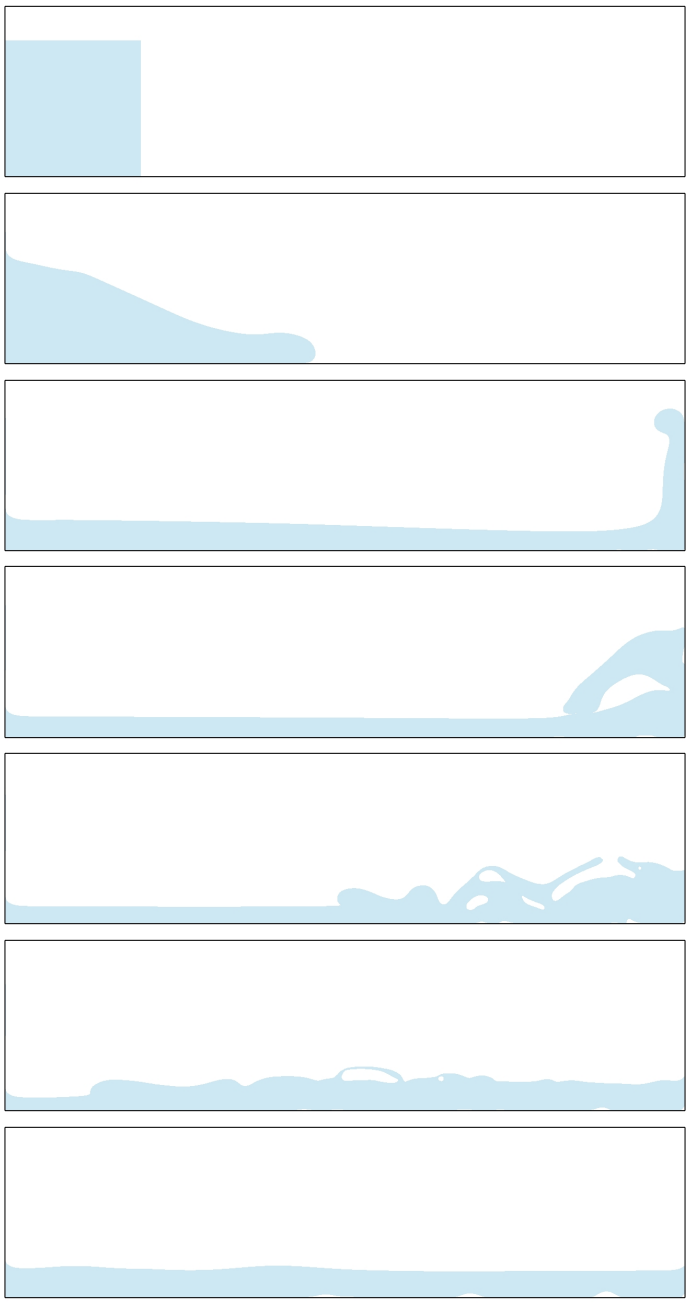

Figure 3.11: Evolution of the water (in blue) at t=0, 0.1, 0.31, 0.44, 0.55, 0.80 and 3 s.

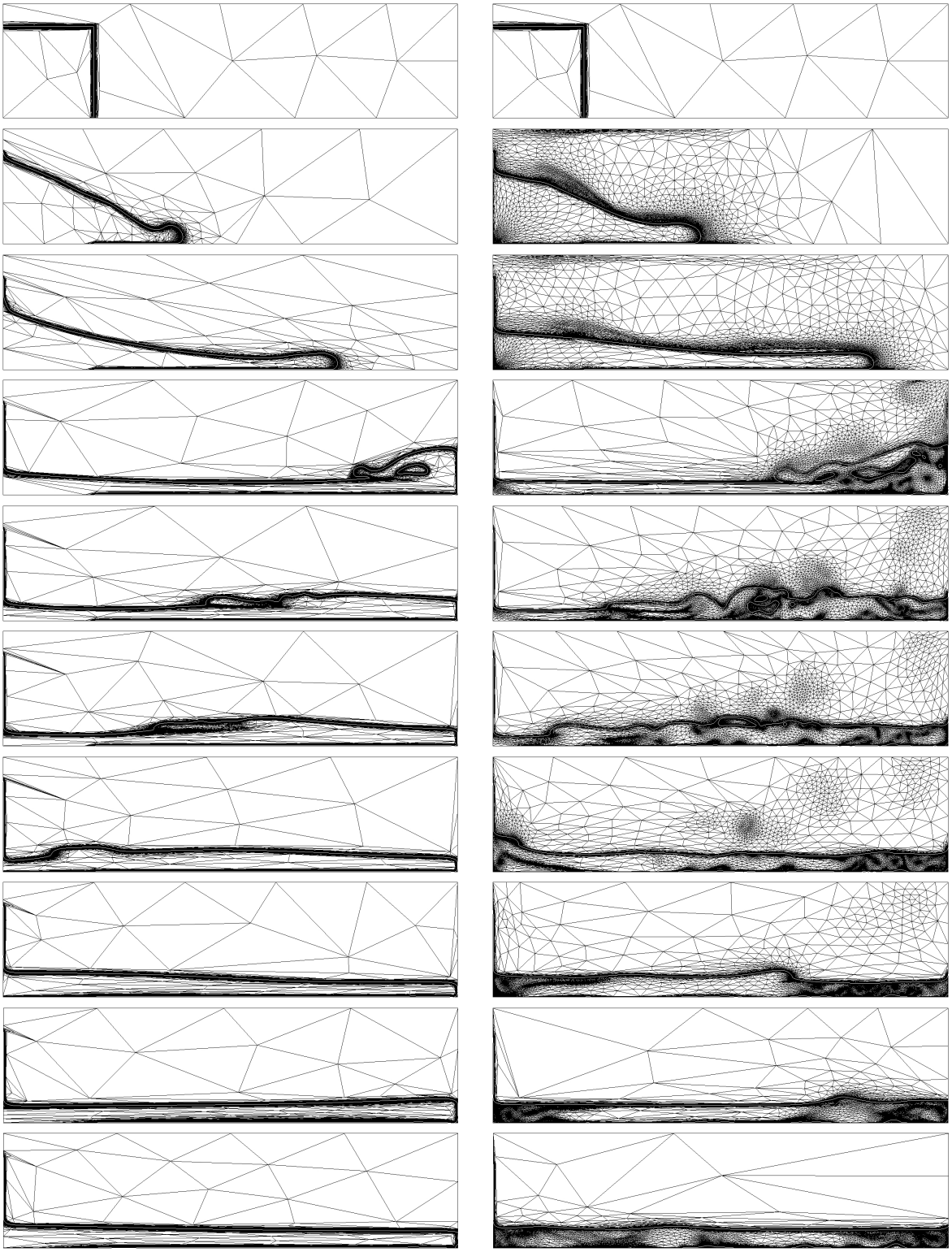

Figure 3.12: From top to bottom, meshes at t=0, 0.1, 0.2, 0.5, 0.7, 0.8, 1, 1.5, 2 and 3s. On the left column, the mesh adaptation criterion is viscous dissipation. On the right, the mesh adaptation criterion is shear stress.

Résumé en français

Dans ce chapitre, la méthode des volumes immergées est présentée. Cette méthode consiste en un cadre eulérien monolithique, dans lequel un unique domaine est considéré et un seul ensemble d'équations est résolu dans tout ce domaine. Les différentes phases en présence sont localisées par l'intermédiaire d'une fonction level set. La fonction level set est une distance signée à l'interface qui permet naturellement des évolutions topologiques complexes de l'interface. La distribution des propriétés physiques des différentes phases est effectuée en calculant une loi de mélange utilisant la level set. L'évolution de l'interface est obtenue par la résolution d'une équation de transport qui, dans certain cas, peut faire perdre à la level set sa propriété de distance, ne permettant plus un mélange exact des propriétés physiques. Ainsi, deux méthodes dites de "réinitialisation" sont présentées, permettant de conserver cette propriété de distance.

La description des différentes phases est améliorée par l'utilisation de méthodes d'adaptation de maillage anisotrope. Ces méthodes permettent de raffiner le maillage proche des interfaces et de le déraffiner ailleurs. La précision des calculs est ainsi grandement améliorée tout en conservant un coût de calcul intéressant. La méthode présentée dans ce travail permet également de travailler à nombre d'éléments constant, ce qui représente un intérêt lorsque les capacités de calculs ne sont pas extensibles. L'extension de cette méthode d'adaptation de maillage anisotrope permet de capturer avec précision les plus forts gradients des solutions du problème, telles que la température et la vitesse, aboutissant ainsi à une précision accrue.

Des cas tests permettent de montrer la pertinence et la précision de la méthode des volumes immergées pour la simulation d'écoulements multiphasiques.

Chapter 4

Stabilized Finite Element method for Computational Fluid Dynamics

Contents

4.1 Context

Today, new developments in Finite Element methods enable accurate resolution of some complex problems such as compressible flows governed by the Navier-Stokes equations or incompressible viscous flows at high Reynolds numbers. It is well known that the essential breakthrough in Computational Fluid Dynamics has first been made in the context of the finite difference and the finite volume methods. However, the use of Finite Element method to study fluid dynamics has grown significantly. Indeed, several Finite Element approaches have been proposed to address the challenging task of solving the Navier-Stokes and the Convection-Diffusion-Reaction (CDR) equations accurately and efficiently in the high Reynolds (Re) and Peclet (Pe) regimes. We will introduce in this chapter the Finite Element method implemented at CEMEF to solve CFD problems.

4.2 State of the art

The incompressible Navier-Stokes equations are used to model a number of important physical phenomena: turbulent flow around airfoils, meteorological prediction, weather, arterial blood flow [71], etc. The standard Galerkin formulations were not robust enough to model complex convection dominated flows. Therefore, a significant effort has been made to develop Finite Element approaches circumventing the weaknesses of the Galerkin method [72, 73, 35]). As a consequence, alternatives to the standard Galerkin FEM have flourished in the literature. Amongst them, we will focus on the Stabilized Finite Element Method (SFEM) and the Variational Multiscale method (VMS). These two classes of Finite Element are no so fundamentally different. Indeed, even if Stabilized Finite Element methods (SFEM) are centered on the modification of the variational formulation while Variational Multiscale method modify the Finite Element basis, it is shown in the literature, that they address the same shortcomings of the classical Galerkin method. They add weighted residual terms to the standard weak formulation of the problem to enhance its stability while maintaining consistency.

Indeed, the stability of the discrete formulation depends on the compatibility restrictions on the choice of the Finite Element spaces for the velocity and the pressure. According to this, standard Galerkin mixed elements with continuous equal order linear/linear interpolation is not a stable discretization since it does not satisfy the Babuska-Brezzi (inf-sup) condition. The lack of stability manifests in uncontrollable oscillations that pollute the solution.

Several methods exist to circumvent the lack of stability in convection-dominated regime and the inf-sup restriction. In [74] was proposed the concept of Mini -Element which consists in the enrichment of the functional space by a space of bubbles function. A stabilized formulation allowing equal order linear interpolation is obtained using the Mini-Element since the bubble functions vanish on the element boundary and are eliminated by static condensation. This method, if appropriate in diffusion dominant regime, the Mini-element formulation of the problem yields very acceptable results. However, when the convection terms dominate, the results are deteriorated and therefore this method requires additional stabilization to achieve acceptable results.

A groundbreaking method is the Streamline Upwind Petrov Galerkin (SUPG) proposed by Brooks and Hughes [75, 76]. This method modifies the test functions by adding weighted residuals to the variational formulation of the problem. This method has proved its efficiency in eliminating the spurious oscillations related to the Galerkin formulation and is now a standard for computational fluid dynamics and heat transfer Finite Element solver.

A history on residual based stabilization methods can be found in the book of Donea and Huerta [77]. The foundations of multiscale methods were made precise in the mid 90's by Hughes *et al.* [32, 78] followed by PSPG (Pressure Stabilized Petrov Galerkin) methods by Tezduyar [79]. The Unusual Stabilized Finite Element method (USFEM) was introduced by Franca and Farhat in [80]. Codina and co-workers introduced lately recent developments of residual based stabilization methods using orthogonal subscales and time dependent subscales [81, 82, 83, 84]. These methods are very promising and can be regarded as an open door to turbulence. At the same level, one can find a complete description on the use of Variational Multiscale method for turbulent flows in [85, 86, 87] where a three scale separation method was developed and applied.

4.3 Flow solver

Turbulent flows can be predicted by resolving the transient Navier-Stokes equations using a Direct Numerical Simulation (DNS) [88] approach with a very fine mesh resolution and adequate time steps. The required computing resources for such computations are tremendous and are not always affordable especially when simulating complex industrial processes. This is the main reason why most engineering computations involving turbulent flows use turbulence modeling, at least for the foreseeable future.

Large numbers of models have been developed and studied in the last few decades. We can classify these modeling approaches into three categories: VMS, LES and RANS. As one progresses from DNS to RANS, more and more of turbulent motions are approximated and, therefore, require less computational resources. This is especially interesting when dealing with industrial application since it opens the choice to the user to decide which methods to use regarding the application at hand. Each method will offer the accuracy of the results with respect to the computational costs.

The Finite Element implementation of the unsteady Navier-Stokes and Convection-Diffusion-Reaction will be briefly described and analyzed in the following sections.

4.3.1 The incompressible Navier-Stokes equations

4.3.1.1 Governing equations

Let $\Omega \subset \mathbb{R}^n$ be the spatial domain at time $t \in [0,T]$, where n is the space dimension. Let Γ denotes the boundary of Ω. We consider the following velocity-pressure formulation of the Navier-Stokes equations governing unsteady incompressible flows:

$$\rho(\partial_t \mathbf{u} + \mathbf{u}\cdot\nabla\mathbf{u}) - \nabla\cdot\sigma = \mathbf{f} \quad \text{in } \Omega\times\ [0,T] \tag{4.1}$$

$$\nabla\cdot\mathbf{u} = 0 \quad \text{in } \Omega\times\ [0,T] \tag{4.2}$$

where ρ and $\mathbf{u}$ are the density and the velocity, $\mathbf{f}$ the body force vector per unit density and σ the stress tensor which reads:

$$\sigma = 2\mu\ \boldsymbol{\varepsilon}(\mathbf{u}) - p\ \mathbf{I_d} \tag{4.3}$$

where p and μ are the pressure and the dynamic viscosity, $\mathbf{I_d}$ the identity tensor and $\boldsymbol{\varepsilon}$ the strain-rate tensor defined as:

$$\boldsymbol{\varepsilon}(\mathbf{u}) = \frac{1}{2}\left(\nabla\mathbf{u} + {}^t\nabla\mathbf{u}\right) \tag{4.4}$$

Dirichlet and natural boundary conditions for equation (4.1) are:

$$\mathbf{u} = \mathbf{g} \quad \text{on } \Gamma_g \times [0,T] \tag{4.5}$$

$$\mathbf{n}\cdot\sigma = \mathbf{h} \quad \text{on } \Gamma_h \times [0,T] \tag{4.6}$$

where Γ_g and Γ_h are complementary subsets of the domain boundary Γ. Functions $\mathbf{g}$ and $\mathbf{h}$ are given and $\mathbf{n}$ is the unit outward normal vector of Γ.

As initial condition, a divergence-free velocity field $\mathbf{u}_0(\mathbf{x})$ is specified over the domain Ω at $t = 0$:

$$\mathbf{u}(\mathbf{x},0) = \mathbf{u}_0(\mathbf{x}) \tag{4.7}$$

4.3.1.2 Weak formulation

The function spaces for the velocity and the pressure are respectively defined by:

$$V = \left\{ \mathbf{u}(\mathbf{x},t) \mid \mathbf{u}(\mathbf{x},t) \in H^1(\Omega)^n,\ \mathbf{u} = \mathbf{g} \text{ on } \Gamma_g \right\} \tag{4.8}$$

$$P = \left\{ p(\mathbf{x},t) \mid p(\mathbf{x},t) \in L^2(\Omega) \right\} \tag{4.9}$$

and the weighting function space for the velocity

$$V_0 = \left\{ \mathbf{u}(\mathbf{x},t) \mid \mathbf{u}(\mathbf{x},t) \in H^1(\Omega)^n,\ \mathbf{u} = \mathbf{0} \text{ on } \Gamma_g \right\} \tag{4.10}$$

$$\tag{4.11}$$

The weak form of system (4.1 - 4.2) consists in finding $\mathbf{u} : [0,T] \to V$, $p : (0,T] \to P$ such that:

$$\begin{cases} (\rho \partial_t \mathbf{u}, \mathbf{w})_\Omega + (\rho \mathbf{u} \cdot \nabla \mathbf{u}, \mathbf{w})_\Omega + (\sigma(p,\mathbf{u}), \boldsymbol{\varepsilon}(\mathbf{w}))_\Omega = (\mathbf{f}, \mathbf{w})_\Omega + (\mathbf{h}, \mathbf{w})_{\Gamma_h} & \forall w \in V_0 \\ (\nabla \cdot \mathbf{u}, q)_\Omega = 0 \quad \forall q \in P \end{cases} \tag{4.12}$$

where $(\varphi, \psi)_\Omega = \int_\Omega \varphi \psi \mathrm{d}\Omega$ is the standard scalar product in $L^2(\Omega)$.

The standard Galerkin approximation consists in decomposing the domain Ω into N_{el} elements K such that they cover the domain and are either disjoint or share a complete edge (or face in 3D). Using this partition $\mathscr{K}_h$, the above-defined functional spaces (4.8) and (4.9) are approached by finite dimensional spaces spanned by continuous piecewise polynomials such that:

$$V_h = \left\{ \mathbf{u}_h \mid \mathbf{u}_h \in C^0(\Omega)^n,\ \mathbf{u}_{h|K} \in P^1(K)^n,\ \forall K \in \mathscr{T}_h \right\} \tag{4.13}$$

$$P_h = \left\{ p_h \mid p_h \in C^0(\Omega),\ p_{h|K} \in P^1(K),\ \forall K \in \mathscr{T}_h \right\} \tag{4.14}$$

The Galerkin discrete problem consists therefore in solving the following mixed problem:

Find a pair $\mathbf{u}_h : [0,T] \to V_h$ and $p_h : (0,T] \to P_h$, such that: $\forall\ (\mathbf{w}_h, q_h) \in V_{h,0} \times P_h$

$$\begin{cases} (\rho \partial_t \mathbf{u}_h, \mathbf{w}_h)_\Omega & + (\rho \mathbf{u}_h \cdot \nabla \mathbf{u}_h, \mathbf{w}_h)_\Omega \\ & + (2\mu \boldsymbol{\varepsilon}(\mathbf{u}_h) : \boldsymbol{\varepsilon}(\mathbf{w}_h))_\Omega - (p_h, \nabla \cdot \mathbf{w}_h)_\Omega = (\mathbf{f}, \mathbf{w}_h)_\Omega + (\mathbf{h}, \mathbf{w}_h)_{\Gamma_h} \\ (\nabla \cdot \mathbf{u}_h, q_h)_\Omega & = 0 \end{cases} \tag{4.15}$$

Recall that the standard Galerkin formulation with equal order linear interpolation is not a stable stabilization and suffers from spurious oscillations that pollute the solution.

4.3.2 The Variational Multiscale method (VMS)

The Variational Multiscale framework, proposed by Hughes [32] to deal with the mixed variational formulation for solving the Navier-Stokes equations, models the effects of the smallest scales of the flow and numerically resolves the largest scales. It considers that the unknowns can be split into two components, coarse and fine, corresponding to different scales or levels of resolution. First, we solve the fine scales in an approximate manner and then we replace their effect into the large scales.

In this work, we contribute in the development of the VMS formulation of the Navier-Stokes equation taking into account additional features such as semi-implicit surface tension, phase change or considering a unified compressible-incompressible flows formulation. We describe in this section the general outline of the VMS formulation for the incompressible Navier-Stokes equation that enables the use of equal order continuous interpolations and prevent oscillations polluting the solution in the convection dominated regime. The ability of this formulation to deal with high Reynolds number flows is demonstrated in [89, 20, 24].

4.3.2.1 Variational formulation

Let us split the velocity and the pressure solution spaces as $V_h \oplus V'$ and $P_h \oplus P'$, respectively. Subscript h is used here and in the following to denote the Finite Element (coarse) component, whereas the prime is used for the so-called subgrid scale (fine) component of the unknowns. The scale decomposition reads:

$$\begin{aligned} \mathbf{u} &= \mathbf{u}_h + \mathbf{u}' \in V_h \oplus V' \\ p &= p_h + p' \in P_h \oplus P' \end{aligned} \tag{4.16}$$

The scale decomposition is also applied to the test function spaces:

$$\begin{aligned} \mathbf{w} &= \mathbf{w}_h + \mathbf{w} \in V_{h,0} \oplus V'_0 \\ q &= q_h + q' \in P_{h,0} \oplus P'_0 \end{aligned} \tag{4.17}$$

The weak formulation of 4.15 using the scale decomposition is:

$$\begin{aligned} (\rho\partial_t(\mathbf{u}_h+\mathbf{u}'),\mathbf{w}_h+\mathbf{w}') + (\rho(\mathbf{u}_h+\mathbf{u}')\cdot\nabla(\mathbf{u}_h+\mathbf{u}'),\mathbf{w}_h+\mathbf{w}') & \\ -(p_h+p',\nabla\cdot(\mathbf{w}_h+\mathbf{w}')) + 2(\mu\varepsilon(\mathbf{u}_h+\mathbf{u}'),\varepsilon(\mathbf{w}_h+\mathbf{w}')) &= (\mathbf{f},\mathbf{w}_h+\mathbf{w}') \quad (4.18) \\ (\nabla\cdot(\mathbf{u}_h+\mathbf{u}'),q_h+q') &= 0 \quad (4.19) \end{aligned}$$

In this work, additional assumption regarding the subscales are proposed, even though the subgrid scales (or subscales) could be approximated without further assumptions and inserted into the previous equations (see [90]), we will make use of some common approximations:

i) The subscales are not tracked in time, therefore, quasi-static subscales are considered here. However, the subscale equation remains quasi time-dependent.

ii) The convective velocity of the non-linear term may be approximated using only the large-scale component, so that $(\mathbf{u}_h+\mathbf{u}')\cdot\nabla(\mathbf{u}_h+\mathbf{u}') \approx \mathbf{u}_h\cdot\nabla(\mathbf{u}_h+\mathbf{u}')$. Moreover, this approximation can be done also if the convective term is written as $\nabla\cdot[(\mathbf{u}_h+\mathbf{u}')\otimes(\mathbf{u}_h+\mathbf{u}')]$, which is relevant when integrating by parts the convective term.

iii) Terms involving subscales can be integrated by parts and the subscales on the element boundaries will be neglected.

The equations for the coarse scales are obtained taking the subscale test functions equal to zero. Furthermore, we can mention that for linear elements used in this work, terms of the form $\nabla\cdot(2\mu\varepsilon(\mathbf{w}_h))$ involving second derivatives within each element can be neglected. Therefore, we get:

$$\begin{aligned} (\rho\partial_t\mathbf{u}_h,\mathbf{w}_h) + (\rho\mathbf{u}_h\cdot\nabla\mathbf{u}_h,\mathbf{w}_h) - (p_h+p',\nabla\cdot\mathbf{w}_h) + 2(\mu\varepsilon(\mathbf{u}_h),\varepsilon(\mathbf{w}_h)) & \\ + \sum_K (\mathbf{u}', -\rho\mathbf{u}_h\cdot\nabla\mathbf{w}_h)_K = (\mathbf{f},\mathbf{w}_h) \quad (4.20) & \\ (\nabla\cdot\mathbf{u}_h, q_h) - \sum_K (\mathbf{u}', \nabla q_h)_K = 0 \quad (4.21) & \end{aligned}$$

where $\sum_K$ stands for the summation over all the elements of the Finite Element partition $\mathscr{K}_h$ and $(\cdot,\cdot)_K$ denotes the L^2 product in each K.

The problem for the fine scales is obtained taking $(\mathbf{w}_h, q_h) = (\mathbf{0}, 0)$ in (4.18)-(4.19) and using approximations i)-iii) described above. Introducing the Finite Element residuals:

$$R_v = \mathbf{f} - \rho\partial_t \mathbf{u}_h - \rho\mathbf{u}_h \cdot \nabla\mathbf{u}_h - \nabla p_h + \nabla\cdot(2\mu\varepsilon(\mathbf{u}_h)) \tag{4.22}$$

$$R_p = -\nabla\cdot\mathbf{u}_h \tag{4.23}$$

and using the same analysis as in [91, 92], it turns out that the subscales may be approximated within each element $K \in \mathscr{K}_h$ by:

$$\mathbf{u}' = \tau_v \Pi_v'(R_v), \quad p' = \tau_p \Pi_p'(R_p),$$

where Π_v' and Π_p' are the projections onto V' and P', respectively, and τ_v and τ_p are the so-called stabilization parameters. The choice is made here to consider the identity as the projection when applied to Finite Element residuals (see [32, 91]). It is also possible to take them as the orthogonal projection to the Finite Element space (see [92] and references therein). Referring to the stabilization parameters, we compute them within each element as:

$$\tau_v = \left[\left(\frac{c_1\mu}{\rho h^2}\right)^2 + \left(\frac{c_2\|\mathbf{u}_h\|_K}{h}\right)^2\right]^{-1/2} \tag{4.24}$$

$$\tau_p = \left[\left(\frac{\mu}{\rho}\right)^2 + \left(\frac{c_2\|\mathbf{u}_h\|_K h}{c_1}\right)^2\right]^{1/2} \tag{4.25}$$

where h is the element size, $\|\mathbf{u}\|_K$ a characteristic norm of $\mathbf{u}_h$ (with the same units as $\mathbf{u}_h$) in element K and c_1 and c_2 are algorithmic constants. We take them as $c_1 = 4$ and $c_2 = 2$ for linear elements (see [93]). Very often, the time step size of the temporal discretization is included in the expression of τ_v. This improves the convergence behavior of the algorithm to deal with the nonlinearity of the problem, but has several conceptual drawbacks, as explained in [93, 94]. In order to make τ_v more uniform over the computational domain and, as a consequence, improve the behavior of the scheme, one may take:

$$\tau_v = \left[\frac{1}{\tau_0^2} + \left(\frac{c_1\mu}{\rho h^2}\right)^2 + \left(\frac{c_2\|\mathbf{u}_h\|_K}{h}\right)^2\right]^{-1/2} \tag{4.26}$$

where τ_0 is a reference value of τ_v given by (4.24) computed over the whole mesh (for example the minimum over all the elements). This value in fact should be related to the time step size of the time discretization, Δt.

Inserting the expression for the subscales obtained in (4.20)-(4.21) we finally obtain the following Finite Element formulation:

$$\begin{aligned}
&(\rho\partial_t\mathbf{u}_h, \mathbf{w}_h) + (\rho\mathbf{u}_h\cdot\nabla\mathbf{u}_h, \mathbf{w}_h) - (p_h, \nabla\cdot\mathbf{w}_h) + 2(\mu\varepsilon(\mathbf{u}_h), \varepsilon(\mathbf{w}_h)) \\
&\quad + \sum_K \tau_v(\rho\partial_t\mathbf{u}_h + \rho\mathbf{u}_h\cdot\nabla\mathbf{u}_h + \nabla p_h - \nabla\cdot(2\mu\varepsilon(\mathbf{u}_h)) - \mathbf{f}, \rho\mathbf{u}_h\cdot\nabla\mathbf{w}_h))_K \\
&\quad + \sum_K \tau_p(\nabla\cdot\mathbf{u}_h, \nabla\cdot\mathbf{w}_h) \quad = \quad (\mathbf{f}, \mathbf{w}_h)
\end{aligned} \tag{4.27}$$

$$(\nabla\cdot\mathbf{u}_h, q_h) + \sum_K \tau_v(\rho\partial_t\mathbf{u}_h + \rho\mathbf{u}_h\cdot\nabla\mathbf{u}_h + \nabla p_h - \nabla\cdot(2\mu\varepsilon(\mathbf{u}_h)) - \mathbf{f}, \nabla q_h)_K \quad = \quad 0 \tag{4.28}$$

When compared with the standard Galerkin method, the proposed formulation involves additional integrals that are evaluated element wise. These additional terms represent the effects of the sub-grid scales and enable to overcome the instability in convection dominated regime.

Writing the formulation using the stabilization parameters and the residuals defined in (4.22)-(4.25) leads to the following formulation:

$$\begin{aligned}
&(\rho\partial_t\mathbf{u}_h,\mathbf{w}_h)+(\rho\mathbf{u}_h\cdot\nabla\mathbf{u}_h,\mathbf{w}_h)-(p_h,\nabla\cdot\mathbf{w}_h)+2(\mu\varepsilon(\mathbf{u}_h),\varepsilon(\mathbf{w}_h))\\
&\quad-\sum_K(\tau_v R_v,\rho\mathbf{u}_h\cdot\nabla\mathbf{w}_h)_K\\
&\quad-\sum_K(\tau_p R_p,\nabla\cdot\mathbf{w}_h) \quad = \quad (\mathbf{f},\mathbf{w}_h) \qquad (4.29)\\
&(\nabla\cdot\mathbf{u}_h,q_h)-\sum_K(\tau_v R_v,\nabla q_h)_K \quad = \quad 0 \qquad (4.30)
\end{aligned}$$

4.3.2.2 Temporal discretization

We will address here the temporal discretization, using Backward Differentiation Formula of order σ referred as BDF-σ. The choice of this method lies in its simplicity of implementation. These are one-step methods that only require the storage of the solution at additional time iteration (few % of the total memory requirement). Only 1st and 2nd order are A-stable and therefore will be considered here. Following the work in [95], we consider semi-implicit BDF schemes using Newton-Gregory backwards polynomials for the extrapolation of the nonlinear terms arising from this temporal schemes.

The time derivative of the velocity is approximated by:

$$\partial_t\mathbf{u}_h\approx\frac{1}{\Delta t}\left(\alpha_\sigma\mathbf{u}_h^{n+1}-\mathbf{u}_h^{n,BDF\sigma}\right) \qquad (4.31)$$

where the leading coefficient is defined by:

$$\alpha_\sigma=\begin{cases}1 & \text{for } \sigma=1\\ \dfrac{3}{2} & \text{for } \sigma=2\\ \dfrac{11}{6} & \text{for } \sigma=3\end{cases} \qquad (4.32)$$

Extrapolation using Newton-Gregory backward polynomials are given for the velocity by:

$$\mathbf{u}_h^{n+1,\sigma}=\begin{cases}\mathbf{u}_h^n & \text{if n}\geqslant 0 \quad \text{for } \sigma=1\\ 2\mathbf{u}_h^n-\mathbf{u}_h^{n-1} & \text{if n}\geqslant 1 \quad \text{for } \sigma=2\\ 3\mathbf{u}_h^n-3\mathbf{u}_h^{n-1}+\mathbf{u}_h^{n-2} & \text{if n}\geqslant 2 \quad \text{for } \sigma=3\end{cases} \qquad (4.33)$$

and are given for the pressure by:

$$p_h^{n+1,\sigma}=\begin{cases}p_h^n & \text{if n}\geqslant 0 \quad \text{for } \sigma=1\\ 2p_h^n-p_h^{n-1} & \text{if n}\geqslant 1 \quad \text{for } \sigma=2\\ 3p_h^n-3p_h^{n-1}+p_h^{n-2} & \text{if n}\geqslant 2 \quad \text{for } \sigma=3\end{cases} \qquad (4.34)$$

The linearized semi-implicit formulation reads:

$$\begin{cases} \left(\frac{\rho}{\Delta t}\left(\alpha_\sigma \mathbf{u}_h^{n+1} - \mathbf{u}_h^{n,BDF\sigma}\right), \mathbf{w}_h\right) + \left(\rho \mathbf{u}_h^{n+1,\sigma} \cdot \nabla \mathbf{u}_h^{n+1}, \mathbf{w}_h\right) \\ + \left(2\mu\varepsilon\left(\mathbf{u}_h^{n+1}\right), \varepsilon\left(\mathbf{w}_h\right)\right) - \left(p_h^{n+1}, \nabla \cdot \mathbf{w}_h\right) + \left(\nabla \cdot \mathbf{u}_h^{n+1}, q_h\right) \\ + \left(\tau_v^{n+1,\sigma} \mathbf{R}_v^{n+1,\sigma}\left(\mathbf{u}_h^{n+1}, p_h^{n+1}\right), \rho \mathbf{u}_h^{n+1,\sigma} \cdot \nabla \mathbf{w}_h + \nabla q_h\right) \\ - \left(\tau_p^{n+1,\sigma} \mathbf{R}_p\left(\mathbf{u}_h^{n+1}\right), \nabla \cdot \mathbf{w}_h\right) \\ = \left(\mathbf{f}^{n+1}, \mathbf{w}_h\right) \end{cases} \tag{4.35}$$

where the stabilization parameters are defined as:

$$\tau_v^{n+1,\sigma} = \left[\left(\frac{c_1 \mu}{\rho h^2}\right)^2 + \left(\frac{c_2 \|\mathbf{u}_h^{n+1,\sigma}\|_K}{h}\right)^2\right]^{-1/2} \tag{4.36}$$

$$\tau_p^{n+1,\sigma} = \left[\left(\frac{\mu}{\rho}\right)^2 + \left(\frac{c_2 \left\|\mathbf{u}_h^{n+1,\sigma}\right\|_K h}{c_1}\right)^2\right]^{1/2} \tag{4.37}$$

and the residuals are defined as:

$$\begin{aligned} &\mathbf{R}_v^{n+1,\sigma}\left(\mathbf{u}_h^{n+1}, p_h^{n+1}\right) = \frac{\rho}{\Delta t}\left(\alpha_\sigma \mathbf{u}_h^{n+1} - \mathbf{u}_h^{n,BDF\sigma}\right) + \rho \mathbf{u}_h^{n+1,\sigma} \cdot \nabla \mathbf{u}_h^{n+1} + \nabla p_h^{n+1} - 2\mu\varepsilon\left(\mathbf{u}_h^{n+1}\right) - \mathbf{f}^{n+1} \\ &\mathbf{R}_p\left(\mathbf{u}_h^{n+1}\right) = \nabla \cdot \mathbf{u}_h \end{aligned} \tag{4.38}$$

4.4 Convection-Diffusion-Reaction equation

In this section, the stabilized finite-element method used to solve equations such as the heat equation, turbulence equation (Spalart-Allmaras, k-ε,...), radiative transport equation (RTE) is outlined briefly. Indeed, these equations can be represented by a single scalar transient convection-diffusion-reaction equation which reads:

$$\partial_t \varphi + \mathbf{u} \cdot \nabla \varphi - \nabla \cdot (\kappa \nabla \varphi) + r\varphi = f \tag{4.39}$$

where φ is the scalar variable, κ the diffusion coefficient, r the reaction coefficient and f a source term. According to the problem to solve, the scalar φ can be a temperature, a dissipation energy, a kinetic energy, a chemical concentration, etc.

4.4.1 Stabilized Finite Element for Convection-Diffusion-Reaction equation

Stabilization methods for transient convection-diffusion-reaction equations are discussed in [96, 97, 98]. The stabilized weak form of equation (4.39) reads:

$$\begin{cases} \text{Find } \varphi \in S_h \text{ such that, } \forall w \in W_h : \\ (\partial_t \varphi + \mathbf{u} \cdot \nabla \varphi, w) + (\kappa \nabla \varphi, \nabla w) + (r\varphi, w) \\ \qquad + \underbrace{\sum_K (R(\varphi), \tau_{\text{SUPG}} \mathbf{u} \cdot \nabla w)_K}_{\text{streamline upwind}} + \underbrace{\sum_K (R(\varphi), \tau_{\text{SCPG}} \tilde{\mathbf{u}} \cdot \nabla w)_K}_{\text{discontinuity-capturing}} = (f, w) \end{cases} \tag{4.40}$$

where S_h and W_h are standard test and weight Finite Element spaces and $R(\varphi)$ is the appropriate residual of equation (4.39), $\mathbf{u}$ is the convection velocity and $\tilde{\mathbf{u}}$ is a function of the temperature gradient. In equation (4.40), the first term labeled as *streamline upwind* refers to the SUPG (Streamline Upwind Petrov Galerkin) stabilization [75, 76] controlling the oscillations in the direction of the streamlines, in the convection dominated regime. The second term, labeled as *discontinuity-capturing* refers to the SCPG (Shock Capturing Petrov Galerkin) stabilization, working in the direction of the gradient of the solution [99]. The latter stabilization adds numerical diffusion in the neighborhood of sharp gradient and boundary layers. The stabilization parameters are defined in the same fashion as (4.24). We refer to [75, 99, 97] for the definition of the stabilization parameters.

4.4.2 Stabilization by entropy viscosity

The stabilization method typically used at Cemef for convection is the SUPG (Streamline Upwind/Petrov Galerkin) method [75]. This method improves the result compared to a standard Galerkin resolution. However, this method has some limits to prevent remaining oscillations near extreme gradients of the solution. In industrial processes, these shocks are present since the system is exposed to extreme conditions (metallic part at 1000°c in water at 20°C). Following the work in [100], we analyze in this section a new stabilization method. This method is inspired by the physics in the sense that we use entropy as a selection principle to add an extra-stability wherever it is needed, without polluting the solution. A more stable and physical solution is therefore obtained.

4.4.2.1 Entropy viscosity for conservation laws

Let consider a general conservation law.

$$\frac{\partial u}{\partial t} + \nabla \cdot f(u) = 0 \tag{4.41}$$

It is known that this problem has a weak solution that is physical and satisfies the following inequality:

$$\frac{\partial}{\partial t} E(u) + \nabla \cdot F(u) \leqslant 0 \tag{4.42}$$

This solution is called the entropy solution. The inequality is verified for a pair $E(u)$ and $F(u) = \int E'(u) f'(u) du$ where $E(u)$ is convex. Equation (4.42) is an equality in the regions where the solution is smooth. If the equality is not verified, it means that the solution is not smooth and that entropy is produced. Equation (4.42) will be used to detect the regions when the stabilization is required. To take into account this stabilization, equation (4.41) is augmented with a dissipation term $-\nabla \cdot \nu \nabla u$ where ν is the entropy viscosity. The computation of the entropy viscosity is the key point of this method since it defines the amount of diffusion to stabilize the solution.

We define the discrete residual D_h of the entropy equation:

$$D_h(x,t) = \frac{\partial}{\partial t} E(u_h) + \nabla \cdot F(u_h) \tag{4.43}$$

where the index h denotes the discrete approximation.

The so-called "entropy viscosity" ν_E is defined as:

$$\nu_{E_{|K}} = c_E h_K^2 \frac{\|D_h\|_{\infty,K}}{\|E(u_h) - \bar{E}(u_h)\|_{\infty,\Omega}} \tag{4.44}$$

where c_E is a tunable constant, h_K smallest edge of an element K,$\|\cdot\|_{\infty,\Omega}$ is the infinity norm in all the domain, $\|\cdot\|_{\infty,K}$ is the infinity norm in an element K and $\bar{E}$ is the average entropy over the domain. The entropy viscosity gives an order of magnitude of the ratio of the entropy produced at the local scale and the maximal variation of entropy at the global scale.

To control the weight of the additional terms, we introduce an upper viscosity defined as follows:

$$\nu_{\max_{|_K}} = c_{\max} h_K \|f'(u)\|_{\infty,K} \tag{4.45}$$

Finally, we set the stabilization viscosity to:

$$\nu_h = \min(\nu_{\max}, \nu_E) \tag{4.46}$$

The new variational formulation reads:

$$\left(\frac{\partial u_h}{\partial t} + \nabla \cdot f(u_h), w_h\right) + \sum_K (\nu_h \nabla u_h, \nabla w_h)_K = 0 \quad \forall w_h \in W_h \tag{4.47}$$

Compared to the SUPG method, an additional residual term is added to the variational formulation. More details are given in the following section.

4.4.2.2 Entropy viscosity for the convected level set method

We recall the convected level set equation:

$$\frac{\partial \alpha}{\partial t} + u \cdot \nabla \alpha + \lambda \mathrm{s}(\alpha)\left(\|\nabla \alpha\| - \left(1 - \left(\frac{\alpha}{E}\right)^2\right)\right) = 0 \tag{4.48}$$

where α is the filtered level set function, λ is a coefficient homogeneous to a velocity and E is the thickness of the truncation. We rewrite the equation in the general form:

$$\frac{\partial \alpha}{\partial t} + V \cdot \nabla \alpha = S \tag{4.49}$$

where $V = u + \lambda s(\alpha)\frac{\nabla \alpha}{\|\nabla \alpha\|}$ is the convective velocity and $S = \lambda s(\alpha)\left(1 - \left(\frac{\alpha}{E}\right)^2\right)$ is the source term. The Galerkin variational formulation of this problem is:

$$\left(\frac{\partial \alpha}{\partial t} + V \cdot \nabla \alpha\,, w\right)_\Omega = (S\,, w)_\Omega \tag{4.50}$$

The classical way to prevent the spurious oscillations due to the convection term is SUPG. It consists to express the test functions as follows:

$$\tilde{w}_h = w_h + \tau_{SUPG} V \cdot \nabla w_h \tag{4.51}$$

The classical discrete formulation with SUPG stabilization reads then:

$$\left(\frac{\partial \alpha_h}{\partial t} + V \cdot \nabla \alpha_h\,, w_h\right)_{\Omega_h} + \sum_K \tau_{SUPG}\left(\frac{\partial \alpha_h}{\partial t} + V \cdot \nabla \alpha_h - S\,, V \cdot \nabla w_h\right)_K = (S\,, w_h)_{\Omega_h} \tag{4.52}$$

One of the difficulties associated with the use of the level set methods is the loss of mass in underresolved region of the flow. A promising way to convect the level set is to use entropy viscosity technique [100]. These methods [57] offer a better respect of mass conversation compared to the actual methods.

We propose to add the stabilization by entropy viscosity:

$$\underbrace{\left(\frac{\partial \alpha_h}{\partial t} + V \cdot \nabla \alpha_h \, , w_h\right)_{\Omega_h}}_{\text{Galerkin}} + \underbrace{\sum_K \tau_{SUPG} \left(\frac{\partial \alpha_h}{\partial t} + V \cdot \nabla \alpha_h - S \, , V \cdot \nabla w_h\right)_K}_{\text{SUPG}} + \underbrace{\sum_K \nu_{h_{|_K}} (\nabla \alpha_h \, , \nabla w_h)_K}_{\text{Entropy viscosity}} = (S \, , w_h)_{\Omega_h} \tag{4.53}$$

If we compare SUPG and entropy viscosity, both are adding residual terms. In SUPG, these terms, for a total of 5, are numerically added to the formulation. In the entropy viscosity case, only one numerical term is added.

The choice of the entropy function $E(\alpha) = \frac{1}{2}\alpha^2$ leads to:

$$\nu_{E_{|_K}} = c_E h_K^2 \frac{\|D_h\|_{\infty,K}}{\|E(u_h) - \bar{E}(u_h)\|_{\infty,\Omega}} \tag{4.54}$$

where the entropy residual is:

$$D_h = \frac{\partial}{\partial t}\left(\frac{\alpha_h^2}{2}\right) + V \cdot \nabla \left(\frac{\alpha_h^2}{2}\right) - S\,\alpha_h \tag{4.55}$$

and the upper viscosity is defined by:

$$\nu_{\max_{|_K}} = c_{\max} \, h_K \, \|V\|_{\infty,K} \tag{4.56}$$

4.4.2.3 Entropy viscosity for convection-diffusion-reaction equations

We will highlight briefly the steps needed to introduce the new stabilization. We consider the general convection-diffusion-reaction equation (4.39) that solves a certain scalar φ.

Using the entropy $E(\varphi) = \frac{1}{2}\varphi^2$, the entropy residual is defined as:

$$D = \frac{\partial}{\partial t}\left(\frac{\varphi^2}{2}\right) + \mathbf{u} \cdot \nabla \left(\frac{\varphi^2}{2}\right) - \varphi \nabla \cdot (\kappa \nabla \varphi) + r\varphi^2 - f\varphi \tag{4.57}$$

The convective term $(\mathbf{u} \cdot \nabla \varphi)$ of (4.39) is the term usually treated using the classical SUPG stabilization. The interest of the entropy viscosity is that all the other terms are taken into account.

The first term of the residual equation (4.57) is very important since this term causes high gradient at the beginning of the computation. Indeed, in a furnace for example, a temperature of 1000°C is injected in a cavity at an initial temperature of 20°C. The gradient is extreme and this term destabilizes the solution. However, when the solution converges in time, this term is close to null.

Finally, the effect of the reaction and source terms are also taken into account with the entropy viscosity, adding consistency to this method compared to others stabilization methods.

The entropy viscosity is:

$$\kappa_{E_{|_K}} = h_K \frac{\|D_h\|_{\infty,K}}{\|\mathbf{u}^2\|_{\infty,\Omega}} \tag{4.58}$$

The stabilization viscosity is defined as follows:

$$\kappa_{E_{|K}} = h_K \min\left(c_1^K \|\mathbf{u}^2\|_{\infty,K}\,,\, c_2^K \nu_{E_{|K}}\right) \tag{4.59}$$

The variational formulation now reads:

$$\left(\frac{\partial \varphi}{\partial t} + \mathbf{u}\cdot\nabla\varphi + r\varphi - f\,,\, w\right)_\Omega + \sum_K \left(\kappa_{E_{|K}} + \kappa\right)(\nabla\varphi\,,\,\nabla w)_K = 0 \tag{4.60}$$

4.5 Synergy between Stabilized Finite Element method and mesh adaptation

We combine in this work anisotropic mesh adaptation with flow solver based on the Variational Multiscale method or with stabilized Finite Element for the Convection-Diffusion-Reaction equation. As a result, we may be able to:

- Produce very good accuracy properties for high Reynolds number flows [24]
- Allow the recovery of the global convergence order of the numerical schemes in the convection dominated regimes [101]
- Reduce the computational cost [26]
- Ensure accurate and oscillation free numerical solutions [25]

However, for a better synergy, it requires particular attention on the stabilization coefficients in both the convective and diffusive terms to take into account highly stretched elements with an anisotropic ratio of 1000:1. Therefore, the use of an appropriate definition of the stabilization parameters using the directional element diameter is highly recommended.

Recall that these stability coefficients weight the extra terms added to the weak formulation in the Navier-Stokes and Convection-Diffusion-Reaction equations. They are defined for each element K of the triangulation. Typically, these coefficients depend on the local mesh size h_K. Many numerical experiments show that good results can be obtained when using the minimum edge length of K [102], while others always use a modified triangle diameter (see [103] for details).

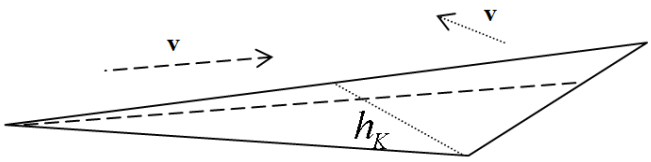

Figure 4.1: Longest triangle length in the streamline direction

Nevertheless, in the case of strongly anisotropic meshes with highly stretched elements, the definition of h_K is still an open problem and plays a critical role in the design of the stabilizing coefficients [104, 81]. In [105] the authors examine deeply the effect of different element length definitions on distorted meshes. In [106] anisotropic error estimates for the residual free bubble

(RFB) method are developed to derive a new choice of the stabilizing parameters suitable for anisotropic partitions. In this work, we adopted the definition proposed in [107] to compute h_K as the diameter of K in the direction of the velocity v (see Figure 4.1):

$$h_K = \frac{2|\mathbf{v}_h|}{\Sigma_{i=1}^{N_K} |\mathbf{v}_h \cdot \nabla \varphi_i|} \tag{4.61}$$

where N_K is the number of vertices of K and $\varphi_1, ..., \varphi_{N_K}$ are the usual basis functions of $P_1(K)$ mapped onto K. Note also that the use of the time step in the definition of the stabilizing parameter (4.26) is another important issue, in particular for small time steps. Several approaches can be found in the literature, in particular the use of dynamic subscales in [84] and the definition of the stabilization parameters computed from element matrices and vectors in [107]. These approaches have been used successfully and in both cases, the steady solution is independent of the time step and are stable for small time steps.

4.6 Validation

Although several test cases will be proposed in the following chapters, we limit here to three representative test cases as first validations. First we consider the open cavity problem to assess the ability of The Navier-Stokes to deal with critical Reynolds number flow. Both 1s and 2nd order of the BDF time discretization will be tested. Then, we will consider the coupling of flow solver with a Spalart -Allmaras model cast into a convection-diffusion-reaction equation. Finally we will consider a 2D-forced convection taking into account the Navier-Stokes equation and the heat equation.

4.6.1 Open cavity

We consider a 2D open square cavity of side h as depicted in Fig. 4.2, upon which lies a channel of height $0.5h$ [108]. For the square, $0 \leqslant x \leqslant h$ and $-h \leqslant y \leqslant 0$. A uniform velocity field is prescribed at the left side of the channel. A free-slip condition with zero tangential stress is prescribed on the lower boundary of the channel, for $(-1.2h \leqslant x \leqslant -0.4h)$ and $(1.75h \leqslant x \leqslant 2.5h)$. No-slip boundary conditions are imposed on $(-0.4h \leqslant x \leqslant 0)$ and $(h \leqslant x \leqslant 1.75h)$

In the following computations, we choose $h = 1$. As it is shown in Fig. 4.3, the prescribed velocity field and boundary conditions lead to the formation of a recirculating eddy in the square cavity. The Reynolds number is set to $Re = 4500$.

The case being unsteady, we are interested in this test case in the comparison of the velocity field u at (0.75;0.05). The velocity u is expected to exhibit oscillations whose frequency and magnitude will serve to compare different flow solver implementations. Results obtained using a DNS (Direct Numerical Simulation) approach are set as the reference. We will perform the same simulation using our Variational Multiscale flow solver and using a time discretization BDF1 and BDF2 schemes.

Fig. 4.3 shows that the flow seems to be steady at the point of interest while the flow is unsteady in Fig. 4.4. Comparison of the evolution in time of the velocity is given in Fig. 4.5. Both DNS and VMS-BDF2 are unsteady while the VMS-BDF1 has reached a steady state. This is due to the important numerical of the first order time discretization. To fix this issue, a higher time discretization is needed. In Fig. 4.6, we show the results at $Re = 5000$. Results confirm the benefit of a higher time discretization. Indeed, even though the velocity field is unsteady for VMS-BDF1, the magnitude of the velocity is damped compared to DNS and VMS-BDF2.

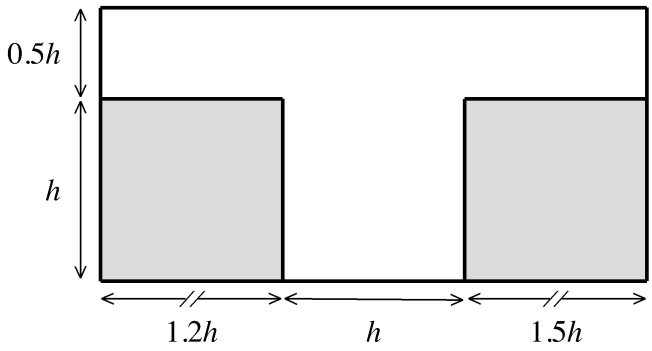

Figure 4.2: Driven flow cavity setup.

A great improvement is therefore obtained using VMS-BDF2. Recall that the computational cost is similar to VMS-BDF1. Only few percent of additional memory are required.

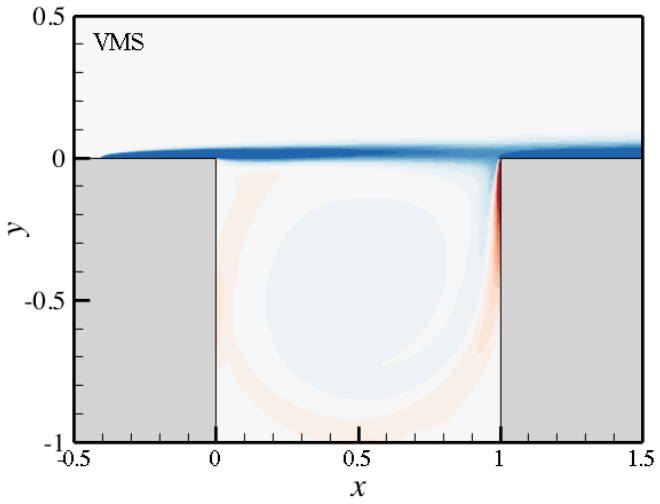

Figure 4.3: Cavity flow at Re=4500. Velocity magnitude obtained using VMS with a BDF-1 time discretization scheme.

4.6.2 Turbulent flow past a 2D prismatic cylinder

We consider the fully turbulent flow past a prismatic cylinder [109]. The prismatic cylinder is used because of the sharp and localized flow features that represent a challenge for the stabilization method. Here, the VMS flow solver will be used combined with the Spalart-Allmaras turbulence model. An extensive use of the mesh adaptation method will be done here to solve more accurately the flow and capture the maximum features. To this end, we will consider the test cases proposed in [110]. The prismatic cylinders is parametrized by two lengths $H1$ and $H2$. According to the value of the ratio H_2/H_1, the cylinder can be a square ($H_2/H_1 = 1$), a triangle ($H_2/H_1 = 0$) or a cone ($H_2/H_1 \notin \{0;1\}$). The configuration of the computational domain is given in Fig.4.7. The cylinder is centered in width, and its front side is located $8H_1$ downstream of the inlet boundary on the left of the domain. We will consider here the ratio $H_2/H_1 = 0.6$. The values of the uniform inlet velocity V_{in} and the dynamic viscosity μ are chosen to yield a Reynolds number based on H_1 equal to $Re = 2.2 \times 10^4$.

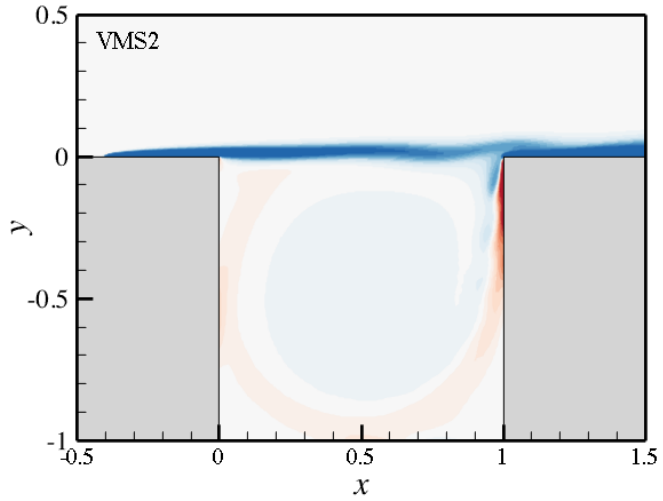

Figure 4.4: Cavity flow at Re=4500. Velocity magnitude obtained using VMS with a BDF-2 time discretization scheme.

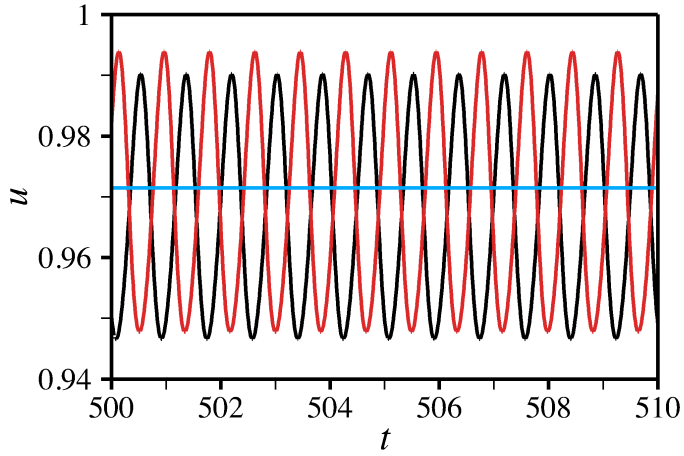

Figure 4.5: Cavity flow at Re=4500. Evolution of the velocity. Black line refers to DNS, blue line refers to VMS-BDF1 and red line refers to VMS-BDF2.

Results in Fig. 4.8, using a fixed mesh, indicate that the flow exhibits Von Karman vortex street. The turbulence model is only active in the restricted area of interest, and the effects of the averaging process and damping function seem to be correctly taken into account since streamlines shown in Figure 4.8 are in agreement with those given in [110] in the cylinder wake.

The results of drag and lift coefficients given in Table 4.1 are in good agreement with the literature presented in [110] and the references therein. Recall that we use for the convection-diffusion-reaction solver a first order time discretization. As it was shown in the previous test case, stabilization technique would benefit from a higher order time discretization [111]. In addition to the use of a first-order implicit time integration scheme, the time splitting error may contribute to this inaccuracy.

We now consider the use of anisotropic mesh adaptation to solve this test case presented in Chapter 3. The mesh adaptation procedure starts from an arbitrary uniform mesh and is iterated every 5 time steps. It considers a multi-criteria adaptivity taking into account the velocity

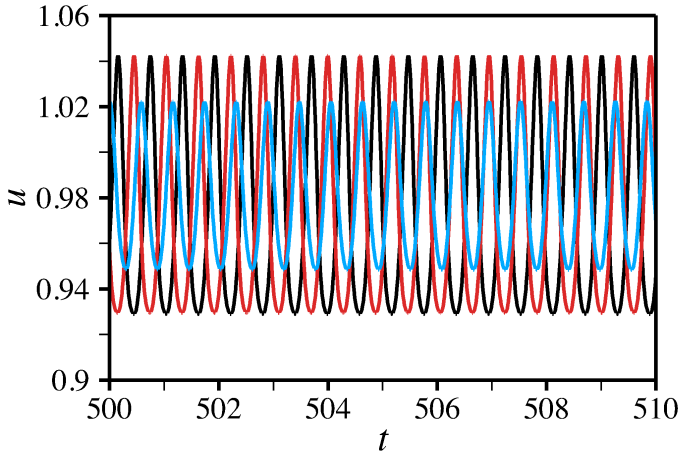

Figure 4.6: Cavity flow at Re=5000. Evolution of the velocity. Black line refers to DNS, blue line refers to VMS-BDF1 and red line refers to VMS-BDF2.

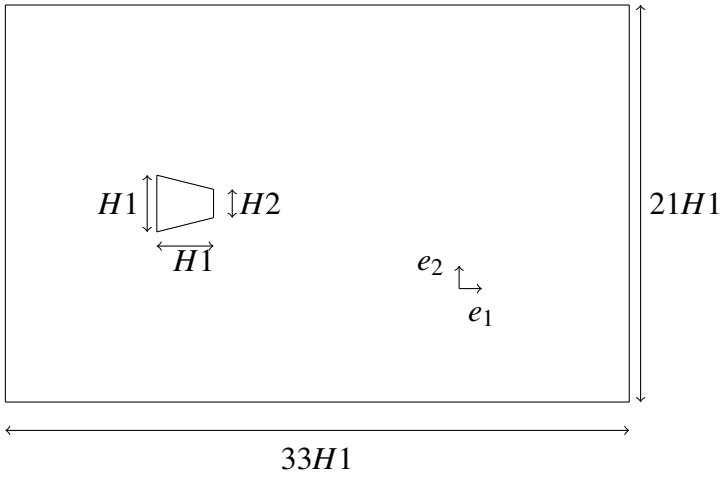

Figure 4.7: Geometry for cylinder case.

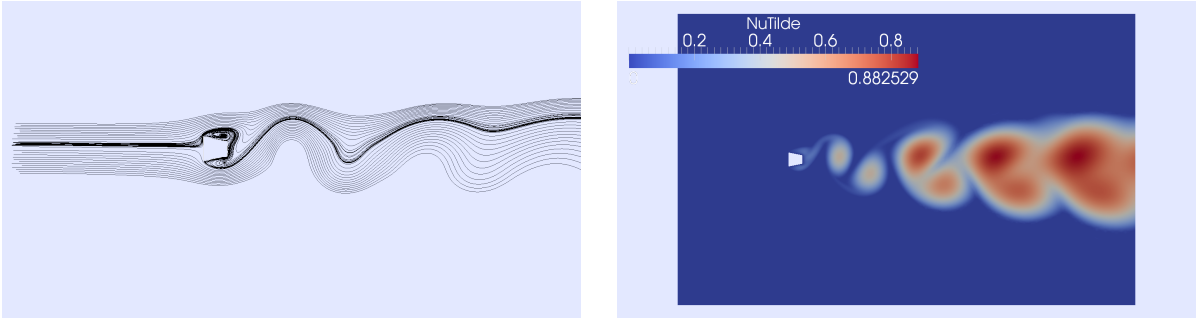

Figure 4.8: Plots of streamlines (*left*) and the turbulent viscosity $\tilde{\nu}$ (*right*) for $H_2/H_1 = 0.6$.

components, the velocity magnitude and the turbulent viscosity. The number of nodes N is set to 10^5. Results using mesh adaptation are given in Fig. 4.9. The evolution of the mesh, under the constraint of a fixed number of elements, is shown in Fig. 4.10. This figure shows that the mesh is refined around the evolving vortices and is automatically coarsened in the regions of less interest far from the cylinder. As it is depicted in Fig. 4.11, we have a concentration of elements not only along the boundary layers but also in the wake region. The zoom-in

Table 4.1: Comparisons of drag and lift coefficients with the literature for $H_2/H_1 = 0.6$.

	mean C_D	r.m.s. C_L
Bao et al. [110]	2.50 ± 0.125	1.7 ± 0.1
Present work	2.57	1.79

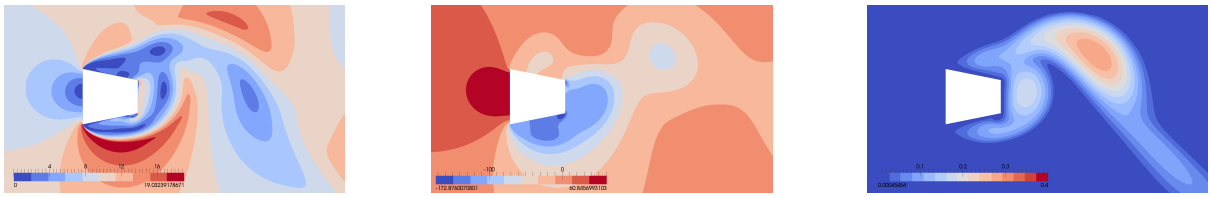

Figure 4.9: Plots of velocity (*left*), pressure (*middle*) and turbulent viscosity (*right*) at $t = 11.64$.

in Fig. 4.12 highlights how sharply the layers are captured. The shape but also the size and the orientation of the elements match the directional features of the flow (boundary layers, flow detachments). The zoom-out in Fig. 4.12 shows how the anisotropic adaptive procedure modifies the mesh in a way that the local mesh resolutions become adequate in all directions.

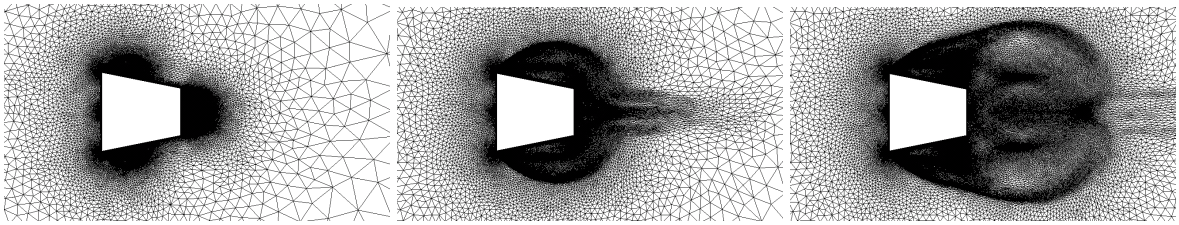

Figure 4.10: Evolution of the adapted meshes.

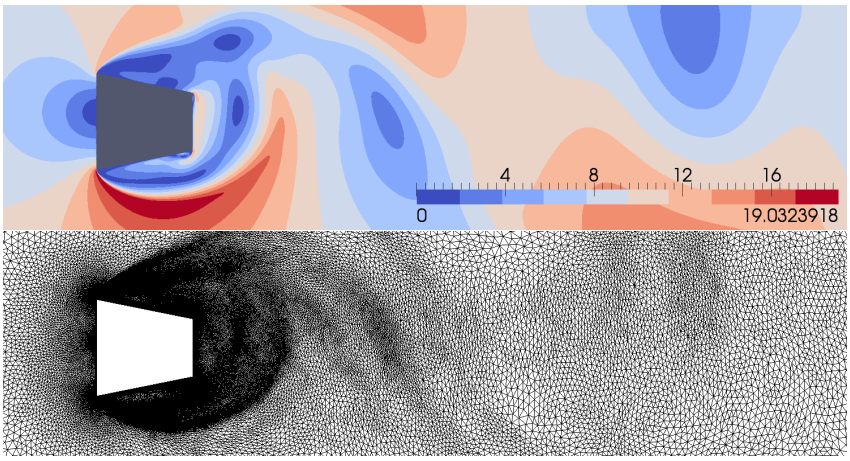

Figure 4.11: Velocity field and corresponding adapted mesh.

Beyond the evolution of the mesh, the evolution of drag and lift coefficients for different aspect ratios H_2/H_1 is given in Fig. 4.13 for both adapted and fixed mesh. Both reach as expected a steady oscillating state, and compare well to the plots shown in [110]. This confirms that the developed stabilized Finite Element methods is shown to be very efficient and robust for solving flows at high Reynolds number using highly stretched elements.

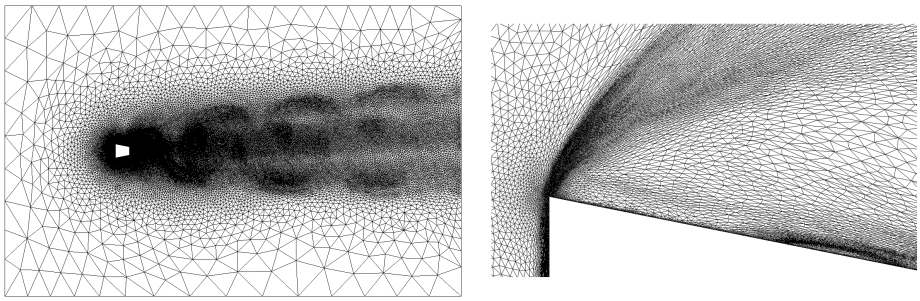

Figure 4.12: Zoom-out with vortex shedding (*left*) and zoom-in the adapted mesh (*right*).

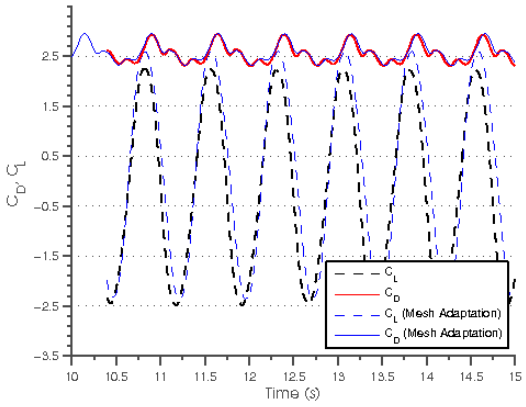

Figure 4.13: Drag (lines) and lift (dots) coefficients for aspect ratios $H_2/H_1 = 0.6$.

4.6.2.1 2D forced convection

To highlight the effect of the entropy viscosity stabilization, we placed ourselves in numerical severe conditions. Therefore, we consider a small cavity of 1m side filled with air at an initial temperature of 20°C (Fig. 4.14). Hot air at 1000°C is injected with an inlet velocity of 1m/s. This cavity can be seen as a small furnace. An outlet enables the air to go out of the cavity. The physical parameters are summarized in Table 4.2. The high gradients of temperature at the beginning of the computation leads to spurious oscillations. The computation is done from t=0s to t=100s with a time step Δt=0.1s. The mesh is isotropic and contains only 10,000 elements.

Table 4.2: Physical parameters for the 2D force convection

ρ [kg/m^3]	μ [Pa·s]	gravity [m/s^2]	v_{inlet} [m/s]	T_{inlet} [°C]
1	10^{-5}	0	1	1000

Fig. 4.15 shows the solution at two different times at the beginning of the computation. The effect of the stabilization with entropy viscosity is clear. The solution is expected to be very unstable due to the high gradients of temperature and velocity at the beginning of the computation. The oscillations are reduced with the entropy viscosity. The temperature front is the same for both methods. This indicates that the diffusion added by the entropy viscosity method does not pollute the solution and does not lead to a nonphysical solution, which is a drawback of several stabilization methods.

Fig. 4.16 shows the evolution of the maximum temperature and the minimum temperature

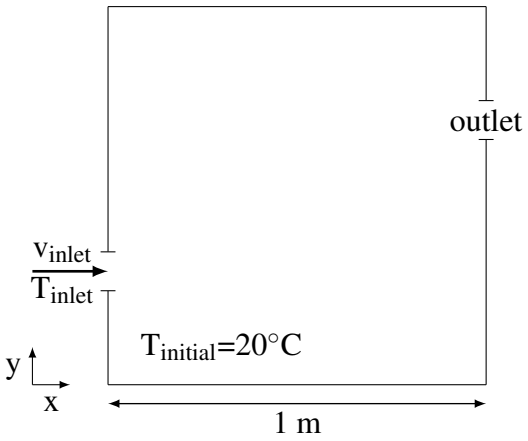

Figure 4.14: Set-up for the 2D forced convection

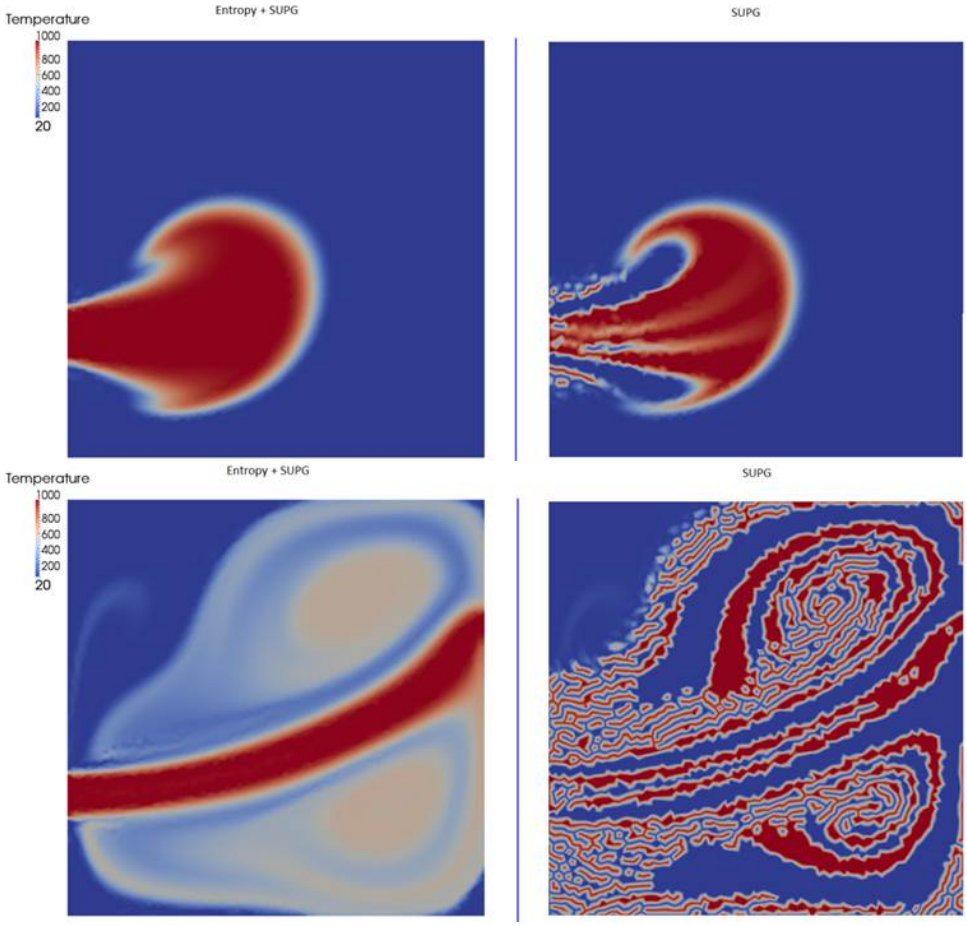

Figure 4.15: Temperature at two different times. Stabilization with entropy viscosity and SUPG (left). Stabilization with SUPG only (right). The temperature scale is fixed to highlight the areas where the solution is nonphysical.

in the cavity. This enables to see the effect of the stabilization on the spurious oscillations. From a physical point of view, since the initial temperature is 20°C and the injected air is at 1000°C, the maximum and minimum temperature should be in the range [20°C - 1000°C]. A value outside this range indicates a nonphysical solution. This test cannot be performed using the standard Galerkin resolution. A stabilization is thus required.

Fig. 4.16a shows the result for the SUPG stabilization typically used for convection. This method exhibits here, for this example, large oscillations and these oscillations remain during a long time in the computation. Performing this test was made possible through the use of mesh adaptation as it can be seen in Fig. 4.16c. The mesh is adapted according to the velocity, the norm of the velocity and the temperature, every 5 time steps.

Fig. 4.16b shows the results obtained with SUPG and entropy viscosity, without mesh adaptation. This figure indicates a drastic reduction of the oscillations and therefore of the nonphysical points in the domain. Coupled with mesh adaptation, the solution obtained in Fig. 4.16d exhibits marginal oscillations.

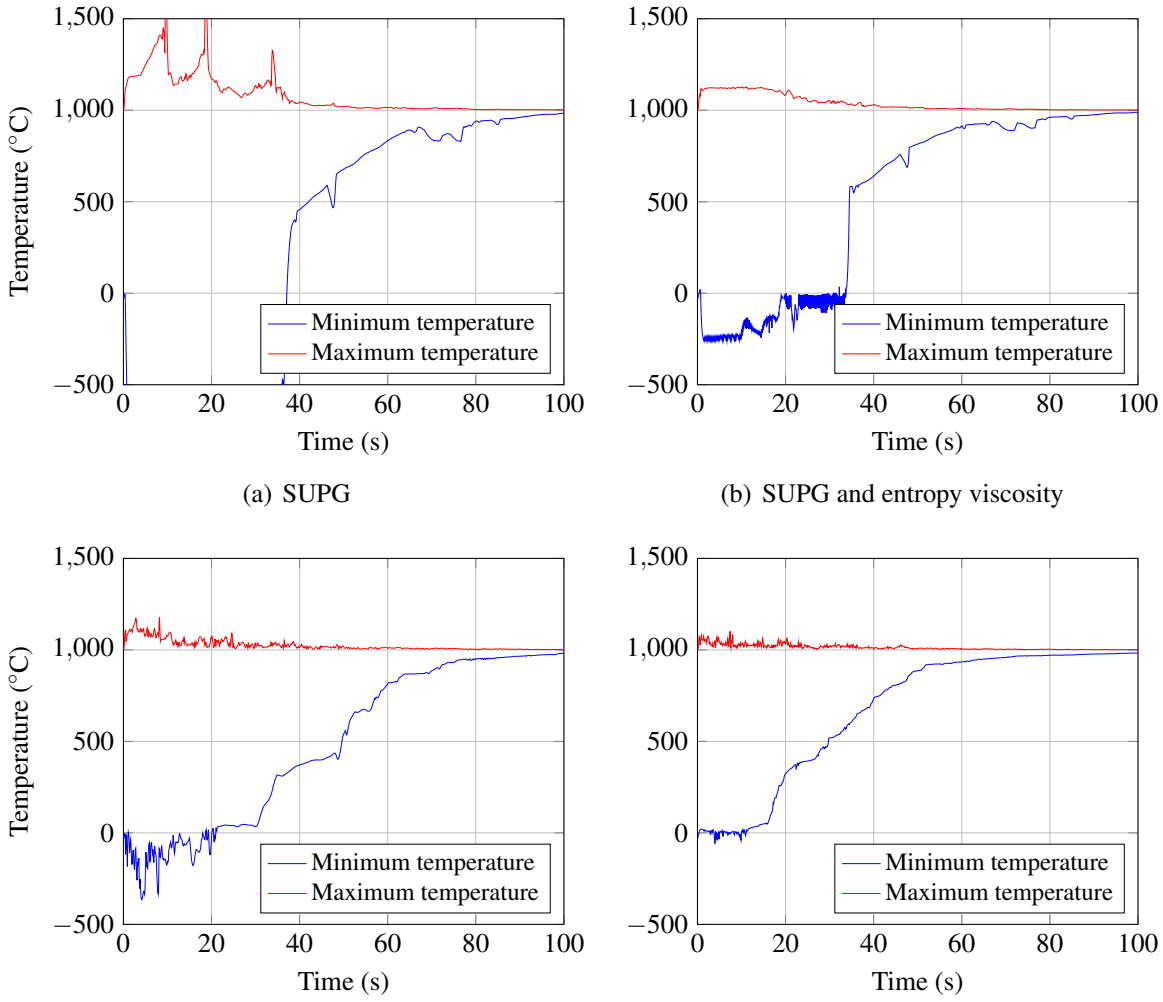

(a) SUPG

(b) SUPG and entropy viscosity

(c) SUPG and mesh adaptation

(d) SUPG, Entropy and mesh adaptation

Figure 4.16: Evolution of the maximum temperature and minimum temperature in the cavity for four different resolution methods: (a) SUPG stabilization, (b) SUPG and entropy viscosity, (c) SUPG and mesh adaptation, (d) SUPG, entropy viscosity and mesh adaptation.

4.7 Conclusion

In this chapter, we presented the Stabilized Finite Element methods for the resolution of the unsteady Navier-Stokes equations and the convection-diffusion-reaction equation. We introduced

and discussed several stabilization methods and derived the corresponding variational formulation to improve the accuracy and the stability of the Galerkin formulation. These methods were validated using various test cases, therefore showing the benefits of the stabilization methods and the validity of the implementation of the proposed methods.

Résumé en français

Dans ce chapitre, les méthodes Eléments Finis utilisées pour la dynamique des fluides numérique sont présentées. Les équations de Navier-Stokes sont résolues par l'intermédiaire d'une méthode variationelle multi-échelles (Variational MultiScale - VMS). En effet, la formulation faible de Galerkin souffre d'instabilités dans les écoulements à convection dominante. De plus, la méthode VMS permet de contourner la condition inf-sup et permet ainsi l'utilisation d'éléments finis P1-P1 pour la vitesse et la pression dans la résolution mixte des équations de Navier-Stokes. Les méthodes d'éléments finis stabilisés utilisant la méthode Streamline Upwind Petrov Galerkin (SUPG) et SCPG (Shock Capturing Petrov Galerkin) pour la résolution de l'équation de convection-diffusion-réaction sont présentées. Une méthode additionnelle dite a viscosité entropique est présentée. Cette méthode repose sur la production d'entropie comme principe de sélection des zones à stabiliser. Une extra-diffusion est ajoutée dans ces zones, permettant de traiter les fortes discontinuités des solutions. Une solution plus stable et plus physique est ainsi obtenue. La modification de ces méthodes de stabilisation pour prendre en compte les particularités des maillages anisotropes utilisés pour la résolution des équations est décrite. Des applications numériques exigeantes sont traitées à l'aide de ces méthodes. La validité des méthodes choisies ainsi que leur précision sont discutées.

Chapter 5

Towards boiling multiphase flows: surface tension

Contents

5.1 Introduction

Many essential features in hydrodynamics are accessible only through extremely detailed analysis that capture different spatial and temporal scales set by the physics and the geometry of the problem. This includes a multitude of applications with great scientific interest such as microfluidic cell separation in biology [112], droplet coalescence in chemistry [113], microfabricated platforms for cancer diagnosis [114], emulsion in food industry [115], and more. For various reasons, these multi-fluid applications are very hard or impossible to investigate experimentally, and thus only reliable computational simulation can open up for detailed study and new insights [116, 117].

In spite of the maturity and popularity of numerical formulations, they are still characterized by a high computational cost and may lack of reliability and generality. In particular, major open challenges of computational multiphase flows include: (i) the discretization mesh for moving interfaces with fast dynamics cannot be easily built in a preprocessing, (ii) the high discontinuity in material properties that represent the interface must be found as a part of the solution, (iii) mass conservation, efficiency and robustness of the computations are difficult to achieve without dynamic adaptive methods and quantitative error estimation and finally, (iv) the capillary time step restriction condition is difficult to respect when treating explicitly the surface tension term in the Navier-Stokes equations [118].

Indeed, the surface tension, as a result of the discontinuity of attractive forces at the interface between two phases, plays an essential role in the mechanical behaviour of this interface. Difficult to solve directly at the molecular scale, different approaches were proposed in the literature to express it as a surface stress condition [119, 120]. A famous approach, known as the Continuum Surface Force (CSF) method, is proposed by Brackbill [121]. It enables to avoid the computation of surface integral by mean of a regularized Dirac function. This can be obtained easily when using either a level set method or a volume of fluid approach.

However, the implementation of the surface tension is generally treated explicitly and inserted as a source term in the Navier-Stokes equations [122, 123]. This implementation may suffer from limitations due to the need to capture the capillary wave. Indeed, one should use a restrictive time step of order of $(\Delta x)^{3/2}$ where Δx is the element size [121]. Hysing in [124] proposed a semi-implicit implementation of the surface tension derived from the CSF method. Using a Laplace-Beltrami operator, the variational formulation of the surface tension is rewritten in its semi-implicit form. In [125, 126], the Laplace-Beltrami operator is written as a function of a standard Laplacian to remove the stiffness caused by the surface diffusion.

Therefore, to address points (i)-(iv), we propose in this work to derive a new adaptive Variational MultiScale (VMS) method [32, 127], designed to circumvent the time step restriction condition due to the use of the surface tension and to handle the abrupt changes at the interface. Indeed, it consists on the decomposition for both the velocity and the pressure fields into coarse/resolved scales and fine/unresolved scales [20], needed to deal with convection dominated problems and pressure instabilities. Note that this choice of decomposition is extended here to account for the surface tension additional terms which in return are shown to be favourable to remove spurious oscillations at the interface and for simulating flows with large density and viscosity ratios. A convected level set method [57, 58] is used to provide a precise position of the interfaces and to enable homogeneous physical properties for each subdomain.

Finally, we combine this new VMS formulation with an a posteriori error estimator for dynamic anisotropic mesh adaptation [24, 26]. It involves building a mesh based on a metric map. It provides both the size and the stretching of elements in a very condensed information data. Consequently, due to the presence of high gradients, it provides highly stretched elements at the interfaces, at the inner and the boundary layers, and thus yields an accurate modelling framework for two-fluid incompressible isothermal flows. We assess the behaviour and accuracy of the proposed formulation in the simulation of several two- and three-dimensional time-dependent challenging numerical examples [122, 128].

5.2 Implicit surface tension

As described previously, a common way to introduce the surface tension as a volume source term in the Navier-Stokes equations is by rewriting the surface force as follows:

$$f_{\mathrm{ST}} \quad = \quad -\gamma\kappa\delta(\Gamma)\mathrm{n} \tag{5.1}$$

where γ is the surface tension coefficient, $\delta(\Gamma)$ is a Dirac function locating the interface Γ, κ is the mean curvature and n is the normal to the interface Γ.

Moreover, the use of a level set function enables the direct computation of the normal as $\mathrm{n} = \nabla\alpha/|\nabla\alpha|$ and the mean curvature as $\kappa = -\nabla\cdot\mathrm{n}$. As a result, the surface tension is expressed as a function of the level set as follows:

$$-\gamma\kappa\delta(\Gamma)\mathrm{n} = \gamma\delta^{\varepsilon}(\alpha)\left[\nabla\cdot\left(\frac{\nabla\alpha}{|\nabla\alpha|}\right)\right]\nabla\alpha \tag{5.2}$$

where $\delta^{\varepsilon}(\alpha)$ is a smoothed Dirac function [118].

As discussed in [124], this implementation imposes a restriction on the time step that must respect the propagation of the capillary wave:

$$\frac{c_\phi \Delta t}{\Delta x} < \frac{1}{2} \tag{5.3}$$

where $c_\phi = \sqrt{\gamma k/(2\bar{\rho})}$ is the capillary wave phase velocity and $\bar{\rho}$ is the average density at the interface. Using the maximum wave-number $k = \pi/\Delta x$, the time step is restricted to:

$$\Delta t < (\Delta x)^{\frac{3}{2}} \sqrt{\frac{\bar{\rho}}{2\pi\gamma}} \tag{5.4}$$

As an example, if we consider an air bubble inside a water channel with a mesh size of $\Delta x = 1mm$ and a surface tension coefficient $\gamma = 0.07$N/m, the maximum time step allowed for the simulation is then $\Delta t_{\max} = 0.001\,s$ and thus penalizing the computational cost of the simulations.

On the other hand, it is stated in [129] that the surface Laplacian of an identity mapping function can be expressed according to the curvature and the normal to this interface as follows:

$$\Delta_s I_\Gamma = \nabla_s \cdot \nabla_s I_\Gamma = -\kappa \mathrm{n} \tag{5.5}$$

Following the work in [124], we express the evolution of the position of the interface in time:

$$\mathrm{I}_\Gamma^{n+1} = \mathrm{I}_\Gamma^n + \mathrm{u}^{n+1}\Delta t \tag{5.6}$$

where the index $n+1$ is the current time and n the previous one. Applying the surface Laplacian operator Δ_S on (5.6) leads to:

$$\Delta_s I_\Gamma^{n+1} = \Delta_s I_\Gamma^n + \Delta t \Delta_s \mathrm{u}^{n+1} \tag{5.7}$$

$$-(\kappa \mathrm{n})^{n+1} = -(\kappa \mathrm{n})^n + \Delta t(\Delta_s \mathrm{u}^{n+1}) \tag{5.8}$$

For sake of simplicity, we drop in the following the exponent n and only use $n+1$ for the unknowns. Multiplying (5.8) by the surface tension coefficient, we obtain:

$$-\gamma(\kappa \mathrm{n})^{n+1} = -\gamma\kappa \mathrm{n} + \gamma\Delta t(\Delta_s \mathrm{u}^{n+1}) \tag{5.9}$$

In [125, 126], we find that the surface Laplacian Δ_S can be decomposed into a standard Laplacian as follows:

$$\Delta_s u = \nabla_s^2 u = \nabla^2 u - \frac{\partial^2 u}{\partial \mathrm{n}^2} - \kappa \frac{\partial u}{\partial \mathrm{n}} \tag{5.10}$$

where $\dfrac{\partial u}{\partial \mathrm{n}} = \nabla u \cdot \mathrm{n}$.

Therefore, the new expression for the surface tension force will finally reads:

$$f_{\mathrm{ST}} = -\gamma\kappa\delta(\alpha)\mathrm{n} - \gamma\delta(\alpha)\Delta t \left(\frac{\partial^2 \mathrm{u}}{\partial \mathrm{n}^2} + \kappa \frac{\partial \mathrm{u}}{\partial \mathrm{n}} - \nabla^2 \mathrm{u}^{n+1} \right) \tag{5.11}$$

The usual term $-\gamma\kappa\delta(\alpha)\mathrm{n}$ is now completed by additional terms proportional to the time step. These additional terms act as an isotropic diffusion minus a diffusion in the normal direction of the interface [125]. Note also that when the time step tends toward zero, the surface tension is defined only by the usual term $-\gamma\kappa\delta(\alpha)\mathrm{n}$ and therefore we retrieve the explicit treatment.

5.3 Variational Multiscale method with surface tension

Flow motion of an incompressible fluid is described by the Navier-Stokes equations given by

$$\rho(\partial_t u + u\cdot\nabla u) - \nabla\cdot(2\mu\varepsilon(u)) + \nabla p = f + f_{ST} \tag{5.12}$$

$$\nabla\cdot u = 0 \tag{5.13}$$

where u, p, ρ, μ and f are the velocity, the pressure, the density, the viscosity and the source term respectively. It is well known that the stability of the discrete formulation of Navier-Stokes depends on appropriate compatibility restrictions on the choice of the Finite Element spaces for the velocity and the pressure. According to this, standard Galerkin mixed elements with continuous equal order linear/linear interpolation is not a stable discretization. This lack of stability manifests in uncontrollable oscillations that pollute the solution.

Many measures may be distinguished to solve and get around these difficulties. In particular, the classical stabilized Finite Element methods may be applied to deal with the instabilities in convection-dominated regime and the velocity-pressure compatibility condition. However, the direct use of such methods may be inadequate when additional terms are inserted in the Navier-Stokes equations or when different physics is applied. Indeed, one needs to seek for a general framework that deal with different and new variant of mixed variational formulations. The Variational Multiscale method, proposed by Hughes [32, 127] offers such an ideal framework. Therefore, terms related to such as Darcy [130], extra stress constraint [21], hydrodynamics [131], turbulence [35], viscoelastic flow [36] among others are treated accordingly and taken into account by the stabilization process.

We briefly described the main steps to derive this formulation. First, it considers that the velocity and the pressure unknowns can be split into two components corresponding to different scales or levels of resolution: resolvable coarse-scale and unresolved fine-scale $u = u_h + \tilde{u}$ and $p = p_h + \tilde{p}$. Likewise, we apply the same decomposition for the weighting functions $v = v_h + \tilde{v}$ and $q = q_h + \tilde{q}$. The unresolved fine-scales are then modeled using residual based terms that are derived consistently. The static condensation consists of substituting the fine-scale solution into the large-scale problem providing additional terms, tuned by a local stabilizing parameter. The latter enhances the stability and accuracy of the standard Galerkin formulation. The enrichment of the functional spaces is performed as follows: $V = V_h \oplus \tilde{V}$, $V_0 = V_{h,0} \oplus \tilde{V}_0$ and $Q = Q_h \oplus \tilde{Q}$. Thus, the mixed-Finite Element approximation of the time-dependent incompressible problem with surface tension can read:

Coarse scale

$$\begin{cases} \left(\rho\dfrac{\partial(u_h+\tilde{u})}{\partial t}, v_h\right) + (\rho(u_h+\tilde{u})\cdot\nabla(u_h+\tilde{u}), v_h) - (p_h+\tilde{p}, \nabla\cdot v_h) \\ +(2\mu\varepsilon(u_h) : \varepsilon(v_h)) = (f + f_{\mathrm{ST}}, v_h) \quad \forall v_h \in V_{h,0} \\ \\ (\nabla\cdot(u_h+\tilde{u}), q_h) = 0 \quad \forall q_h \in Q_h \end{cases} \tag{5.14}$$

Fine scale

$$\begin{cases} \left(\rho\dfrac{\partial(u_h+\tilde{u})}{\partial t}, \tilde{v}\right) + (\rho(u_h+\tilde{u})\cdot\nabla(u_h+\tilde{u}), \tilde{v}) - (p_h+\tilde{p}, \nabla\cdot\tilde{v}) \\ +(2\mu\varepsilon(\tilde{u}) : \varepsilon(\tilde{v})) = (f + f_{\mathrm{ST}}, \tilde{v}) \quad \forall \tilde{v} \in \tilde{V} \\ \\ (\nabla\cdot(u_h+\tilde{u}), \tilde{q}) = 0 \quad \forall \tilde{q} \in \tilde{Q} \end{cases} \tag{5.15}$$

At this level, two assumptions can be made to simplify the resolution of the fine scale equation as proposed in [24]: the subscales are considered quasi-static and the convection is approximated by $(u_h+\tilde{u}).\nabla(u_h+\tilde{u}) \approx u_h.\nabla(u_h+\tilde{u})$. Therefore, by formulating the expression of $\tilde{u}$ and $\tilde{p}$ as in [24], by substituting them into the large-scales equation, and applying integration by parts, the system to solve becomes:

$$\begin{cases} \rho(\partial_t u_h, v_h)_\Omega + \rho(u_h^i.\nabla u_h, v_h)_\Omega - \sum_{K\in\mathscr{T}_h}(\tau_K\mathscr{R}_M, \rho u_h\nabla v_h)_K + (2\mu\varepsilon(u_h):\varepsilon(v_h))_\Omega \\ \qquad -(p_h, \nabla\cdot v_h)_\Omega + \sum_{K\in\mathscr{T}_h}(\tau_C\mathscr{R}_C, \nabla\cdot v_h)_K = (f, v_h)_\Omega + (f_{\mathrm{ST}}, v_h)_\Omega \\ \\ (\nabla u_h, q_h)_\Omega - \sum_{K\in\mathscr{T}_h}(\tau_K\mathscr{R}_M, \nabla q_h)_K = 0 \end{cases} \tag{5.16}$$

with $\mathscr{R}_M$ and $\mathscr{R}_C$ the residuals defined by

$$\begin{aligned} \mathscr{R}_M &= f + f_{\mathrm{ST}} - \rho\partial_t u_h - \rho u_h^i\cdot\nabla u_h - \nabla p_h \\ \mathscr{R}_C &= -\nabla\cdot u_h \end{aligned} \tag{5.17}$$

where u_h^i is the velocity at Newton iteration i. Finally, replacing the expression of f_{ST} in (5.16) and (5.17) we obtain:

$$\begin{cases} \rho(\partial_t u_h, v_h)_\Omega + \rho(u_h^i.\nabla u_h, v_h)_\Omega - \sum_{K\in\mathscr{T}_h}(\tau_K\mathscr{R}_M, \rho u_h\nabla v_h)_K + (2\mu\varepsilon(u_h):\varepsilon(v_h))_\Omega \\ \qquad -(p_h, \nabla\cdot v_h)_\Omega + \gamma\delta(\alpha)\Delta t\,(\nabla u_h:\nabla v_h)_\Omega + \sum_{K\in\mathscr{T}_h}(\tau_C\mathscr{R}_C, \nabla\cdot v_h)_K = \\ \qquad \left(f - \gamma\delta(\alpha)\kappa\mathrm{n} - \gamma\delta(\alpha)\Delta t\left(\partial_{nn}u_h^i + \kappa\partial_n u_h^i\right), v_h\right)_\Omega \\ \\ (\nabla u_h, q_h)_\Omega - \sum_{K\in\mathscr{T}_h}(\tau_K\mathscr{R}_M, \nabla q_h)_K = 0 \end{cases} \tag{5.18}$$

where τ_K and τ_C are the known stabilization parameters (see [81] for details). Note that in the case of strongly anisotropic meshes with highly stretched elements, the definition of the stabilization parameters is still an open problem and plays a critical role in the design of the stabilizing coefficients. In [24] the authors propose a particular choice of the stabilizing parameters suitable for anisotropic partitions that we adopt it again here.

$\mathscr{R}_M$ and $\mathscr{R}_C$ are now defined by:

$$\begin{aligned} \mathscr{R}_M &= f - \gamma\delta(\alpha)\kappa\mathrm{n} - \gamma\delta(\alpha)\Delta t\left(\partial_{nn}u_h^i + \kappa\partial_n u_h^i - \nabla^2 u_h\right) - \rho\partial_t u_h - \rho u_h^i\cdot\nabla u_h - \nabla p_h \\ \mathscr{R}_C &= -\nabla\cdot u_h \end{aligned} \tag{5.19}$$

By comparing the standard Galerkin method with the proposed stable formulation, additional integrals that are evaluated element-wise are involved. These additional terms, obtained by replacing the approximated $\tilde{u}$ and $\tilde{p}$ into the large-scale equation, represent the effects of the sub-grid scales and above all take into account the modified surface tension terms. They are introduced in a consistent way to the Galerkin formulation and enable to overcome the instability of the standard formulation arising in convection dominated flows and to deal with the pressure instabilities [20].

5.4 Numerical test cases

In order to validate the proposed methods, two- and three-dimensional time-dependent numerical test cases are presented in this section. The results obtained with the proposed approach are

compared with either analytic solutions or with those obtained by other approaches that can be found in the literature. Some test cases cannot be handled using classical model in particular for high property ratios and in $3D$ attest of the benefit of adaptive VMS formulation.

5.4.1 Oscillating square bubble

In this test case, we assess the new implementation of the surface tension source term in the Navier-Stokes equations. Therefore, we analyze an ethanol square bubble placed in a cavity filled with air. This test case is proposed in [132]. The initial configuration is provided in Figure 5.1. No gravity is applied and the surface tension is constant. The physical parameters are summarized in Table 5.1. The ethanol bubble interface, initially set as a square is expected to become a circle since the surface tension tends to minimize the energy of the surface (proportional in 2D to the length of the interface). The minimal value of energy is found for a circular shape. The bubble will oscillate until it reaches its final shape. If the time step exceeds the criterion given in equation (5.4), numerical oscillations lead to an unstable interface.

We use an unstructured mesh of about 15000 triangular elements. The average size of the elements is 9.5×10^{-3}m. According to (5.4), the time step restriction for the explicit treatment of the surface tension is about 0.0015s. We perform simulations for Δt=0.001s, 0.005s, 0.01s and 0.05s.

Figures 5.2-5.4 present the shape of the bubble obtained using different time step that exceed gradually the given criterion. As expected, the explicit treatment deviates the solution gradually from the stable one and exhibits numerical oscillations that end up by a deteriorated solution in particular for Δt=0.05s. Whereas, the new implementation shows as expected very stable solution even for large time step.

Table 5.1: Physical parameters for the oscillating square bubble

ρ_{liquid}	ρ_{gas}	η_{liquid}	η_{gas}	gravity	γ
797.88	1.1768	1.2×10^{-3}	1.0×10^{-5}	0	0.02361

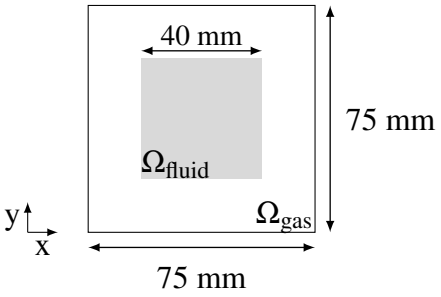

Figure 5.1: Set-up for the oscillating bubble

To quantify further the effect of the non-physical oscillations on the interface of the bubble due to the treatment of the surface tension, we computed the degree of circularity found in [128] and defined by :

$$\mathbf{c} = \frac{\text{perimeter of area-equivalent circle}}{\text{perimeter of the bubble}} \tag{5.20}$$

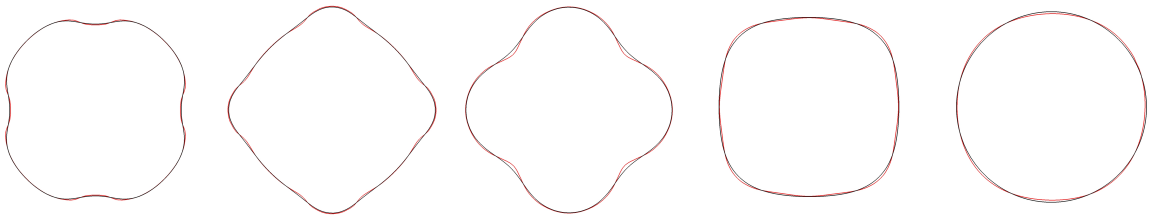

(a) t=0.1s (b) t=0.2s (c) t=0.3s (d) t=1.0s (e) t=6.0s

Figure 5.2: Interface shape for Δt=0.005s. Black line refers to the implicit formulation of the surface tension, red line refers to its explicit treatment.

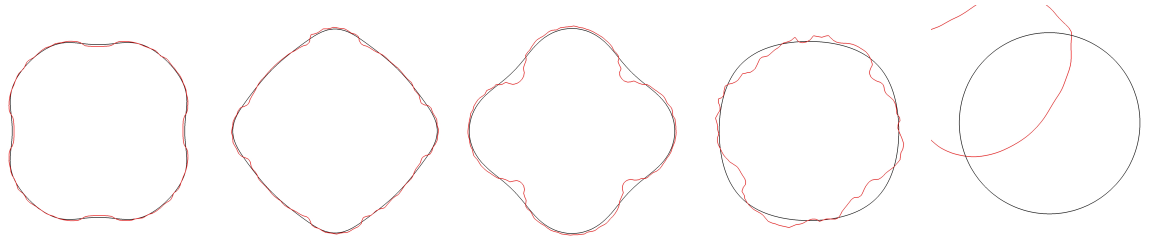

(a) t=0.1s (b) t=0.2s (c) t=0.3s (d) t=1.0s (e) t=6.0s

Figure 5.3: Interface shape for Δt=0.01s. Black line refers to the implicit formulation of the surface tension, red line refers to its explicit treatment.

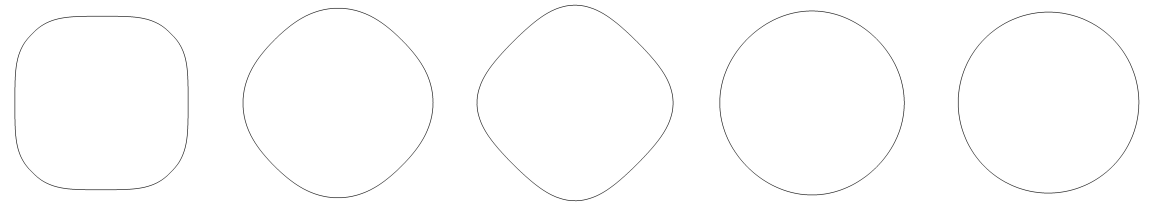

(a) t=0.1s (b) t=0.2s (c) t=0.3s (d) t=1.0s (e) t=6.0s

Figure 5.4: Interface shape for Δt=0.05s. Black line refers to the implicit formulation of the surface tension.

If a bubble is perfectly circular, the circularity is equal to 1. If the bubble is deformed, the circularity decreases. In Figure 5.5, we plot the circularity for all the simulations performed. According to the results obtained for Δt=0.001s, we notice that after few seconds, the shape of the bubble is circular and therefore that the problem is not physically unstable. Furthermore, if we increase the time step, the amplitude of the oscillations in the circularity increases only when using an explicit treatment of the surface tension. The implicit treatment of the surface tension does not result in higher amplitude. It is obvious that increasing the time step does not enable us to capture all the physical oscillations (see the curve for Δt=0.05s).

5.4.2 Rayleigh-Taylor instability

The two dimensional Rayleigh-Taylor instability benchmark [122, 133] is investigated in this section. It consists of two fluids placed in a closed cavity and submitted to gravity ($g =$

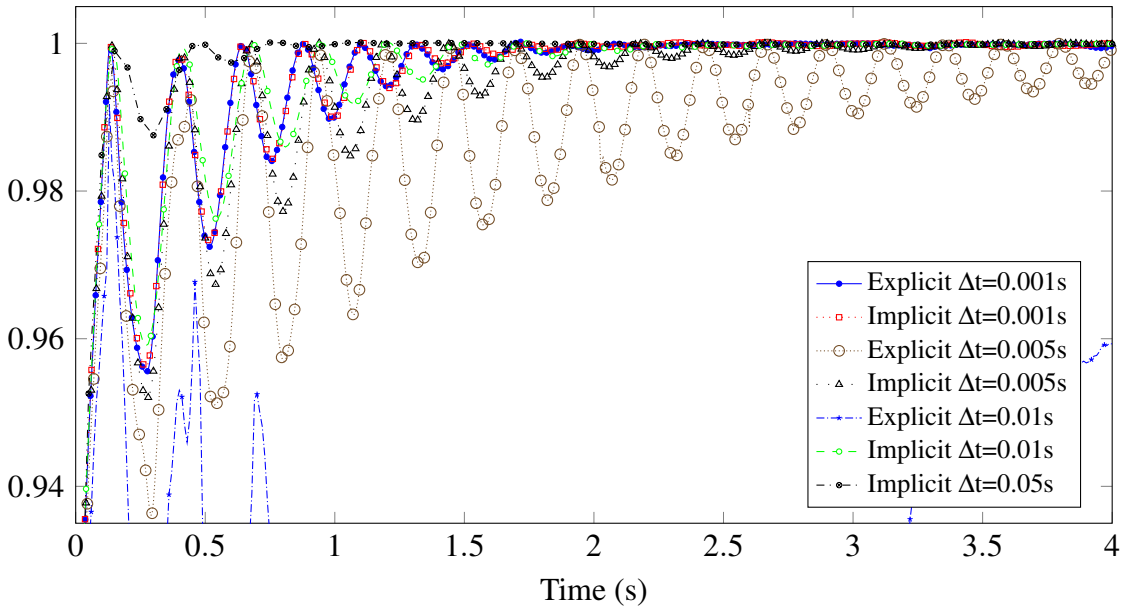

Figure 5.5: Circularity of the oscillating bubble for different time step.

$(0,-10)m/s^2$). This benchmark represents a challenge due to the fast dynamics of the system and due to the appearance of swirls, difficult to capture. The upper side of the cavity is occupied by a fluid with a density $\rho = 3kg/m^3$ and a viscosity $\eta = 0.0135kg/(m \cdot s)$ (see Case#1 in Table 5.2). The lower part is occupied with a fluid of density $\rho = 1kg/m^3$ and viscosity $\eta = 0.0045kg/(m \cdot s)$. As shown in Figure 5.6, the initial shape of the interface between the two fluids is a cosine function defined as $y = 0.05\cos(2\pi x)$ and the fluids are at rest at the initial time. The criteria chosen for the adaptive meshing is both the velocity (in direction and magnitude) and the level set function. The simulation is performed using 16000 elements and the time step is set to $\Delta t = 0.01s$. The surface tension is first set to zero.

In Figure 5.7, we can see the evolution of the two-fluid interface and the deformation of its shape. A very good agreement is found with [122] and [133] in term of front position, general shape of the perturbation and swirls shape. Figure 5.8 shows how the mesh is coupled to the evolution of the system and is refined close to the interface. This enables a more accurate capturing of such interface dynamics.

We repeated the same simulation using only 8000 elements to assess the ability to capture the swirls. Figure 5.9 shows that even for a low number of elements, swirls are still well captured. The mesh at t=1.25s in Figure 5.9 and the mesh at t=1.25s in Figure 5.8 show that the finest elements are concentrated close to the swirls. Since the velocity field far from the interface is still close to null, the elements far from the interface are coarsened.

Table 5.2: Physical parameters defining the test case for the Rayleigh-Taylor instability

	ρ_1	ρ_2	η_1	η_2	gravity
Case #1	1	3	0.0045	0.0135	10
Case #2	1	1.5	0.0022	0.0033	10

Finally, we repeated the same test case using the surface tension (see Case#2 in Table 5.2). Figure 5.10 presents the obtained results at t=1.85s for different values of surface tension.

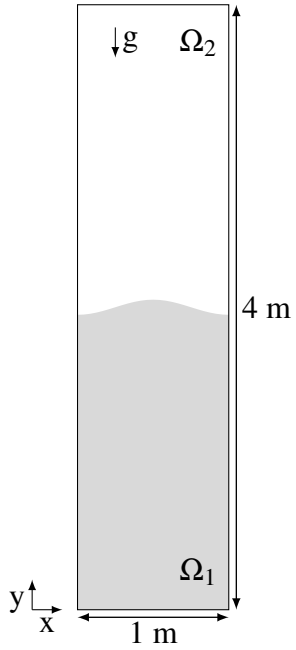

Figure 5.6: Setup for the 2D Rayleigh-Taylor instability

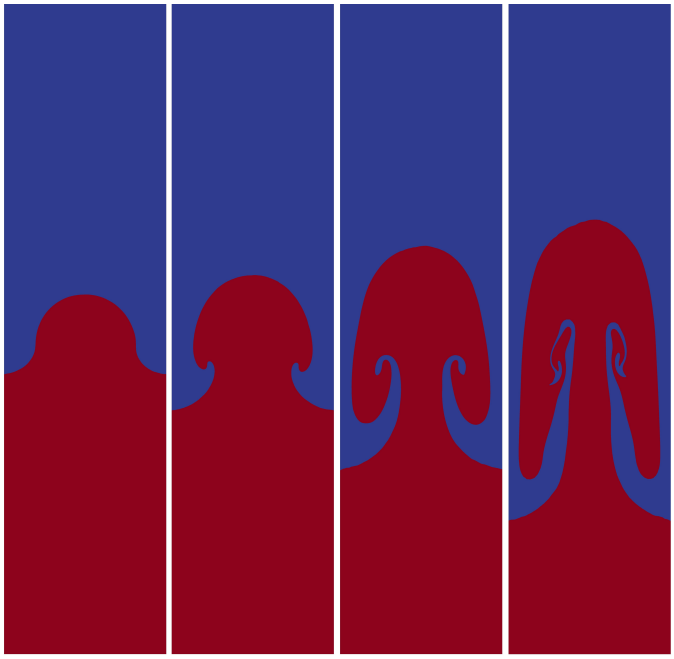

Figure 5.7: The interface shape of the Rayleigh-Taylor instability at t=0.5s, t=0.70s, t=1s and t=1.25s.

Again, the results are in very good agreement with the reference.

5.4.3 2D Rising bubble

We simulate the rising bubble benchmark from [128]. A bubble of diameter 0.5 centered at (0.5,0.5) is surrounded by a liquid of higher density and viscosity (see Figure 5.11). A free slip boundary condition is prescribed on the vertical walls and a no-slip condition is prescribed on the top and the bottom of the cavity. The motion of the bubble is only due to the buoyancy force.

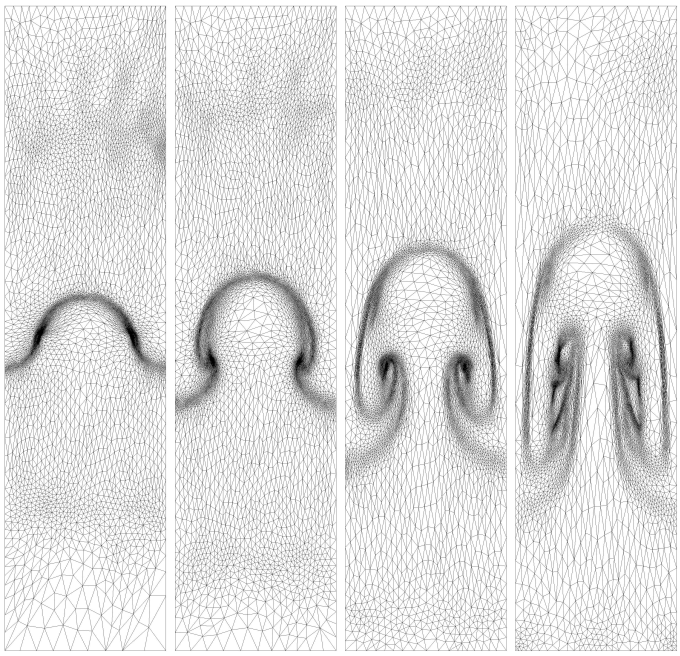

Figure 5.8: The obtained meshes for the Rayleigh-Taylor instability benchmark at t=0.5s, t=0.70s, t=1s and t=1.25s.

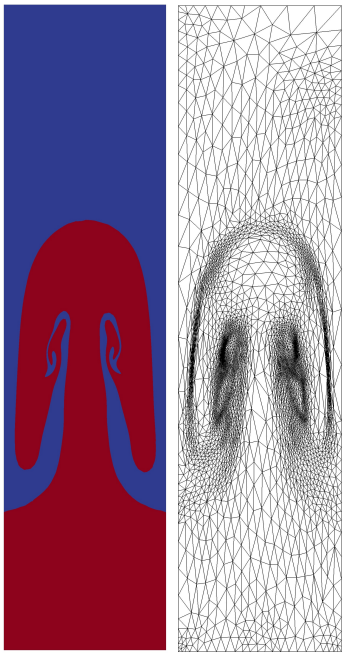

Figure 5.9: The interface shape (left) and the obtained mesh(right) of the Rayleigh-Taylor instability at t=1.25s using 8000 elements.

The simulations are performed for two different sets of parameters (see Table 5.3) respectively Case #1 and Case #2. The ratio between the physical parameters leads to different shapes of the bubble. In Case #1, the ratio between the physical property is 10. The high surface tension coefficient maintains the bubble as an ellipsoid. Case #2 is more challenging due to the high ratio between the physical properties of the two phases. Furthermore, the break up of the bubble represents an additional challenge for the level set method.

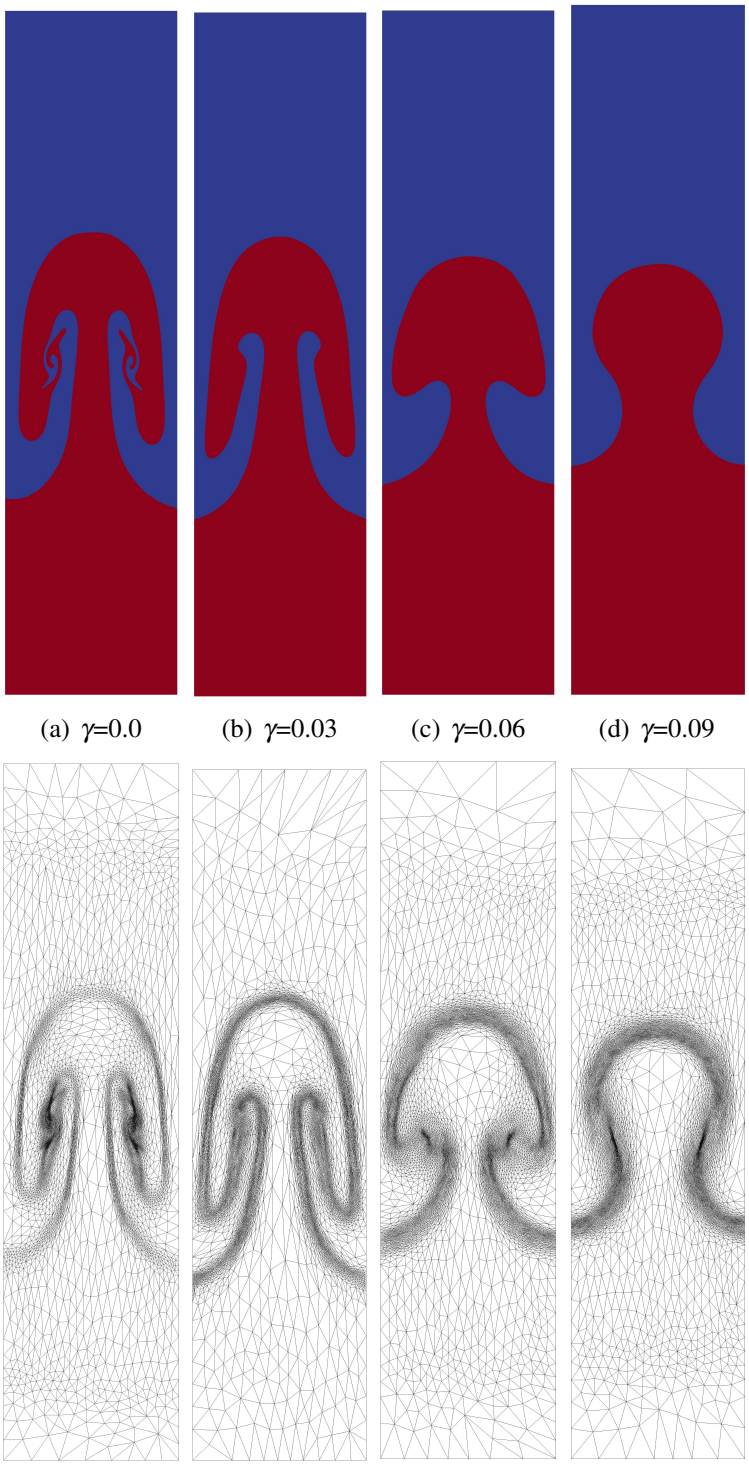

(a) γ=0.0 (b) γ=0.03 (c) γ=0.06 (d) γ=0.09

Figure 5.10: Rayleigh-Taylor instability at t=1.85s for different values of surface tension.

Figure 5.12 compares the shape obtained in the current work and the shape obtained by other teams in [128] for Case #2. Four different methods of resolution give four different final shapes of the bubble. It is therefore difficult to assess the accuracy of the methods. Since the visual evolution of the shape of the bubble is not rigorous enough to compare results provided by different methods of resolution, Hysing et al. decided in [128] to define benchmark quantities such as the position of the center of mass of the bubble and the rise velocity of the center

Table 5.3: Physical parameters defining the test case for the 2D rising bubble

	ρ_{liquid}	ρ_{gas}	η_{liquid}	η_{gas}	gravity	γ
Case #1	1000	100	10	1	0.98	24.5
Case #2	1000	1	10	0.1	0.98	1.96

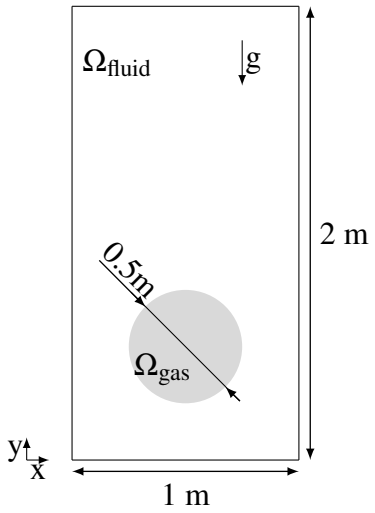

Figure 5.11: Setup for the 2D rising bubble case

of mass. The position of the center of mass of the bubble is defined by $\mathbf{X}_c = \int_{\Omega_g} \mathbf{x}\,dx / \int_{\Omega_g} 1\,dx$ whereas the rise velocity of the center of mass is defined by $\mathbf{U}_c = \int_{\Omega_g} \mathbf{u}\,dx / \int_{\Omega_g} 1\,dx$.

For each case, we perform two simulations, using adaptive anisotropic meshing, under the constraint of a fixed number of elements. The criteria chosen for the adaptive meshing is again both the velocity (in direction and magnitude) and the level set function. The first simulation is performed using about 5000 elements and the second simulation is performed using about 10000 elements. The time step is set to $\Delta t = 0.002s$. The results of the two simulations are compared to the simulations performed with the finest grids in [128]. Table 5.4 gives a general overview on the used number of elements and iterations for each code.

Table 5.4: Number of elements and iterations for the 2D rising bubble

		Mesh	Iteration
Case #1	TP2D	204800 rectangles	15360
	FreeLIFE	102400 structured triangles	960
	MooNMD	8066 degrees of freedom at the interface	6000
	Current work	5000/10000 unstructured and anisotropic	1500
Case #2	TP2D	819200 rectangles	30720
	FreeLIFE	102400 structured triangles	960
	MooNMD	8066 degrees of freedom at the interface	6000
	Current work	5000/10000 unstructured and anisotropic	1500

Figure 5.13 shows the comparison with the three methods described in [128] for the position of the center of mass. Figure 5.14 shows the comparison for the rising velocity of the center of mass. Figure 5.15 compares the shape of the bubble at t=3s.

For Case #1, as expected, the shape at the final time is found to be ellipsoidal. The results from all simulations are in very good agreement. This shows the ability of the proposed adaptive meshing procedure to accurately solve the problem, not only by refining the mesh close to the interface but also wherever it is relevant from a physical point of view, as it is depicted in Figure 5.16.

For Case #2, during the rise of the bubble, thin filaments are developed and eventually break up for some methods. The break of the filaments has an effect on the rise of the bubble and could explain the differences found in Figure 5.13 and Figure 5.14. In [128], simulations performed with MooNMD, using Arbitrary Lagragian Eulerian technique to follow the interface and remeshing according to the degree of deformation, show the formation of thin filaments. Simulations performed in fixed meshes with TP2D and FreeLIFE, using level set method to follow the interface, show that the break up does not occur when the mesh is very fine. The adaptive meshing used in the current work enables the formation of two thin filaments even for a low number of elements. Once again, the ability of the proposed method is well highlighted in Figure 5.17 by capturing with high fidelity the characteristics of the flow at the interface and under the bubble where the velocity gradients are important due to the ascending motion of the bubble.

To assess the formation of the thin filaments, we perform a simulation using a very fine structured mesh with 409600 elements and a time step $\Delta t = 0.0002s$. Figure 5.18 shows that the results obtained using an adaptive meshing with 10000 elements (40 times less elements) remain in a very good agreement with the reference solution.

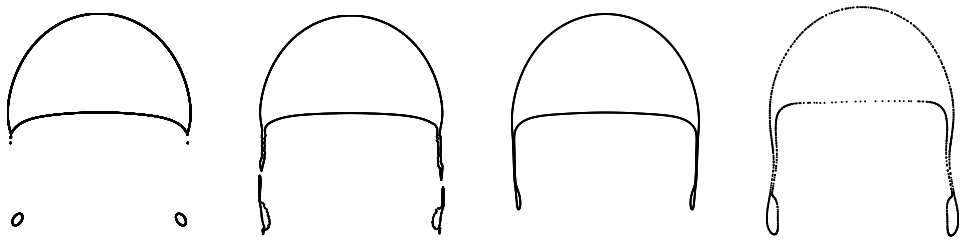

Figure 5.12: 2D rising bubble: Results from different teams for Case #2

5.4.4 3D Rising bubble

The final case examined here is the three-dimensional rising bubble of diameter D in a closed cavity from [122]. The setup of this case is depicted in Figure 5.19 and the physical parameters are summarized in Table 5.5. The bubble is at rest at initial time and the center of the bubble is located at z=-D. A free slip boundary condition is prescribed on all the walls. The motion of the bubble is only due to the buoyancy force. The simulations are performed using the proposed adaptive meshing technique with 128000 elements. The time step is set to $\Delta t = 0.002s$. Two cases are considered. In the first one, the diameter is fixed to D=0.05m. Since the surface tension is null, this case is challenging for the level set method due to the skirted shape of the bubble. The adaptive meshing enables easily the formation of the skirt of the bubble and no break up occurs during the simulation as it is depicted in Figure 5.20. In the second case, the diameter is set to D=0.01m. Due to the surface tension effects, the form of the bubble is

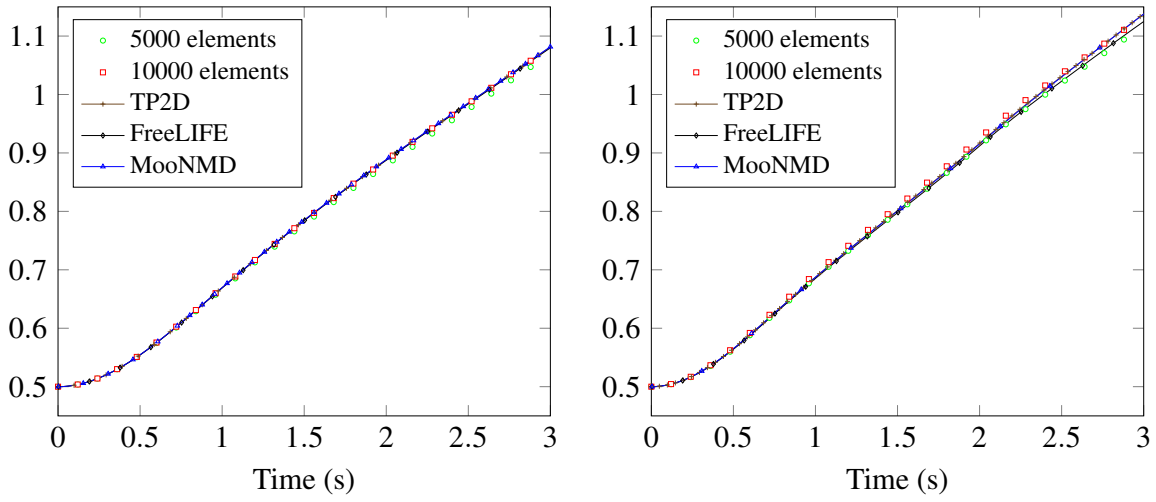

(a) Case#1 (b) Case#2

Figure 5.13: Evolution of the position of the center of mass

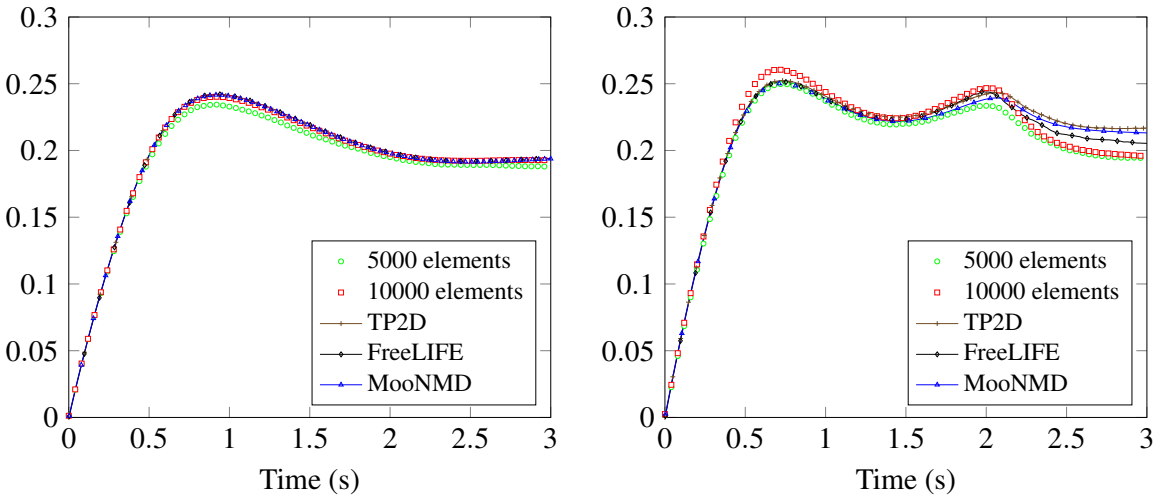

(a) Case#1 (b) Case#2

Figure 5.14: Evolution of the rising velocity of the center of mass

expected to be ellipsoidal. The shape and the mesh for this case are presented in Figure 5.21 and agree with the reference [122].

Table 5.5: Physical parameters defining the test case for the 3D rising bubble

D	ρ_{liquid}	ρ_{gas}	η_{liquid}	η_{gas}	gravity	γ
0.05	1000	1.225	0.35	0.00358	9.81	0
0.01	1000	1.225	0.35	0.00358	9.81	0.11

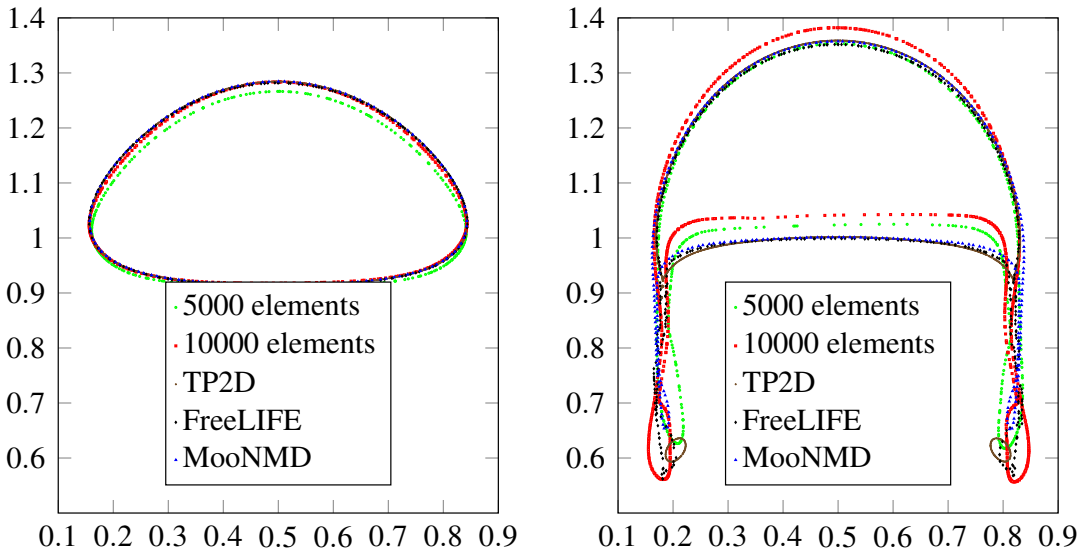

(a) Case#1 (b) Case#2

Figure 5.15: Shape of the bubble at t=3s

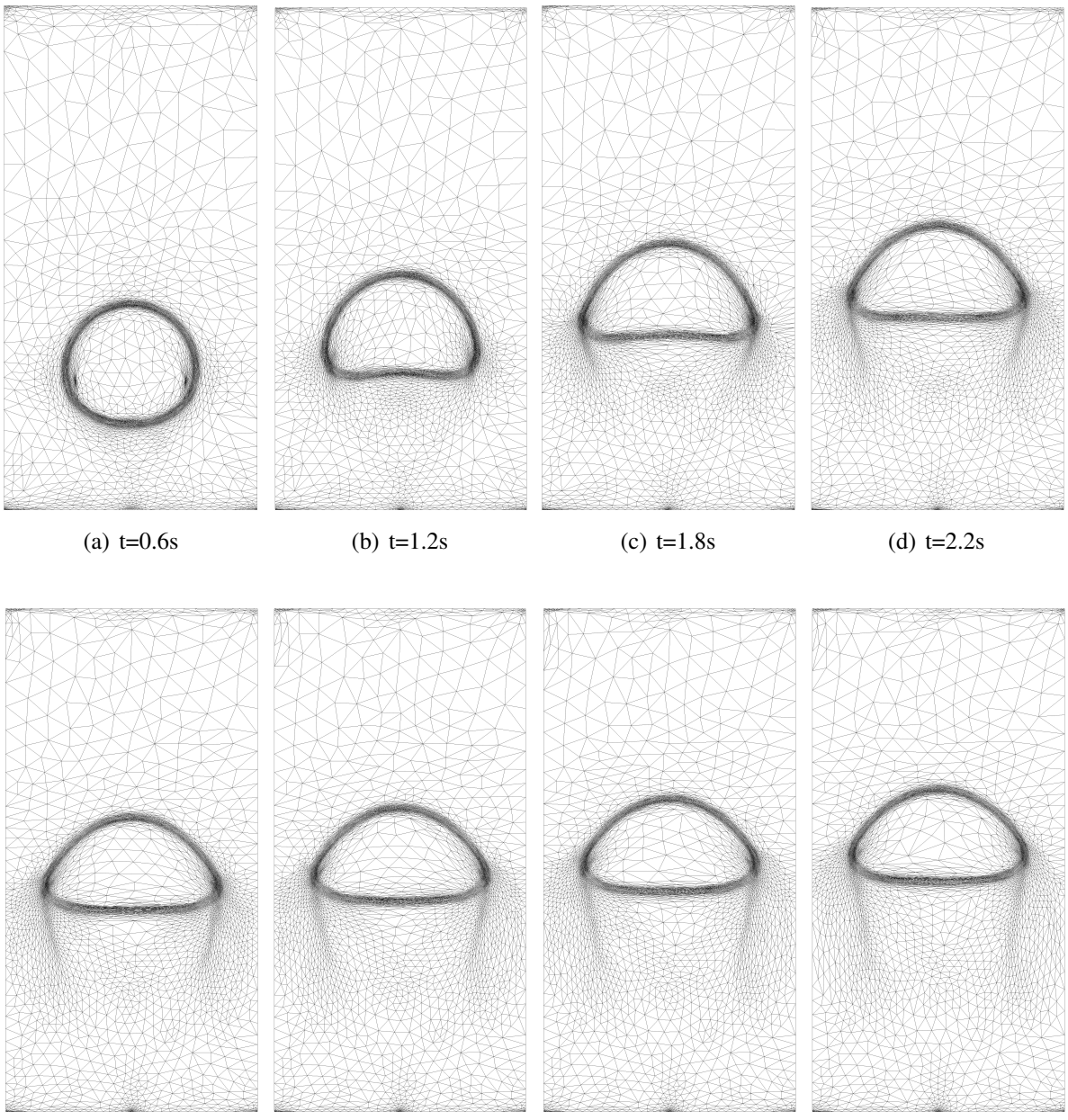

(a) t=0.6s (b) t=1.2s (c) t=1.8s (d) t=2.2s

(e) t=2.4s (f) t=2.6s (g) t=2.8s (h) t=3.0s

Figure 5.16: 2D rising bubble: Case #1 mesh (10000 elements) at different times.

(a) t=0.6s (b) t=1.2s (c) t=1.8s (d) t=2.2s

(e) t=2.4s (f) t=2.6s (g) t=2.8s (h) t=3.0s

Figure 5.17: 2D rising bubble: Case #2 mesh (10000 elements) at different times.

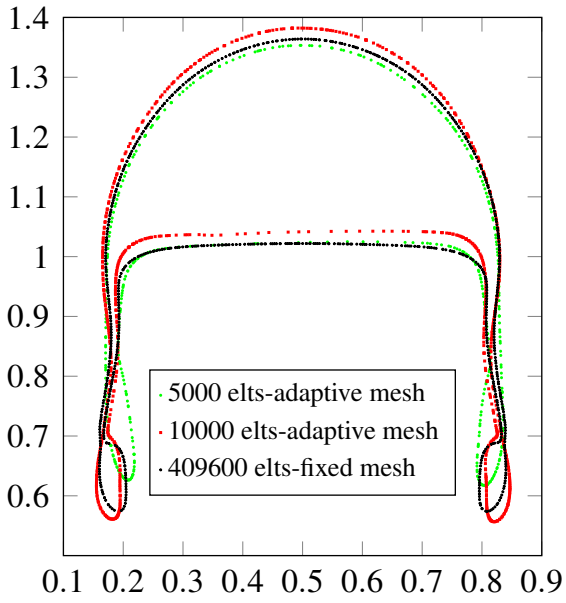

Figure 5.18: 2D rising bubble: Shape of the bubble at t=3s for Case #2. Simulations performed with 5000 and 10000 elements using mesh adaptation are compared with a simulation performed with 409600 structured elements.

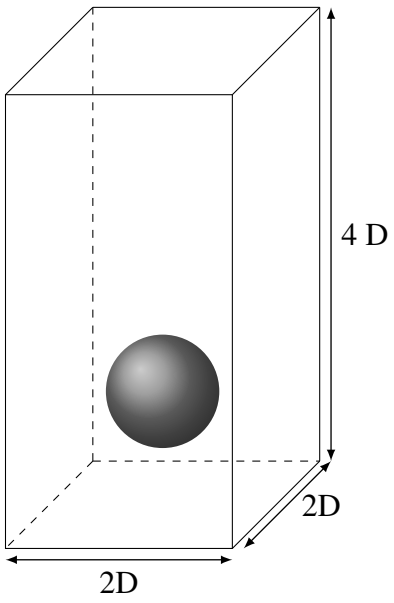

Figure 5.19: Set-up for the 3D rising bubble case

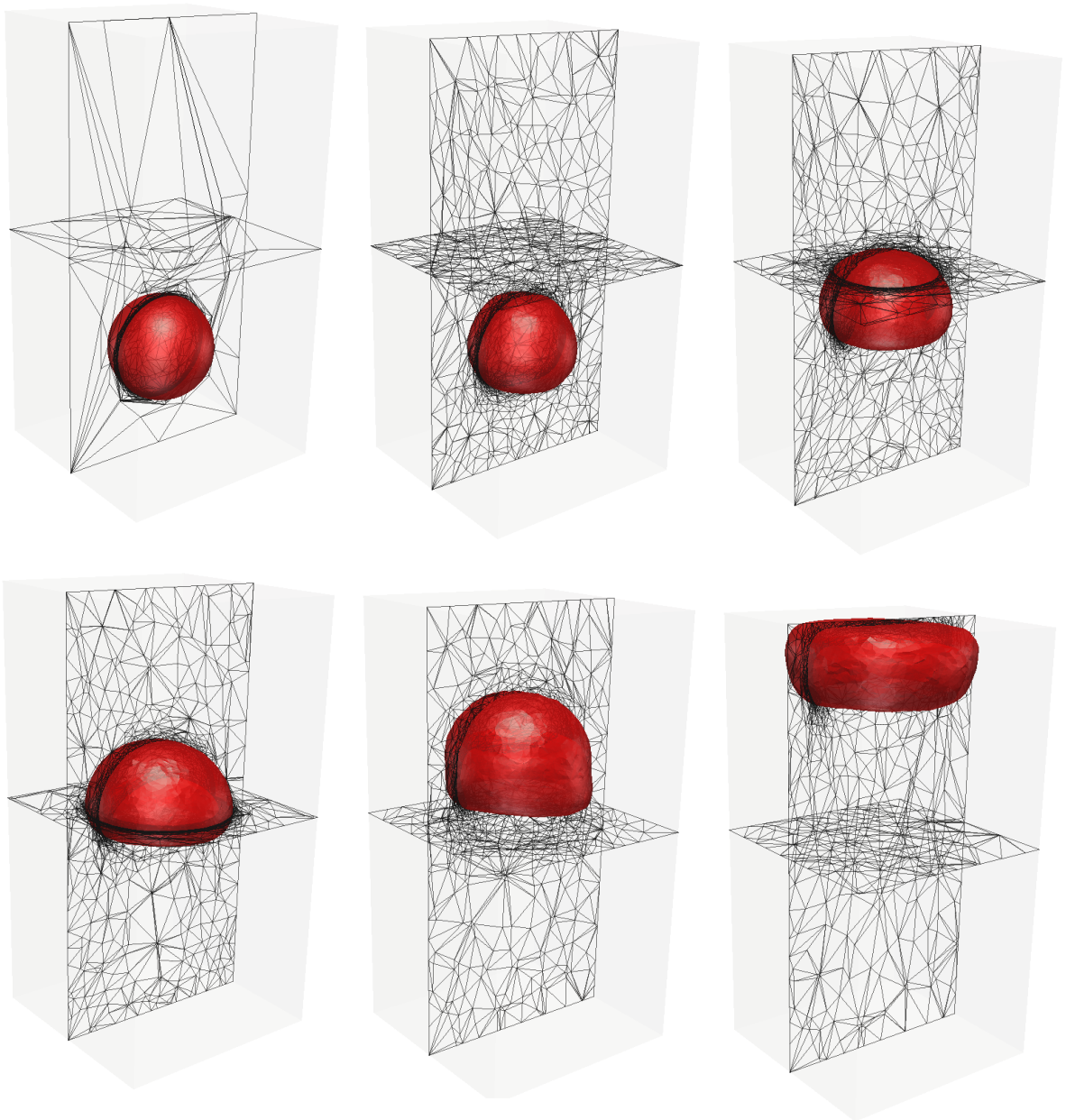

Figure 5.20: 3D rising bubble ($\gamma = 0.0$) at t=0, 0.04, 0.12, 0.18, 0.26, 0.42 s.

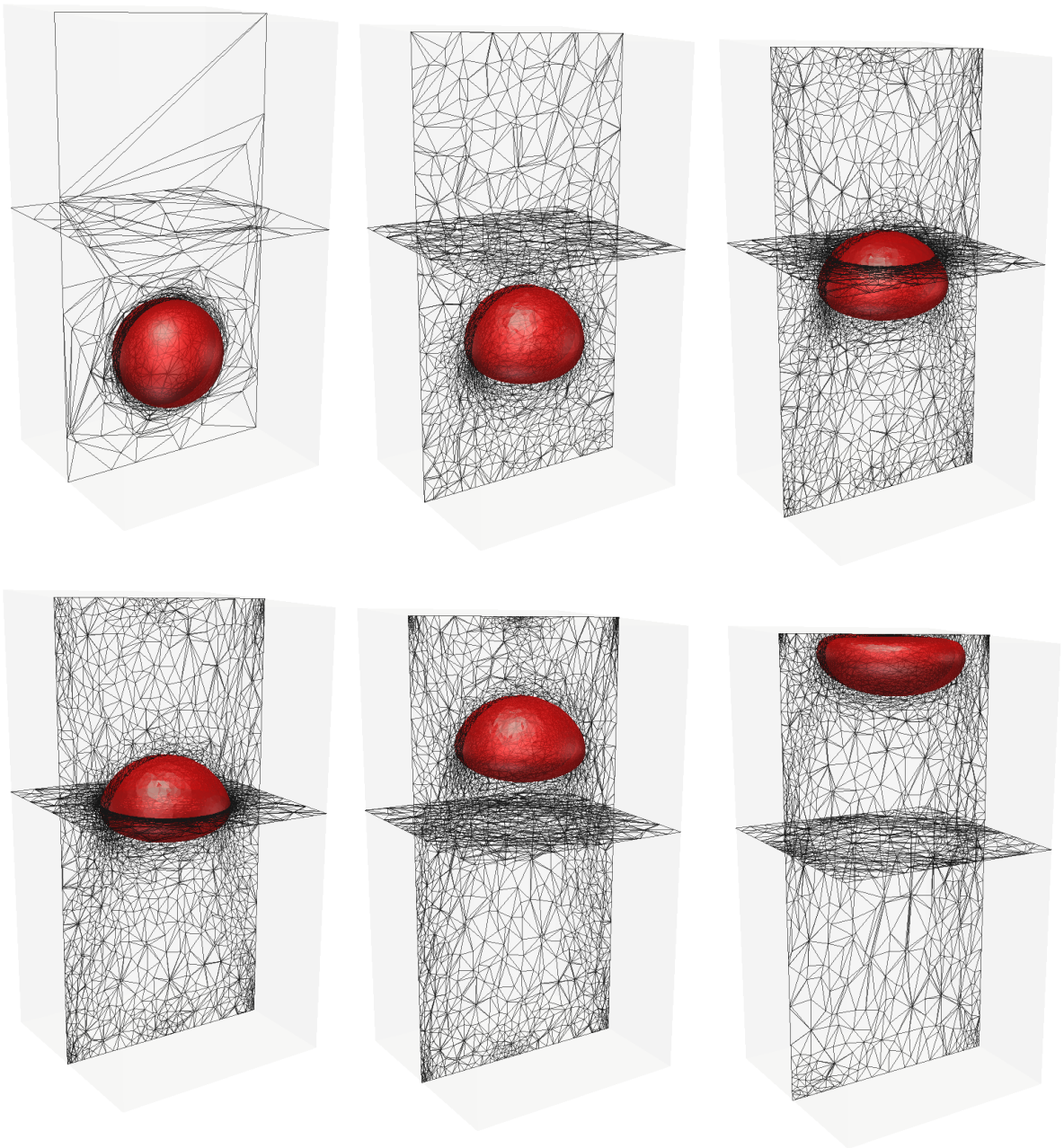

Figure 5.21: 3D rising bubble ($\gamma = 0.11$) at t=0, 0.04, 0.1, 0.12, 0.18, 0.26 s.

5.5 Conclusion

We have proposed in this chapter an implicit formulation of the surface tension to simulate incompressible two phase flows and to circumvent the numerical time step restriction due to the surface tension implementation. We have demonstrated the efficiency of the proposed framework by performing challenging cases in 2 and 3 dimensions. The results of the numerical tests show that this approach produces accurate numerical solutions. The comparison with the literature shows that despite a limited number of elements, simulations do not suffer any instabilities and a good accuracy is obtained. The computational cost is therefore drastically reduced.

Résumé en français

Dans ce chapitre, le développement et l'implémentation de la tension de surface dans les équations de Navier-Stokes multiphasiques sont présentées. Grâce à l'utilisation de la méthode level set, la dérivation des termes nécessaires au calcul de la tension de surface est directe. L'implémentation explicite en temps de cette force comme un terme source dans l'équation de conservation de mouvements mène à une sévère restriction du pas de temps, pénalisant ainsi les simulations multiphasiques. Si cette condition en temps n'est pas respectée, des oscillations parasites déstabilisant l'interface apparaissent. Cette condition est encore plus sévère avec l'utilisation d'outils d'adaptation de maillage anisotrope. A l'aide d'un théorème de géométrie différentielle et d'un opérateur de Laplace-Beltrami, il est possible d'exprimer la tension de manière semi-implicite. Cette nouvelle formulation empêche l'apparition de ces oscillations parasites, permettant ainsi l'utilisation de pas de temps plus grands. L'implémentation de cette méthode dans le cadre de la méthode VMS est décrite. La validation de cette approche et de son implémentation sur des cas tests en 2D et 3D permet de montrer la grande précision de cette méthode pour un coût dérisoire en comparaison avec les méthodes généralement utilisées dans la littérature.

Chapter 6

Towards boiling multiphase flows: unified compressible-incompressible solver

Contents

6.1 Introduction

Multiphase flows describe a wide variety of natural and industrial problems arising mostly in fluid mechanics, environmental applications and nuclear and chemical engineering. Indeed, it plays an important role to understand the physical phenomena such as bubble dynamics, groundwater flow, oil propagation, phase change and evaporation, and blood flow in biomechanical applications. Therefore, it is essential in most of these situations to well consider each phase and to treat precisely the dynamics of the interface (e.g. liquid-gas mixture). For instance, in bubbly flows (see Figure 6.1), bubbles are compressible while the water is incompressible, raising the question of whether or not the compressibility should be considered in the modeling and simulation of such phenomenon.

In the literature, several advanced computational approaches have treated both phases as incompressible fluids. To cite few, we refer to the sharp interface method in [134], hybrid particle level set method in [135], a front-tracking method proposed in [136], SPH method in [137], high order finite difference method suggested in [138], and recently a conservative sharp interface method in [139]. At the same level, numerous works investigated compressible multiphase flows, in particular for applications related to underwater explosion, fuel injections, bubble dynamics and confined flows among many others [140, 141, 142, 143, 144, 145]. However, the

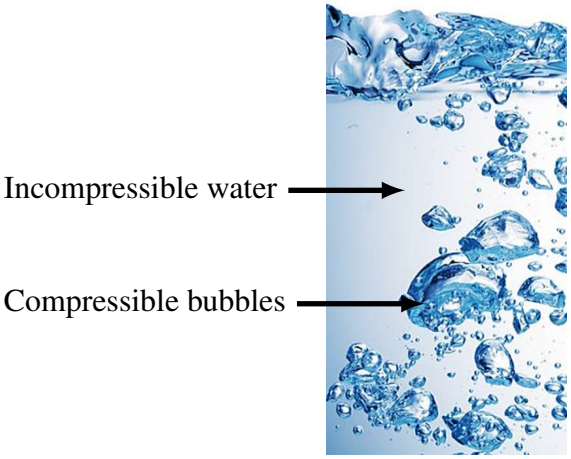

Figure 6.1: Bubbles rising in water

use of a single model encounters several numerical issues, in particular when simulating coupled complex problems. Indeed, the assumption that both fluids are treated as incompressible does not allow the change of volume, whereas if we assume that both gas and liquids are compressible, using an equation of state to mimic the incompressibility in the liquid phase, then the mass conservation is not controlled. These difficulties among many others have motivated the development of unified formulations. In this context, there is a renewed interest in modeling appropriately and in a coupled manner the properties of each phase [146]. The remaining challenge is to provide a numerical strategy to each component ensuring: (i) mass conservation, (ii) the ability to deal with large density and viscosity ratios, and (iii) accurate transmission of waves across the interface.

Only few attempts in the literature can be found that deals with the coupling of incompressible liquid and compressible gas. We can mention the coupling of sharp interface method with Ghost fluid approach proposed in [147], the use of multiple pressure variable approach [148], the use of the level set method to simulate small gas bubble clusters [149] and also the application of Galerkin Least Square method to the modified Navier-Stokes equation with a level set approach in [150].

In this work, we derived a new unified adaptive Variational MultiScale (VMS) method for liquid-gas flows. First, the same set of primitive unknowns and equations is described everywhere and the coupling between the pressure and the flow velocity is ensured by introducing mass conservation terms in the momentum equation. The main reasons for this choice of global description of the flow are stability, robustness and computational efficiency (see [151, 152]). The obtained system is then solved using a new derived Variational MultiScale stabilized Finite Element method designed to handle the abrupt changes at the liquid-gas interface. Indeed, it consists on the decomposition for both the velocity and the pressure fields into coarse/resolved scales and fine/unresolved scales [32, 33, 34, 20], needed to deal with convection dominated problems and pressure instabilities. Note that this choice of decomposition is extended here to the pressure equation which in return is shown to be favorable for simulating flows at high Reynolds number and to remove spurious oscillations at the interface due to the high discontinuity in the material properties. A conservative level set method is used in this case to provide a precise position of the interfaces and to enable homogeneous physical properties for each subdomain [16].

Finally, we combine this new Variational MultiScale formulation with an a posteriori error estimator for dynamic anisotropic mesh adaptation [16]. It involves building a mesh based

on a metric map. It provides both the size and the stretching of elements in a very condensed information data. Consequently, due to the presence of high gradients in the primitive variables, it provides highly stretched elements at the interfaces, at the inner and the boundary layers, and thus yields an accurate modeling framework for two-phase compressible and incompressible isothermal flows. We assess the behavior and accuracy of the proposed formulation in the simulation of three time-dependent challenging numerical examples.

6.2 Governing equations for compressible-incompressible coupling

In this section, the general equations of the global compressible-incompressible model are presented. The same set of primitive unknowns will be used by introducing mass conservation terms in the momentum and energy equations. To keep the presentation simple, we sidestep the surface tension effects and we assume no slip condition at the interface and that the viscous part of the stress tensor is negligible in comparison to the pressure contribution. The mass and momentum equations are first formulated in the following conservative form:

$$\frac{\partial \rho}{\partial t} + \nabla \cdot (\rho u) = 0 \tag{6.1}$$

$$\rho \frac{\partial u}{\partial t} + \rho u \cdot \nabla u - \nabla \cdot \sigma = \rho g \tag{6.2}$$

where ρ, g and u are the density, the gravity and the velocity, and σ the stress tensor which reads:

$$\sigma = 2\mu\ \varepsilon(u) - p\ I_d \tag{6.3}$$

with p and μ the pressure and the dynamic viscosity, ε the deviatoric part of the strain rate tensor and I_d the identity tensor .

The system must be closed by a state equation relating the density, the thermodynamic pressure and the temperature.

$$\rho = \rho(T, p) \tag{6.4}$$

In order to express the global model, and assuming that the fluid is divariant, we reformulate the density as function of the pressure and the temperature (see [151, 152]):

$$\frac{d\rho}{dt} = \left.\frac{\partial \rho}{\partial T}\right|_p \frac{dT}{dt} + \left.\frac{\partial \rho}{\partial p}\right|_T \frac{dp}{dt} \tag{6.5}$$

Consequently, the mass conservation equation can be reformulated as an equation for the pressure

$$\frac{1}{\rho}\left.\frac{\partial \rho}{\partial p}\right|_T \frac{dp}{dt} + \frac{1}{\rho}\left.\frac{\partial \rho}{\partial T}\right|_p \frac{dT}{dt} + \nabla \cdot u = 0 \tag{6.6}$$

By introducing

$$\chi_p = \frac{1}{\rho}\left.\frac{\partial \rho}{\partial p}\right|_T \quad \text{and} \quad \chi_T = -\frac{1}{\rho}\left.\frac{\partial \rho}{\partial T}\right|_p \tag{6.7}$$

as the isothermal compressibility coefficient and the thermal expansion coefficient respectively, the mass conservation now reads

$$\nabla \cdot u + \chi_p \frac{\partial p}{\partial t} + \chi_p u \cdot \nabla p = \chi_T \frac{dT}{dt} \tag{6.8}$$

Finally, the system of equations (6.1)-(6.2) is now transformed in a unified form that can be used for both incompressible and compressible flows as follow:

$$\rho \frac{\partial u}{\partial t} + \rho u \cdot \nabla u - \nabla \cdot (2\mu\varepsilon(u)) + \nabla p = \rho g \tag{6.9}$$

$$\nabla \cdot u + \chi_p \frac{\partial p}{\partial t} + \chi_p u \cdot \nabla p = \chi_T \frac{dT}{dt} \tag{6.10}$$

The following Table 6.1 resumes all the required physical parameters and coefficients needed in (6.9)-(6.10) to simply solve an incompressible liquid with a compressible gas. We used in this case the perfect gas equation of state with R as the perfect gas constant.

Table 6.1: Model parameters

liquid	ρ_l	$\chi_l = (0\,,\,0)$	μ_l
gas	$\rho_g = p/RT$	$\chi_g = (1/T\,,\,1/p)$	μ_g

6.3 Variational MultiScale method for the unified solver

It is well known, that the stability of the discrete formulation of Navier-Stokes depends on appropriate compatibility restrictions on the choice of the Finite Element spaces for the velocity and the pressure. According to this, standard Galerkin mixed elements with continuous equal order linear/linear interpolation is not a stable discretization. This lack of stability manifests in uncontrollable oscillations that pollute the solution.

Many measures may be distinguished to solve and get around these difficulties. In particular, the classical stabilized Finite Element methods may be applied to deal with the instabilities in convection-dominated regime and the velocity-pressure compatibility condition. However, the direct use of such methods may be inadequate when additional terms are inserted in the Navier-Stokes equations or when different physics is applied. Indeed, one needs to seek for a general framework that deal with different and new variant of mixed variational formulations. The Variational MultiScale method, proposed by Hughes [32, 33, 34, 127] offers such an ideal framework. Therefore, terms related to such as Darcy [130], extra stress constraint [153], hydrodynamics [131], turbulence [34, 35], viscoelastic flow [36] among others are treated accordingly and taken into account by the stabilization process.

Accordingly, in this section, we derive a new Variational MultiScale formulation for the unified two-phase compressible and incompressible isothermal flows. It considers that the unknowns of the mixed problem (6.9)-(6.10) can be split into two components, coarse and fine, corresponding to different scales or levels of resolution.

Following the lines in [32], we consider a direct sum decomposition of the velocity and the pressure fields into resolvable coarse-scale and unresolved fine-scale $u = u_h + \tilde{u}$ and $p = p_h + \tilde{p}$. Likewise, we apply the same decomposition for the weighting functions $v = v_h + \tilde{v}$

and $q = q_h + \tilde{q}$. The unresolved fine-scales are usually modeled using residual based terms that are derived consistently. The static condensation consists of substituting the fine-scale solution into the large-scale problem providing additional terms, tuned by a local stabilizing parameter. The latter enhances the stability and accuracy of the standard Galerkin formulation. The enrichment of the functional spaces is performed as follows: $V = V_h \oplus \tilde{V}$, $V_0 = V_{h,0} \oplus \tilde{V}_0$ and $Q = Q_h \oplus \tilde{Q}$. Thus, the mixed-Finite Element approximation of the time-dependent unified compressible-incompressible problem can read:

Coarse scale

$$\begin{cases} \left(\rho \dfrac{\partial (u_h+\tilde{u})}{\partial t}, v_h\right) + (\rho(u_h+\tilde{u})\cdot\nabla(u_h+\tilde{u}), v_h) - (p_h+\tilde{p}, \nabla\cdot v_h) + (2\mu\varepsilon(u_h) : \varepsilon(v_h)) \\ = (f_v, v_h) \quad \forall v_h \in V_{h,0} \\ \\ (\nabla\cdot(u_h+\tilde{u}), q_h) + \chi_p \left(\dfrac{\partial (p_h+\tilde{p})}{\partial t}, q_h\right) + \chi_p\left((u_h+\tilde{u})\cdot\nabla(p_h+\tilde{p}), q_h\right) = (f_p, q_h) \quad \forall q_h \in Q_h \end{cases} \tag{6.11}$$

Fine scale

$$\begin{cases} \left(\rho \dfrac{\partial (u_h+\tilde{u})}{\partial t}, \tilde{v}\right) + (\rho(u_h+\tilde{u})\cdot\nabla(u_h+\tilde{u}), \tilde{v}) - (p_h+\tilde{p}, \nabla\cdot \tilde{v}) + (2\mu\varepsilon(\tilde{u}) : \varepsilon(\tilde{v})) \\ = (f_v, \tilde{v}) \quad \forall \tilde{v} \in \tilde{V} \\ \\ (\nabla\cdot(u_h+\tilde{u}), \tilde{q}) + \chi_p \left(\dfrac{\partial (p_h+\tilde{p})}{\partial t}, \tilde{q}\right) + \chi_p\left((u_h+\tilde{u})\cdot\nabla(p_h+\tilde{p}), \tilde{q}\right) = (f_p, \tilde{q}) \quad \forall \tilde{q} \in \tilde{Q} \end{cases} \tag{6.12}$$

To simplify the notation, we used f_v and f_p as the source terms in (6.9)-(6.10). To derive the stabilized formulation, we first solve the fine scale problem, defined on the sum of element interiors and written in terms of the time-dependent large-scale variables. Then we substitute the fine-scale solution back into the coarse problem, thereby eliminating the explicit appearance of the fine-scale while still modeling their effects. At this stage, two important remarks have to be made in order to deal with the time-dependency and the non-linearity of the momentum equation of the subscale system:

i) the subscales are not tracked in time, therefore, quasi-static subscales are considered here (see [154] for a justification of this choice); however, the subscale equation remains quasi time-dependent since it is driven by the large-scale time-dependent residual. For time-tracking of subscales, see [84].

ii) the convective velocity of the non-linear term may be approximated using only large-scale part so that $(u_h+\tilde{u})\cdot\nabla(u_h+\tilde{u}) \approx u_h^c \cdot \nabla(u_h+\tilde{u})$ where u_h^c is the convection velocity (see [20]).

The equations for the coarse scales are obtained taking the subscale test functions equal to zero. Therefore, using the previous assumptions, we have

$$\begin{cases} \left(\rho\dfrac{\partial u_h}{\partial t}, v_h\right) + (\rho u_h^c \cdot \nabla u_h, v_h) - (p_h + \tilde{p}, \nabla \cdot v_h) + (2\mu\varepsilon(u_h) : \varepsilon(v_h)) \\ + \sum\limits_{K\in\mathscr{T}_h} \left(\tilde{u}, -\rho u_h^c \cdot \nabla v_h\right) \quad = \quad (f_v, v_h) \qquad \forall v_h \in V_{h,0} \\ \\ (\nabla \cdot u_h, q_h) + \chi_p \left(\dfrac{\partial p_h}{\partial t}, q_h\right) + \chi_p \left(u_h^c \cdot \nabla p_h, q_h\right) \\ - \sum\limits_{K\in\mathscr{T}_h} (\tilde{u}, \nabla \cdot q_h) - \sum\limits_{K\in\mathscr{T}_h} \left(\tilde{p}, \chi_p u_h^c \cdot \nabla q_h\right) = (f_p, q_h) \qquad \forall q_h \in Q_h \end{cases} \tag{6.13}$$

for all $(v_h, q_h) \in V_{h,0} \times P_{h,0}$, where $\sum_K$ stands for the summation over all the elements of the Finite Element partition $\mathscr{K}_h$ and $(\cdot,\cdot)_K$ denotes the L^2 product in each K. The problem for the fine scales is obtained from (6.12) and using approximations i) and ii) described above. Introducing the Finite Element residuals

$$\begin{aligned} R_u &= f_v - \rho\frac{\partial u_h}{\partial t} - \rho u_h^c \cdot \nabla u_h + \nabla \cdot (2\mu\varepsilon(u_h)) - \nabla p_h \\ R_c &= f_p - \nabla \cdot u_h - \chi_p \frac{\partial p_h}{\partial t} - \chi_p u_h^c \cdot \nabla p_h \end{aligned} \tag{6.14}$$

and using the same ideas as in [91], it turns out that the subscales may be approximated within each element $K \in \mathscr{K}_h$ by

$$\begin{aligned} \tilde{u} &= \sum_{\mathscr{T}_h} \tau_u \tilde{P}_u(R_u) \\ \tilde{p} &= \sum_{\mathscr{T}_c} \tau_c \tilde{P}_c(R_c) \end{aligned} \tag{6.15}$$

where $\tilde{P}_v$ and $\tilde{P}_p$ are the projections onto $\tilde{V}$ and $\tilde{Q}$, respectively, and τ_u and τ_c are the so called stabilization parameters. The most common choice is to take the former as the identity when applied to Finite Element residuals (see [32]), and this is what we will do here, although it is also possible to take them as the projection orthogonal to the Finite Element space (see [90] and references therein).

Inserting the expression for the subscales, we finally obtain the stabilized Finite Element problem. The new variational formulation reads:

$$\begin{cases} \left(\rho\dfrac{\partial u_h}{\partial t}, v_h\right) + (\rho u_h^c \cdot \nabla u_h, v_h) - (p_h, \nabla \cdot v_h) + (2\mu\varepsilon(u_h) : \varepsilon(v_h)) \\ + \sum\limits_{K\in\mathscr{T}_h} \tau_u \left(\rho\dfrac{\partial u_h}{\partial t} + \rho u_h^c \cdot \nabla u_h - \nabla \cdot (2\mu\varepsilon(u_h)) + \nabla p_h - f_v \,,\, \rho u_h^c \cdot \nabla v_h\right) \\ + \sum\limits_{K\in\mathscr{T}_h} \tau_c \left(\nabla \cdot u_h + \chi_p \dfrac{\partial p_h}{\partial t} + \chi_p u_h^c \cdot \nabla p_h - f_p, \nabla \cdot v_h\right) \quad = \quad (f_v, v_h) \qquad \forall v_h \in V_{h,0} \\ \\ (\nabla \cdot u_h, q_h) + \chi_p \left(\dfrac{\partial p_h}{\partial t}, q_h\right) + \chi_p \left(u_h^c \cdot \nabla p_h, q_h\right) \\ + \sum\limits_{K\in\mathscr{T}_h} \tau_u \left(\rho\dfrac{\partial u_h}{\partial t} + \rho u_h^c \cdot \nabla u_h - \nabla \cdot (2\mu\varepsilon(u_h)) + \nabla p_h - f_v, \nabla q_h\right) \\ + \sum\limits_{K\in\mathscr{T}_h} \tau_c \left(\nabla \cdot u_h + \chi_p \dfrac{\partial p_h}{\partial t} + \chi_p u_h^c \cdot \nabla p_h - f_p, \chi_p u_h^c \cdot \nabla q_h\right) = (f_p, q_h) \qquad \forall q_h \in Q_h \end{cases} \tag{6.16}$$

When compared with the standard Galerkin method and even to the Variational MultiScale method for the incompressible Navier-Stokes equations, the proposed stable formulation involves new additional integrals that are evaluated element-wise. These additional terms, obtained by replacing the approximated $\tilde{u}$ and $\tilde{p}$ into the large-scale equation (6.13), represent the effects of the sub-grid scales in both incompressible and compressible phases. This is the first attempt that takes into account these new terms. They are introduced in a consistent way to the Galerkin formulation and are multiplied by stabilizing parameters and enable to overcome the instability of the classical formulation arising in convection dominated flows and to deal with the pressure instabilities. Similar conclusions were obtained in other applications such as in shock hydrodynamics [131].

6.4 Numerical test cases

In order to validate the proposed unified formulation, three time-dependent numerical test cases are presented in this section. The results obtained with the proposed approach are compared with either analytic solutions or with those obtained by other approaches that can be found in the literature. Some test cases cannot be handled using classical incompressible model for liquid and gas and attest of the benefit of a unified compressible-incompressible formulation.

6.4.1 Shrinking Bubble

The first test case is the shrinking bubble as proposed in [155]. An air bubble of radius $r = 0.03$ m is compressed by water in a closed cavity of length side equal to 0.1 m (see Fig. 6.2). The water is injected at a velocity of u_0=0.0025 m.s^{-1}, in the direction normal to the boundaries of the domain. The gravity and the surface tension are set null. The evolution in time of the density is given by the analytic solution $\rho(t) = \rho_0 / \left(1 - \frac{qt}{\pi R^2}\right)$ where q=0.001 m^2.s^{-1} is the flow rate of injected water and ρ_0 is the initial density. The isothermal compressibility coefficients for gas and liquid are set to $\chi_p^g = 9.8692327 \times 10^{-6}$ Pa^{-1} and $\chi_p^l = 0.444 \times 10^{-9}$ Pa^{-1}.

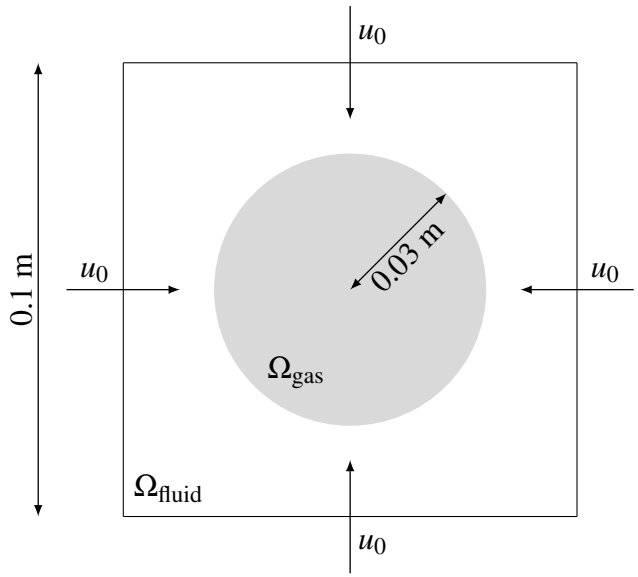

Figure 6.2: Set-up for the shrinking bubble.

Figure 6.3 shows how quickly the bubble volume is decreasing until it collapses. The number of nodes is set to $10,000$ and the mesh adaptation criteria are both the level set and the velocity (in direction and in norm).

As expected, the nodes are concentrated along the interface of the bubble and follows the change of direction of the velocity. This reflects how, for a controlled number of nodes, the mesh is naturally and automatically coarsened in smooth regions while extremely refined near the interface. It also illustrates the right orientation and deformation of the mesh elements (longest edges parallel to the boundary). This yields a great reduction of the number of triangles compared to [155] and consequently a reduction in the computational cost.

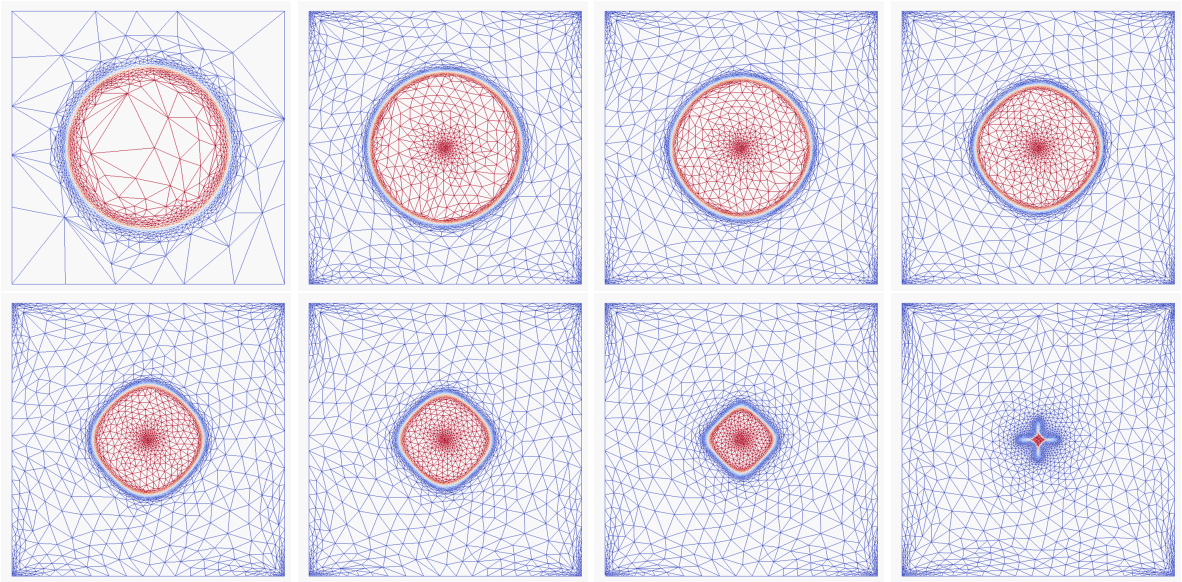

Figure 6.3: Shrinking bubble: Anisotropic adapted mesh at different times.

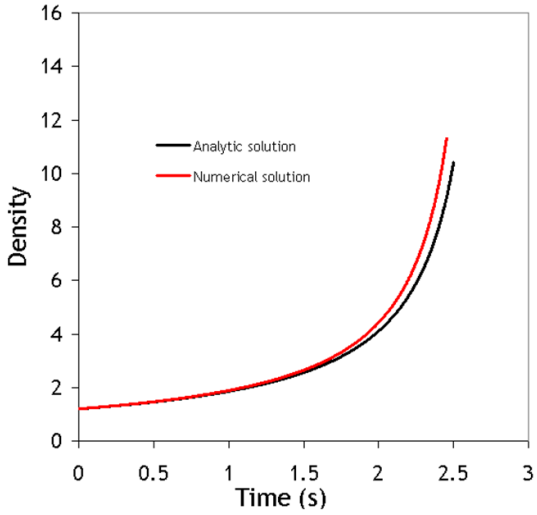

Figure 6.4: Shrinking bubble: Evolution in time of the density

Figure 6.4 shows a very good agreement between the numerical results for the evolution of the density and the analytic solution.

6.4.2 One sided bubble compression

We consider the 2D bubble compression test case inside a cavity of 1m side as presented in [150]. A bubble of radius 0.25m is initially placed at the center of the square and surrounded by an incompressible liquid (see Fig. 6.5). The liquid is injected in the square at an inflow velocity defined by :

$$u(t)|_{x=0} = 100t(y-0.75)(0.25-y) \text{ m.s}^{-1} \text{ for y} \in [0.25;0.75] \tag{6.17}$$

Gravity and surface tension are neglected. The initial pressure is the atmospheric one (10^5 Pa). We assume the flow isothermal with a sound speed c = 317 m.s^{-1} in the gas. Densities and viscosities are summarized in Table 6.2.

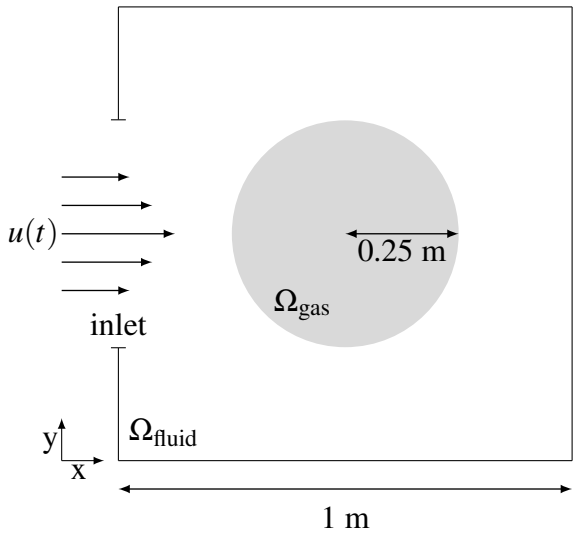

Figure 6.5: Set-up for the bubble compression

Table 6.2: Physical parameters for the bubble compression.

ρ_g	ρ_l	μ_g	μ_l	g	ρ_l/ρ_g	μ_l/μ_g
1	1000	0.01	1	0	1000	100

As the liquid is progressively injected inside the closed cavity, the gas bubble is compressed. In Figure 6.6, we show a very good agreement between a reference solution and the current obtained results at two different time step. We highlight also that the interfaces do not show instabilities and this is mainly due to the use of adaptive Variational MultiScale method. The results here are obtained using a decreased number of elements and allow further the compression of the bubble. Indeed, Figure 6.7 shows new obtained results for the time evolution of the interface until a quasi complete compression.

Again, all the main directional features characterizing the velocity inside the cavity are detected and well captured by the anisotropic error estimator. The mesh elements are highly stretched along the direction of the layers, at the detachment regions and around the interface. Once again, the developed adaptive unified VMS solver is shown to be very efficient and robust to deal with discontinuities using highly stretched elements. For a given constraint on the number of elements we can find the mesh that maximizes the accuracy of the numerical solution.

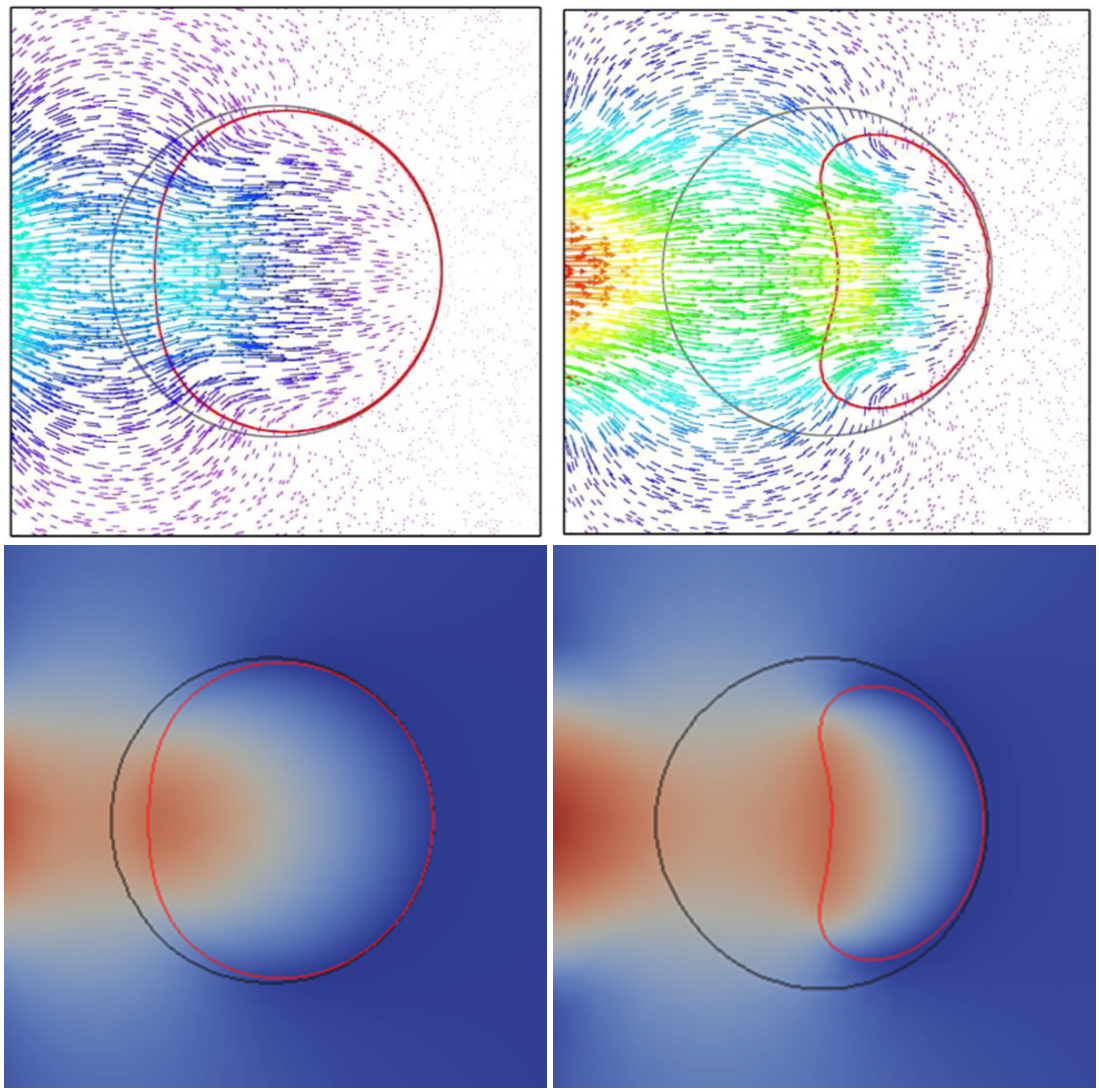

Figure 6.6: Bubble compression velocity field. The red line represents the interface at t=0.165s (left) and t=0.331s (right). Comparison between *Billaud et al.* (top) and current work (bottom).

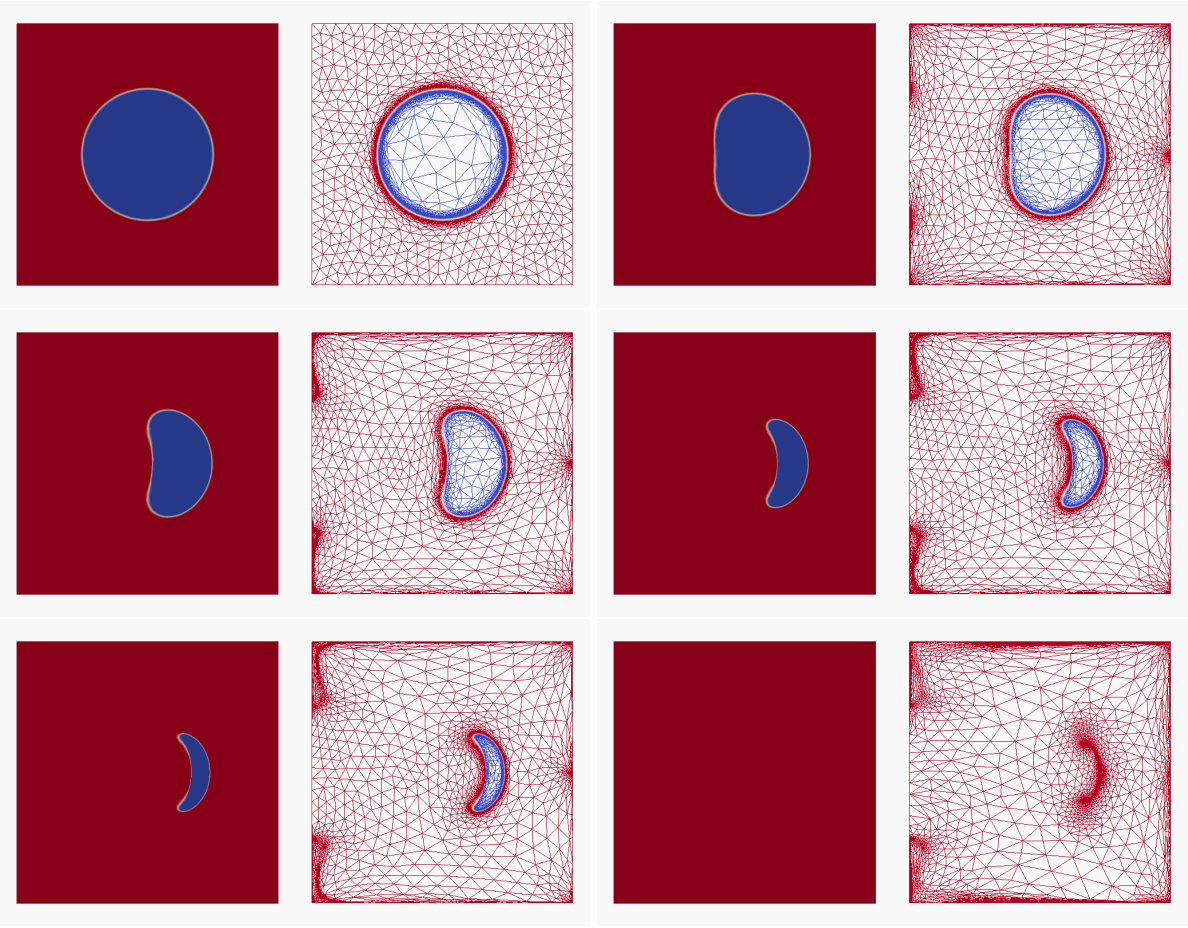

Figure 6.7: Bubble compression: evolution in time of the bubble shape and the mesh.

The zoom on the interface and at the right side of the cavity in Figure 6.8 highlights how sharply the interface and the layers can be captured. It shows the correct orientation and deformation of the mesh elements (longest edges parallel to the boundary). This yields a great reduction of the number of triangles. These results give confidence that the extension of the approach to take into account different components seems to work very well and plays an important role for transient flows.

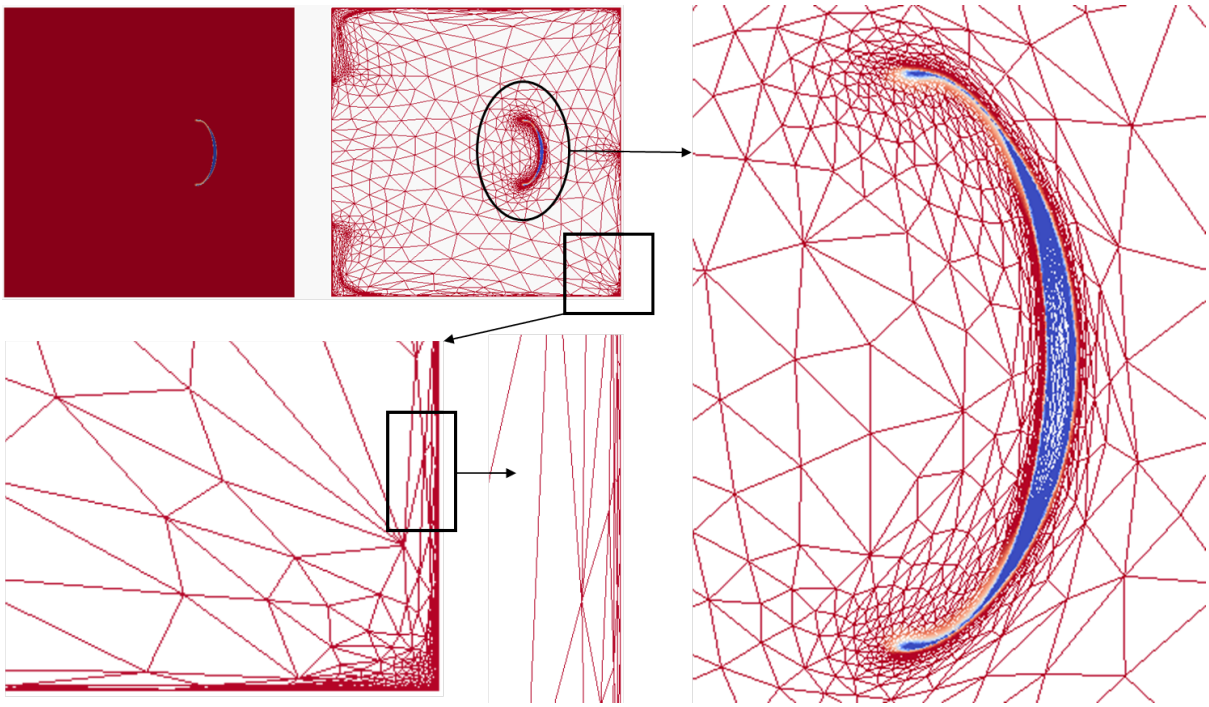

Figure 6.8: Bubble compression: focus on the mesh adaptation around the bubble and at the boundaries. Highly stretched elements are found at the interface of the bubble, allowing an accurate capture of physical phenomena.

The evolution of the volume is given by $V(t) = \frac{\pi}{16} - \frac{100t^2}{96}$. Finally, comparison with this analytic solution in Figure 6.9 shows a good agreement.

6.4.3 Rising bubble

In this numerical example, we consider the test case of the rising bubble inside a 2D cavity of 0.3 m side [150]. A circular bubble of radius 0.05 m is initially placed at the center of the square and surrounded by an incompressible liquid (see Fig. 6.10). The system being initially at rest, the motion of the bubble is driven by the buoyancy force only.

Two test cases are considered, defined by the density ratio ρ_l/ρ_g and the viscosity ratio μ_l/μ_g. Densities and viscosities are summarized in Table 6.3.

Table 6.3: Physical parameters for the rising bubble test cases.

	g	Re	ρ_l/ρ_g	μ_l/μ_g
Case #1	10	10	100	100
Case #2	10	100	1000	100

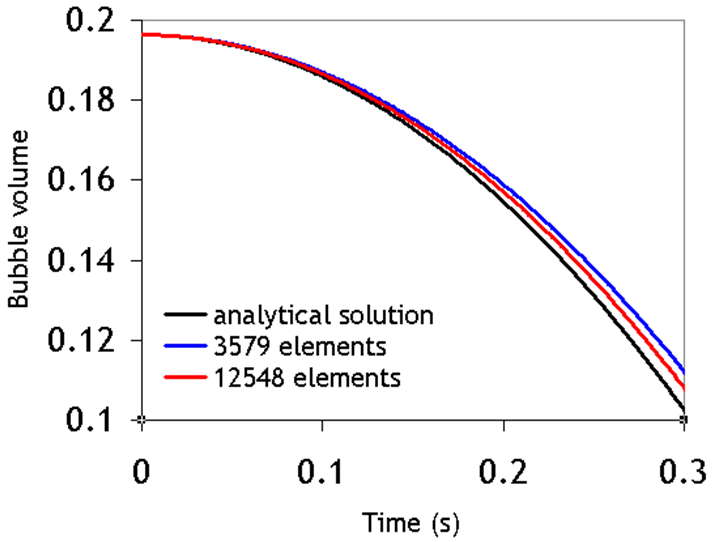

Figure 6.9: Bubble compression: evolution in time of the bubble volume using two meshes

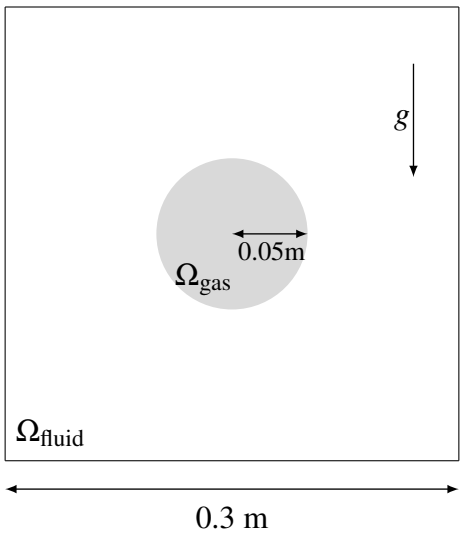

Figure 6.10: Set-up for the rising bubble

Figures 6.11 and 6.12 show the evolution of the bubble shape in time. The obtained results are in good agreement with those obtained by [156]. We can clearly see the impact of using different density and viscosity ratio. It is also worth mentioning that we show additional snapshots of the results until the bubble gets closer to the top wall. Whereas in the literature, comparisons stops at the middle of the cavity. This is mostly due to the use of a dynamic anisotropic mesh adaptation with multi-criteria. Indeed, the interfaces are very well captured and the boundary layers as well as the detachments are automatically detected. This again highlights the capacity of the developed adaptive unified to treat accurately liquid-gas flows.

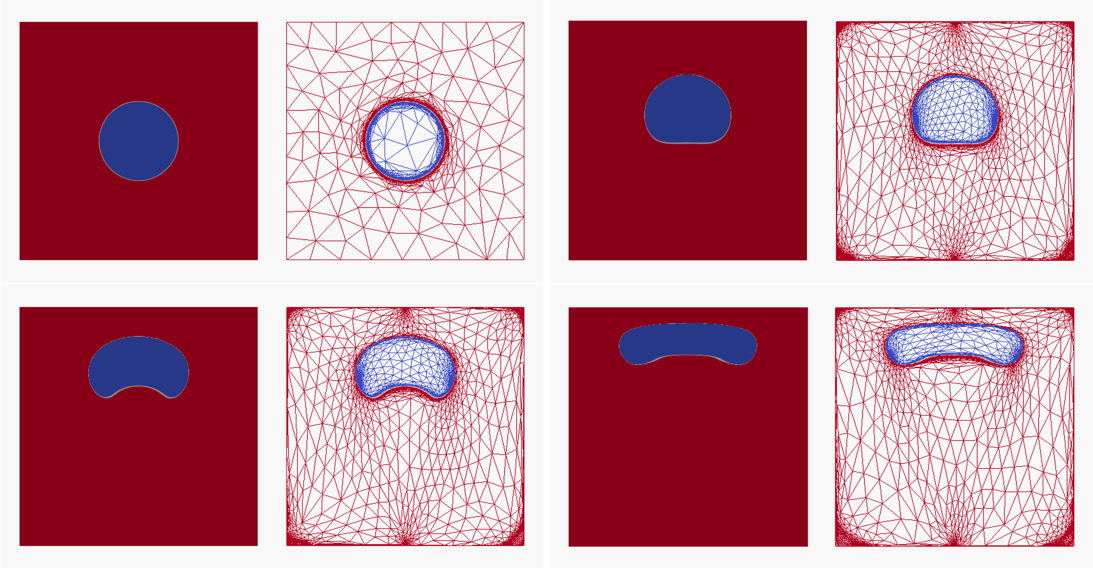

Figure 6.11: Rising bubble #1: Evolution in time of the bubble shape and the mesh.

6.5 Conclusion

We proposed in this chapter a new unified Variational MultiScale method to address easily the coupling between two-phase compressible and incompressible flows. Using a level set function that describes implicitly the interface between the two phases, combined with an edge based error estimator for anisotropic mesh adaptation, it results in a simple and accurate framework that allows simulating liquid-gas flows. All the details to implement the new derived stabilized Finite Element method were presented. Several time-dependent test cases, where the compressibility effects are important, were presented. The numerical results and the comparisons with the literature show that the new solver is able to exhibit good stability and accuracy properties on anisotropic meshes with highly stretched elements.

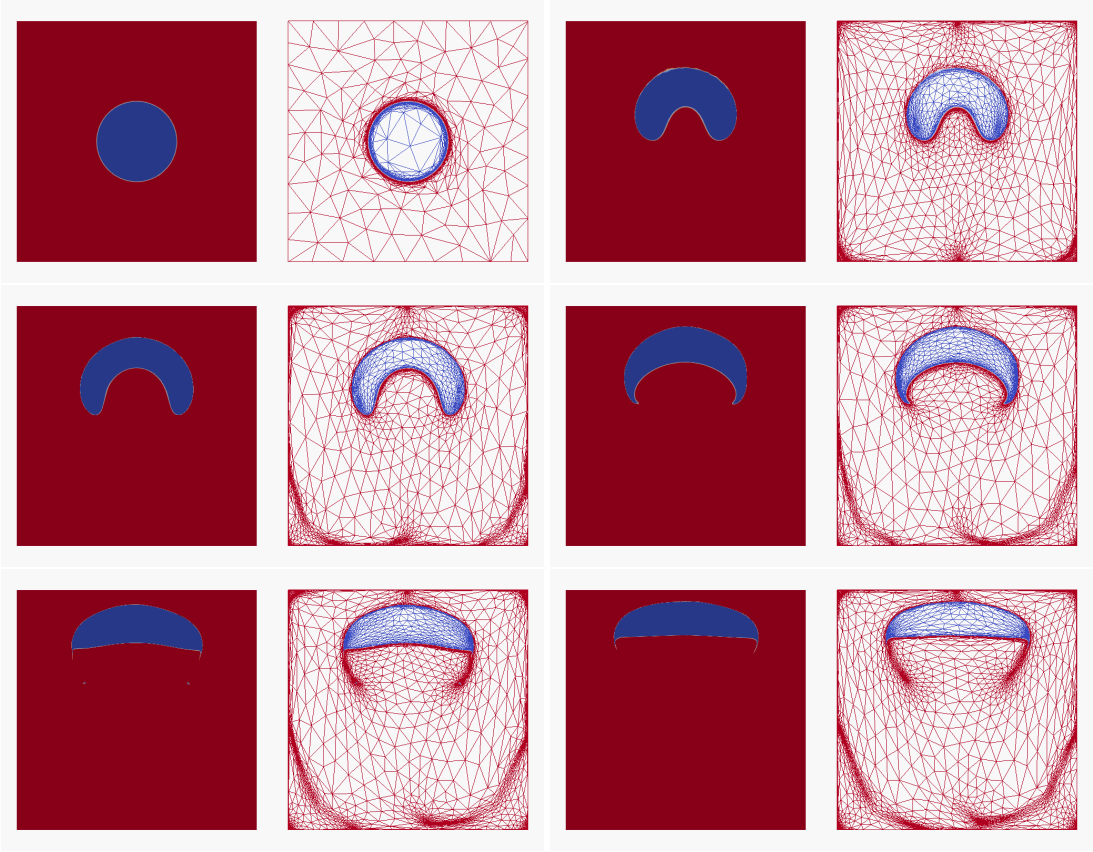

Figure 6.12: Rising bubble #2: Evolution in time of the bubble shape and the mesh.

Résumé en français

Dans ce chapitre, une nouvelle formulation des équations de Navier-Stokes permettant de prendre en compte de manière unifiée une phase compressible et une phase incompressible est présentée. Pour un fluide divariant, l'équation de conservation de la masse est réécrite en fonction de la vitesse, de la pression et de la température en utilisant des variables thermodynamiques dérivées de l'équation d'état utilisée pour la phase compressible. L'implémentation de cette méthode dans le cadre de la méthode VMS est présentée. L'étude de plusieurs cas permet de valider l'approche et la comparaison avec les solutions analytiques ou provenant de la littérature montre la robustesse et la précision de l'approche proposée.

Chapter 7

Boiling multiphase flows: phase change model

Contents

7.1 Introduction

An accurate and robust simulation of the boiling is still an ongoing challenge. Indeed, the complexity of boiling lies in the wide range of scales to consider and in the physics involved. From the nucleation of a vapor bubble to the film boiling, one needs to consider scales from μm to the m. In industrial processes, such as quenching of a solid hot metallic part, the variety of configurations and the complexity of the surrounding flow must be taken into account. Indeed, they have direct impacts on changing mechanical properties, controlling microstructure and releasing residual stresses.

The classical well known methods for thermal treatment of a solid generally refer to the use of experimentally deduced heat transfer coefficients. However, these latter are only useful for a particular configuration in term of geometry, orientation of the surface, range of temperature and flow motion. Therefore, heat transfer coefficients are not suitable to analyze different industrial processes and cannot be generalized to all configurations. Only a direct numerical simulation can take into account all the physics and all the scales involved in boiling.

Therefore an abundant research has been devoted to the simulation of boiling. Several approaches can model such phenomenon. These approaches fall into two categories that depend on the thickness of the interface: sharp interface and diffuse interface. The sharp interface

approach considers the presence of different phases that interact through the interface using boundary conditions. Within this approach, two methods are commonly used. In interface tracking methods, the interface is represented by a set of nodes. This set of nodes moves accordingly to the interface. This requires particular mesh movements at each iteration and also requires a special treatment of complex topological configurations [157, 158, 42, 159]. Interface capturing methods consist in a implicit definition of the interface. A volume fraction (Volume-Of-Fluid) or a signed distance function (Level Set) is convected using a transport equation [160, 161, 162, 163, 164, 165, 166, 167, 168]. These methods are popular due to the simplicity of implementation and the fact that complex topology changes such as the coalescence of bubbles are handled naturally. An excellent literature review of these methods applied to boiling is given by Kharangate and Mudawar in [169]. Other approaches in the literature can be mentioned. Phase-field approaches seem the most promising one [170, 171, 172]. An order parameter is used to distinguish different phases and its evolution gives access to the interface location. The interface is assumed to have a thickness of few nanometers. However, an equation of state is required for the fluid that introduces complexity from a mathematical and numerical point of view. Furthermore, this approach introduces high-order differential terms that are stiff and require innovative discretization techniques.We can also mention the fluid mixtures approaches [173, 174] considering two compressible phases. A complete hyperbolic system is derived using conservation equations for each phase. An equation of state that reproduces the phase diagram is usually required to close the system.

We propose in this work an adaptive Eulerian framework for dealing at the same time with an immersed solid and a fluid experiencing phase change. We follow the different interfaces using a level set method. We propose a pseudo-compressible Variational Multiscale method for the Navier-Stokes accounting for the mass transfer between the phases at the interface. Combined with an a posteriori error estimator for dynamic anisotropic mesh adaptation [27, 54, 109], leading to highly stretched anisotropic elements, it yields an accurate modeling framework for such multiphase flows. It was shown that this framework is very favorable for the simulation of Newtonian flows [37, 68, 175], yield stress fluids [176], compressible and incompressible flows [38]. This framework will be extended in this work to deal with phase change.

7.2 Phase change model

In this section, we derive a pseudo-compressible model accounting for mass transfer at the interface. Such derivation has already be done in the previous work of Denis [43], in the context of finite difference method.

7.2.1 Derivation of the governing equations for the phase change

We recall the Navier-Stokes equations:

$$\rho(\partial_t u + u\cdot\nabla u) - \nabla\cdot(2\mu\varepsilon(u)) + \nabla p = f_{ST} + f \tag{7.1}$$

$$\frac{\partial\rho}{\partial t} + \nabla\cdot(\rho u) = 0 \tag{7.2}$$

where u, p, ρ, μ, f_{ST} and f are the velocity, the pressure, the density, the viscosity, the surface tension force and additional source term of the momentum equation respectively.

The derivation of the model relies on the mixing law used to distribute the density in space. Therefore, we first define a mixing law for the density:

$$\rho = (\rho_v - \rho_l)H(\alpha) + \rho_l \tag{7.3}$$

where H is a Heaviside function defined using a level set function α. The mass conservation in the domain Ω reads:

$$\frac{\partial \rho}{\partial t} + \nabla \cdot (\rho u) = 0 \tag{7.4}$$

We define a mass transfer between the liquid and vapor phases:

$$\frac{\partial}{\partial t}(\rho_v H(\alpha)) + \nabla \cdot (\rho_v H(\alpha) u) = \dot{m}|\nabla \alpha|\delta(\alpha) \tag{7.5}$$

$$\frac{\partial}{\partial t}((1 - H(\alpha))\rho_l) + \nabla \cdot (\rho_l (1 - H(\alpha))u) = -\dot{m}|\nabla \alpha|\delta(\alpha) \tag{7.6}$$

where $\dot{m}$ is the mass transfer rate ($kg \cdot m^{-2} \cdot s^{-1}$).

Developing (7.5) and (7.6) leads to:

$$\rho_v \frac{\partial H(\alpha)}{\partial t} + \rho_v H(\alpha)\nabla \cdot u + \rho_v u \cdot \nabla H(\alpha) = \dot{m}|\nabla \alpha|\delta(\alpha) \tag{7.7}$$

$$-\rho_l \frac{\partial H(\alpha)}{\partial t} + \rho_l (1 - H(\alpha))\nabla \cdot u - \rho_l u \cdot \nabla H(\alpha) = -\dot{m}|\nabla \alpha|\delta(\alpha) \tag{7.8}$$

By dividing (7.7) and (7.8) by their respective density and summing, we obtain the new mass conservation equation:

$$\nabla \cdot u = \dot{m}\left(\frac{1}{\rho_v} - \frac{1}{\rho_l}\right)|\nabla \alpha|\delta(\alpha) \tag{7.9}$$

The velocity is not divergence free since a mass transfer occurs at the interface between the vapor and the liquid.

Summing (7.7) and (7.8) and dividing by $(\rho_v - \rho_l)$ leads to:

$$\frac{\partial H(\alpha)}{\partial t} + u \cdot \nabla H(\alpha) = \frac{\rho}{\rho_l - \rho_v}\nabla \cdot u \tag{7.10}$$

Considering the derivative w.r.t. time of the Heaviside function:

$$\frac{\partial H(\alpha)}{\partial t} = \frac{\partial H(\alpha)}{\partial \alpha}\frac{\partial \alpha}{\partial t} = \delta(\alpha)\frac{\partial \alpha}{\partial t}$$

and the derivative w.r.t. space:

$$\nabla H(\alpha) = \delta(\alpha)\nabla \alpha$$

we obtain:

$$\delta(\alpha)\frac{\partial \alpha}{\partial t} + \delta(\alpha)u \cdot \nabla \alpha = \frac{\rho}{\rho_l - \rho_v}\nabla \cdot u \tag{7.11}$$

Replacing $\nabla \cdot u$ by (7.9):

$$\delta(\alpha)\frac{\partial \alpha}{\partial t} + \delta(\alpha)u \cdot \nabla \alpha = \frac{\rho}{\rho_l - \rho_v}\dot{m}\left(\frac{1}{\rho_v} - \frac{1}{\rho_l}\right)|\nabla \alpha|\delta(\alpha) \tag{7.12}$$

Extending in the whole domain and simplifying, it leads to:

$$\frac{\partial \alpha}{\partial t} + u \cdot \nabla \alpha = \frac{\rho}{\rho_l \rho_v} \dot{m} |\nabla \alpha| \tag{7.13}$$

The level set equation now reads:

$$\frac{\partial \alpha}{\partial t} + \left[u - \frac{\rho}{\rho_l \rho_v} \dot{m} \frac{\nabla \alpha}{|\nabla \alpha|} \right] \cdot \nabla \alpha = 0 \tag{7.14}$$

Neglecting the heat generated by viscosity forces and capillary forces, the energy equation reads:

$$\rho c_p \left(\frac{\partial T}{\partial t} + u \cdot \nabla T \right) - \nabla \cdot (k \nabla T) = - \left(L + (c_p^v - c_p^l)(T - T_{\text{sat}}) \right) \dot{m} \delta(\alpha) |\nabla \alpha| \frac{\rho^2}{\rho_v \rho_l} \tag{7.15}$$

The formulation accounts naturally for the thickness of the mixing law. It is a generic formulation that requires the definition of the mass transfer rate $\dot{m}$.

7.2.2 Derivation of the mass transfer rate

The mass transfer rate is defined using the heat released by a volume V of liquid that has vaporized between the time t and $t + \Delta t$. We consider a domain composed of water and vapor (see Figure 7.1). The position of the interface at the time t is given by $s(t)$.

Figure 7.1: Volume that has vaporized between t and $t + \Delta t$

The heat released Q by a volume V of liquid that has vaporized during the elapsed time between t and $t + \Delta t$ is:

$$Q = \rho V L \tag{7.16}$$

where L is the enthalpy of vaporization (latent heat). The heat fluxes are defined on a surface of area A, respectively in the vapor and the liquid by $\phi_v = -k_v \nabla T_v$ and $\phi_l = -k_l \nabla T_l$:

$$Q = \int_t^{t+\Delta t} \int_A \phi_v \cdot \vec{e_x} + \phi_l \cdot (-\vec{e_x}) dA \, dt \tag{7.17}$$

Dividing by Δt and passing to the limit:

$$\lim_{\Delta t \to 0} \rho L \frac{s(t+\Delta t) - s(t)}{\Delta t} = \lim_{\Delta t \to 0} \frac{1}{\Delta t} \int_t^{t+\Delta t} (-k_v \nabla T_v + k_l \nabla T_l) \cdot \vec{e_x} dt \tag{7.18}$$

We obtain the velocity of the interface, the so-called Stefan condition:

$$\rho L \frac{ds}{dt} = (-k_v \nabla T_v + k_l \nabla T_l) \cdot \vec{e}_x \tag{7.19}$$

Eq. (7.19) requires the evaluation of the balance of fluxes at the interface. This evaluation is not straightforward when using an implicit definition of the interface. We therefore propose an approximation of this balance of fluxes using a delta Dirac function. Approximating the surface integral by mean of a delta Dirac function leads to:

$$Q = \int_t^{t+\Delta t} \left(\int_V \delta(\alpha) \left(\phi_v \cdot \vec{e}_x + \phi_l \cdot (-\vec{e}_x) \right) dV \right) dt = \int_t^{t+\Delta t} \left(\int_V \delta(\alpha) \left(-k_v \nabla T_v + k_l \nabla T_l \right) \cdot \vec{e}_x dV \right) dt \tag{7.20}$$

Passing to the limit:

$$\lim_{\Delta t \to 0} \rho L \frac{s(t+\Delta t) - s(t)}{\Delta t} \int_V \delta(\alpha) dV = \lim_{\Delta t \to 0} \frac{1}{\Delta t} \int_t^{t+\Delta t} \left(\int_V \delta(\alpha) \left(-k_v \nabla T_v + k_l \nabla T_l \right) \cdot \vec{e}_x dV \right) dt \tag{7.21}$$

We obtain the velocity of the interface for an implicit interface, without any interpolation:

$$\rho L \frac{ds}{dt} = \frac{\int_V \delta(\alpha) \left(-k_v \nabla T_v + k_l \nabla T_l \right) \cdot \vec{e}_x dV}{\int_V \delta(\alpha) dV} \tag{7.22}$$

7.3 Variational Multiscale method for phase change

Following the developments from previous sections, we generalize the Navier-Stokes equations, into:
Find the velocity u and the pressure p such that:

$$\rho(\partial_t u + u \cdot \nabla u) - \nabla \cdot (2\mu\varepsilon(u)) + \nabla p = f_{ST} + f \tag{7.23}$$

$$\nabla \cdot u = f_c \tag{7.24}$$

where ρ, μ, f_{ST}, f and f_c are the density, the viscosity, the surface tension force, additional source term of the momentum equation and the source term of the continuity equation respectively.

Recall that the surface tension is defined by:

$$f_{\mathrm{ST}} = -\gamma\kappa\delta\mathrm{n} - \gamma\delta\Delta t \left(\frac{\partial^2 \mathrm{u}}{\partial \mathrm{n}^2} + \kappa \frac{\partial \mathrm{u}}{\partial \mathrm{n}} - \nabla^2 \mathrm{u}^{n+1} \right) \tag{7.25}$$

To simplify the notation, we use f_m and f_c as the source terms in (7.23)-(7.24), adding the explicit terms of (7.25) into f_m. Inserting the expression for the subscales, we finally obtain the stabilized Finite Element problem. The new variational formulation reads:

Coarse scale

$$\begin{cases} (\rho\partial_t(u_h + \tilde{u}), v_h) + (\rho(u_h + \tilde{u}) \cdot \nabla(u_h + \tilde{u}), v_h) - (p_h + \tilde{p}, \nabla \cdot v_h) \\ + (2\mu\varepsilon(u_h) : \varepsilon(v_h)) + (\gamma\delta\Delta t \nabla(u_h + \tilde{u}) : \nabla v_h) = (f_m, v_h) \quad \forall v_h \in V_{h,0} \\ (\nabla \cdot (u_h + \tilde{u}), q_h) = (f_c, q_h) \quad \forall q_h \in Q_h \end{cases} \tag{7.26}$$

Fine scale

$$\begin{cases} (\rho\partial_t(u_h+\tilde{u}),\tilde{v})+(\rho(u_h+\tilde{u})\cdot\nabla(u_h+\tilde{u}),\tilde{v})-(p_h+\tilde{p},\nabla\cdot\tilde{v}) \\ +(2\mu\varepsilon(\tilde{u}):\varepsilon(\tilde{v}))+(\gamma\delta\Delta t\nabla(u_h+\tilde{u}):\nabla\tilde{v}) \quad = \quad (f_m,\tilde{v}) \quad \forall\tilde{v}\in\tilde{V} \\ (\nabla\cdot(u_h+\tilde{u}),\tilde{q}) \quad = \quad (f_c,\tilde{q}) \quad \forall\tilde{q}\in\tilde{Q} \end{cases} \tag{7.27}$$

By substituting the small scale variables into the coarse scale equations, and applying integration by parts, the system to solve becomes finally:

$$\begin{cases} (\rho\partial_t u_h,v_h)+(\rho u_h^c\cdot\nabla u_h,v_h)-(p_h,\nabla\cdot v_h)+(2\mu\varepsilon(u_h):\varepsilon(v_h))+(\gamma\delta\Delta t\nabla u_h:\nabla v_h) \\ -\sum_{K\in\mathscr{T}_h}\left(\tau_u R_u\,,\rho u_h^c\cdot\nabla v_h\right)-\sum_{K\in\mathscr{T}_h}(\tau_c R_c,\nabla\cdot v_h) \quad = \quad (f_m,v_h) \quad \forall v_h\in V_{h,0} \\ (\nabla\cdot u_h,q_h)-\sum_{K\in\mathscr{T}_h}(\tau_u R_u,\nabla q_h) \quad = \quad (f_c,q_h) \quad \forall q_h\in Q_h \end{cases} \tag{7.28}$$

where R_u and R_c are the residuals defined by:

$$\begin{aligned} R_u &= f_m-\rho\partial_t u_h-\rho u_h^c\cdot\nabla u_h-\nabla p_h \\ R_c &= f_c-\nabla\cdot u_h \end{aligned} \tag{7.29}$$

7.4 Numerical test cases

In this section, two well known benchmark will be used to asses the validity of the approach developed in this chapter. The results obtained with the proposed approach are then compared with either analytical solutions or with results obtained by other approaches found in the literature. Some test cases cannot be handled using classical model in particular for high property ratios and this will be the opportunity to demonstrate the benefit of adaptive VMS formulation.

7.4.1 Stefan problem

First, we consider the one-dimensional Stefan benchmark. It is a well known problem and serves as a benchmark to assess the accuracy of phase change models [160, 163, 177]. It is defined schematically in Figure 7.2. The domain is initially filled with water. The temperature at the wall is set constant and higher to the saturation temperature. The water is at saturation temperature. At $t>0$, a phase change occurs and induces a motion of the interface between the vapor and the water. The convective term in the energy conservation equation is neglected in both phases.

The position of the interface is given by:

$$s(t)=2\chi\sqrt{\alpha_v t} \tag{7.30}$$

The temperature in the vapor at a given time t is given by:

$$T(x,t)=T_{\text{wall}}+\frac{T_{\text{sat}}-T_{\text{wall}}}{\text{erf}(\chi)}\,\text{erf}\left(\frac{x}{2\sqrt{\alpha_v t}}\right) \tag{7.31}$$

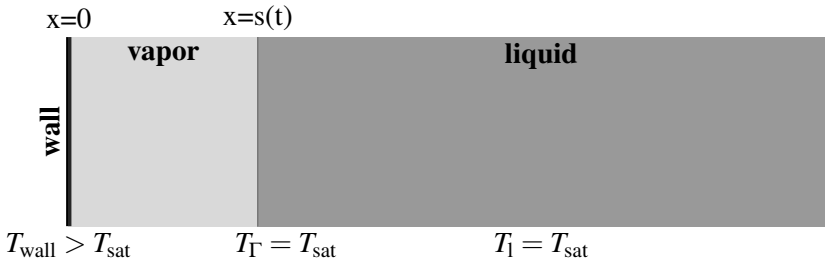

Figure 7.2: Initial setup for the classic Stefan problem.

where α_v is the thermal diffusivity defined by $\alpha = k_v/(\rho_v c_p^v)$ and s is the position of the interface. If the temperature in the liquid is constant, we find the following transcendental equation describing the evolution of the interface:

$$\frac{T_{sat} - T_w}{\sqrt{\pi} L} c_p^v = \chi \, \mathrm{erf}(\chi) \exp\left(\chi^2\right) \tag{7.32}$$

We consider the physical properties for the water and the vapor given in Table 7.1 and we consider $T_w - T_{sat} = 10$K. We solve the transcendental equation using a Newton algorithm to find the value of χ.

Figure 7.3 shows the evolution of the position of the interface for both the analytical and the numerical solution having good agreement.

Table 7.1: Density, dynamic viscosity, specific heat and thermal conductivity for the vapor and the water at atmospheric pressure

	ρ [kg/m^3]	μ [Pa·s]	c_p [J/(kg·K)]	k [W/(m·K)]	L_{sat} [J/kg]
Vapor	0.597	1.26×10^{-5}	2030	0.025	
Water	958.4	2.8×10^{-4}	4216	0.679	2.26×10^6

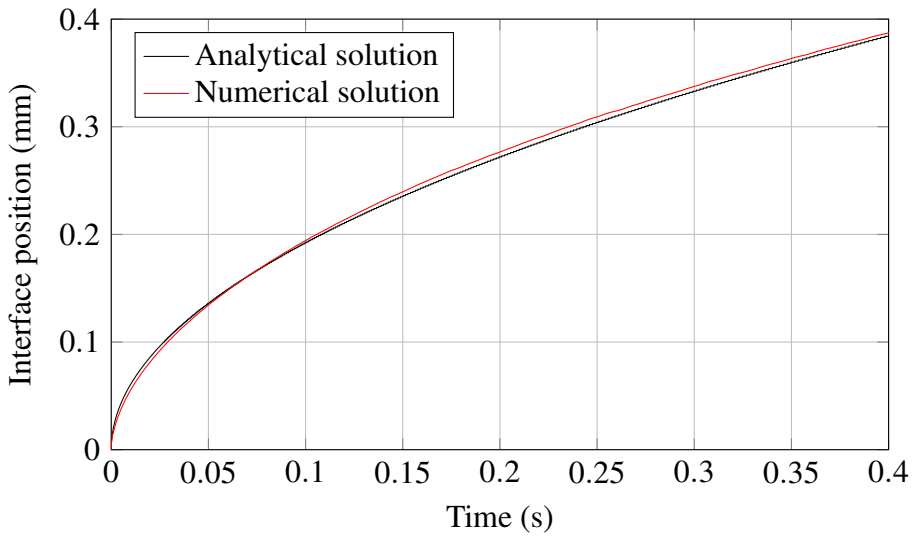

Figure 7.3: Evolution of the interface position for the Stefan problem

Figure 7.4 shows that the use of a delta Dirac function to compute the mass transfer rate results in a better convergence. This comparison was done by prescribing a maximum number of iteration (3000) to reach a residual (10^{-7}) using the GMRES method for the resolution of the linear system.

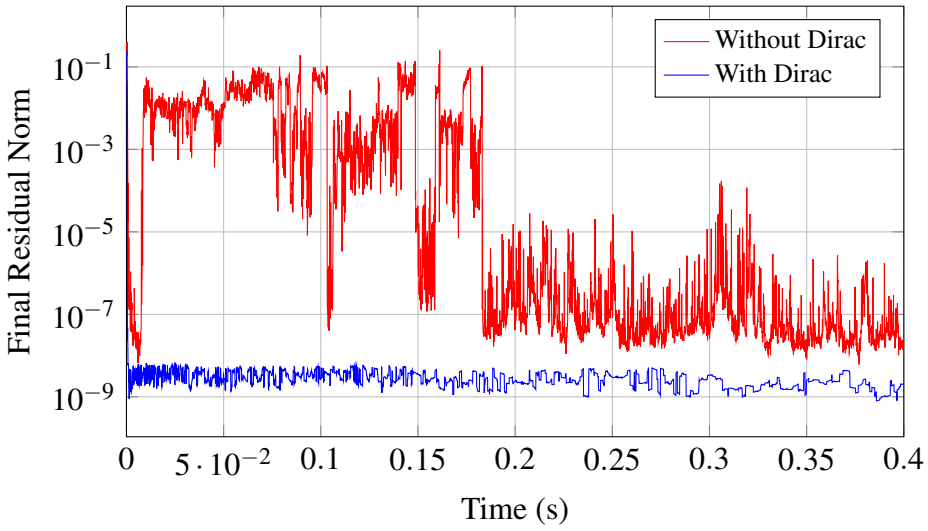

Figure 7.4: Final residual norm for the level set solver.

7.4.2 2D Film boiling

This test case serves as a validation for the phase change model in several articles [157, 160, 178]. Indeed, when the temperature at the wall is much greater than the saturation temperature, a persistent layer of vapor forms and remains between the wall and the water. This regime is known as film boiling. In the configuration depicted in Figure 7.5, a Rayleigh-Taylor instability is triggered due to the low density fluid below the high density fluid. Furthermore, the phase change will induce a growth of the film, amplifying the instability.

For a Rayleigh Taylor instability, the most unstable Taylor wavelength is in 2D:

$$\lambda_0 = 2\pi \left(\frac{3\gamma}{(\rho_l - \rho_g)g} \right)^{1/2} \tag{7.33}$$

where γ is the surface tension.

The physical parameters taken from [160] are given in Table 7.2. For this set of parameters, the most unstable wavelength is about $\lambda_0 \approx 0.078$m. Figure 7.5 shows the initial profile of the interface, defined by the following function:

$$y = 0.5 + 0.4\cos(2\pi x/\lambda_0) \tag{7.34}$$

Two cases will be studied. For the first case, the temperature at the wall is maintained constant at a temperature of 5K above the saturation temperature and for the second, 10K.

To assess the accuracy of the computations, the authors in [157, 160, 178] used space-averaged Nusselt number obtained from the numerical simulation and compare it to correlation found in the literature. The local Nusselt number defined as the dimensionless heat flux through the wall is:

$$N_{\mathrm{u}} = \frac{\lambda_0}{T_w - T_{\mathrm{sat}}} \frac{\partial T}{\partial y}\bigg|_{y=0} \tag{7.35}$$

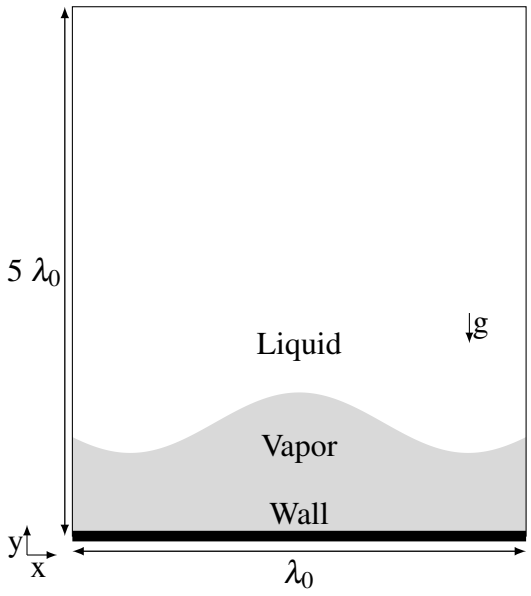

Figure 7.5: Setup for the 2D film boiling

Regarding the correlation of the Nusselt number in the literature, we use the correlation of Berenson [179] and Klimenko [180] given by:

$$Nu_B = 0.425(GrPr/Ja)^{1/4} \tag{7.36}$$

and:

$$Nu_K = 0.1691(GrPr/Ja)^{1/3} \text{ for } Ja < 0.71 \tag{7.37}$$

where the Grashof number $Gr = \rho_v(\rho_l - \rho_v)g\lambda_0/\mu_v^2$ represents the ratio of the buoyancy force over the viscous force, the Prandtl number $Pr = \mu_v c_p^v/k_v$ represents the ratio of the momentum diffusivity over the thermal diffusivity and the Jakob number $Ja = c_p^v(T_w - T_{\text{sat}})$ the ratio of sensible heat over latent heat.

Table 7.2: Density, dynamic viscosity, specific heat and thermal conductivity for the vapor and the water at atmospheric pressure

	ρ [kg/m^3]	μ [Pa·s]	c_p [J/(kg·K)]	k [W/(m·K)]	L_{sat} [J/kg]
Vapor	5.0	0.005	200	1.0	
Water	200	0.1	400	40	10^4

Figure 7.6 shows the evolution of the temperature field and the interface for $\Delta T = 10K$. The vapor film grows to a mushroom shape due to the Rayleigh-Taylor instability. Since we performed 2D computations, no break up occurs due to surface tension. Therefore the mushroom cap rises along the channel followed by a long and thin filament. Notice that due to the width of the channel, there is clearly an effect of the lateral confinement on the shape of the vapor mushroom. Figure 7.7 shows the evolution of the mesh. The mesh is adapted using the anisotropic mesh adaptation procedure presented in this paper, using only 25,000 elements. Therefore the mesh is very fine at the vapor/water interface and at the bottom when the thermal gradient is the highest. The mesh remains coarse far from the interface, where the thermal gradient is null and the velocity field is still 0.

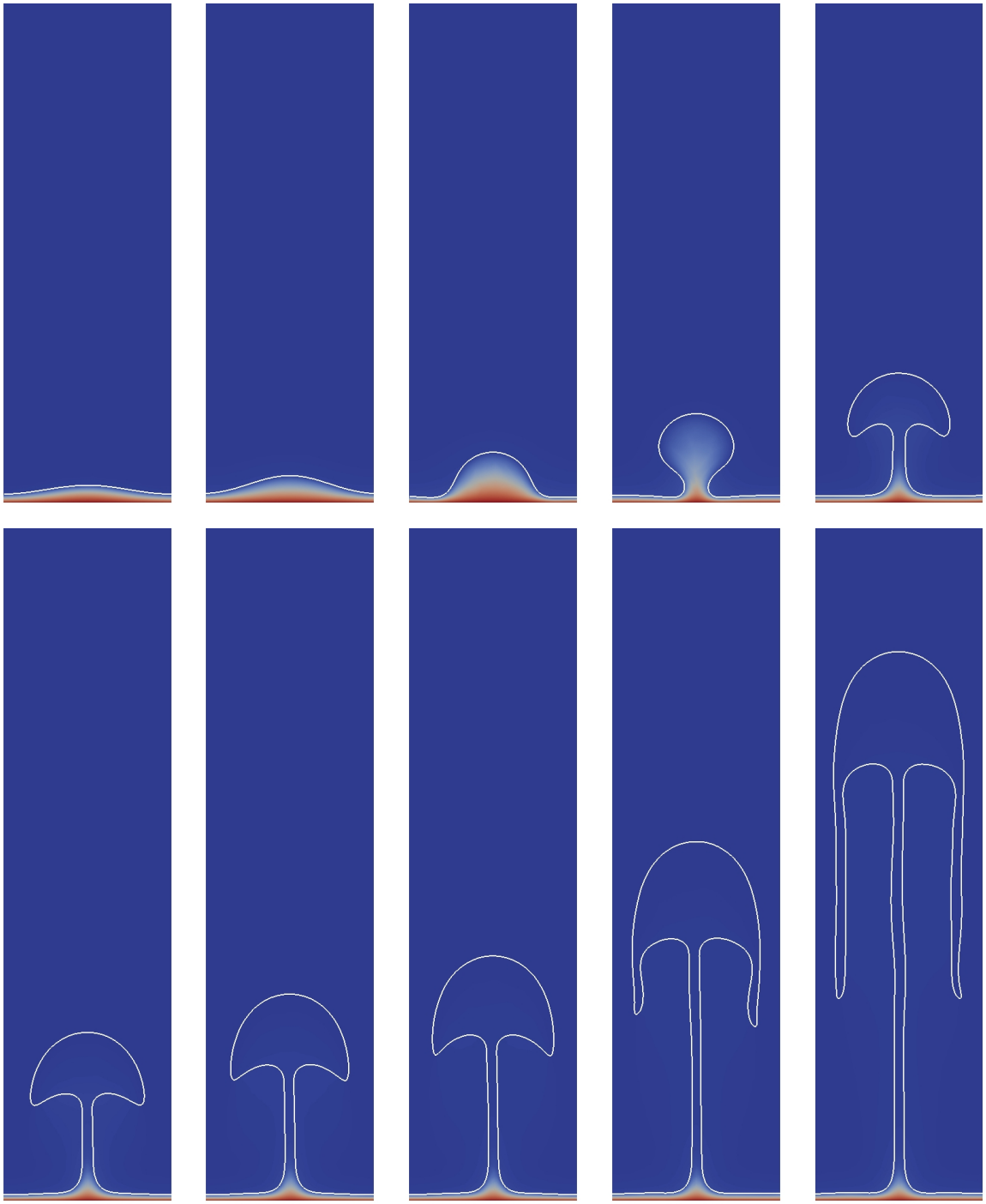

Figure 7.6: 2D Film boiling for $\Delta T = 10K$. Temperature field and interface location at t=0.01, 0.1, 0.2, 0.3, 0.4, 0.5, 0.6, 0.7, 1.0 and 1.5s. The interface is represented by the white line.

The evolution of the space-averaged Nusselt number is depicted in Figure 7.8. The comparison with the correlation of Berenson and Klimenko shows a good agreement for both cases.

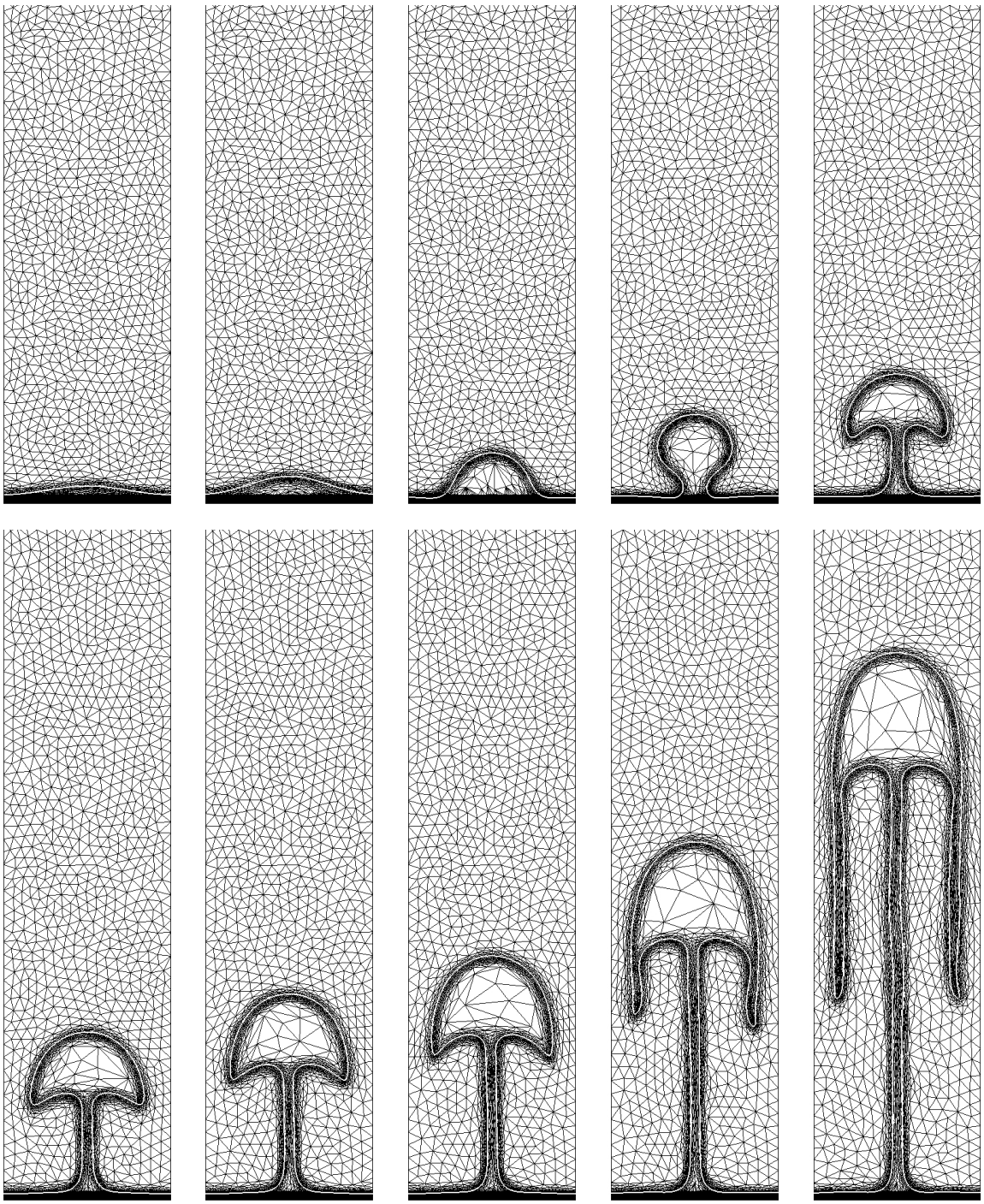

Figure 7.7: 2D Film boiling for $\Delta T = 10K$. Evolution of the mesh and the interface location at t=0.01, 0.1, 0.2, 0.3, 0.4, 0.5, 0.6, 0.7, 1.0 and 1.5s. The interface is represented by the white line.

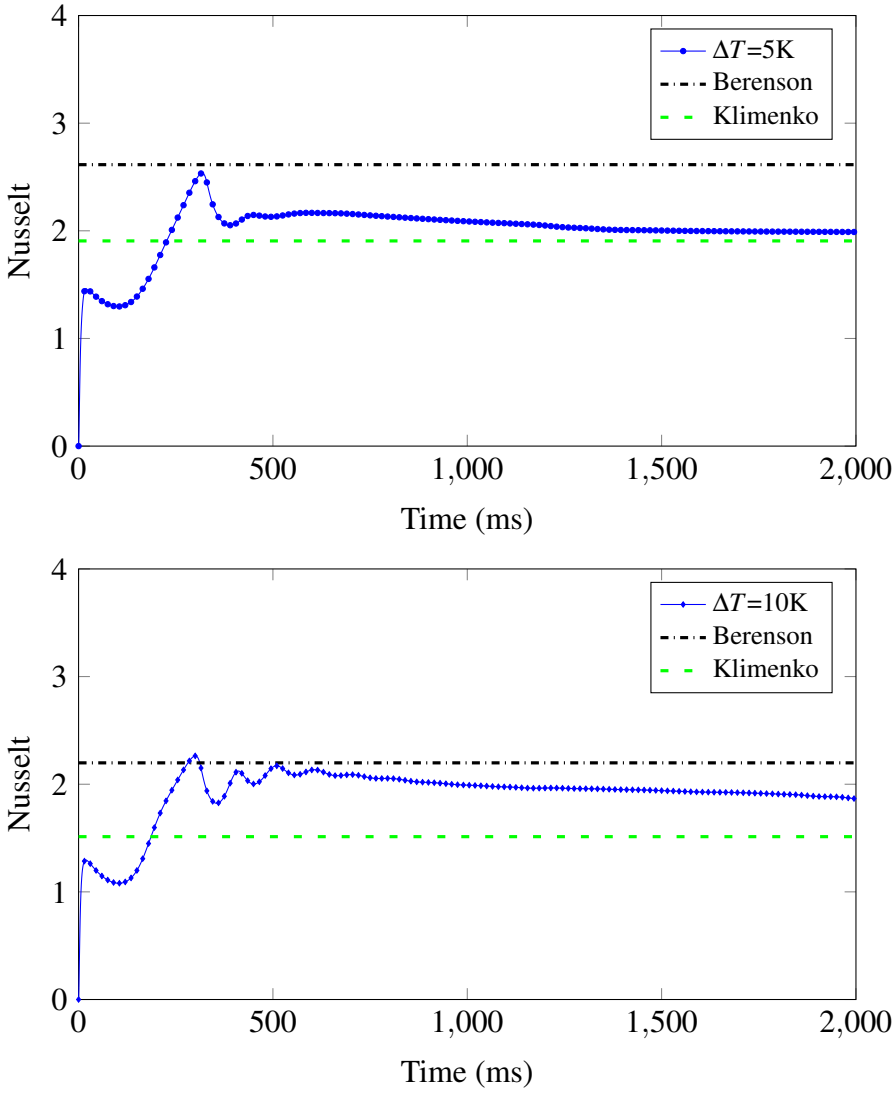

Figure 7.8: Evolution of the space-averaged Nusselt number for $\Delta T = 5K$ (top) and $\Delta T = 10K$ (bottom).

7.5 Conclusion

We proposed in this chapter a new Eulerian framework for the numerical simulation of phase change. A Variational Multiscale Finite Element formulation for the Navier-Stokes equation taking into account the transfer of mass occurring during the phase change is presented. The dynamics of the vapor phase is given by the surface tension, implemented in a semi-implicit way to circumvent the usual severe capillary time step restriction. We have demonstrated the efficiency of this adaptive framework by performing validation test cases in 2 dimensions. More challenging computations, including comparison with experimental data are performed in the next chapter. We will show that the direct numerical simulation of industrial water quenching using the approach developed in this chapter can be performed accurately.

Résumé en français

Le changement de phase dans le cas diphasique nécessite le développement d'un modèle permettant de décrire l'échange de masse et d'énergie entre deux phases. Les équations de Navier-Stokes prenant en compte de tels échanges sont dérivées dans ce chapitre. Ainsi, l'équation de conservation de la masse, de l'énergie et de transport de la fonction level set sont complétées par des termes dépendant d'un taux de transfert de masse. Cette nouvelle quantité est déterminée à l'aide d'un modèle quasi-statique dérivé du problème de Stefan. La modification des équations dans le cadre VMS est montrée et la validation de ce modèle est faite pour des problèmes avec solution analytique ou des problèmes avec corrélation expérimentale.

Chapter 8

Industrial applications

Contents

8.1 Context

In the previous chapters of this thesis, all the components of the new numerical framework have been introduced. We recall that one main objective of this work is to be able to simulate 3D industrial processes taking into account the direct solid-liquid-vapor interactions.

However, in this thesis we did not explore the thermomechanical behavior and characteristic of the solid part. Indeed, most of the metallic alloys experience phases transformation, meaning that the microstructure of the material is inhomogeneous in the part due to the difference of cooling rate in the different area of a part. This leads to variation, sometimes large, of the thermal and mechanical properties of the solid. These analyses are well covered by different research groups at CEMEF and in particular through the well-known software Forge. But until recently, the quenching environment was simply replaced by experimentally deduced transfer coefficients. This makes any simulation generally limited and suffers from systematic re-validation when facing new materials, new geometries or new thermomechanical conditions.

In this chapter, we will highlight further this issue and will show how the new developments in all the previous chapters make this novel Eulerian adaptive framework very efficient to simulate 3D boiling and phase change inside quench water tanks. To do so, several test cases will be presented that allow us to investigate easily different quenching parameters such as orientation, geometry, positioning and to deal with different quenching processes.

First we will consider the quenching of a solid and comparison to unclassified experimental data to validate the proposed numerical tools. It will enable to assess the accuracy and robustness of the proposed approach to help us closing the bridge between experiment and numerical simulation.

Then we will move on more challenging configurations with different quenching parameters. We increase the size of the part and consider different geometries. This will show the

ability of the proposed innovative numerical framework to be a predictive tool for manufacturers.

Finally we consider an extreme challenging case, the water jet cooling. It consists in projecting at high velocity a water jet to cool down a part. This process aims at avoiding the formation of a vapor film counting on high convective regime. To the best of the author's knowledge, such 3D validations and simulations have never been performed.

8.2 Quenching of a solid and comparison to experimental data

We will now consider the quenching of a solid into water. We consider a domain of size $0.60 \times 0.60 \times 0.40$ m^3, three-quarters full of water, in which a metallic sample, made of Inconel 718 alloy, of dimension $0.075 \times 0.075 \times 0.0015$ m^3, is immersed (see Figure 8.1). The temperature of the sample is $T_{\text{solid}} = 880°C$ and the temperature of the water is $T_{\text{water}} = 25°C$. A thermocouple is placed at the core of the metallic sample. From a practical point of view, due to the small thickness of the part, the temperature at the core reflects the behavior of the temperature field at the interface.

A free slip boundary condition is prescribed on all the walls. The motion of the vapor film is due to the buoyancy force and the surface tension force. The simulations are performed using the proposed adaptive meshing technique with 100,000 tetrahedra and then $200,000$ tetrahedra. The time step is set to $\Delta t = 0.002s$.

All the physical parameters related to each phase are presented in Table 8.1.

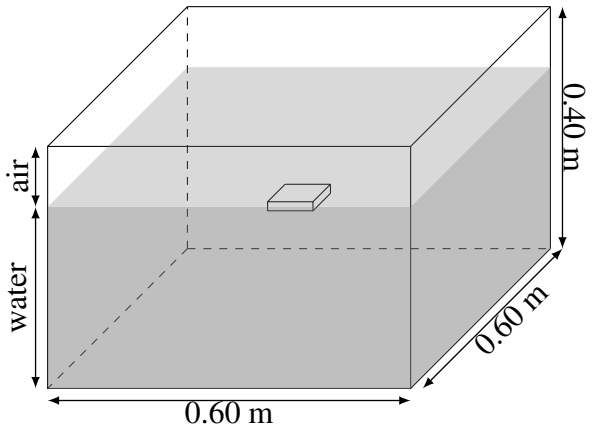

Figure 8.1: Set-up for the 3D industrial quenching

Table 8.1: Initial physical parameters for the 3D industrial quenching

	ρ [kg/m^3]	μ [Pa·s]	c_p [J/(kg·K)]	k [W/(m·K)]	L_{sat} [J/kg]
Vapor	1.0	1.2×10^{-5}	2010	0.025	2.26×10^6
Water	1000	1.0×10^{-3}	4185	0.6	
Solid	8000		435	11.4	

The evolution of the liquid-vapor phase is depicted in Figure 8.2 and shows again the ability of the proposed framework with adaptive meshing to deal with such challenging test case.

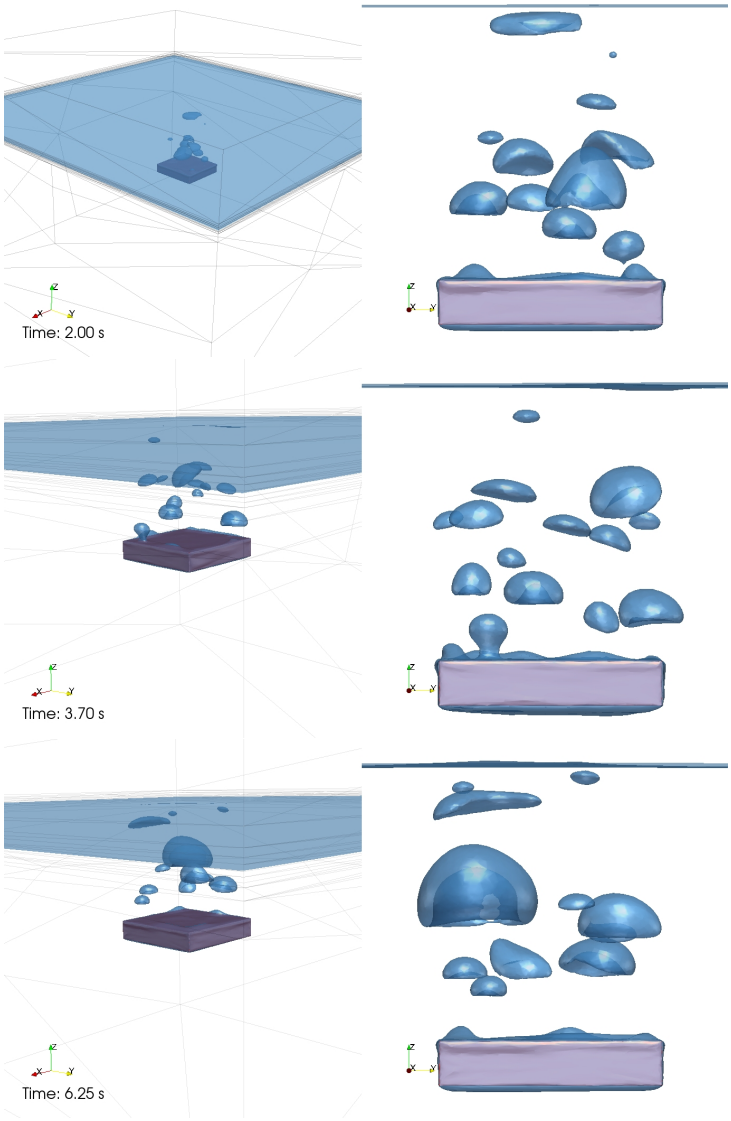

Figure 8.2: Industrial quenching. Results at t=2, 3.70 et 6.25 s. Perspective view (left), front view (right). The zero isovalue of the level set is represented in blue.

Figure 8.3 represents a clip of the quenching tank. Water is depicted in blue and the solid in red. A slice enables to visualize the adaptive mesh over time. At the top left corner, the picture shows the initial mesh, mostly concentrated around the part and the free surface. As the simulation starts and bubbles form, the mesh is adapted automatically according to the level set interface but also the velocity and the temperature. Under the constraint of a fixed number of elements, one can notice that the mesh is coarsened automatically at the bottom of the tank, where the variation of the solution is small.

Finally, Figure 8.4 shows a good agreement for the temperature evolution between the experimental data and the numerical simulation without the need to adjust the physical paramaters. Moreover, the strong coupling between the solid, the water and the vapor enables to perform such simulation without the use of a heat transfer coefficient at the solid boundaries. The anisotropic mesh adaptation enables to capture the high thermal gradient as well as the

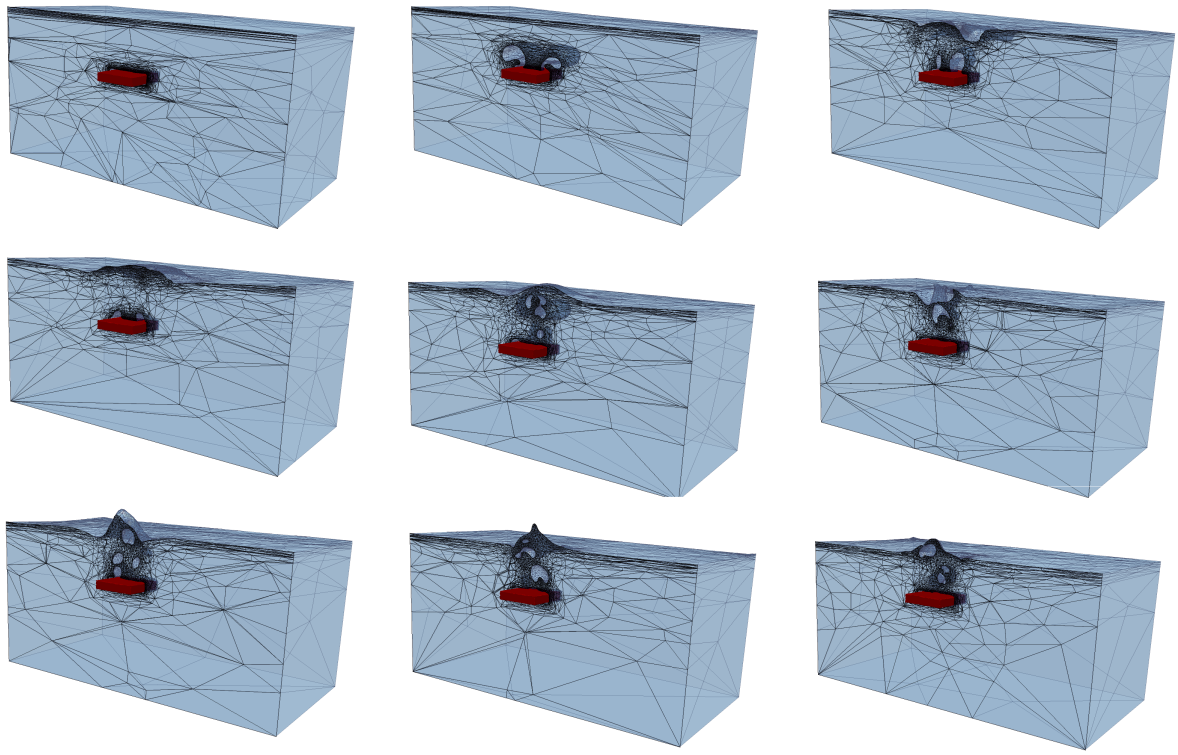

Figure 8.3: Industrial quenching: Results at different time. The solid is represented in red. A clip of the quenching tank, with visible adapted mesh.

complexity of the flow.

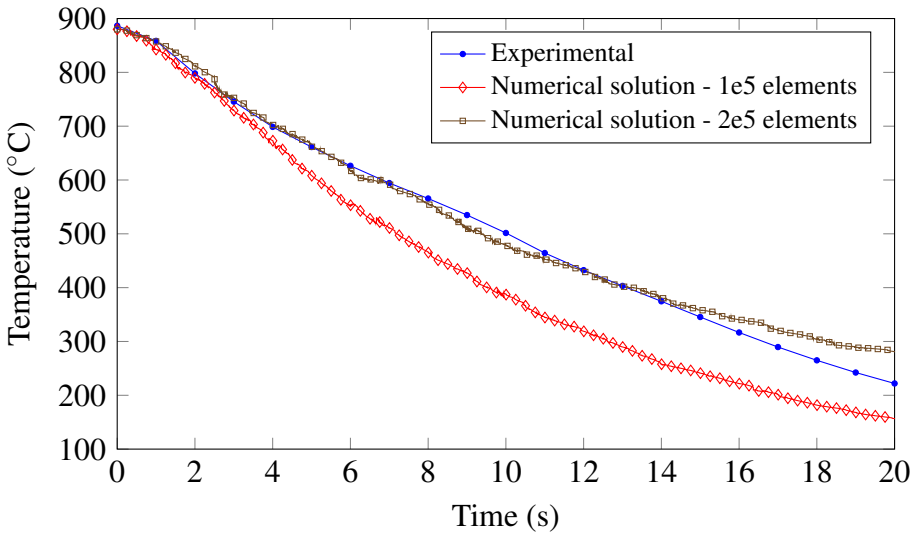

Figure 8.4: Evolution of the temperature at the core of the sample.

8.3 Numerical quenching water tank

Several studies show that heat transfer at the surface of quenched part is dependent on different parameters: orientation, position, shape and size, agitation rate, fluid viscosity, and other variables. In this test case, we will analyze at least the first three parameters. The objective is to show that the physical phenomena taking place are complex and that the experimental investigation remains generally limited. Indeed, the latter suffers from systematic revalidation of heat transfer coefficients when dealing with each parameter. Numerical simulation provides some insight of the effects of each quenching parameter.

To achieve this purpose, we consider a water tank of dimension $L \times L \times L$ (see Figure 8.5), filled to three quarters. Two geometries are proposed; a hot metallic cylinder of length 0.5m and diameter 0.1m with L=1m and a hot hollow cylinder (see Figure 8.9) of inner radius 3cm and outer radius of 6cm with L=0.40m.

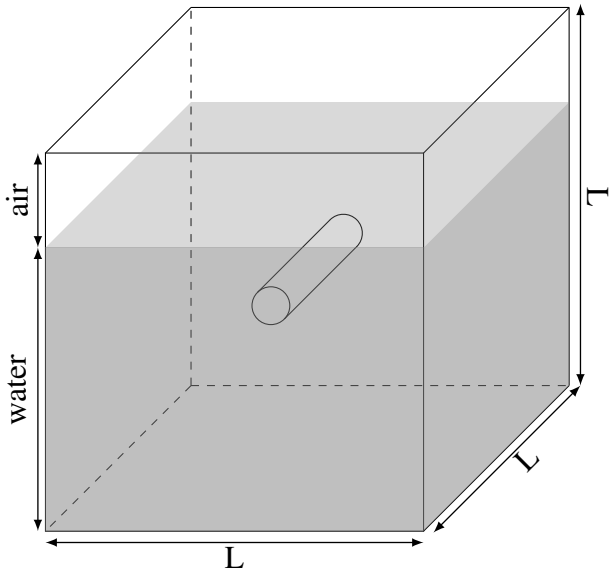

Figure 8.5: Set-up for the 3D film boiling.

For the first geometry, three different configurations are considered. The cylinder is immersed horizontally at mid-height (see Figure 8.6), at a quarter of the height of the tank (see Figure 8.7) or vertically (see Figure 8.8).

Figure 8.6 shows a persistent vapor film surrounding the cylinder. As expected, the position of the cylinder has an important effect on the film evolution and thus on the cooling velocity of the cylinder. Furthermore, such distance from the cylinder to the free surface has a direct impact on the overall flow inside the quenching bath. The larger the distance, the larger the velocity of the vapor phase breaking up at the surface.

Whereas, when the cylinder is immersed vertically inside the water tank, the shape of the film is totally different. Indeed, we can notice in Figure 8.8 a periodic release of the film all along the surface. Thus, the distribution of the flow is more concentrated in the upper part of the cylinder. This is due to the vaporization of water nearby but also due to the rise of vapor from the lower part of the cylinder. Therefore this induces lower cooling velocity when compared to the previous case. Information of this kind usually requires a thorough knowledge of hydrodynamic theory. It is worth mentioning that most of quenching tanks do not enable to get an inside view of the process, except from the free surface.

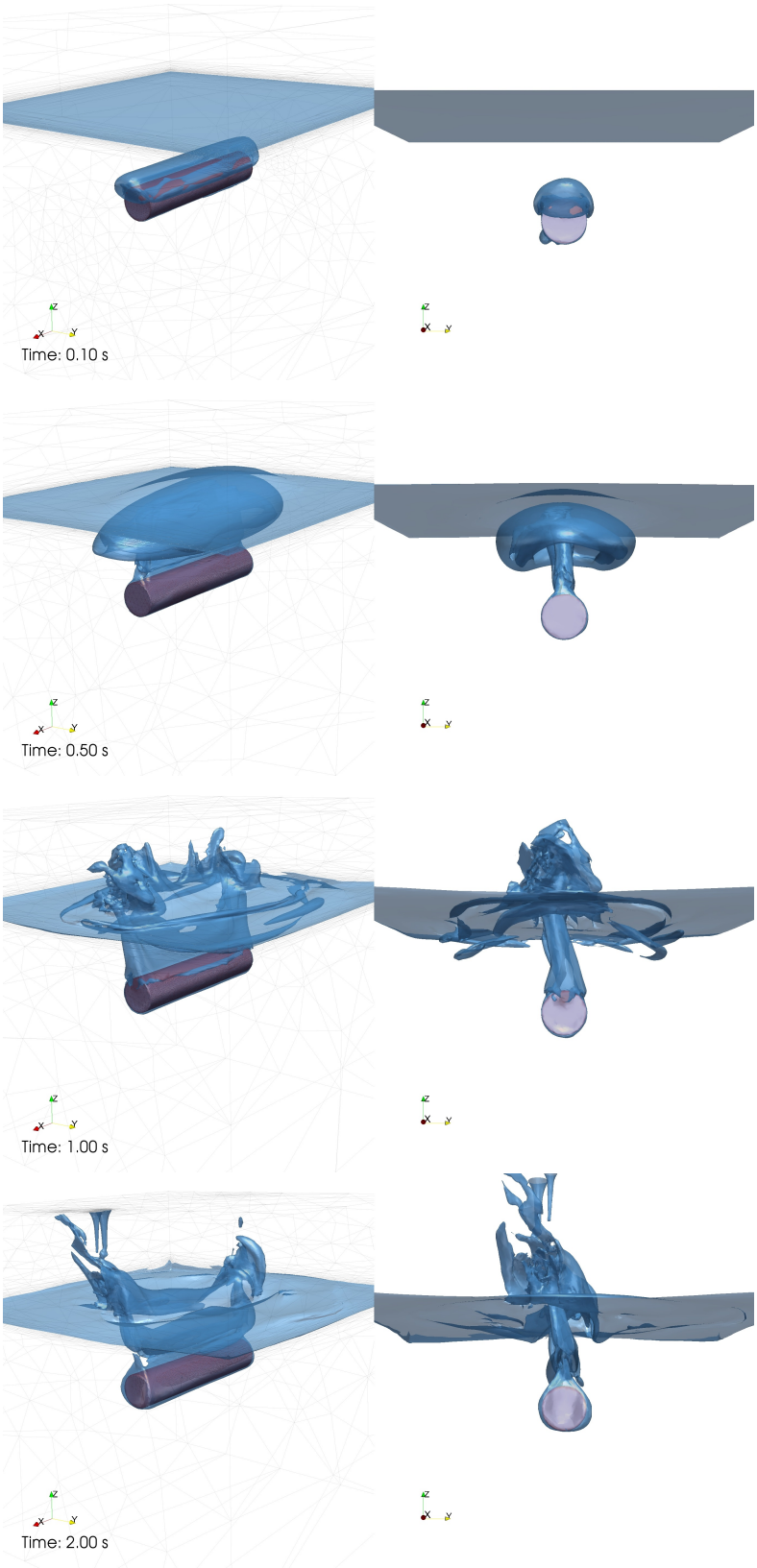

Figure 8.6: Cylinder at mid-height. Results at t=0.1, 0.5, 1 and 2 s. Perspective view (left), front view (right).

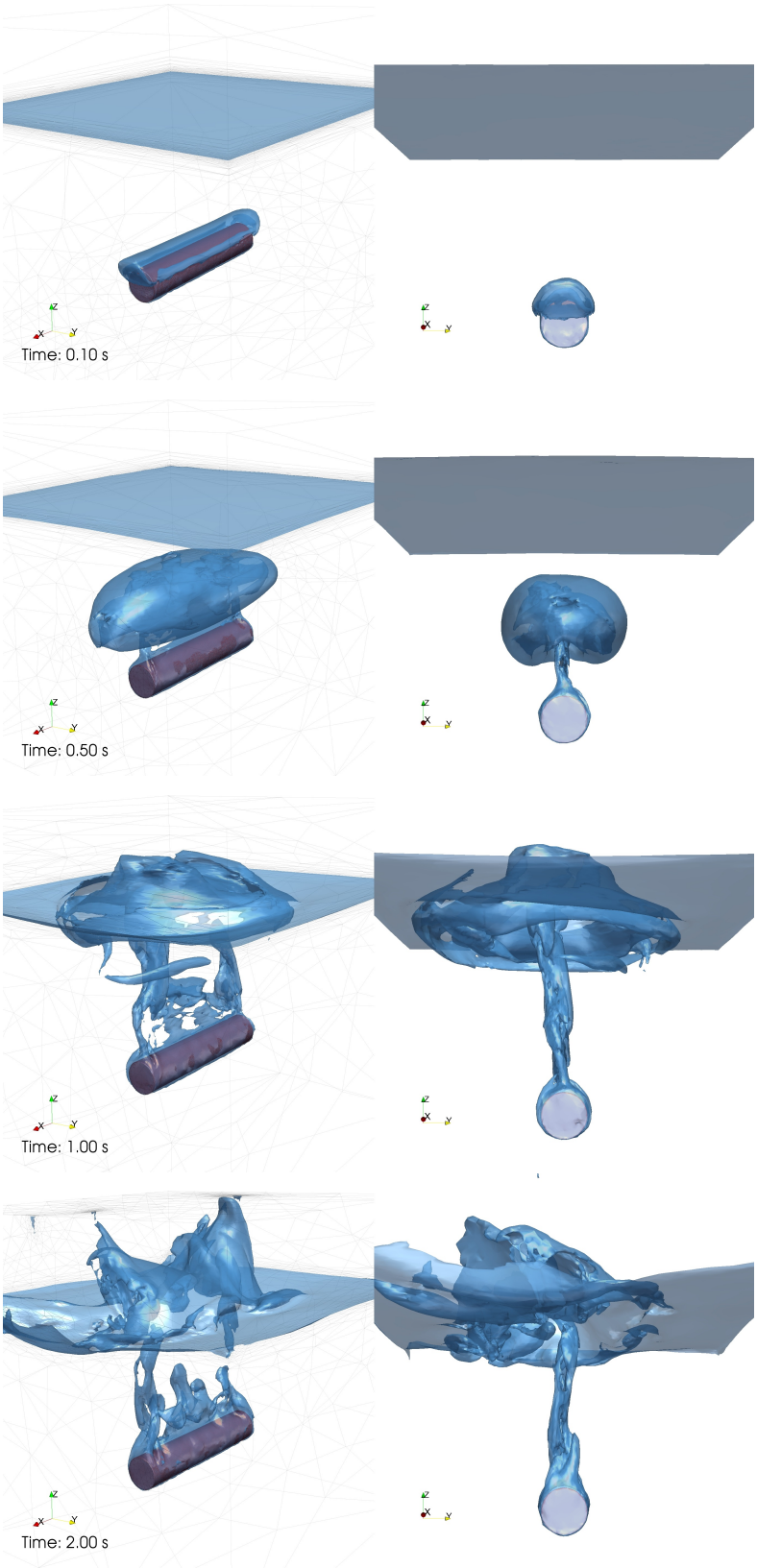

Figure 8.7: Cylinder at a quarter of the height. Results at t=0.1, 0.5, 1 and 2 s. Perspective view (left), front view (right).

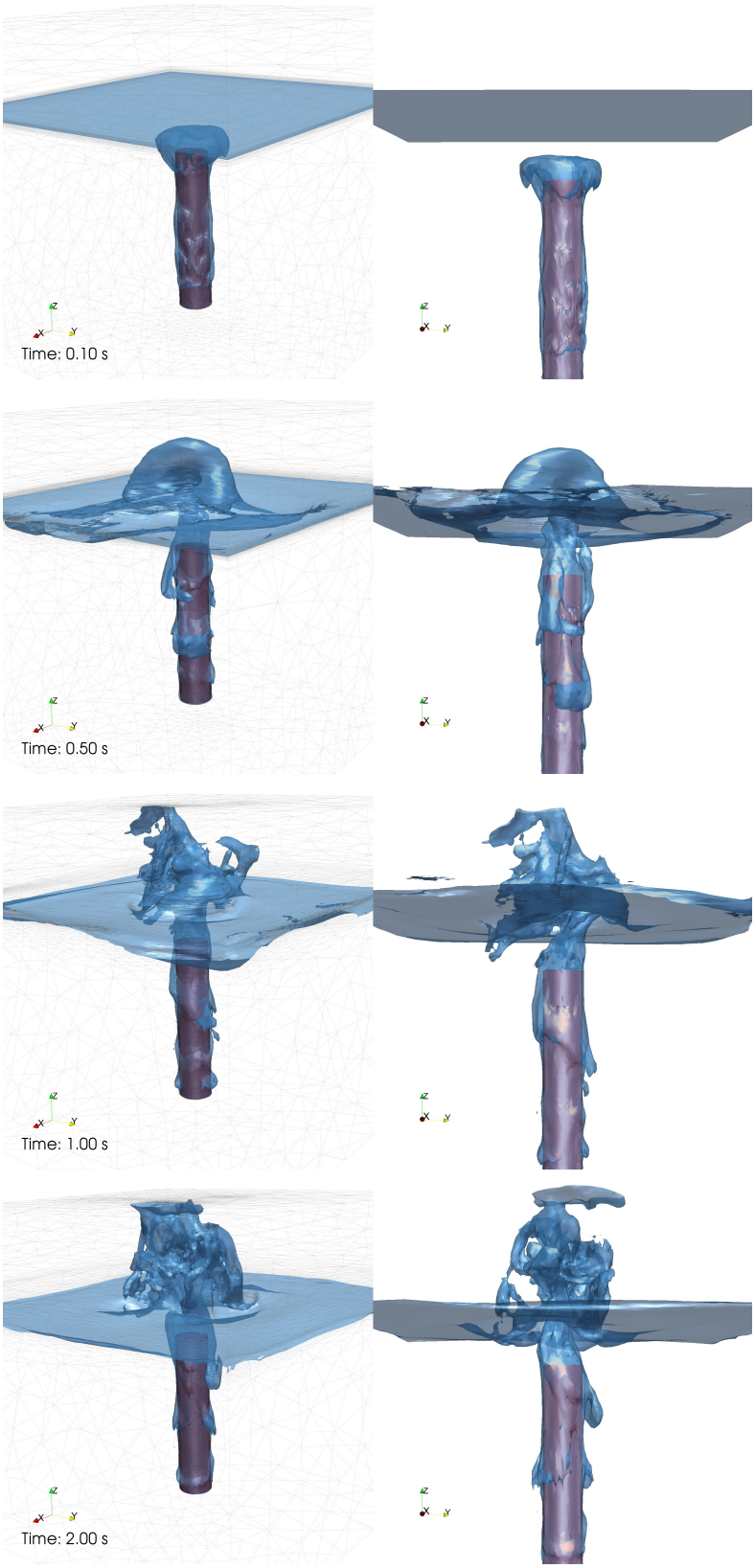

Figure 8.8: Vertical cylinder. Results at t=0.1, 0.5, 1 and 2 s. Perspective view (left), front view (right).

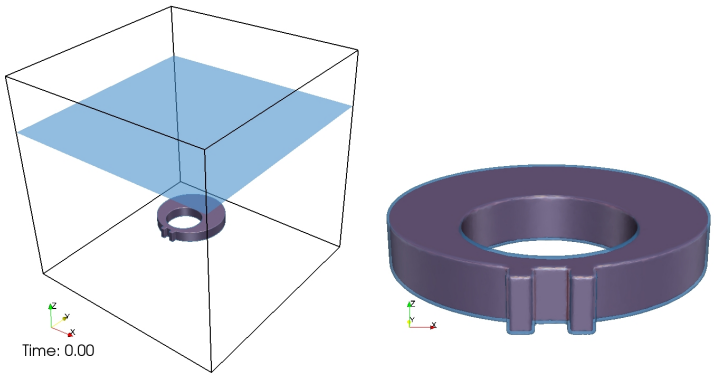

Figure 8.9: Hollow cylinder : Full domain with the ring (in red) and the gas-liquid interface in blue(left). Zoom on the ring (right)

Let us now consider the hollow cylinder. Figure 8.10 shows this time that both the size of the hallow cylinder and its geometrical features seem to affect completely the flow. Sharp edges of the sample encourage the formation of bubbles instead of a vapor film. The vapor film is well guided by the top surface with additional concentration along the extremity. This test case highlights the suitability of the numerical framework developed in this thesis to predict the behavior of the vapor film during quenching. Manufacturers can already investigate the relevance of their operating conditions in terms of position of the part, its orientation as well as to handle easily optimal combination of these parameters.

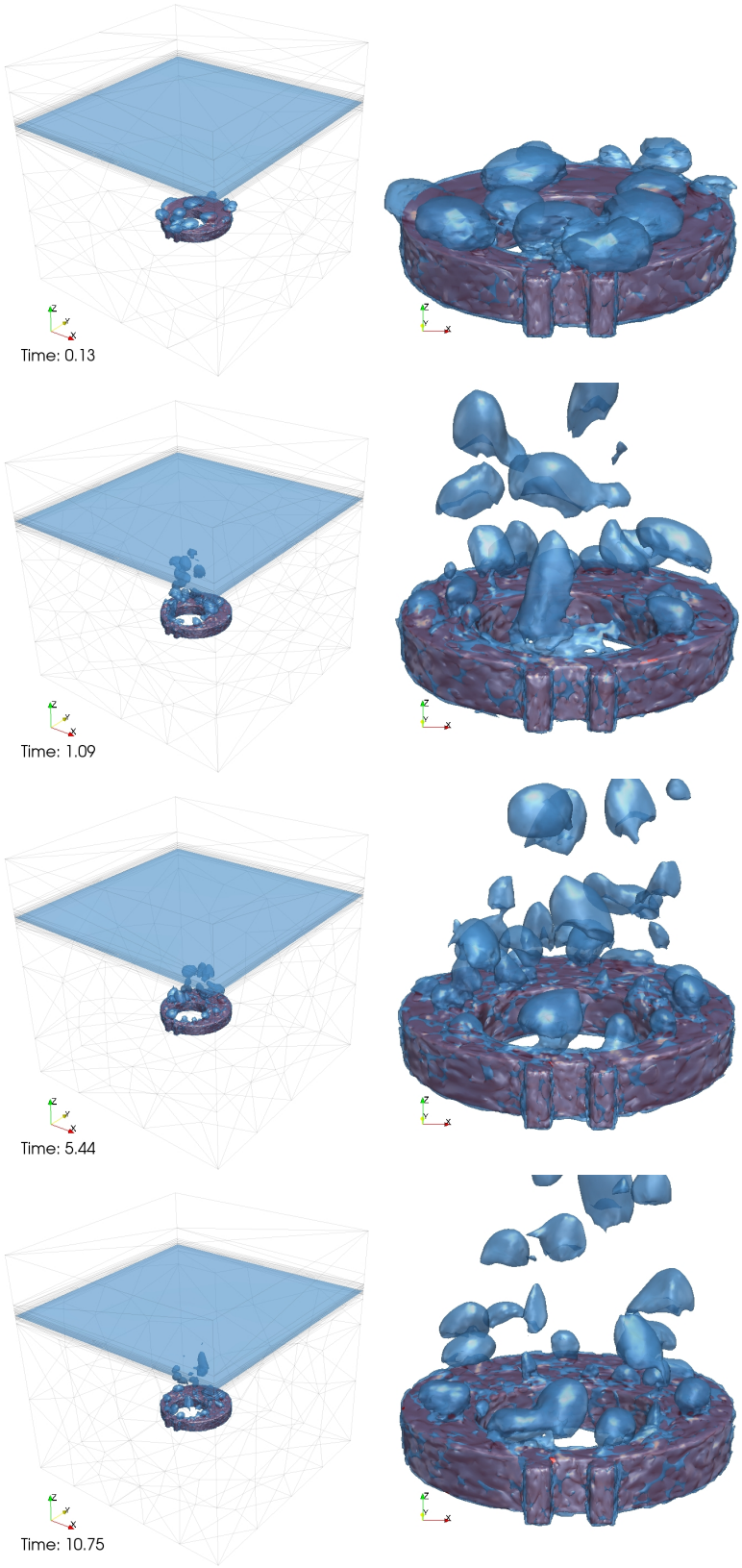

Figure 8.10: Hollow cylinder. Results at t=0.13, 1.09, 5.44 and 10.75 s. Perspective view (left), front view (right).

8.4 Extension to water jet cooling

We propose in this section to simulate the water jet cooling of a static sheet. This represents a different setup for the process since the part is not immersed in a quenching tank. However it consists in a drastic test to investigate the effect of convection (agitation in the case of quenching tanks) on the cooling efficiency. Indeed a further refinement should take into account the collapsing of the vapor film due to convection or pressure forces.

Fig. 8.11 shows the initial setup for the water jet cooling. Water is injected through a rounded nozzle and impinges the surface of the sheet. In this challenging process inhomogeneous cooling could lead to severe distortion of the metal and, as a consequence, the sheet is discarded.

The interest in the simulation is to improve the homogeneity of the cooling by optimizing the jet velocity, the jet orientation and the geometry of the nozzle.

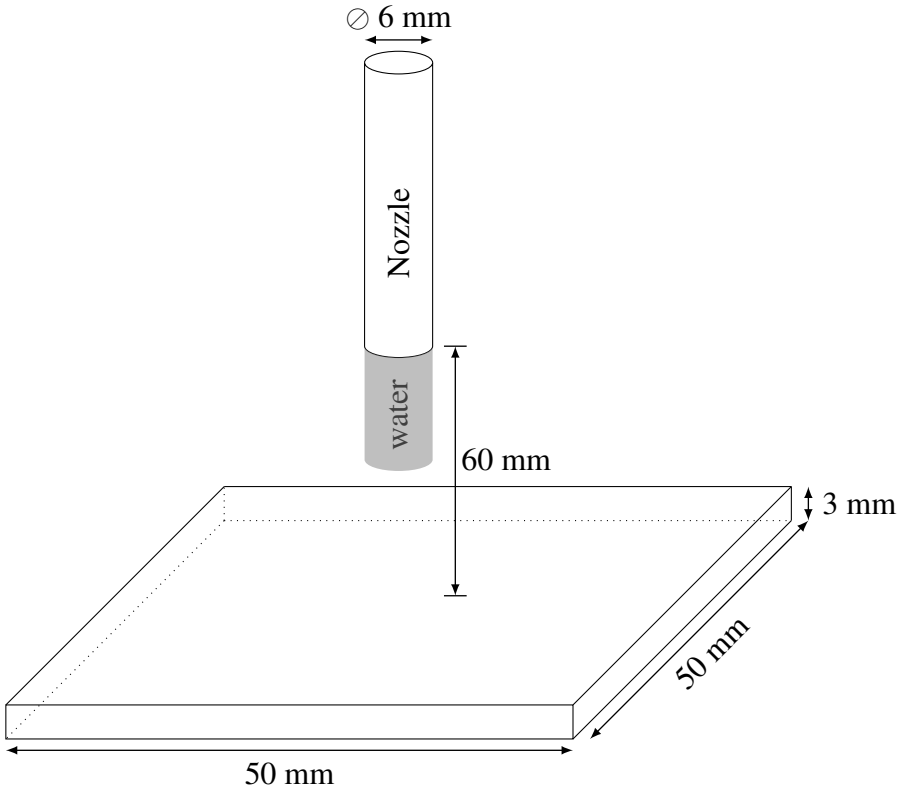

Figure 8.11: Set-up for the 3D water jet cooling

The purpose is to investigate the robustness of the proposed method when simulating a very challenging case such as 3D water jet quenching. A nickel sheet of 3mm thickness and 50mm length is heated at a temperature of 451°C. Water is injected through a nozzle of 6mm diameter. The exit velocity of the jet from the nozzle is 6.1 m/s. The distance between the nozzle and the sheet is 60mm. The temperature at the bottom surface is obtained by infrared camera beneath the sample.

In the computations, we consider 3 phases: solid, water and gas. First, we perform a 2D simulation using 50,000 elements. The wall are adiabatic in this simulation. The evolution of the temperature and the evolution of the adaptive mesh are shown in Fig. 8.12.

We also perform a 3D simulation using 700,000 tetrahedra, where the sheet is immersed in a domain of dimension $90 \times 90 \times 93\text{mm}^3$ as it is depicted in Fig. 8.13. First results of this

simulation are shown in Fig. 8.14 and Fig. 8.15. Despite the low number of elements, interfaces are well described and the mesh is fine enough at the interface to expect a good accuracy in the heat and mass transfer during the simulation.

Enriching this simulation with a vapor film collapse model should provide a complete tool for water jet cooling simulations.

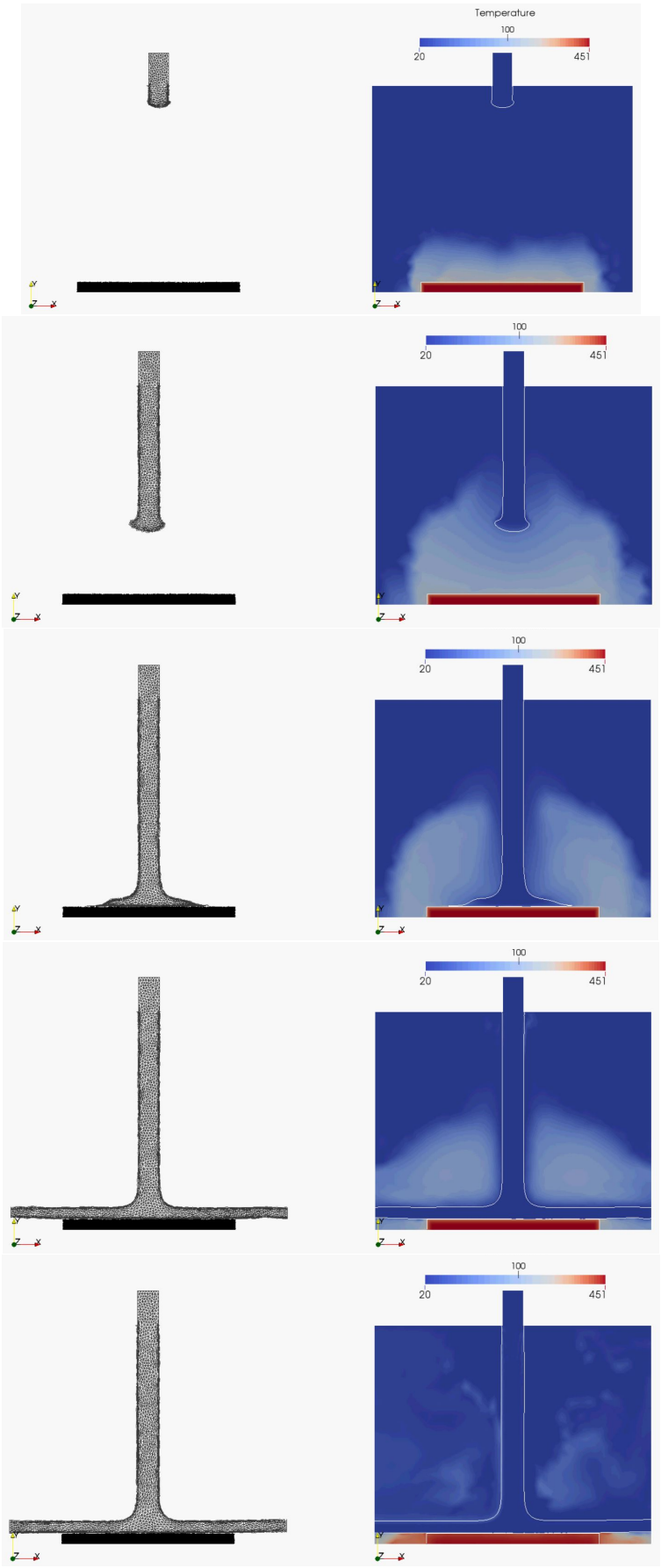

Figure 8.12: 2D Water jet cooling. Results from top to bottom at t=1ms, 8ms, 13ms, 22ms, 86ms and 250ms. On the left is depicted the mesh evolution. The mesh of the gas phase is not displayed. On the right, evolution of the temperature.

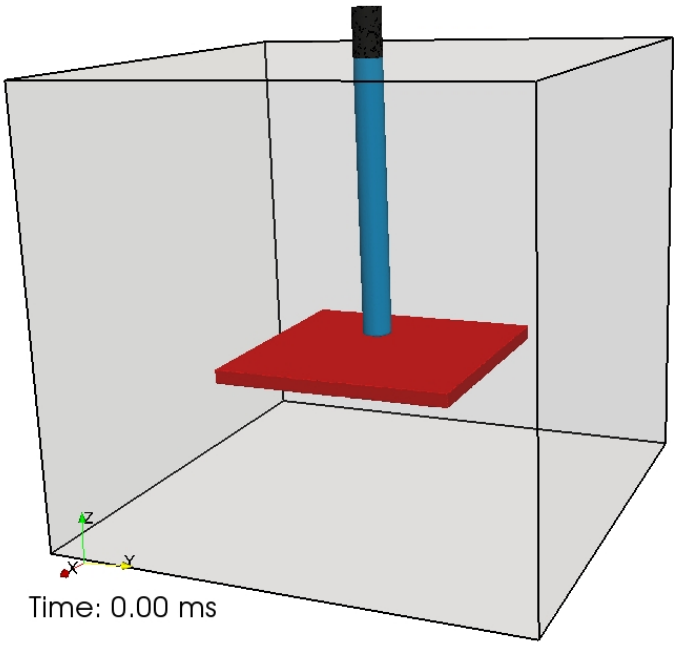

Figure 8.13: 3D Water jet cooling. Results at t=0ms.

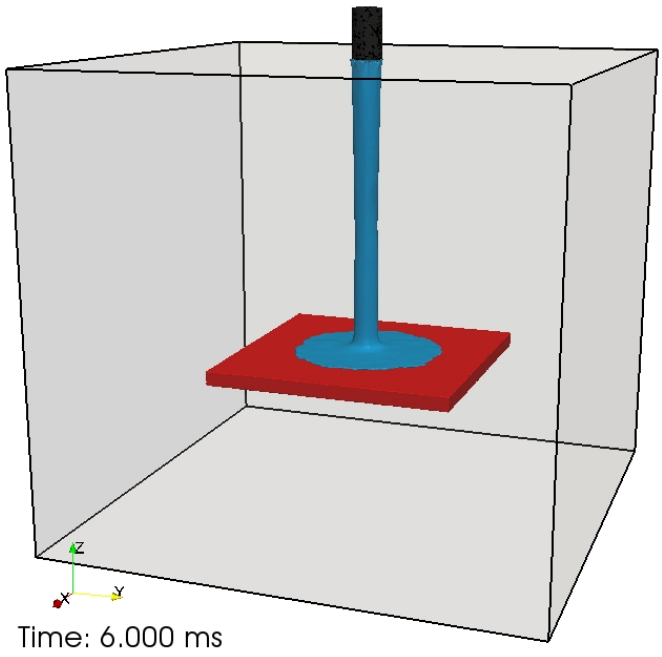

Figure 8.14: 3D Water jet cooling. Results at t=6ms.

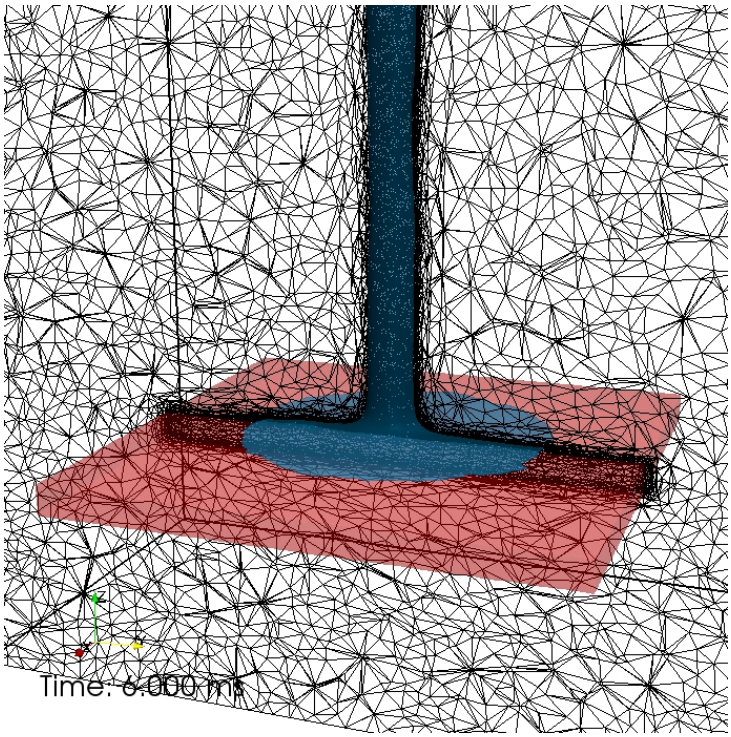

Figure 8.15: 3D Water jet cooling. Results at t=6ms. View of the adapted mesh.

8.5 Conclusion

In this chapter, we presented the simulation of quenching industrial processes using the numerical framework developed in this thesis. The cases simulated here represent very challenging cases due to the complexity of the coupled phenomena involved, the large span of space and time scales to consider and due to the extreme operating conditions such as high thermal gradients, high ratio of the physical properties or high convection.

The results obtained from the first simulation demonstrate that we provide a useful tool to predict the evolution of the temperature in immersed quenching with a very good agreement. Recall that the number of non physical parameters to achieve the simulation has been reduced to the minimum. The second test case shows the further use of this numerical framework as a predictive tool for manufacturers to investigate and improve their quenching processes. We increased the complexity of the test cases by considering water jet cooling. This test case is used to assess the potential of the proposed method.

Résumé en français

L'ensemble des outils développés dans ce manuscript sont utilisés pour la simulation numérique directe des procédés de trempe. Dans un premier temps, la simulation de la trempe d'un échantillon provenant d'un partenaire industriel est effectuée. L'évolution de la température au coeur de cet échantillon est très proche de celle relevée expérimentalement. Cela prouve la pertinence et la capacité du nouveau cadre numérique à reproduire fidèlement les résultats d'un procédé aussi exigeant que la trempe. Dans un deuxième temps, l'outil numérique est utilisé tel un outil prospectif pour l'étude de différents scénarios de trempe. Ainsi, en considérant l'orientation et la position d'un cylindre dans un bain de trempe, la simulation numérique se révèle être d'une aide précieuse dans la description de la dynamique du film de vapeur entourant la pièce. Cela permet d'utiliser la simulation numérique pour optimiser le procédé de trempe. Finalement, une trempe par jet d'eau impactant est étudiée. L'ensemble des outils développés permettent une simulation robuste de ce procédé. Cependant un modèle de fermeture du film de vapeur doit être considéré pour parvenir à simuler ce procédé. Les résultats montrés dans ce chapitre représentent les premiers résultats de simulation numérique directe de trempe à l'échelle industrielle.

Chapter 9

Conclusion & Perspectives

This thesis was devoted to the development of an innovative numerical framework to accurately and robustly simulate an industrial process as demanding as quenching. In this work, we balanced physical modeling, numerical methods and industrial applications.

The physics involved in the process are numerous and complex. We have investigated some of these physical mechanisms, ranging from boiling to the expansion of a vapor film. We decomposed boiling into simpler problems in order to quantify its characteristic scales and characteristic times. It was demonstrated that to be able to model correctly boiling, several mechanisms should be included in our numerical framework. According to this investigation, we decided to develop new numerical methods in the context of the Immersed Volume Method and to extend the software THOST, dedicated firstly for the heating in furnaces, to the cooling in quenching water tank.

This work took advantage of the previous developments in the parallel Finite Element library CimlibCFD developed by the Computing & Fluids group at CEMEF, a research center of MINES ParisTech-PSL Research University. The Immersed Volume Method was used in this work for its ability to take into account all the features of the process in a unified way. This method is a monolithic approach, meaning that only a single set of equation is solved in a single domain, all the phases being immersed by mean of level set functions. This enables to consider conjugate heat transfer without the need of heat transfer coefficients. Thermal coupling are therefore handled naturally. Furthermore, the use of an anisotropic mesh adaptation method provides a better description of the interfaces. Coupled with an a posteriori error estimator, this method enables to increase the accuracy of the computation by following all the physical features of the flow. The numerical framework can be extended and readily devoted to other research field such as rheology, microfluidic, etc (see [Art4] and [Art9]).

We propose here a summary of the argumentation supported during the thesis. In Chapter 1, we have introduced the quenching process and the numerous difficulties arising from the simulation of this process. The common heat transfer computations considering only the solid with heat transfer coefficients (obtained from inverse analysis) fail to be predictive. Therefore we have proposed a direct numerical simulation of the process, in the context of the Immersed Volume method, considering the vapor-liquid-solid couplings.

We have discussed in Chapter 2 the complexity of boiling in quenching tanks. Several physical mechanisms are involved and make the understanding of this phenomenon difficult to achieve. We have proposed to decompose the process into simpler problems and compare their influence on the dynamics of the vapor film. This gave us an insight into the relevant mechanisms to model and simulate in the following chapters. Some conclusions have been

drawn about the requirements for the new numerical framework.

In Chapter 3, we have presented the Immersed Volume Method within which the current work has been done. We have introduced all the component of this Eulerian framework enabling to consider complex geometries by mean of level set function, to refine the mesh according to the interface and the features of the flows, and to deal naturally and accurately with conjugate heat transfer without the need of heat transfer coefficients.

We have described in Chapter 4 the stabilized Finite Element method (SFEM) dedicated to Computational Fluid Dynamics. Standard Galerkin mixed Finite Element suffer from instabilities when using equal order interpolation and exhibit oscillation of the solution in convection dominated regime. Several stabilization methods such as SUPG, VMS or the recent entropy viscosity have been introduced. The capability of SFEM to circumvent numerical instabilities has been demonstrated.

In Chapter 5, we have shown that the usual implementation of surface tension suffers from a severe time restriction that is prohibitive for large computations. Therefore we have proposed a semi-implicit time discretization of surface tension and we have implemented it in the context of Variational Multiscale method, to alleviate this computational burden and to enable large simulation involving surface tension.

The issue of the compressibility of a gaseous phase has been addressed in Chapter 6. Considering bubbly flows only using incompressible approaches does not allow the change of volume in the gas phase. Whereas using a compressible approach and an equation of state that mimics the incompressibility in the liquid is not mass conservative. Therefore we have proposed a new adaptive Variational Multiscale formulation for the Navier-Stokes equations taking into account a compressible phase and an incompressible one in a natural way.

In Chapter 7, we have proposed a phase change model to simulate the heat and mass transfer occurring during boiling. We have derived the Navier-Stokes equations taking into account heat and mass transfer in the context of regularized interface. We have demonstrated the accuracy of the proposed model using physical analytical solution.

In Chapter 8, we have validated against experimental data the numerical tools developed in this thesis. First, we have considered an unclassified experiment to assess the accuracy of the proposed approach. We have found an excellent agreement between the numerical and experimental temperature fields. Then, we have increased the complexity of the test cases by considering larger parts and more complex geometries. The robustness of the new numerical framework has been demonstrated.

It is worth mentioning that all the numerical methods developed in this work will be implemented by the software company Sciences Computers Consultants into the software THOST and will be made available to the industrial in the upcoming version of the software.

Apart from using and adapting the Immersed Volume Method, the edge based anisotropic mesh adaptation technique and the CFD tools, I highlight here the main direct contributions of this thesis:

A new physical modeling for phase change (Chapters 2 & 7, [Art6]) :

We proposed to identify the relevant mechanisms involved in boiling. We quantified their relevance and their effect on the dynamics of the vapor film surrounding the hot part in quenching tanks. We obtained characteristic times and scales enabling us to draw conclusions on the physical mechanisms to simulate. Therefore, we considered using a balance of heat fluxes at the water/vapor interface to quantify the heat and mass transfer during boiling. The Navier-

Stokes equations formulation, dedicated to this phase change model, was derived. The model was validated using analytical solution and test cases from the literature.

A new Navier-Stokes solver with implicit surface tension (Chapter 5, [Art1],[Art8]) :

We proposed an adaptive variational multiscale method for two-fluid flows with surface tension. A level set function is used to provide a precise position of the interfaces. The implementation of the surface tension in the context of the Continuum Surface Force is proposed to circumvent the capillary time step restriction. The obtained system is then solved using a new derived Variational Multiscale stabilized finite element method designed to handle the abrupt changes at the interface and large density and viscosity ratios. Combined with an a posteriori error estimator, we show that anisotropic mesh adaptation provides highly stretched elements at the interfaces and thus yield an accurate modeling framework for two-phase incompressible isothermal flows. Stable and accurate results are obtained for all two- and three-dimensional numerical examples. To the best of our knowledge, these are the first simulation results for representative time-dependent three-dimensional two-fluid flow problems using an implicit treatment of the surface tension and a dynamic unstructured anisotropic mesh adaptation.

A unified Navier-Stokes solver for compressible-incompressible two phase flows (Chapter 6 and [Art2]) :

We presented a new stabilized Finite Element method to solve the two phase compressible-incompressible fluid flow problems using the level set method. The coupling between the pressure and the flow velocity is ensured by introducing mass conservation terms in the momentum equation. Therefore, the same set of primitive unknowns and equations is described for both phases. The unified system is solved using a new derived Variational MultiScale formulation. It was tested and validated on several time-dependent liquid-gas interface problems. The numerical results show good stability and accuracy properties, allowing also to deal with important compressibility effect, high density ratio, and extremely stretched anisotropic elements.

3D boiling using a level set framework (Chapters 7 & 8, [Art6], [Art7]) :

We proposed a novel numerical framework, for simulating the cooling of an immersed 3D solid with boiling and evaporation at the liquid-gas interfaces. Standard numerical methods may not able to deal with these heat transfer interactions simultaneously: gas-liquid-solid phase changes, vapor formations and dynamics, and 3D quenching of a heated solid. Therefore, we proposed a full adaptive Eulerian framework to achieve this challenging task. A Variational Multiscale solver for the Navier-Stokes equations, which can deal with turbulent multiphase flows, is extended using the implicit treatment of the surface tension. The use of an a posteriori error estimator leading to highly stretched anisotropic elements at the interface enables to drastically reduce the interface thickness. Therefore the phase change is performed without the use of conforming mesh. This avoids the need of interface reconstruction or interpolation procedure. Finally, a series of 2D and 3D problems are solved to validate the efficiency and accuracy of the proposed framework. The cooling of an immersed solid is also presented and shows good agreement with the experimental results.

Several perspectives have be drawn from this work. These outlooks are not only considering numerical aspects but also physical aspects to obtain a better understanding of the phenomena involved in quenching:

- **Conservative interpolation**: The anisotropic mesh adaptation procedure requires an interpolation from mesh to mesh that can lead to accumulation of error. To reduce this error inherent to interpolation, a conservative interpolation technique ensuring consistency, continuity and accuracy of the solution is thus required. A PhD thesis by Chahrazade Bahbah has already started on this topic in 2016 [181].

- **Moving meshes**: From the furnaces to the quenching tank, heat transfer between the solid and its surrounding environment take place and make difficult to obtain realistic initial condition. A promising way of circumventing this issue is to simulate at once the whole process using moving meshes for the solid parts in order to alleviate the computational cost of remeshing. However, the simulation of physical phenomena involving moving bodies undergoing large displacements still represents a real challenge. Wafa Daldoul, a PhD student is currently addressing these issues [182].

- **Experimental investigations**: Further experimental investigations are necessary to improve our immersed framework, to validate it and to generate experimental database. Indeed the development of physically based robust numerical models for simulating quenching environments requires to get a better understanding of the involved physical phenomena such as contact angle, wetting, nucleation and many others.

- **Thermomechanical behavior**: The prediction of residual stresses and thermo-elasto-plastic stresses developed during heat treatment and the investigation of the effect of phase transformation and temperature dependence of material properties.

- **Radiation**: In film boiling, since a permanent vapor film surrounds the solid and due to the poor thermal conductivity, it is obvious that radiation plays a major role. Radiation models in liquid are not common in the literature. A new PhD student Carlos Mensah has started in 2017 to work on radiative heat transfer [183].

Finally, a new setup of experimental investigation is sought to have new physical insights. Indeed, comparison between experiment and numerical simulation is not straightforward in quenching processes. Indeed, quenching processes suffer from a lack of direct observation. When a part is immersed in quenching tank, water boils, bubbles rise to the free surface and therefore visualization of the phenomena occurring is not possible. Therefore, the vapor film dynamics in quenching is not well known. Another issue inherent to quenching is the carriage of the hot part from the furnaces to the quenching tank. At this occasion, thermal exchanges with the surrounding environment take place. Radiation through the air and thermal conduction by the carrying tools prevent the prediction of the temperature field shortly before the immersion in the tank. As a consequence, a thorough comparison between numerical simulation and experiment is not possible unless the carriage time is short enough to consider a homogeneous temperature field.

To overcome these obstacles we designed the new experimental device shown in Figure 9.1 and Figure 9.2. The working principle is the following. A part is heated inside a tank full of water. Thermocouples measure the temperature field in the part. When a steady state is reached, heat supplier is shut down, enabling the cooling of the part. We perform the corresponding simulation of the heating and cooling phases, thus enabling us to obtain a realistic initial temperature field for the cooling phase and to assess the accuracy of the numerical simulation. Furthermore the visualization of the formation of the vapor film and its dynamics is straightforward since the part is heated at the bottom of the transparent tank. Quantities such as vapor film thickness and vapor formed during the process can be measured.

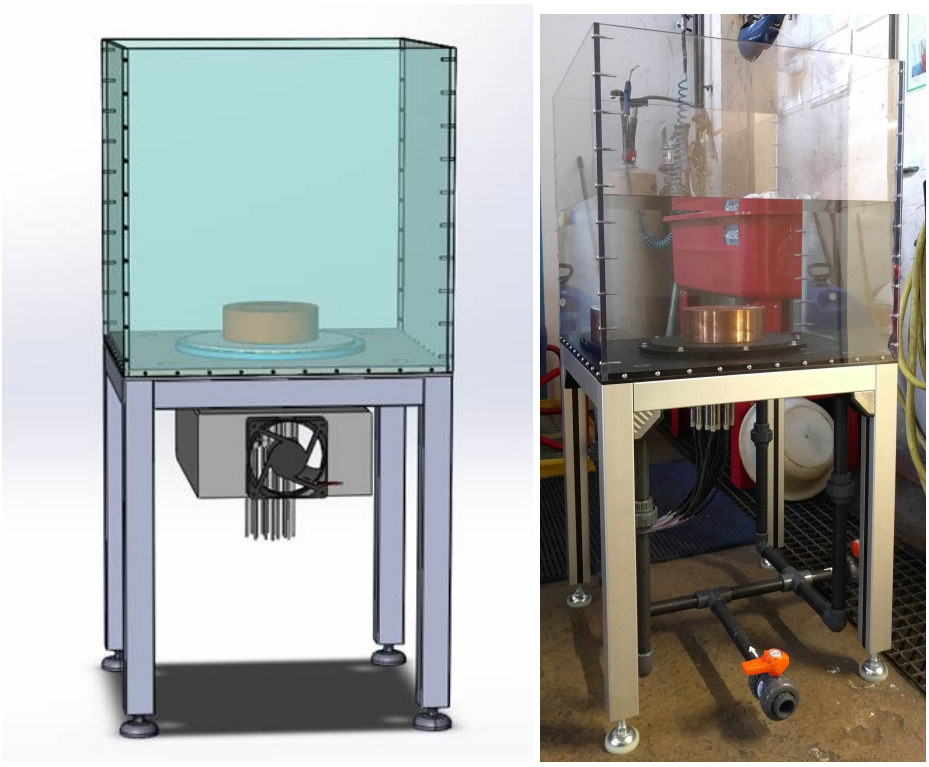

Figure 9.1: New in-situ multi-task quenching device

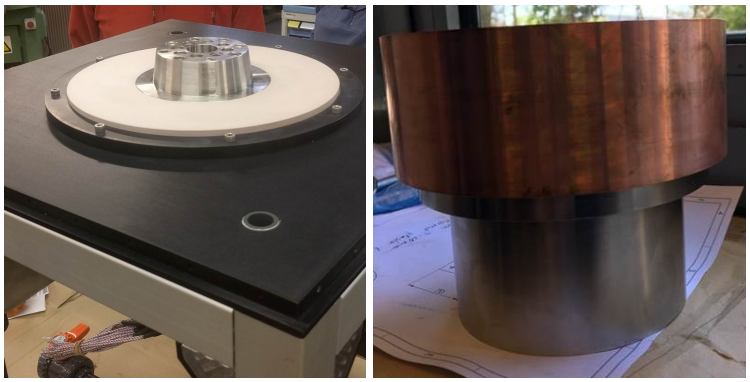

Figure 9.2: Zoom on the heater (left) and assembly heater/solid part (right). Different sizes and geometries of the part can easily be considered.

Résumé en français

Dans ce manuscrit, la construction d'un cadre numérique permettant une simulation numérique robuste et précise des procédés de trempe a été décrite. Tout d'abord, les différents mécanismes présents dans le procédé de trempe ont été étudiés. Des échelles et des temps caractéristiques ont été donnés permettant de connaître l'influence de chacun de ces mécanismes sur l'évolution de la phase vapeur. Cette étude a permis de dégager les principaux axes de développement numérique.

Les outils développés vont intégrer un cadre numérique existant utilisant la méthode des volumes immergées. Ce paradigme allie la méthode level set pour la description des interfaces, des lois de mélange pour distribuer en espace les propriétés physiques respectives et une méthode d'adaptation de maillage anisotrope pour une meilleure résolution des équations dans le domaine. Ainsi, les transferts thermiques aux interfaces s'opèrent naturellement sans utilisation de coefficient de transfert thermique.

Les équations de la mécanique sont résolues en utilisant une méthode d'Eléments Finis stabilisés permettant de simuler des écoulements turbulents et de traiter les régimes à convection et à diffusion dominantes. Les différents solveurs et notamment le solveur concernant les équations de conservation de la masse et de mouvement sont modifiés pour prendre en compte des physiques additionnelles.

Une méthode implicite de tension de surface permettant de s'affranchir de la restriction du pas de temps capillaire a été utilisée et implémentée. L'utilisation de cette méthode avec l'adaptation de maillage anisotrope résulte en un puissant outil, robuste, précis et peu coûteux pour la simulation des écoulements multiphasiques avec tension de surface.

Une formulation unifiée des équations de Navier-Stokes prenant en compte une phase compressible et une phase incompressible a été développée. Elle permet de considérer la phase vapeur comme une phase compressible tout en considérant l'eau comme incompressible. Cela permet de décrire plus précisément la dynamique du film de vapeur lorsqu'il est soumis à une forte agitation dans le bain de trempe.

La modélisation du changement de phase nécessite une modification de l'ensemble des équations. Des termes additionnels quantifiant l'échange de masse et d'énergie à travers l'interface vapeur/eau apparaissent et doivent être intégrés dans la résolution de ces équations. Le taux de transfert de masse est dérivé à l'aide d'un modèle quasi-statique. La validation de ce dernier est effectuée en utilisant aussi bien des problèmes analytiques que des corrélations expérimentales sur les gradients thermiques.

Finalement, l'ensemble des outils de ce nouveau cadre numérique est utilisé pour la simulation numérique directe des procédés de trempe. La comparaison avec des résultats expérimentaux montre d'ores et déjà la validité, la robustesse et la précision de l'approche proposée. Les outils proposés peuvent ainsi être utilisés pour optimiser le procédé en étudiant différentes orientations, positions et différentes géométries.

Pour aller plus loin dans la compréhension du procédé de trempe, un nouveau banc expérimental a été développé durant cette thèse. Ce banc permettra de suivre la montée en température d'un échantillon jusqu'à un état stationnaire et le refroidissement de cet échantillon dans un contexte de trempe par immersion. La phase d'immersion, présente dans les procédés de trempe et difficile à contrôler, est ainsi supprimée. Le but recherché est d'obtenir un historique complet du champ de température dans la pièce, pouvant être reproduit par la simulation numérique. De plus, l'observation directe du bain par l'intermédiaire de caméras rapides permettra de calculer les épaisseurs du film de vapeur à différents instants, avec ou sans agitation. Cela permettra ainsi de valider le modèle de changement de phase dans un environnement contrôlé.

Bibliography

[1] Guy MURRY. Traitements thermiques dans la masse des aciers. partie 1. *Techniques de l'ingénieur Traitements thermiques des aciers, des alliages et des fontes*, 2000. *2 citations pages 2 and 6*

[2] D. S. Mackenzie. History of quenching. *International Heat Treatment and Surface Engineering*, 2(2):68–73, 2008. *Cited page 4*

[3] D. R. Garwood, J. D. Lucas, R. A. Wallis, and J. Ward. Modeling of the flow distribution in an oil quench tank. *Journal of Materials Engineering and Performance*, 1(6):781–787, Dec 1992. *2 citations pages 4 and 6*

[4] Vedanth Srinivasan, Kil-Min Moon, David Greif, De Ming Wang, and Myung hwan Kim. Numerical simulation of immersion quenching process of an engine cylinder head. *Applied Mathematical Modelling*, 34(8):2111 – 2128, 2010. *2 citations pages 4 and 6*

[5] Bohumil Taraba, Steven Duehring, Ján Španielka, and Štefan Hajdu. Effect of agitation work on heat transfer during cooling in oil isorapid 277hm. *Strojniški vestnik - Journal of Mechanical Engineering*, 58(2):102–106, 2012. *Cited page 6*

[6] P. Cavaliere, E. Cerri, and P. Leo. Effect of heat treatments on mechanical properties and fracture behavior of a thixocast a356 aluminum alloy. *Journal of Materials Science*, 39(5):1653–1658, Mar 2004. *Cited page 6*

[7] C. Simsir, C. Hakan Gur, and P. Leo. A simulation of the quenching process for predicting temperature, microstructure and residual stresses. *Journal of Mechanical Engineering*, 56:93–103, 2010. *Cited page 6*

[8] Nailu Chen, Lizhan Han, Weimin Zhang, and Xiaowei Hao. Enhancing mechanical properties and avoiding cracks by simulation of quenching connecting rods. *Materials Letters*, 61(14):3021 – 3024, 2007. *Cited page 6*

[9] J Olivier, B Clement, JJ Debie, and F Moreaux. Stirring of quenchants fluids: design considerations and metallurgical consequences. *Trait. Therm*, 206:29–42, 1986. *Cited page 6*

[10] FZ Lemmadi, A Chala, S Ferhati, F Chabane, and S Benramache. Structural and mechanical behavior during quenching of 40crmov5 steel. *Journal of Science and Engineering*, 3(1):1–6, 2013. *Cited page 6*

[11] John D. Bernardin and Issam Mudawar. Validation of the quench factor technique in predicting hardness in heat treatable aluminum alloys. *International Journal of Heat and Mass Transfer*, 38(5):863 – 873, 1995. *Cited page 6*

[12] Lauralice de Campos Franceschini Canale and George E. Totten. Quenching technology: a selected overview of the current state-of-the-art. *Materials Research*, 8:461 – 467, 12 2005. *Cited page 6*

[13] Vijay K Dhir. Mechanistic prediction of nucleate boiling heat transfer–achievable or a hopeless task? *Journal of Heat Transfer*, 128(1):1–12, 2006. *Cited page 6*

[14] Gihun Son, Vijay K Dhir, and N Ramanujapu. Dynamics and heat transfer associated with a single bubble during nucleate boiling on a horizontal surface. *Journal of Heat Transfer*, 121(3):623–631, 1999. *Cited page 6*

[15] Gihun Son, N Ramanujapu, and Vijay K Dhir. Numerical simulation of bubble merger process on a single nucleation site during pool nucleate boiling. *Journal of Heat Transfer*, 124(1):51–62, 2001. *Cited page 6*

[16] M. Sussman. A level set approach for computing solutions to incompressible two-phase flow. *Journal of Computational Physics*, 114(1):146–159, 1994. *3 citations pages 6, 28, and 92*

[17] David Jacqmin. Calculation of two-phase navier–stokes flows using phase-field modeling. *Journal of Computational Physics*, 155(1):96 – 127, 1999. *Cited page 6*

[18] Ruben Scardovelli and Stéphane Zaleski. Direct numerical simulation of free-surface and interfacial flow. *Annual Review of Fluid Mechanics*, 31(1):567–603, 1999. *Cited page 6*

[19] E. Hachem, T. Kloczko, H. Digonnet, and T. Coupez. Stabilized finite element solution to handle complex heat and fluid flows in industrial furnaces using the immersed volume method. *International Journal for Numerical Methods in Fluids*, 68(1):99–121, 2012. *2 citations pages 7 and 27*

[20] E. Hachem, B. Rivaux, T. Kloczko, H. Digonnet, and T. Coupez. Stabilized finite element method for incompressible flows with high reynolds number. *Journal of Computational Physics*, 229(23):8643–8665, 2010. *6 citations pages 7, 51, 70, 73, 92, and 95*

[21] E. Hachem, S. Feghali, R. Codina, and T. Coupez. Immersed stress method for fluid–structure interaction using anisotropic mesh adaptation. *International Journal for Numerical Methods in Engineering*, 94(9):805–825, 2013. *2 citations pages 7 and 72*

[22] E. Hachem, H. Digonnet, N. Kosseifi, E. Massoni, and T. Coupez. Enriched finite element spaces for transient conduction heat transfer. *Applied Mathematics and Computation*, 217(8):3929 – 3943, 2010. *Cited page 7*

[23] E. Hachem, S. Feghali, R. Codina, and T. Coupez. Anisotropic adaptive meshing and monolithic variational multiscale method for fluid–structure interaction. *Computers & Structures*, 122:88 – 100, 2013. *Cited page 7*

[24] T. Coupez and E. Hachem. Solution of high-reynolds incompressible flow with stabilized finite element and adaptive anisotropic meshing. *Computer Methods in Applied Mechanics and Engineering*, 267:65 – 85, 2013. *5 citations pages 7, 51, 58, 70, and 73*

[25] T. Coupez, G. Jannoun, N. Nassif, H.C. Nguyen, H. Digonnet, and E. Hachem. Adaptive time-step with anisotropic meshing for incompressible flows. *Journal of Computational Physics*, 241:195 – 211, 2013. *2 citations pages 7 and 58*

[26] G. Jannoun, E. Hachem, J. Veysset, and T. Coupez. Anisotropic meshing with time-stepping control for unsteady convection-dominated problems. *Applied Mathematical Modelling*, 39(7):1899–1916, 2015. *4 citations pages 7, 36, 58, and 70*

[27] Y. Mesri, M. Khalloufi, and E. Hachem. On optimal simplicial 3d meshes for minimizing the hessian-based errors. *Applied Numerical Mathematics*, 109:235 – 249, 2016. *4 citations pages 7, 28, 33, and 108*

[28] Laure Billon, Youssef Mesri, and Elie Hachem. Anisotropic boundary layer mesh generation for immersed complex geometries. *Engineering with Computers*, 33(2):249–260, Apr 2017. *2 citations pages 7 and 32*

[29] Niphon Wansophark, Atipong Malatip, and Pramote Dechaumphai. Streamline upwind finite element method for conjugate heat transfer problems. *Acta Mechanica Sinica*, 21(5):436–443, Nov 2005. *Cited page 7*

[30] Thomas Richter. A fully eulerian formulation for fluid–structure-interaction problems. *Journal of Computational Physics*, 233:227 – 240, 2013. *Cited page 7*

[31] Guillermo Hauke and Thomas JR Hughes. A comparative study of different sets of variables for solving compressible and incompressible flows. *Computer Methods in Applied Mechanics and Engineering*, 153(1):1–44, 1998. *Cited page 7*

[32] T.J.R. Hughes. Multiscale phenomena: Green's functions, the dirichlet-to-neumann formulation, subgrid scale models, bubbles and the origins of stabilized methods. *Computer Methods in Applied Mechanics and Engineering*, 127(1-4):387–401, 1995. *9 citations pages 7, 48, 50, 52, 70, 72, 92, 94, and 96*

[33] T.J.R. Hughes, G. Scovazzi, P.B. Bochev, and A. Buffa. A multiscale discontinuous galerkin method with the computational structure of a continuous galerkin method. *Computer Methods in Applied Mechanics and Engineering*, 195(19-22):2761–2787, 2006. *3 citations pages 7, 92, and 94*

[34] Y. Bazilevs, V.M. Calo, J.A. Cottrell, T.J.R. Hughes, A. Reali, and G. Scovazzi. Variational multiscale residual-based turbulence modeling for large eddy simulation of incompressible flows. *Computer Methods in Applied Mechanics and Engineering*, 197(1-4):173–201, 2007. *3 citations pages 7, 92, and 94*

[35] U. Rasthofer and V. Gravemeier. Multifractal subgrid-scale modeling within a variational multiscale method for large-eddy simulation of turbulent flow. *Journal of Computational Physics*, 234(1):79–107, 2013. *4 citations pages 7, 48, 72, and 94*

[36] E. Castillo and R. Codina. Variational multi-scale stabilized formulations for the stationary three-field incompressible viscoelastic flow problem. *Computer Methods in Applied Mechanics and Engineering*, 279:579–605, 2014. *3 citations pages 7, 72, and 94*

[37] M. Khalloufi, Y. Mesri, R. Valette, E. Massoni, and E. Hachem. High fidelity anisotropic adaptive variational multiscale method for multiphase flows with surface tension. *Computer Methods in Applied Mechanics and Engineering*, 307:44 – 67, 2016. *2 citations pages 7 and 108*

[38] E. Hachem, M. Khalloufi, J. Bruchon, R. Valette, and Y. Mesri. Unified adaptive variational multiscale method for two phase compressible—incompressible flows. *Computer Methods in Applied Mechanics and Engineering*, 308:238 – 255, 2016. *2 citations pages 7 and 108*

[39] S Nukiyama. Film boiling water on thin wires. *Society of Mechanical Engineering*, 37, 1934. *Cited page 14*

[40] Vasilios Alexiades and Alan D. Solomon. *Mathematical Modeling of Melting or Freezing Processes*. Hemisphere Pub. Corp, Washington, 1993. *Cited page 18*

[41] V Alexiades and J.B. Drake. *Free Boundary Problems Involving Solids : A weak formulation for phase change problems with bulk movement due to unequal densities*, volume 281. Longman, 01 1993. *Cited page 18*

[42] Damir Juric and Grétar Tryggvason. Computations of boiling flows. *International Journal of Multiphase Flow*, 24(3):387 – 410, 1998. *2 citations pages 18 and 108*

[43] Roland Denis. *Modelisation and simulation of Leidenfrost effect in micro-droplets*. Phd thesis, Université de Grenoble, November 2012. *2 citations pages 18 and 108*

[44] F. Font, T. G. Myers, and S. L. Mitchell. A mathematical model for nanoparticle melting with density change. *Microfluidics and Nanofluidics*, 18(2):233–243, Feb 2015. *Cited page 19*

[45] D.H. Sharp. An overview of rayleigh-taylor instability. *Physica D: Nonlinear Phenomena*, 12(1):3 – 18, 1984. *Cited page 20*

[46] H. Johansen and P. Colella. A cartesian grid embedded boundary method for poisson's equation on irregular domains. *Journal of Computational Physics*, 147:60–85, 1998. *Cited page 27*

[47] CS. Peskin. Flow patterns around heart valves: a numerical method. *Journal of Computational Physics*, 10:252–271, 1972. *Cited page 27*

[48] R. Glowinski, TW. Pan, AJ. Kearsley, and J. Periaux. Numerical simulation and optimal shape for viscous flow by a fictitious domain method. *International Journal for Numerical Methods in Fluids*, 20:695–711, 2005. *Cited page 27*

[49] HO. Kreiss and A. Petersson. A second-order accurate embedded boundary method for the wave equation with dirichlet data. *SIAM Journal on Scientific Computation*, 27:1141–1167, 2006. *Cited page 27*

[50] C. Farhat, A. Rallu, K. Wang, and T. Belytschko. Robust and provably second-order explicit-explicit and implicit-explicit staggered time-integratorsfor highly nonlinear fluid-structure interaction problems. *International Journal for Numerical Methods in Engineering*, 84(1):73–107, 2010. *Cited page 27*

[51] C. Farhat, K. Maute, B. Argrow, and M. Nikbay. A shape optimization methodology for reducing the sonic boom initial pressure rise. *AIAA Journal of Aircraft*, 45:1007–1018, 2007. *Cited page 27*

[52] F. Ilinca and J.-F. Hetu. A finite element immersed boundary method for fluid flow around rigid objects. *International Journal for Numerical Methods in Fluids*, 65:856–875, 2011. *Cited page 27*

[53] R. Abgrall, H. Beaugendre, and C. Dobrzynski. An immersed boundary method using unstructured anisotropic mesh adaptation combined with level-sets and penalization techniques. *Journal of Computational Physics*, 257(Part A):83 – 101, 2014. *Cited page 27*

[54] T. Coupez. Metric construction by length distribution tensor and edge based error for anisotropic adaptive meshing. *Journal of Computational Physics*, 230(7):2391–2405, 2011. *5 citations pages 28, 33, 34, 35, and 108*

[55] S. Osher and R. Fedkiw. *Level set methods and dynamic implicit surfaces*. Springer, 2003. *Cited page 28*

[56] L. Ville, L. Silva, and T. Coupez. Convected level set method for the numerical simulation of fluid buckling. *International Journal for Numerical Methods in Fluids*, 66(3):324–344, 2011. *Cited page 30*

[57] Andrea Bonito, Jean-Luc Guermond, and Sanghyun Lee. Numerical simulations of bouncing jets. *International Journal for Numerical Methods in Fluids*, 80(1):53–75, 2016. *3 citations pages 30, 56, and 70*

[58] Thierry Coupez, Luisa Silva, and Elie Hachem. Implicit boundary and adaptive anisotropic meshing. In *New Challenges in Grid Generation and Adaptivity for Scientific Computing*, volume 5, pages 1–18. Springer International Publishing, 2015. *2 citations pages 30 and 70*

[59] T.J.R. Hughes, J.A. Cottrell, and Y. Bazilevs. Isogeometric analysis: Cad, finite elements, nurbs, exact geometry and mesh refinement. *Computer Methods in Applied Mechanics and Engineering*, 194(39):4135 – 4195, 2005. *Cited page 31*

[60] J. Dompierre, M. G. Vallet, M. Fortin, W. G. Habashi, S. Boivin, Y. Bourgault, and A. Tam. Edge-based mesh adaptation for cfd. international conference on numerical methods for the euler and navier-stokes equations. In *8th IEEE Symp. pn Parallel and Distributed Processing*, pages 265–299, Montréal, Sept. 1995. *Cited page 32*

[61] P. J. Frey and F. Alauzet. Anisotropic mesh adaptation for cfd computations. *Computer Methods in Applied Mechanics and Engineering*, 194(48-49):5068–5082, 2005. *Cited page 32*

[62] J.-F. Remacle, X. Li, M.S. Shephard, and J.E. Flaherty. Anisotropic adaptive simulation of transient flows. *International Journal for Numerical Methods in Engineering*, 62:899–923, 2005. *Cited page 32*

[63] C. Gruau and T. Coupez. 3D tetrahedral, unstructured and anisotropic mesh generation with adaptation to natural and multidomain metric. *Computer Methods in Applied Mechanics and Engineering*, 194:4951–4976, 2005. *Cited page 32*

[64] Gerd Kunert and R Verfürth. Edge residuals dominate a posteriori error estimates for linear finite element methods on anisotropic triangular and tetrahedral meshes. *Numer. Math.*, 86(2):283–303, 2000. *Cited page 35*

[65] Frédéric Alauzet and Pascal Frey. Estimateur d'erreur géométrique et métriques anisotropes pour l'adaptation de maillage. Partie I : aspects théoriques. Research Report RR-4759, INRIA, 2003. *Cited page 37*

[66] Suhas V. Patankar. *Numerical Heat Transfer And Fluid Flow*. Series In Computational And Physical Processes In Mechanics And Thermal Sciences. Taylor & Francis, 1980. *Cited page 38*

[67] J.C. Martin and W.J. Moyce. An experimental study of the collapse of liquid columns on a rigid horizontal plane. *Philosophical Transactions of the Royal Society of London. Series A, Mathematical and Physical Sciences*, 244:312–324, 1952. *2 citations pages 39 and 42*

[68] L. Marioni, M. Khalloufi, F. Bay, and E. Hachem. Two-fluid flow under the constraint of external magnetic field: revisiting the dam-break benchmark. *International Journal of Numerical Methods for Heat & Fluid Flow*, 27:1–17, 2017. *3 citations pages 40, 42, and 108*

[69] A. Murrone and H. Guillard. A five equation reduced model for compressible two phase flow problems. *Journal of Computational Physics*, 202:664–698, 2005. *2 citations pages 40 and 42*

[70] R. N. Elias and A. Coutinho. Stabilized edge-based finite element simulation of free-surface flows. *International Journal of Numerical Methods in Fluids*, 54:965–993, 2007. *2 citations pages 40 and 42*

[71] A. Quarteroni. What mathematics can do for the simulation of blood circulation. Technical report, MOX Report, 2006. *Cited page 48*

[72] A. Masud and R. Calderer. A variational multiscale method for incompressible turbulent flows: Bubble functions and fine scale fields. *Computer Methods in Applied Mechanics and Engineering*, 200:2577–2593, 2011. *Cited page 48*

[73] O. Guasch and R. Codina. Statistical behavior of the orthogonal subgrid scale stabilization terms in the finite element large eddy simulation of turbulent flows. *Computer Methods in Applied Mechanics and Engineering*, 261:154–166, 2013. *Cited page 48*

[74] D.N. Arnold, F. Brezzi, and M. Fortin. A stable finite element for the Stokes equations. *Calcolo*, 23(4):337–344, 1984. *Cited page 48*

[75] A. N. Brooks and T. J.R. Hughes. Streamline upwind/Petrov-Galerkin formulations for convection dominated flows with particular emphasis on the incompressible Navier-Stokes equations. *Computer Methods in Applied Mechanics and Engineering*, 32(1 - 3):199 – 259, 1982. *2 citations pages 48 and 55*

[76] T.J.R. Hughes, L.P. Franca, and M. Balestra. A new finite element formulation for computational fluid dynamics: V. circumventing the Babuska-Brezzi condition: A stable

Petrov-Galerkin formulation of the Stokes problem accommodating equal-order interpolations. *Computer Methods in Applied Mechanics and Engineering*, 59:85–99, 1987. *2 citations pages 48 and 55*

[77] Jean Donea and Antonio Huerta. *Finite element methods for flow problems*. John Wiley & Sons, 2003. *Cited page 48*

[78] F. Brezzi, L. P. Franca, T. J. R. Hughes, and A. Russo. $b = \int g$. *Computer Methods in Applied Mechanics and Engineering*, 145:329–339, 1997. *Cited page 48*

[79] T.E. Tezduyar, R. Shih, S. Mittal, and S.E. Ray. Incompressible flow computations with stabilized bilinear and linear equal-order-interpolation velocity-pressure elements. *Computer Methods in Applied Mechanics and Engineering*, 95:221–242, 1992. *Cited page 48*

[80] L.P. Franca and Farhat C. Bubble functions prompt unusual stabilized finite element methods. *Computer Methods in Applied Mechanics and Engineering*, 123:229–308, 1995. *Cited page 48*

[81] R. Codina. Stabilization of incompressibility and convection through orthogonal subscales in finite element methods. *Computer Methods in Applied Mechanics and Engineering*, 190:1579–1599, 2000. *3 citations pages 48, 58, and 73*

[82] R. Codina. Stabilized finite element method for the transient Navier-Stokes equations based on a pressure gradient projection. *Computer Methods in Applied Mechanics and Engineering*, 182(3-4):277–300, 2000. *Cited page 48*

[83] R. Codina. Pressure stability in fractional step finite element methods for incompressible flows. *Journal of Computational Physics*, 170:112–140, 2001. *Cited page 48*

[84] R. Codina and J. Principe. Dynamic subscales in the finite element approximation of thermally coupled incompressible flows. *International Journal for Numerical Methods in Fluids*, 54:707–730, 2007. *3 citations pages 48, 59, and 95*

[85] V. Gravemeier. Scale-separating operators for variational multiscale large eddy simulation of turbulent flows. *Journal Of Computational Physics*, 212(2):400–435, 2006. *Cited page 48*

[86] V. Gravemeier. A consistent dynamic localization model for large eddy simulation of turbulent flows based on a variational formulation. *Journal Of Computational Physics*, 218(2):677–701, 2006. *Cited page 48*

[87] V. Gravemeier, W. A. Wall, and E. Ramm. A three-level finite element method for the instationary incompressible Navier-Stokes equations. *Computer Methods in Applied Mechanics and Engineering*, 193(15-16):1323–1366, 2004. *Cited page 48*

[88] R. Moser, J. Kim, and R. Mansour. DNS of turbulent channel flow up to Re = 590. *Physics of Fluids*, 11:943–945, 1999. *Cited page 49*

[89] Elie Hachem. *Stabilized finite element method for heat transfer and turbulent flows inside industrial furnaces*. PhD thesis, École Nationale Supérieure des Mines de Paris, 2009. *Cited page 51*

[90] R. Codina. Stabilized finite element approximation of transient incompressible flows using orthogonal subscales. *Computer Methods in Applied Mechanics and Engineering*, 191(39-40):4295–4321, 2002. *2 citations pages 51 and 96*

[91] S. Badia and R. Codina. Stabilized continuous and discontinuous galerkin techniques for darcy flow. *Computer Methods in Applied Mechanics and Engineering*, 199(25-28):1654–1667, 2010. *2 citations pages 52 and 96*

[92] R. Codina. Finite element approximation of the three field formulation of the Stokes problem using arbitrary interpolations. *SIAM Journal on Numerical Analysis*, 47:699–718, 2009. *Cited page 52*

[93] R. Codina, J. Principe, O. Guasch, and S. Badia. Time dependent subscales in the stabilized finite element approximation of incompressible flow problems. *Computer Methods in Applied Mechanics and Engineering*, 196:2413–2430, 2007. *Cited page 52*

[94] S. Badia and R. Codina. On a multiscale approach to the transient Stokes problem. Transient subscales and anisotropic space-time discretization. *Applied Mathematics and Computation*, 207:415–433, 2009. *Cited page 52*

[95] Davide Forti and Luca Dedè. Semi-implicit bdf time discretization of the navier–stokes equations with vms-les modeling in a high performance computing framework. *Computers & Fluids*, 117(Supplement C):168 – 182, 2015. *Cited page 53*

[96] R. Codina. Comparison of some finite element methods for solving the diffusion-convection-reaction equation. *Computer Methods in Applied Mechanics and Engineering*, 156:185–210, 1998. *Cited page 54*

[97] S. Badia and R. Codina. Analysis of a stabilized finite element approximation of the transient convection-diffusion equation using an ALE framework. *Journal on Numerical Analysis*, 44:2159–2197, 2006. *2 citations pages 54 and 55*

[98] R. Codina, J.M. González-Ondina, G. Díaz-Hernández, and J. Principe. Finite element approximation of the modified boussinesq equations using a stabilized formulation. *International Journal for Numerical Methods in Fluids*, 57:1249–1268, 2008. *Cited page 54*

[99] A.C. Galeão and E.G.D. do Carmo. A consistent approximate upwind Petrov-Galerkin method for convection-dominated problems. *Computer Methods in Applied Mechanics and Engineering*, 68(1):83–95, 1988. *Cited page 55*

[100] J.-L. Guermond, R. Pasquetti, and B. Popov. Entropy viscosity method for nonlinear conservation laws. *Journal of Computational Physics*, 230(11):4248–4267, 2011. *2 citations pages 55 and 56*

[101] E. Hachem, G. Jannoun, J. Veysset, and T. Coupez. On the stabilized finite element method for steady convection-dominated problems with anisotropic mesh adaptation. *Applied Mathematics and Computation*, 232:581 – 594, 2014. *Cited page 58*

[102] S. Mittal. On the performance of high aspect ratio elements for incompressible flows. *Computer Methods in Applied Mechanics and Engineering*, 188:269–287, 2000. *Cited page 58*

[103] S. Micheletti, S. Perotto, and M. Picasso. Stabilized finite elements on anisotropic meshes: A priori error estimates for the advection-diffusion and the stokes problems. *SIAM Journal on Numerical Analysis*, 41:1131–1162, 2004. *Cited page 58*

[104] I. Harari and T. J. R. Hughes. What are c and h?: inequalities for the analysis and design of finite element methods. *Computer Methods in Applied Mechanics and Engineering*, 97:157–192, 1992. *Cited page 58*

[105] C. Förster, W. A. Wall, and E. Ramm. Stabilized finite element formulation for incompressible flow on distorted meshes. *International Journal for Numerical Methods in Fluids*, 60(10):1103–1126, 2009. *Cited page 58*

[106] A. Cangiani and E. Süli. The residual-free-bubble finite element method on anisotropic partitions. *SIAM Journal on Numerical Analysis*, 45(4):1654–1678, 2007. *Cited page 58*

[107] T. E. Tezduyar and Y. Osawa. Finite element stabilization parameters computed from element matrices and vectors. *Computer Methods in Applied Mechanics and Engineering*, 190(3-4):411–430, 2000. *Cited page 59*

[108] D. Sipp and A. Lebedev. Global stability of base and mean flows: a general approach and its applications to cylinder and open cavity flows. *Journal of Fluid Mechanics*, 593:333–358, 2007. *Cited page 59*

[109] J. Sari, F. Cremonesi, M. Khalloufi, F. Cauneau, P. Meliga, Y. Mesri, and E. Hachem. Anisotropic adaptive stabilized finite element solver for rans models. *International Journal for Numerical Methods in Fluids*, 2017. fld.4475. *2 citations pages 60 and 108*

[110] Yan Bao, Dai Zhou, Cheng Huang, Qier Wu, and Xiang-qiao Chen. Numerical prediction of aerodynamic characteristics of prismatic cylinder by finite element method with spalart–allmaras turbulence model. *Computers & structures*, 89(3):325–338, 2011. *3 citations pages 60, 61, and 63*

[111] J. Volker. Reference values for drag and lift of a two-dimensional time-dependent flow around a cylinder. *International Journal for Numerical Methods in Fluids*, 44(7):777–788, 2004. *Cited page 61*

[112] Mohsen Maleki, Brian Seguin, and Eliot Fried. Kinematics, material symmetry, and energy densities for lipid bilayers with spontaneous curvature. *Biomechanics and Modeling in Mechanobiology*, 12(5):997–1017, 2013. *Cited page 69*

[113] Luca Scarbolo, Federico Bianco, and Alfredo Soldati. Coalescence and breakup of large droplets in turbulent channel flow. *Physics of Fluids*, 27(7):073302, 2015. *Cited page 69*

[114] Li Ying and Qi Wang. Microfluidic chip-based technologies: emerging platforms for cancer diagnosis. *BMC Biotechnology*, 13(1):76, 2013. *Cited page 69*

[115] M. Nitschke and S.G.V.A.O. Costa. Biosurfactants in food industry. *Trends in Food Science & Technology*, 18(5):252 – 259, 2007. *Cited page 69*

[116] Gilou Agbaglah, Sébastien Delaux, Daniel Fuster, Jérôme Hoepffner, Christophe Josserand, Stéphane Popinet, Pascal Ray, Ruben Scardovelli, and Stéphane Zaleski. Parallel simulation of multiphase flows using octree adaptivity and the volume-of-fluid method. *Comptes Rendus Mécanique*, 339(2 - 3):194 – 207, 2011. *Cited page 69*

[117] Y. Ling, S. Zaleski, and R. Scardovelli. Multiscale simulation of atomization with small droplets represented by a lagrangian point-particle model. *International Journal of Multiphase Flow*, 76:122 – 143, 2015. *Cited page 69*

[118] S. P. van der Pijl, A. Segal, C. Vuik, and P. Wesseling. A mass-conserving level-set method for modelling of multi-phase flows. *International Journal for Numerical Methods in Fluids*, 47(4):339–361, 2005. *2 citations pages 69 and 71*

[119] Y.C. Chang, T.Y. Hou, B. Merriman, and S. Osher. A level set formulation of eulerian interface capturing methods for incompressible fluid flows. *Journal of Computational Physics*, 124(2):449 – 464, 1996. *Cited page 70*

[120] T.E. Tezduyar, M. Behr, S. Mittal, and J. Liou. A new strategy for finite element computations involving moving boundaries and interfaces—the deforming-spatial-domain/space-time procedure: Ii. computation of free-surface flows, two-liquid flows, and flows with drifting cylinders. *Computer Methods in Applied Mechanics and Engineering*, 94(3):353 – 371, 1992. *Cited page 70*

[121] J.U Brackbill, D.B Kothe, and C Zemach. A continuum method for modeling surface tension. *Journal of Computational Physics*, 100(2):335 – 354, 1992. *Cited page 70*

[122] U. Rasthofer, F. Henke, W.A. Wall, and V. Gravemeier. An extended residual-based variational multiscale method for two-phase flow including surface tension. *Computer Methods in Applied Mechanics and Engineering*, 200(21 - 22):1866 – 1876, 2011. *5 citations pages 70, 75, 76, 81, and 82*

[123] Zhihua Xie, Dimitrios Pavlidis, James R. Percival, Jefferson L.M.A. Gomes, Christopher C. Pain, and Omar K. Matar. Adaptive unstructured mesh modelling of multiphase flows. *International Journal of Multiphase Flow*, 67, Supplement:104 – 110, 2014. *Cited page 70*

[124] S. Hysing. A new implicit surface tension implementation for interfacial flows. *International Journal for Numerical Methods in Fluids*, 51(6):659–672, 2006. *2 citations pages 70 and 71*

[125] Jian-Jun Xu and Hong-Kai Zhao. An eulerian formulation for solving partial differential equations along a moving interface. *Journal of Scientific Computing*, 19(1-3):573–594, 2003. *2 citations pages 70 and 71*

[126] W. Zheng, J.-H. Yong, and J.-C. Paul. Simulation of bubbles. *Graphical Models*, 71(6):229 – 239, 2009. *2 citations pages 70 and 71*

[127] T.J.R. Hughes, G.R. Feijóo, L. Mazzei, and J.-B. Quincy. The variational multiscale method - a paradigm for computational mechanics. *Computer Methods in Applied Mechanics and Engineering*, 166(1-2):3–24, 1998. *3 citations pages 70, 72, and 94*

[128] S. Hysing, S. Turek, D. Kuzmin, N. Parolini, E. Burman, S. Ganesan, and L. Tobiska. Quantitative benchmark computations of two-dimensional bubble dynamics. *International Journal for Numerical Methods in Fluids*, 60(11):1259–1288, 2009. *6 citations pages 70, 74, 77, 79, 80, and 81*

[129] Gustavo C. Buscaglia and Roberto F. Ausas. Variational formulations for surface tension, capillarity and wetting. *Computer Methods in Applied Mechanics and Engineering*, 200(45 - 46):3011 – 3025, 2011. *Cited page 71*

[130] K.B. Nakshatrala, D.Z. Turner, K.D. Hjelmstad, and A. Masud. A stabilized mixed finite element method for darcy flow based on a multiscale decomposition of the solution. *Computer Methods in Applied Mechanics and Engineering*, 195(33-36):4036–4049, 2006. *2 citations pages 72 and 94*

[131] G. Scovazzi. Lagrangian shock hydrodynamics on tetrahedral meshes: A stable and accurate variational multiscale approach. *Journal of Computational Physics*, 231(24):8029–8069, 2012. *3 citations pages 72, 94, and 97*

[132] L. Štrubelj, I. Tiselj, and B. Mavko. Simulations of free surface flows with implementation of surface tension and interface sharpening in the two-fluid model. *International Journal of Heat and Fluid Flow*, 30(4):741 – 750, 2009. *Cited page 74*

[133] Emilie Marchandise and Jean-François Remacle. A stabilized finite element method using a discontinuous level set approach for solving two phase incompressible flows. *Journal of Computational Physics*, 219(2):780 – 800, 2006. *2 citations pages 75 and 76*

[134] M. Sussman, K.M. Smith, M.Y. Hussaini, M. Ohta, and R. Zhi-Wei. A sharp interface method for incompressible two-phase flows. *Journal of Computational Physics*, 221(2):469–505, 2007. *Cited page 91*

[135] D. Enright, R. Fedkiw, J. Ferziger, and I. Mitchell. A hybrid particle level set method for improved interface capturing. *Journal of Computational Physics*, 183(1):83–116, 2002. *Cited page 91*

[136] S.O. Unverdi and G. Tryggvason. A front-tracking method for viscous, incompressible, multi-fluid flows. *Journal of Computational Physics*, 100(1):25–37, 1992. *Cited page 91*

[137] X.Y. Hu and N.A. Adams. An incompressible multi-phase sph method. *Journal of Computational Physics*, 227(1):264–278, 2007. *Cited page 91*

[138] O. Desjardins, G. Blanquart, G. Balarac, and H. Pitsch. High order conservative finite difference scheme for variable density low mach number turbulent flows. *Journal of Computational Physics*, 227(15):7125–7159, 2008. *Cited page 91*

[139] J. Luo, X.Y. Hu, and N.A. Adams. A conservative sharp interface method for incompressible multiphase flows. *Journal of Computational Physics*, 284:547–565, 2015. *Cited page 91*

[140] R. Saurel and R. Abgrall. Simple method for compressible multifluid flows. *SIAM Journal on Scientific Computing*, 21(3):1115–1145, 1999. *Cited page 91*

[141] C. Farhat, J.-F. Gerbeau, and A. Rallu. Fiver: A finite volume method based on exact two-phase riemann problems and sparse grids for multi-material flows with large density jumps. *Journal of Computational Physics*, 231(19):6360–6379, 2012. *Cited page 91*

[142] R.P. Fedkiw, T. Aslam, B. Merriman, and S. Osher. A non-oscillatory eulerian approach to interfaces in multimaterial flows (the ghost fluid method). *Journal of Computational Physics*, 152(2):457–492, 1999. *Cited page 91*

[143] S.Y. Kadioglu, M. Sussman, S. Osher, J.P. Wright, and M. Kang. A second order primitive preconditioner for solving all speed multi-phase flows. *Journal of Computational Physics*, 209(2):477–503, 2005. *Cited page 91*

[144] T.G. Liu, B.C. Khoo, and C.W. Wang. The ghost fluid method for compressible gas-water simulation. *Journal of Computational Physics*, 204(1):193–221, 2005. *Cited page 91*

[145] R. Valette, M.R. Mackley, and G.H.F. del Castillo. Matching time dependent pressure driven flows with a rolie poly numerical simulation. *Journal of Non-Newtonian Fluid Mechanics*, 136(2-3):118–125, 2006. *Cited page 91*

[146] F. Xiao, R. Akoh, and S. Ii. Unified formulation for compressible and incompressible flows by using multi-integrated moments ii: Multi-dimensional version for compressible and incompressible flows. *Journal of Computational Physics*, 213(1):31–56, 2006. *Cited page 92*

[147] R. Caiden, R.P. Fedkiw, and C. Anderson. A numerical method for two-phase flow consisting of separate compressible and incompressible regions. *Journal of Computational Physics*, 166(1):1–27, 2001. *Cited page 92*

[148] C.-D. Munz, S. Roller, R. Klein, and K.J. Geratz. The extension of incompressible flow solvers to the weakly compressible regime. *Computers and Fluids*, 32(2):173–196, 2003. *Cited page 92*

[149] J. Bruchon, A. Fortin, M. Bousmina, and K. Benmoussa. Direct 2d simulation of small gas bubble clusters: From the expansion step to the equilibrium state. *International Journal for Numerical Methods in Fluids*, 54(1):73–101, 2007. *Cited page 92*

[150] M. Billaud, G. Gallice, and B. Nkonga. A simple stabilized finite element method for solving two phase compressible-incompressible interface flows. *Computer Methods in Applied Mechanics and Engineering*, 200(9-12):1272–1290, 2011. *3 citations pages 92, 99, and 102*

[151] G. Hauke and T.J.R. Hughes. A comparative study of different sets of variables for solving compressible and incompressible flows. *Computer Methods in Applied Mechanics and Engineering*, 153(1-2):1–44, 1998. *2 citations pages 92 and 93*

[152] G. Hauke and T.J.R. Hughes. A unified approach to compressible and incompressible flows. *Computer Methods in Applied Mechanics and Engineering*, 113(3-4):389–395, 1994. *2 citations pages 92 and 93*

[153] E. Hachem, S. Feghali, R. Codina, and T. Coupez. Immersed stress method for fluid-structure interaction using anisotropic mesh adaptation. *International Journal for Numerical Methods in Engineering*, 94(9):805–825, 2013. *Cited page 94*

[154] T. Dubois, F. Jauberteau, and R. Temam. *Dynamic Multilevel Methods and the Numerical Simulation of Turbulence*. Cambridge University Press, Cambridge, UK New York, 1999. *Cited page 95*

[155] J.-P. Caltagirone, S. Vincent, and C. Caruyer. A multiphase compressible model for the simulation of multiphase flows. *Computers and Fluids*, 50(1):24–34, 2011. *2 citations pages 97 and 98*

[156] D. Bhaga and M.E. Weber. Bubbles in viscous liquids: Shapes, wakes and velocities. *Journal of Fluid Mechanics*, 105:61–85, 1981. *Cited page 104*

[157] Asghar Esmaeeli and Grétar Tryggvason. Computations of film boiling. part i: numerical method. *International Journal of Heat and Mass Transfer*, 47(25):5451 – 5461, 2004. *2 citations pages 108 and 114*

[158] Asghar Esmaeeli and Grétar Tryggvason. Computations of film boiling. part ii: multi-mode film boiling. *International Journal of Heat and Mass Transfer*, 47(25):5463 – 5476, 2004. *Cited page 108*

[159] G. Tryggvason, A. Esmaeeli, and N. Al-Rawahi. Direct numerical simulations of flows with phase change. *Computers & Structures*, 83(6–7):445 – 453, 2005. Frontier of Multi-Phase Flow Analysis and Fluid-StructureFrontier of Multi-Phase Flow Analysis and Fluid-Structure. *Cited page 108*

[160] Samuel W.J. Welch and John Wilson. A volume of fluid based method for fluid flows with phase change. *Journal of Computational Physics*, 160(2):662 – 682, 2000. *3 citations pages 108, 112, and 114*

[161] Samuel W.J. Welch. Local simulation of two-phase flows including interface tracking with mass transfer. *Journal of Computational Physics*, 121(1):142 – 154, 1995. *Cited page 108*

[162] Yohei Sato and Bojan Ničeno. A sharp-interface phase change model for a mass-conservative interface tracking method. *Journal of Computational Physics*, 249:127 – 161, 2013. *Cited page 108*

[163] S. Hardt and F. Wondra. Evaporation model for interfacial flows based on a continuum-field representation of the source terms. *Journal of Computational Physics*, 227(11):5871 – 5895, 2008. *2 citations pages 108 and 112*

[164] Sébastien Tanguy, Thibaut Ménard, and Alain Berlemont. A level set method for vaporizing two-phase flows. *Journal of Computational Physics*, 221(2):837 – 853, 2007. *Cited page 108*

[165] Jan Schlottke and Bernhard Weigand. Direct numerical simulation of evaporating droplets. *Journal of Computational Physics*, 227(10):5215 – 5237, 2008. *Cited page 108*

[166] Jaewon Lee, Gihun Son, and Han Young Yoon. Numerical simulation of the quenching process in liquid jet impingement. *International Communications in Heat and Mass Transfer*, 61:146 – 152, 2015. *Cited page 108*

[167] Miad Yazdani, Thomas Radcliff, Marios Soteriou, and Abbas A. Alahyari. A high-fidelity approach towards simulation of pool boiling. *Physics of Fluids*, 28(1), 2016. *Cited page 108*

[168] V. Mihalef, B. Unlusu, D. Metaxas, M. Sussman, and M. Y. Hussaini. Physics based boiling simulation. In *Proceedings of the 2006 ACM SIGGRAPH/Eurographics Symposium on Computer Animation*, SCA '06, pages 317–324, Aire-la-Ville, Switzerland, Switzerland, 2006. Eurographics Association. *Cited page 108*

[169] Chirag R. Kharangate and Issam Mudawar. Review of computational studies on boiling and condensation. *International Journal of Heat and Mass Transfer*, 108, Part A:1164 – 1196, 2017. *Cited page 108*

[170] Ju Liu, Chad M. Landis, Hector Gomez, and Thomas J.R. Hughes. Liquid-vapor phase transition: Thermomechanical theory, entropy stable numerical formulation, and boiling simulations. *Computer Methods in Applied Mechanics and Engineering*, 297:476 – 553, 2015. *Cited page 108*

[171] Jesus Bueno and Hector Gomez. Liquid-vapor transformations with surfactants. phase-field model and isogeometric analysis. *Journal of Computational Physics*, 321:797 – 818, 2016. *Cited page 108*

[172] Jesus Bueno, Carles Bona-Casas, Yuri Bazilevs, and Hector Gomez. Interaction of complex fluids and solids: theory, algorithms and application to phase-change-driven implosion. *Computational Mechanics*, 55(6):1105–1118, 2015. *Cited page 108*

[173] Richard Saurel and Rémi Abgrall. A multiphase godunov method for compressible multifluid and multiphase flows. *Journal of Computational Physics*, 150(2):425 – 467, 1999. *Cited page 108*

[174] R. Saurel, F. Petitpas, and R. Abgrall. Modelling phase transition in metastable liquids: application to cavitating and flashing flows. *Journal of Fluid Mechanics*, 607:313–350, 2008. *Cited page 108*

[175] L. Marioni, F. Bay, and E. Hachem. Numerical stability analysis and flow simulation of lid-driven cavity subjected to high magnetic field. *Physics of Fluids*, 28(5):057102, 2016. *Cited page 108*

[176] S. Riber, R. Valette, Y. Mesri, and E. Hachem. Adaptive variational multiscale method for bingham flows. *Computers & Fluids*, 138:51 – 60, 2016. *Cited page 108*

[177] Frédéric Gibou, Liguo Chen, Duc Nguyen, and Sanjoy Banerjee. A level set based sharp interface method for the multiphase incompressible navier–stokes equations with phase change. *Journal of Computational Physics*, 222(2):536 – 555, 2007. *Cited page 112*

[178] Mohammad W. Akhtar and Stanley J. Kleis. Boiling flow simulations on adaptive octree grids. *International Journal of Multiphase Flow*, 53:88 – 99, 2013. *Cited page 114*

[179] P. J. Berenson. Film-boiling heat transfer from a horizontal surface. *Journal of Heat Transfer*, 83(3):351 – 356, 1961. *Cited page 115*

[180] V.V. Klimenko. Film boiling on a horizontal plate - new correlation. *International Journal of Heat and Mass Transfer*, 24(1):69 – 79, 1981. *Cited page 115*

[181] Chahrazade Bahbah. *Simulation of the quenching process and conservative interpolation from mesh to mesh*. PhD thesis, MINES ParisTech - PSL Research University, 2016-2019. *Cited page 142*

[182] Wafa Daldoul. *Moving and conformal mesh for complex geometries*. PhD thesis, MINES ParisTech - PSL Research University, 2016-2019. *Cited page 142*

[183] Carlos Tevi Mensah. *Finite element methods for the simulation of radiative transfers*. PhD thesis, MINES ParisTech - PSL Research University, 2017-2020. *Cited page 142*

Résumé

Les procédés de trempe sont largement répandus dans l'industrie en particulier dans le domaine de l'automobile, du nucléaire et de l'aérospatiale car ils ont un impact direct sur la microstructure, les propriétés mécaniques et les contraintes résiduelles de pièces critiques. La trempe est un processus fortement non-linéaire à cause des couplages forts entre la mécanique des fluides, les transferts thermiques aux différentes interfaces, les transformations de phase du solide et l'ébullition du milieu de trempe. Malgré les progrès effectués par la simulation numérique, ce procédé reste extrêmement difficile à modéliser.

Dans ce travail, nous proposons le développement d'outils numériques permettant la simulation réaliste de ce procédé à l'échelle industrielle. La mécanique des fluides est simulée en utilisant une méthode d'Elements Finis stabilisés permettant de considérer des écoulements à haut nombre de Reynolds. Les transferts thermiques sont calculés directement sans l'utilisation de coefficients de transferts empiriques, en utilisant le couplage fort entre le fluide et le solide. Nous avons développé un modèle de changement de phase pour l'eau permettant de considérer les différents régimes d'ébullition. Une formulation unifiée des équations de Navier-Stokes, considérant une phase compressible et une phase incompressible a été développée afin de prendre en compte plus précisément la dynamique de la vapeur et de l'eau. Une procédure dynamique d'adaptation anisotrope de maillage, permettant une description plus fine des interfaces et une prise en compte plus précise des caractéristiques des écoulements est utilisée. Des exemples numériques exigeants ainsi qu'une validation expérimentale permettent d'évaluer la précision et la robustesse des outils proposés.

Les outils développés permettent ainsi l'optimisation du mode opératoire du procédé, des ressources consommées et servent ainsi d'outils prospectifs pour la conception de produits.

Mots Clés

Procédés de trempe, Ebullition, Ecoulements multiphasiques, Eléments Finis stabilisés, Level Set, Adaptation de maillage anisotrope.

Abstract

Quenching processes of metals are widely adopted procedures in the industry, in particular automotive, nuclear and aerospace industries, since they have direct impacts on changing mechanical properties, controlling microstructure and releasing residual stresses of critical parts. Quenching is a highly nonlinear process because of the strong coupling between the fluid mechanics, heat transfer at the interface solid-fluid, phase transformation in the metal and boiling. In spite of the maturity and the popularity of numerical formulations, several involved mechanisms are still not well resolved.

Therefore we propose a Direct Numerical Simulation of quenching processes at the industrial scale dealing with these phenomena. The fluid mechanics is simulated using a Finite Element Method adapted for high convective flows allowing the use of high stirring velocity in the quenching bath. Heat transfers are computed directly without the use of heat transfer coefficients but using the strong coupling between the fluid and the solid. We use a phase change model for the water that models all boiling regimes. A unified formulation of the Navier-Stokes equations, taking into account a compressible gas and an incompressible liquid is developed to model more accurately the vapor-water dynamics. A dynamic mesh adaptation procedure is used, increasing the resolution in the description of the interfaces and capturing more accurately the features of the flows. We assess the behavior and the accuracy of the proposed formulation in the simulation of time-dependent challenging numerical examples and experimental results.

These recent developments enable the optimization of the process in terms of operating conditions, resources consumed and products conception.

Keywords

Quenching processes, Boiling, Multiphase flows, Stabilized Finite Element Method, Level Set, Anisotropic mesh adaptation